Development of a multi-scale approach using chemical kinetics and reactive force field molecular dynamics to model soot formation and oxidation

Michel Keller

INSTITUT POLYTECHNIQUE DE PARIS

NNT : 2019IPPAE005

Thèse de doctorat

Development of a Multi-Scale Approach using Chemical Kinetics and Reactive Force Field Molecular Dynamics to model Soot Formation and Oxidation

Thèse de Doctorat de l'Institut Polytechnique de Paris
préparée à l'IFP Energies nouvelles

École Doctorale n°626 : de l'Institut Polytechnique de Paris
(ED IP Paris)
Spécialité de Doctorat: Ingénierie Mécanique et Energétique

Thèse présentée et soutenue à Rueil Malmaison, 19/12/2019, par

Michel Keller

Composition du Jury :

Benoit Fiorina Professeur, Centrale Supelec (– EM2C)	Président
Kai Leonhard Professeur, RWTH Aachen (– LTT)	Rapporteur
Baptiste Sirjean Professeur, Université de Lorraine (– LRGP)	Rapporteur
Dominique Costa Directrice de Recherche, Chimie ParisTech (– IRCP)	Examinateur
Nabiha Chaumeix Directrice de Recherche, CNRS Orléans (– ICARE)	Examinateur
Mickaël Matrat Chercheur, IFP Energies nouvelles	Examinateur
Theodorus de Bruin Chercheur, IFP Energies nouvelles	Examinateur
Laurent Catoire Professeur, ENSTA Paris (– UCP)	Directeur de thèse
André Nicolle Chercheur, Aramco Overseas	Invité

Abstract

In this PhD study a multiscale approach has been applied to model processes during soot inception and early soot oxidation. For this macroscopic detailed gas-phase kinetic calculations are employed, using Chemkin, to model the combustion gas-phase of a model fossil fuel in a heterogeneous closed reactor under various conditions. In order to investigate the impact of temperature, fuel mixture and equivalence ratio, i.e., the fuel to air ratio, on the soot formation process, a range of these three parameters has been scanned. The range of tested equivalence ratios and temperatures were chosen to ensure elevated soot formation, that is high equivalent ratios and temperatures are taken. Fuel mixtures of n-decane and toluene have been tested, to model the impact of aliphatic and aromatic fuels and mixtures of both. From the results of the reaction kinetic calculations, molecules relevant to soot formation, so-called soot precursors, have been extracted according to certain criteria. This is done in order to allow to introduce these soot precursor compositions in simulation boxes to model bond formation between soot precursor molecules with reactive force field molecular dynamics modeling.

In order to get the best description of the soot formation processes, three reactive force fields are evaluated and compared to ab initio calculations. Furthermore, the capability of the three force fields to form clusters at different temperatures is tested. The influence of simulation parameters used in the reactive force field molecular modeling approach, such as temperature and time step, on the accuracy of the calculations is investigated to confirm the optimal modeling conditions.

The impact on the composition of the simulated gas-phase due to changes of the scanned parameters in the macroscopic kinetic gas-phase calculations translate well to the soot precursor compositions. The influence of the different compositions has been investigated on the rate and structure of the molecules produced through bond-formation between soot

precursors. The resulting structures compare well to previously reported experimental results. Furthermore, the bond formation rate between soot precursors is found to be linearly correlated with the temperature at which the soot precursors are generated, while fuel and equivalence ratio does not have a direct impact on the reaction rate.

The generated growth structures are lumped into three structural classes: 1) directly linked, 2) pericondensed polycyclic and 3) aliphatically linked hydrocarbons. It is found that the amount of aliphatically linked molecules, as well as the presence of sidechains in the modeled structures, increases with the amount of aliphatic content of fuel mixture. In addition, a reaction scheme is presented displaying the most representative reaction pathways to form growth structures in each lumping class and their eventual interconversion.

Moreover, the impact of structural differences in the structures, generated by bond formation between soot precursor, on their oxidation kinetics is tested. For this, the species are further differentiated for the presence of a sidechain or not in addition to the above presented structural groups. Then the interactions of the species of each structural group and four different oxidizers are modeled.

The main products of the oxidation reactions are analyzed, and the reaction pathways investigated. It can be shown that the kinetics are different for species that possess an aliphatic sidechain compared to those that do not. Furthermore, the kinetics of the oxidation reactions with the nascent soot structures are investigated. Finally, activation energies for the oxidation reactions are estimated, by plotting the rate constant, obtained by exponential fitting of the decay of oxidizer molecules, over the inverse temperature.

The present work – that applies a combined approach of macroscopic gas-phase kinetic calculations and atomistic reactive force field simulations – offers a good methodology to obtain structural differences of nascent soot for a broad range of thermodynamic conditions and detailed reaction mechanisms for soot inception and oxidation processes.

Résumé

Dans cette thèse doctorale, une approche multi-échelles a été appliquée aux processus de modélisation pendant la formation de la suie et l'oxydation précoce de la suie. En effet, des calculs cinétiques macroscopiques en phase gazeuse ont été réalisés, à l'aide du code Chemkin, pour modéliser la combustion d'un combustible fossile modèle en phase gazeuse dans un réacteur fermé et hétérogène, à diverses conditions thermochimiques. L'impact de la température, la nature de carburant et le rapport carburant/oxygène ont notamment été étudiés, sur le processus de formation de suie. Afin de s'assurer que la formation de suie se produise, des rapports de carburant/oxygène et des températures élevées ont été sélections. Des mélanges de n-décane et de toluène ont été testés pour modéliser l'impact des carburants aliphatiques et aromatiques. À partir des résultats des calculs de cinétique macroscopiques, des molécules pertinentes pour la formation de suie, appelées précurseurs de suie, ont été extraites en fonction de certains critères. Ceci permet d'introduire de compositions de précurseurs de suie dans des boîtes de simulation pour modéliser la formation de liaisons entre les molécules de précurseurs de suie avec un champ de force réactive empirique en utilisant des simulations de dynamique moléculaire.

En amont, trois champs de forces réactives différents ont été évalués et comparés aux calculs ab initio pour valider que le champ de force décrit correctement les réactions chimiques impliquées dans le processus de formation de suie. Les variables pour les calculs dynamiques moléculaires, comme la température et le pas de temps ont été optimisés, afin d'obtenir le meilleur rapport temps de simulation par temps de CPU.

L'impact des trois paramètres utilisés dans les calculs cinétiques macroscopiques se traduit dans les compositions des précurseurs de suie obtenues avec les simulations dynamiques moléculaires. Il s'avère que la température joue un rôle clé dans la formation des liaisons chimiques entre les précurseurs de suie. En effet, les structures de croissance augmentent de la

façon linéaire avec une augmentation de la température, tandis que le rapport carburant/oxygène et le rapport décane/toluène n'ont quasi n'ont pas d'incidence directe sur le taux de réaction.

Les produits de croissance générés pouvaient être regroupés selon leur structure en trois classes: 1) des composés aromatiques polycycliques directement liés, 2) des polycycliques péricondensés et 3) des composés aromatiques liés par une chaine alkyle aliphatique. On a pu constater que le nombre de molécules dans classe 3, ainsi que la présence des chaînes alkyles latérales, augmente avec la quantité de décane dans le mélange initial. De plus, un schéma réactionnel a été présenté montrant les voies de réaction les plus représentatives pour former les structures de croissance de chaque classe et leur interconversion éventuelle.

La cinétique d'oxydation des structures de croissances des trois classes, et la présence éventuelle des chaines alkyle latérales, a été étudiée par dynamique moléculaire avec quatre oxydants différents. Les principaux produits des réactions d'oxydation ont été analysés et les voies de réaction étudiées. On a pu démontrer que la cinétique diffère selon le classement des produits de croissance, mais également la présence de chaines alkyles impacte la cinétique d'oxydation. Les énergies d'activation des réactions d'oxydation ont été calculées en utilisant la loi d'Arrhenius.

Le présent travail - qui applique une approche combinée de calculs cinétiques macroscopiques en phase gazeuse et de simulations avec un champ de forces réactives atomiques empirique – correspond à une méthodologie originale pour générer des précurseurs de suie naissants, dont la structure chimique diffère selon les conditions thermodynamiques appliquées et étudier leur oxydation.

Acknowledgements

I like to thank Laurent Catoire for directing this thesis and his participation in this work. I appreciate the support he gave me and the valuable input. Especially since he was not initially planned as a thesis director, I recognize the value of him stepping up for me in my time of need. Thank you wholeheartedly for this.

Moreover, I would like to thank Theodorus de Bruin and Mickaël Matrat for the supervision of my thesis. I am grateful for the opportunity to conduct my research in such a great environment with two dynamic supervisors. I learned a lot from you and enjoyed the input I received, as well as the discussion we had.

I also want to thank my colleagues from the IFPEN, which provided a nice work environment. Especially all the other Ph.D. students I met along the way, which helped me as we could relate to each other's struggles. Also, thanks to Pascal Mougin, Jean-Charles de Hemptinne, and Chaouki Habchi, who always showed interest in me and my research. I would like to express my general acknowledgment to IPFEN and all employees for making this work possible. In addition thanks to the language teachers of the IFP School, who provided me with a great environment to be able to learn the French language.

Special thanks to the EU H2020 innovative training network titled "Effect of 4500 bar injection pressure and supercritical phase change of surrogate and real-world fuels enriched with additives and powering Diesel engines, on soot emissions reduction", by giving me this opportunity by providing funding from the European Union's Horizon 2020 research and innovation programme under the Marie Sklodowska-Curie grant agreement No 675528. I enjoyed the seminars and meeting we had in this project and would like to thank all other ESRs from the ITN for the great time we shared. In addition, I would like to acknowledge Professor Manolis Gavaises and Nikolaos Chatziarsenis for always reminding us of deadlines

and keeping the project well managed. Also, thanks to AVL, especially Mijo Trvdojević and Peter Priesching, for hosting me during my secondment.

Thanks to all my friends, who supported me throughout my life and always manage to cheer me up.

Of course, I want to thank my parents and my family for giving me all the support over the recent years. I could not imagine a better environment to grow up in. I truly love my parents and sisters and am forever grateful to have you by my side. Also special thanks to my grandparents who unfortunately cannot witness me finishing my Ph.D.

Lastly, I want to thank my girlfriend Nathalie. You supported me and stood by my side like no one else during the hardest times. It is still a dream come true to have found someone I can relate to so much and share my inner thoughts and deepest feelings with. I love you and always will.

I. Table of Contents

II. Table of Figures

III. Table of Tables

1. Introduction

Soot particles are carbonaceous products that form under incomplete fuel combustion, meaning incomplete oxidation of the feedstock, and hence they can have several sources, such as furnaces or forest fires, and internal combustion engines. Soot particles influence global climate change and soot has been placed as high as the second main source for radiative forcing.(1) These particles have been shown to not only contribute to global warming due to solar radiation absorption but also their deposition on ice and snow and the mixing in liquids, mixed phases and ice clouds has significant effects on weather and the environment.(2) Another great concern is the impact of soot on human health. When inhaled the nanoparticles are deposed in the respiratory tract and due to diffusion, they can be spread over the body.(3) It is known that the chemical composition of the particles does play a role in the impact on health,(4) but the precise relationship is not well understood, yet.(5)

As the number of combustion engines globally operated still increases (6,7) the problem of soot reduction in the atmosphere is currently addressed politically by more stringent emission regulations.(8) These regulations aim to reduce the harmful impact of exhaust gases, targeting fine particles (<20nm), known to be the most harmful, by including soot mass in exhaust gases and the number of particles. A decrease in particulate matter from the exhaust gases is mostly addressed by post-treatment, where up to 95% of the soot can be captured and burned in particulate filters.(9) However, particles not captured and released prove to be the fine particles.

Furthermore, soot formation influences engine performance,(10) due to the fact that the presence of soot in the combustion chamber modifies heat transfer and impacts mechanical components. On the other hand, the radiative heat transfer of soot is used favorably in some of the practical combustion systems and despite the modern categorization of soot as an unwanted by-product of combustion,

practical use of soot has been documented.(11–13) Evidence was found that soot was used as a pigment in prehistoric cave paintings and tattoos.(14,15) Carbon black, which is soot manufactured under controlled conditions, is to date used as pigment for printing paints, coatings or plastics and has useful applications as an active filler in rubber products, such as tires.(16,17)

Due to the above-mentioned reasons, a precise understanding of the physical and chemical processes leading to soot formation in combustion is necessary to improve the combustion conditions and regulate the amount of soot formed. Especially predictive models for soot formation are needed in order to help design combustion chambers to address the specific needs of their operators.(18) The process of soot formation is delicate as it is a concerted phenomenon driven by complex chemistry, thermodynamics, fluid dynamics, and particle physics. Furthermore, the conditions under which the soot is formed can widely change its characteristics.(19,20) Studies have shown that the fuel composition, the flame temperature, the pressure, the air to fuel ratio, addition of additives to the fuel or the soot after combustion, lubricants mixing into the fuel during combustion, or fuel-air mixing and turbulence, can all influence the amount of soot formed during the combustion process.(21–28) Predicting the influence of all of the mentioned factors is challenging. Hence, the processes of the formation and oxidation of soot particles, the influence of combustion conditions on soot nanostructure and on their reactivity have been investigated by experiments in the combustion chamber or model flames and numerous models have been proposed to describe the phenomena found.(19,24,29–34) Soot formation and oxidation have been an important research subject for several decades by now(28,35–40) and the progress of research has been reviewed multiple times. (10,13,32,41–47)

Flame diagnostics play an important role in the process of understanding the influences of combustion conditions on soot formation. The element of fire always has kindled the curiosity of

mankind and the first scientific investigations of flames date back centuries.(48) The experimental apparatus has significantly expanded over the recent decades, however. Laser-based optical techniques today can give insight into the in-situ processes of soot formation and intrusive measurements and subsequent analysis by atomic force or electron microscopy can unravel the nanostructure of the soot particles.(49–56) Furthermore, gas-phase chromatography can illustrate the different chemical species present during combustion.(57–60)

Accordingly, the understanding of the soot formation process evolved in recent years, from a mainly phenomenological viewpoint to more sophisticated theoretical models, aided by the rise of computational power.(13) Consequently, a number of software packages describing the combustion process on a large scale have been developed in recent years.(61–63) The soot models employed in these computer programs still contain some amount of phenomenological or semi-empirical parameters, however, and chemical species are not tracked explicitly.(32) As a result tracking of the chemical composition and detailed nanostructure of the soot particles is not possible.

Molecular models, on the other hand, can give insight into the complete chemical process during combustion. Theoretical chemical techniques, such as kinetic Monte Carlo approaches or reactive molecular modeling, allow for the simulation of combustion processes while keeping track of the exact chemical composition of the modeled space.(64–66) As a consequence, the size of the model is very limited, prohibiting to model the complete combustion process.

This work aims to understand the impact of fuel compositions and combustion conditions on the formation and the oxidation kinetics of soot particles and their nanostructure. In order to do so, a coupled multi-scale approach was developed and is presented in this work. This approach uses macroscopic gas-phase kinetic calculations to model the gas phase during combustion and combines the results with atomistic reactive force field simulations, with the aim of modeling the chemical

process of soot inception. This allows investigating the changes in nanostructure of the modeled soot particles as a function of the combustion conditions and subsequently the change in reactivity during oxidation.

The manuscript is structured as follows: The second chapter provides a review of the literature relevant in the field of soot. Differentiation and description of the relevant parts of the soot nanostructure are given, before giving an overview of the processes leading to the molecules relevant for soot formation, the so-called soot precursors. Moreover, a review of the state of the art for the understanding of the process for soot growth and soot oxidation is given.

In chapter 3 the theoretical background of the multi-scale approach presented in chapters 4 to 7 is given. Chapter 4 presents the detailed chemical kinetic gas-phase calculations. The procedure of translating the relevant molecules from the generated gas phase to the molecular modeling simulations is explained and validated. Changes of the molecular compositions extracted for the reactive force field simulations due to the scanned combustion conditions are discussed and rationalized.

Chapter 5 describes a case study on the capabilities of different reactive force field parameter sets to model the combustion dynamics. Additionally, the impact of general simulations parameters on the results of the reactive force field simulations is investigated.

In chapter 6 the results of the modeling of soot inception, using the molecular compositions acquired from the calculations performed in chapter 4, are presented. The resulting structures compare well to previously reported experimental results. Furthermore, the impact of the combustion parameters scanned in chapter 4 on the rate of bond formation and the nanostructure of the generated structures is investigated. The growth structures can be categorized into three different structural groups, and the influence of the change in molecular compositions due to

different parameters of the chemical kinetic gas-phase calculations on the number of structures formed for each group is analyzed. Additionally, the most representative reaction pathways to produce species of each of the respective structural groups are discussed.

In chapter 7 a study on the impact of the different structural groups and features on the reaction kinetics of the oxidation process is performed. Four different oxidizers are tested for their capabilities to oxidize the structures detected in chapter 6, the differences in reactivity due to different structural features are discussed and the most common reaction pathways portrayed. Moreover, the kinetics of the consumption of two of the four oxidizers is investigated and the results compared to literature.

Finally, Chapter 8 summarizes the conclusions of the thesis.

2. Soot Formation in Combustion

In this chapter, a review of the current state of the art on the processes leading to soot in combustion is given. Soot formation is complex as it consists of multiple chemical and physical processes. The first step of soot formation is the chemical formation of soot precursor molecules, so-called polycyclic aromatic hydrocarbons (PAH). These precursors condense, known as soot inception, and grow through chemical reactions and physical adsorption into larger structures, known as nascent soot particles. These nascent soot particles coalesce or agglomerate with one another and can adsorb more PAHs to grow larger. During this growth also chemical growth through smaller chemical species or chemical reactions between the precursors in the soot particle is possible, which leads to a graphitized structure of the mature soot particle.

2.1 Soot Particle Nanostructure

When talking about soot, and especially when concerned with the nanostructure, one has to be specific, since in the general language one often does not differentiate between char, coke or soot. While all of these are products of the pyrolysis of organic matter, there are differences in their main structural features, such as the degree of graphitization. The degree of graphitization/crystallinity (structural order as indicated by the diameters of graphitic domains, the degree of sp2 hybridization and the aromaticity) directly impacts the concentration of structural defects, which influences soot oxidative reactivity, as represented by the turnover frequency (TOF). To get the overall reaction rate, this site-dependent TOF should be integrated over the progress-dependent active surface area.

While industrial soot, called carbon black, is formed under controlled conditions (through hydrocarbon pyrolysis, i.e. in absence of oxygen), other soot is a randomly formed particulate carbon that is usually the product of incomplete combustion or pyrolysis. It can exhibit different

properties, like coarse, fine and/or colloidal structures, dependent on its origin.(67) Its core region consists of amorphous carbon and the outer shell of graphitic sheets.(68) Soot can exhibit impurities (69–71) which are inorganic compounds from additives of the fuels or the lubricant and ash. Also, soot from combustion engines is covered with the so-called soluble organic fraction, which includes heavy hydrocarbons from unburned fuel and from the engine lubricating oil, sulfur and water which is collected during the gas cooling phase.(72)

Mature soot particles show a fractal structure. These structures result from the clustering of primary particles.(10,71,73) Soot particle structure is described by fractal dimensions, the radius of gyration and/or projected area. The radius of gyration is used to describe non-spherical shapes of the particles, as it accounts for the variation in the distribution of mass around the center of mass. Fractal dimension gives an estimate of the complexity of the structure of the clustered primary particles. The projected area is a 2D projection of the particle shape. These parameters are generally obtained by measuring the mass of mobility diameter or scattering and/or microscopy measurements and provide the number of primary particles clustered in soot particles.(26,27,74)

One can define a basal structure unit (BSU) for the composition of soot. The BSU consist of a stack of several parallel graphite layers.(75) These structures can exhibit some amount of curvature. The length of the layers within a BSU can differ but also differs between BSUs. As the BSUs are in general not tightly packed, pores exist between them.

The pores allow smaller gas-phase species, like oxygen and oxygen-containing radicals, to penetrate the particles, resulting in oxidation from inside.(68,76) As oxidation of particles occurs the pore number changes and hence the penetration of particles by gas-phase molecules increases.(77) Once the core of a particle is sufficiently burned out the shell of the particle rearranges, leading to graphitization and making the particle more inert.(76,78) Nonetheless, not all soot has the same

reactivity and hence one has to differentiate and investigate how the reactivity is influenced by the local nanostructure.

The reason for the difference in reactivity is determined by the molecular nanostructure and due to that one discriminates different structural features of the graphitic fringes in soot. These are the fringe length, fringe separation, and orientation of the fringes, and tortuosity and curvature. The fringe length plays an important role in soot reactivity as carbon atoms on the edge of the graphitic layers are more reactive in comparison to the basal plane carbon atoms and hence shorter fringe lengths lead to higher reactivity.(79,80) The fringes are shorter in the particle center as it consists of amorphous carbon layers. Also, it has been shown that during the growth of soot particles the fringe length of the shell increases, as graphitization takes place due to surface reactions and rearrangement of the shell.(80)

The fringe separation distance is related to the orientation of the layers as the interspacing between fringes in stacked structures is denser than in randomly ordered regions. Therefore, fringe separation distance is generally higher in the amorphous core than in the graphitic shell and as a result, the fringe density is lower. It has been suggested that larger fringe separation distance can promote the access of oxygen to the edge-site carbon atoms and hence increase reactivity.(81)

Curvature and tortuosity also have an effect on the reactivity of the fringes, since more curvature in the fringe leads to a larger bond strain and thus increases chemical reactivity.(79) The term of tortuosity was introduced as a measure in HRTEM studies and is defined as the ratio of the length of a fringe to the distance between its ends. Studies showed that due to the strain, a break-up of curved graphitic sheets is more probable.(20) Also, tortuosity is higher in the center of the particles, hence providing an additional explanation for the particle burn-out.(78)

Table 1: Findings for differing nanostructures of soot from different fuels and laboratory conditions. The first column gives the study under which the findings were obtained, the second the laboratory conditions and in the third column the general findings are summarized.

Reference	Configuration	Observations
(19,20,79)	Premixed laminar flame	Benzene flames produce more amorphous regions than acetylene flames. Ethanol flames show more curvature in the graphitic layers. The curvature of the planes in the acetylene, benzene and indene flames is influenced by the flow rate (via reaction progress). The higher reactivity towards oxidation to curvature is related to the strain on the graphitic plane. Due to better accessibility C atoms on edge sites an amorphous structure shows higher reactivity.
(80)	Premixed laminar flame	While the nanostructure of soot formed from methane does not change significantly during its aging process, ethylene formed soot shows a continuous increase in graphitization The same behavior was observed for the cyclohexane and benzene soot, but in these flames also nascent soot particles showed a higher degree of graphitization than ethylene soot.
(82)	Laminar diffusion flame	The primary particle size in benzene soot is higher than in toluene or m-xylene but had a smaller degree of graphitization. Also, higher oxygen content in the benzene soot compared to the methylated aromatics was measured. The C/H ratio in soot is a good indicator for active site population and hence increased C/H ratio results in higher reactivity. The oxygen content in fuel has an influence on the soot oxidation reactivity.
(24,25,54,78,83–86)	Engine bench	Blending fuels with biodiesel alters the oxidation reactivity of soot particles by increasing the number of amorphous structures inside the particle. Biodiesel soot is more amorphous than Fischer Tropsch soot and hence has higher reactivity, due to the different oxygen contents. The oxygen content in biodiesel soot is higher, which does account for the higher reactivity. Different oxidation behaviors can be distinguished between the compared soot. The soot from biodiesel shows faster burn-out than soot from the other two fuels (conventional diesel and FT fuels). The soot nanostructure depends on the fuel, the running conditions of the engine and exhaust gas recirculation. The fringe tortuosity and fringe separation decrease during soot growth, while the fringe lengths increase. A change occurs in fractal structure and particle diameter between the early and the late combustion phase.

Soot nanostructure is influenced by the conditions under which the soot forms and the fuels from which it forms. There have been several studies linking the formation and structure of soot to the conditions and fuels giving some insights into the general influences these parameters have. Table 1 summarizes different studies on the differences in soot nanostructures from different fuels

2.2 Gas-phase Chemistry of Soot Precursor Formation

Stein and Fahr in 1985 showed that the formation of larger molecules by acetylene addition under high temperatures favors aromatic ring systems thermodynamically over the open aliphatic systems.(87) Furthermore, the most stable polyaromatic systems show a high number of C_6-rings. As a result, these so-called “stabilomers” are considered to be the major soot precursor molecules, since the nucleation process seems to involve relatively light species (100- 300 amu) and a number of experimental and theoretical studies support this finding.(10,59,88–91) Therefore aromatic structures are crucial to soot precursors, the formation of these molecules during combustion needs to be described when modeling soot formation. Over the recent years, a multitude of chemical mechanisms describing the formation of such soot precursors has been developed.(89,92–98)

2.2.1 Formation of the First Aromatic Ring

One important step in the formation of aromatic systems is the formation of the first aromatic ring from smaller molecules. Reactions of smaller nonaromatic species are not good monomers for nucleation, as the nucleation efficiency and dimer stability decrease rapidly with the size of the monomer as the Leonard-Jones-well involved in dimerization becomes shallower. Therefore, these smaller molecules only play an indirect role in soot formation and take part in surface growth. The pathways that are most crucial to the formation of the first ring are shown in Figure 1.

Reactions a and b show the formation of the first aromatic ring by an acetylene addition to a C_4 radical. This reaction is either described as a two-step process via the n-C_6H_X intermediate or by a direct chemically activated reaction. Frenklach and Wang argued that this pathway is the most significant one, since acetylene is present in high concentrations in fuel combustion and intermediate products do not require intramolecular rearrangements to form benzene.(89) Other studies have argued against this, showing that the isomerization of the n-C_4H_X species to the less reactive i-C_4H_X species occurs on a very fast basis.(35,99,100) Also, reactions of other C_4H_x species with C_2H or C_2H_3 are usually taken into account in the formation of the first aromatic ring but these are assumed not to play a major role.(89,93,95,99)

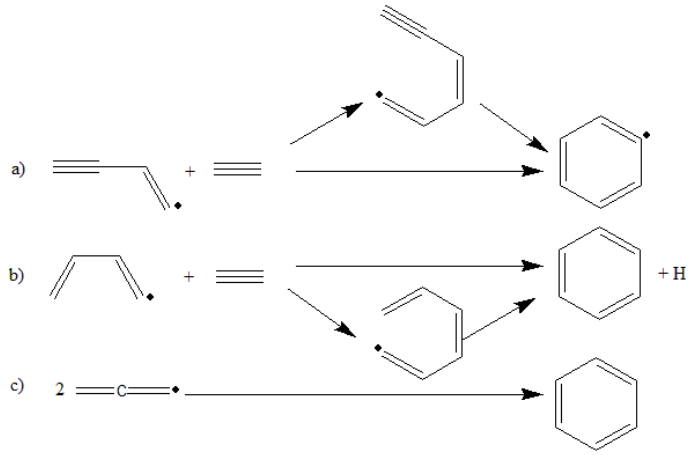

Figure 1. Three major pathways to the formation of the first aromatic ring

The formation of benzene through a recombination process of two propargyl radicals (reaction c) is not as straightforward as it appears. After collision the propargyl radicals undergo a number of rearrangement reactions and can form different C_6H_6 isomers. Recent theoretical studies and experimental findings have shown that it is probably one of the major pathways in which the first aromatic species form under sooting conditions.(35,90,100–102) Since the complete description of

all pathways including different isomers is rather difficult, however, the reaction is often described as one irreversible combination step.(92,93,95)

Reactions of benzene and phenyl formation considering C_5 species as reactants(57,92,99,103), mainly lead to fulvene, which then has to undergo a reorganization to form phenyl or benzene. A C_5 species found under sooting conditions is the cyclopentadienyl radical.(92,99) It is the smallest stable ring under high-temperature conditions, as it is resonantly stabilized, and plays a role in the further growth of aromatics. Hence its formation is included in some models.(95,104)

Other reaction pathways to form the first aromatic ring are ones that form substituted aromatic rings.(95) While the formation of substituted one-ring aromatics mainly occurs via the benzene and phenyl educts, a Diels-Alder reaction of smaller aliphatic molecules is also possible.(105) This is usually described by the recombination of C_4 species with propargyl for benzyl and toluene molecules.

2.2.2 Formation of Polyaromatic Hydrocarbons

One crucial pathway for the formation of polycyclic aromatic hydrocarbons (PAHs) beyond the first ring considered in all of the models is the H-abstraction-carbon-addition (HACA) mechanism proposed by Frenklach and Wang (right-hand side, Figure 2) and by Bittner and Howard (left-hand side, Figure 2).(89,106,107) These mechanisms are the most important to growth beneath the first ring due to the high acetylene concentrations in the flame and have been verified by experiment.(107,108)

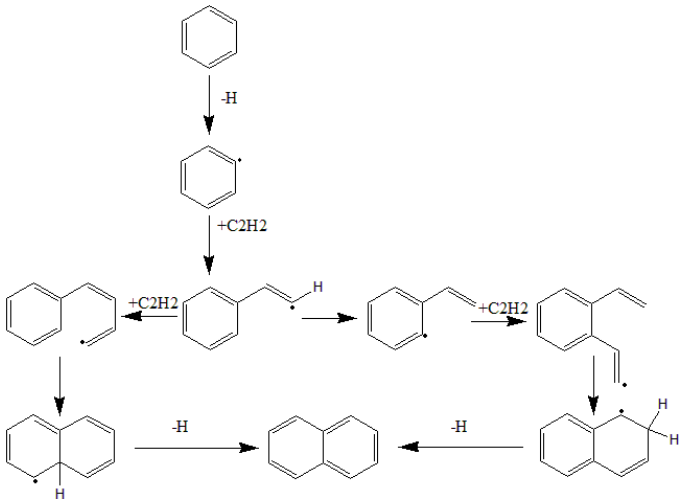

Figure 2. H-abstraction-carbon-addition mechanism for the growth of the second aromatic ring.

While the formation of two ring systems from educts formed by the oxidation of fuels can be described by the HACA mechanism, there are also other possible ways of formation for naphthalene and indene. Another formation reaction of naphthalene is the self-combination of two cyclopentadienyl radicals.(30,57,92,103) Here first a covalent bond between the two radicals is formed and through reorganization and ring openings of the C_5 rings naphthalene is formed consecutively. Indene can be formed by a combination of benzyl and a propargyl radical or by the combination of cyclopentadienyl with C_4 species.(57,92,104) Recent mechanisms include the formation of two-ring systems with other species than acetylene as well.(93,95) A recent quantum chemical investigation has also shown the relevance of the reactions of benzene and phenyl-radicals with species other than acetylene for the growth of two ring species under combustion conditions.(109) Finally, the production of naphthalene through dibenzofuran oxidation seems feasible.(98)

The formation of three-membered ring aromatics happens again mostly through the stepwise addition of acetylene to a smaller aromatic system. One other reaction for the formation of

phenanthrene, which is widely considered in literature, is the combination reaction of indene and cyclopentadiene radicals.(57,92,95,103,104) The reaction mechanism is similar to the cyclopentadiene self-combination reaction. Reactions leading to even larger aromatics are usually not described explicitly anymore and are lumped into the reactions concerning soot particles.

Due to the high acetylene concentration in combustion, the HACA mechanism is considered the major pathway to give larger PAHs. Also, several experiments have proven that the mechanism is plausible and intermediate products can be found in experiments.(110,111) For growth beyond the first ring, one has to consider the site at which the H-abstraction occurs on the PAH.(112)

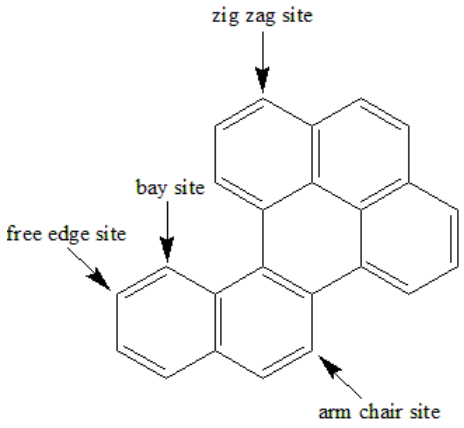

Figure 3. Different H-abstraction sites of PAHs.

The different sites for H-abstraction are shown in Figure 3. H-abstraction with further acetylene addition on the free edge site follows the path which is shown for the growth from the first to the second aromatic ring, but the other sites can have different mechanisms. On the bay site addition of an additional carbon atom leads to ring closure and the formation of a new ring. On the arm chair site addition of an acetylene molecule also leads to a formation of a new C_6-ring by a reaction with the ring on the other side of the arm-chair site.

On the zig-zag site, a direct cyclization can occur after an H-atom is abstracted and the addition of acetylene, leading to an aromatic C_5-ring. In general, the formation of a C_6 ring via acetylene addition is energetically more favorable, over the formation of a C_5-ring. This is due to the lower activation energies of the reaction steps. The reason for that is the higher ring strain in the smaller ring.(113) Nonetheless, as PAHs grow the edge sites develop more zigzag character, compared to free edge or arm-chair sites. Due to this C_5-ring formation is favored, since it results from a single acetylene addition to the zig-zag site, while for C_6-ring formation further addition of propylene or a methyl group after the initial addition of acetylene is needed.(114) After that, the C_5-ring can migrate over the edge of PAHs and also convert to C_6-rings.(114,115) None the less not all C_5-rings are converted and as a result, it is argued that soot precursors and subsequent PAH growth should include C_5-rings.(113,116–118)

A quantitative comparison of the performance of certain chemical mechanisms has been done recently by Roy et al. and the interested reader is referred to this study for further information.(119) Furthermore, Wang performed a sensitivity study for the formation of pyrene regarding flame chemistry and the formation of aromatics in a recent review.(13) These studies show that the chemistry in combustion processes is difficult to assess completely as there is a multitude of reactive species.(120) This makes it difficult to predict reactions, reaction rates, and concentrations accurately, since the concentration of different chemical species depends strongly on the description of the chemistry forming these species and hence the chemical soot composition.

Wang argues that the chemical kinetics of the formation of aromatics and soot precursors needs further research to get complete closure. This is a challenging demand regarding the number of different combustion engines and fuels that can be involved in these processes. Hence, he poses the question if there is a finite number of pathways for PAH formation and if the topic will ever find

closure.(13) He highlights the importance of experimental data in this process which can help to further understand the problem.

The remarks of Wang show, however, how essential the chemical mechanism for the formation of aromatics from fuel combustion processes is for the precise description of PAH precursor species. These species greatly influence the number, size and chemical composition of the soot particles and it has been shown that there are many differences in different flames.(121,122) Hence understanding these chemical processes makes a long way to understanding the formation of soot particles.

2.3 Soot Particle Growth

Modeling soot production is a challenging task since the processes involved occur at the solid-gas-phase boundary. This means one does not only need a precise description of the gas-phase species, but also an accurate picture of the physical and chemical composition of soot particles. The general agreement is that the production of soot particles can be divided into three sections: particle inception, coagulation and condensation, and surface reactions.

Crucial for modeling soot formation are experimental findings to which models can be compared. Based on the results of experiments models for the formation of soot are postulated. Normally one differentiates between three types of soot models: empirical, semi-empirical and detailed soot models.(32,43)

The difference, already given in the name, of these model approaches, lies in the way how the model is set up. Empirical models draw their parameters, like kinetics rate constants, and system functions, like rate equations, from empirical findings and their correlations. These are in good agreement with experimental results but give little to no insight on how the systems mechanisms are set up and how they change under different conditions.

Semi-empirical approaches often start from a predefined set of functions, conducted via a theoretical description of a system, and then use empirical parameters to solve these functions to get a good description of the system.(32) While these semi-empirical models bring a good understanding of the basic connections between theory and experiment, they often have reduced chemistry in their description of the system.

The detailed models start from an extensive description of the chemistry of the system, consisting of several hundred reactions. To achieve this they employ ab initio calculations to calculate reaction rates for the gas-phase chemistry and then use a kinetic Monte Carlo scheme to generate a gas-phase composition.(37,114,115) Like this, it is possible to derive the conditions and measurable results from a full description of the system.(32) These models often take in a high amount of computational cost and are therefore very expensive computationally. They give the most insight into the underlying mechanisms of soot formation and, hence, deliver a lot of information, however. Recently the development of ReaxFF has added to the detailed approach, by modeling gas-phase chemistry with a molecular modeling approach. It could be shown in numerous studies that combustion phenomena, as well as soot properties, could be modeled employing ReaxFF.(123–132)

2.3.1 Soot Particle Inception

Particle inception, or nucleation, refers to the formation of a soot particle from smaller particles. This step is most crucial to soot formation as it bridges from the gas to the solid phase. There is an uncertainty in the description of this initial phase as it involves both chemical and physical phenomena.(13,133) Experiments have shown that the fuel and flame conditions largely affect nascent soot particle structures, which has a major impact on the production of the soot particles.(19,134)

The range of mechanisms for particle inception has been differentiated into three concepts as shown: aliphatic linkage of PAHs, the stepwise chemical growth forming fullerene-like structures and physical agglomeration of PAHs forming dimers.(13) While the first two mechanisms are based on chemical linkage of the gas-phase molecules, the latter is based on physical interactions of soot precursor particles, i. e., Van der Waals forces. It has been argued that the pure chemical growth of soot particles through the HACA mechanism is too slow to account for the observed soot-nucleation rates.(13,106) Hence moderately sized aliphatic and aromatic molecules are likely to play a role in the mechanism of soot particle inception. Resonantly stabilized aromatic radicals have been shown to quickly form bonds due to the radical character, leading to a low energetic barrier of the reaction.(135) Since the radical character is kept after bond formation, resonance stabilized aromatic radicals might induce a chain-reaction, explaining the rapid growth of soot particles while still using a mechanism that is chemically driven.

There is experimental evidence of fullerene-like structures in flames (70) and measurements of H/C ratios showed that some amount of curvature must be present in soot particles.(136) This suggests that chemical growth plays a role in soot formation. A study by Frenklach et al. showed that by just considering growth via the HACA mechanism structures with a significant amount of curvature could be produced.(114) Recent studies have indicated that the formation of five-membered rings, and hence curvature, could also be explained by oxidation of PAHs with O_2.(137)

A quantum dynamics study by Violi et al. showed that the chemical growth of soot with PAHs by the linkage of two PAHs followed by further reorganizational and ring-closing reactions is feasible giving graphitic or fullerene-like structures.(138)

Taking into account aliphatic and aromatic radicals into the growth simulation, as well as rearrangement reactions and ring closure, Violi et al. were able to produce particles consisting of

large aromatic structures, with a broad range of C/H ratios and showed good agreement with experimental results.(30,64,139) With this approach particles with a high amount of curvature, as well as flat particles with several PAH like planes could be constructed.(113,140,141) They were able to link the structural dependence of particles to the type of fuel burned in premixed flames (30,141) and also different running conditions in counter-flow diffusion flames.(142,143)

Including oxygen chemistry to the growth mechanism also leads to compositions of the soot precursor molecules that include oxygen.(144,145) Violi et al. showed that these structures have a significant influence on the particle structures and growth, and hence soot inception.(144,146)

In the past years also, several approaches using ReaxFF to model chemical growth of soot particles were shown. Qian et al. showed that the generation of fullerene-like structures could be achieved with ReaxFF from benzene combustion by gradually removing hydrogen from the simulation boxes.(130) In a later study Han et al. showed that the formation of graphitic sheets and fullerene-like structure could be modeled using ReaxFF and a model jet fuel.(66) The densities and fuel-to-air ratios employed in this study are rather high, however, and therefore are lacking comparability with in-engine conditions. Xue et al. modeled fullerene-like nanocavities by simulating the pyrolysis of methane with ReaxFF.(131) Mao et al. did a study on the formation of soot by homomolecular dimerization from different PAHs at varying temperatures using ReaxFF.(125,126,147) They also showed with ReaxFF calculations that trace metal atoms might assist the soot formation process.(127) Yuan et al. estimated mixtures of PAHs and smaller radicals and modeled soot inception at different flame temperatures yielding soot particles of chemically linked PAHs.(148)

The most widely accepted mechanism for soot particle inception is the dimerization of two PAHs, with the smallest dimerizing PAH being pyrene due to its thermodynamic stability.(149) Experiments have shown that the size distribution of soot particles in flames shows a bimodal

behavior,(121) which is very well reproduced by models using dimerization as the inception step for soot particles.(13,134) The experimental evidence of excimers of aromatic aggregates in flames suggests that dimerization plays a role.(52) The argument for dimerization is that during the growth of PAHs the non-bonding interactions increase and at some point are able to accommodate for the sticking together of particles. Hence, a variety of soot models assume the irreversible dimerization of pyrene molecules to be the initial step to soot nucleation.(93,150,151) However, just recently Eaves et al. showed the importance of reversibility in soot inception with a nucleation study that accounts for reversibility.(152–154)

The sticking coefficient related to inception by physical dimerization is typically evaluated from the Lennard-Jones potential, which is, in turn, a function of the Hamaker constant.(155) There have been studies arguing that Van der Waals forces in pyrene are strong enough to plausibly describe the formation of dimers under flame conditions.(149,156) On the other side, there have been concerns regarding the dimerization mechanism of pyrene and recent studies have argued against this phenomenon.(13,157–159) A computation of the equilibrium constants of the dimerization using an updated PAH interaction potential(160,161) has shown that pyrene dimerization is unlikely to play a role in nucleation (158), and an investigation of the free energy surface by Violi et al. supports this finding, showing that dimerization of pyrene at high temperatures is thermodynamically unfavorable.(159)

However, an involvement of species larger than pyrene like ovalene and coronene may be involved in the nucleation step due to dimerization.(158,159) These large molecules are typically formed at the sub-ppm level in combustion conditions. Another explanation for dimerization are the findings of Violi et al. that PAHs substituted with aliphatic chains are more likely to form dimers.(159,162) Due to the additional states of freedom of the chain, the kinetic energy of the collision can be

converted to more vibrational and rotational modes and the dimer is stabilized. Zhang et al. showed that this kind of PAHs could be generated by a carbon-addition and hydrogen-migration reaction.(163)

Another interesting class for dimerization are aromatic moieties that are linked by aliphatic chains (AALH). Experimental findings show that these species occur under chemical growth conditions.(45) Wong et al. found in a molecular dynamics study that dimers of small AALH have lifetimes comparable to lifetimes of larger PAHs, but they found that for larger AALHs the lifetimes are shorter than those of comparable PAHs.(142) In a recent study Chung et al. also investigated AALHs, but could not find a better dimerization tendency of these species than PAHs.(162)

In the recent years, several studies have argued for isomeric PAH structures including 5-membered rings.(53,113,116–118,164) These species could be interesting for describing physical dimerization of PAHs as they possess a curvature of the graphitic plane and Kraft et al. recently showed that curved PAHs inhibit a polarization.(165) Hence, this polarization could be the key factor in strengthening the interactions between PAHs leading to dimerization.

Another suggestion to explain the rapid dimerization of PAHs was recently given by Wang.(13) He argued that moderately sized PAHs can be assumed to have radical or even diradical characteristics resulting from localized π-electron states. Following that assumption, this would significantly enhance the binding properties of PAH dimers and larger clusters to an amount that the π-bonds in PAH stacks are close to the strength of covalent bonds. Experimental or theoretical proof of this phenomenon has not yet been shown, however, leaving this hypothesis without further support.

2.3.2 Coalescence and Coagulation

Another important mechanism to soot growth is particle coagulation. In this process soot particle size increases though collision of two particles, which subversively stick together. Experiments have shown that these processes occur, as in mature soot multiple particle nuclei can be found.(55) The fact that the particles colliding differ in size and chemical composition makes a microscopical treatment of the physical forces acting upon collision very complicated. For this reason, coagulation is usually described by aerosol dynamics solving population balance equations.(166) For this, Smoluchowski's equations are used, to describe the meeting and subsequent sticking together of two particles in space. They contain the number density of particles of a certain mass per volume and a collision kernel. This symmetric rate kernel describes the rate at which a particle with a certain size meets another particle. Smoluchowski's initial description of the collision kernel was perikinetic accounting only for the cohesion of two particles. This was later updated by Smoluchowski to an orthokinetic model where shear forces are included in the description of the collisions. Several other orthokinetic collision kernels have been proposed as well. Some collision kernels account for sedimentation, which occurs in a gravitational field where particles of different sizes exhibit different velocities. Velocity correlated collision kernels, furthermore, account for particle velocity fluctuations in the flow field as well as gravity.(167) Most models use phenomenological values as collision efficiencies to accommodate for the forces holding particles together.(168,169) Also, most models were not developed to describe soot formation but rather the formation of other nanoparticles. Nonetheless, the general underlying phenomenology remains the same and hence the mechanisms describing coagulation can also be applied to soot particles.

The difference between the two processes of coagulation and coalescence is that during coagulation the initial particles keep their shape upon meeting with each other. During coalescence, the particles

fuse and form one new particle with a different shape. Therefore, one uncertainty in the models for coagulation is the description of the shape of the particles during and after coagulation. The reason for this is that it is still debated if the particles do coalesce after the initial coagulation. For example, models for other nanoparticles, such as silica particles, assume particles to be liquid up to a certain size(170), so coagulation is followed by coalescence and sintering. Soot particles, on the other hand, are rather rigid and mostly treated with solid-phase physics. Experimental results show a fractal structure of soot clusters, thus complete coalescence is unlikely.(55) For this reason, the concept of fractal dimension is applied in most coagulation models for soot particles. There have been some discussions about the actual value of the fractal dimension, however, as values from 1.3 up to 2.5 have been found.(171) The transferability of other coagulation models is not easy for the description of soot growth and more differentiated models have been developed in recent years.

Early models for coagulation of soot assumed the particles to have an initial spherical shape and also the coagulated particles were described with a spherical shape, which is obviously a rough approximation.(166,172) While mature soot particles are mostly spherical, this is probably due to surface growth and not due to instantaneous coalescence upon collision.(173) The following models improved this description by taking into account the volume and the surface of particles.(174) Recent studies improved this approach by additionally taking into account the number of active free sites or by tracking the number of aggregates and primary particles.(175) One limitation of these models is that they assume the primary particles to be monodisperse.(166) One promising recent model, developed by Sander et al., tracks the primary particles and describes the growth and changes in the shape of the coagulated particles using a stochastic approach based on matrices. These store the initial information of the primary particles and describe the shape change of the coagulated particles.(176) In comparison with experiments, this model proved to be very accurate.

Initially developed for the description of SiO_2 nanoparticles the model has been updated in further work to describe the coagulation of soot particles.(177)

Recent studies of Chen et al. have tackled the topic of sintering, showing that also a size-dependent behavior can be assumed for soot particles for their liquid-like and solid-like behavior.(178,179) There is experimental evidence supporting the assumption that to some extent nascent soot behaves liquid-like as the PAHs, which form the soot particle, restructure in the hot flame zones. This tends to indicate that coalescence and sintering of soot particles in the flame zone take place to some amount.(180) Early models including coalescence of soot particles assumed instantaneous merging of the particles.(181,182) The model of Sander et al. assumes a characteristic sintering time and also partial coalescence. The same approach was later also adopted by D'Anna et al.(183) Veshkini et al. also tested two different models for soot particle coalescence showing the improvement which can be achieved by including coalescence.(184)

The liquid-like behavior of nascent soot particles has some other impacts as well. For example, restructuring of the PAHs inside a soot particle makes more dense particles and can also form an outer shell of graphite-like structures.(19,185,186) The formation of this shell could also explain the variety of H/C ratios observed in mature soot particles as has been shown by Kholghy et al.(187) However, only very few models have a differentiated description of the movement of PAHs inside nascent soot particles, even though they show that this topic plays a significant role in the description of surface reactions, as nascent soot particles possess more reactive sites on the outer surface than mature particles.(187,188)

2.3.3 Soot Surface Growth Processes

Another soot growth process is the condensation of PAHs onto soot particles. Note that during this process no chemical bonds are formed at first and the sticking occurs again solely due to Van der

Waals forces. Hence, it is often described as similar to coagulation. Obviously, coalescence and sintering processes do not play a role in PAH condensation. Condensation influences the shape of the particle surface. However, studies have shown that the rounding of soot particles during aging may be due to the growth mechanism condensation and surface site reactions instead of coalescence.(173) The latter is described in the following section.

The process of particle surface site reactions is described by smaller particles that collide onto active radical surface sites of the soot particles forming σ-bonds. The chemical growth of soot particles is, in general, the same as the chemical growth of soot precursor molecules and subsequent chemical growth to nascent soot particles, as discussed before. Hence, it is essentially described by the HACA-mechanism and radical recombination of larger gas-phase molecules with the soot surface.(106) The difference in chemical growth of soot particles is the detail in the description of the soot reactivity towards the gas phase, as a complete atomistic description is not feasible anymore due to the size of the particles.

The reactivity of soot particles is therefore estimated by a phenomenological factor α, called aging factor or active surface site fraction, accounting for the active surface sites of a soot particle. This factor is included in the surface reaction kinetics since experiments show that there is a decrease of C_{soot}—H sites for aging soot.(189) Initially, a constant fraction of active surface sites was assumed, which was later updated to be a function of flame temperature and also of mean particle size.(93,190,191) Further studies have correlated the description of active surface sites to the age of soot particles accounting for the higher reactivity of nascent soot particles.(192) They introduced the concept of thermal age, which is the integral of temperature to which a particle has been exposed in its pathway over time. Additionally studies by Seneca et al. have shown that for

describing thermal annealing and aging of carbon structures correctly one has to take into account for the time dependence of both oxidation and graphitization.(193,194)

Except for the first model by Frenklach and Wang, where the aging factor is chosen to be constant in a fashion that it reproduces experimental data, all other calculations for this factor produced values close to unity, which is the maximal theoretical value for α. This gives the somewhat unphysical interpretation that the number of active surface sites for chemical reaction is close to the number of available soot surface sites. Dworkin et al. argue that due to the difference in soot particle growth for different regions of a laminar flame, which is more inception-dominated at the centerline of the flame and more surface growth-dominated at the wings, the models used such high values for α in order to make up for inaccuracies in their inception model.(120) Using a regional approach Veshkini et al. calculated a functional form of α using the concept of thermal aging.(189)

A precise calculation of the number density of the C_{soot}—H sites proves to be difficult as this needs a complete description of the soot primary particles and their composition in the soot particle. Since this is not known, the first models estimated the number density of soot sites by assuming that the surface is covered by benzene stacks. Since the distance in such stacks is known, the number density of surface sites was estimated by assuming that two C—H bonds per benzene molecule are available. This gives a maximum value of soot surface site density if one assumes that all the sites are armchair sites. Later models used similar assumptions using stacks of 4- or 8-ring aromatics. Veshkini et al. show that such assumptions can lead to widely differing numbers for the soot surface site density.(189) The model of Chen et al. has been used to investigate this topic, using a solvent excluded surface approach.(195)

2.4 Oxidation of Soot

The processes described so far all work towards the formation of soot particles. In a typical engine cycle, however, the vast majority of produced soot is subsequently oxidized to CO/CO_2 leading to shrinkage of soot particles. Hence, to get an accurate description of the particle size distribution and particle emission the interplay between soot formation, soot growth and oxidation plays a crucial role.

In a flame environment different oxidizers like O_2, radical O, OH, NO, NO_2, H_2O, and CO can be found.(72,196–198) Among these oxidants, the two species contributing the most to soot oxidation are O_2 and OH and hence these have been the main focus of the scientific research.(199,200)

To determine oxidation kinetics experimentally a common approach is thermogravimetric analysis.(18,201,202) With this method, one has to take into account that the oxidation of solid soot particles by gaseous species involves not only chemical kinetics but also external mass transport inside the particle bed. To oxidize the carbon the gaseous oxidant must be transported to the surface of the soot particle, form an intermediate structure and then desorb. This process is often accompanied by previous rearrangements, to give the gaseous oxidation products. The surface of the carbon particle can be inside a pore. However, in this case, the diffusion of the oxidant and the oxidation product(s) into the particle has to be taken into account as well.

A minimal pore model(203) describes the evolution of active surface area per unit mass as a function of conversion and a structural parameter $\psi = \frac{4\pi L(1-\varepsilon)}{S_0^2}$ according to $\frac{S}{S_0} = \sqrt{1 - \psi \ ln(1-x)}$, with S being the reaction surface of the pores per unit volume, L is the length of the overlapped system, ε is the porosity and x is the conversion of the carbon.

One can distinguish the oxidation of soot into three regimes(72,202,204): the first regime where full penetration of the soot particle by the oxidant takes place and all inner surface is reacting, also

called chemical kinetic regime. The second regime where the penetration is partial due to insufficient diffusion, hence not all inner surface reacts, and regime three, where reactions only take place on the outer surface of the soot particle. To determine which of these processes is dominant one usually uses a Thiele Modulus, which is the ratio between diffusion rate and intrinsic reaction rate in steady-state conditions, and determines an effectiveness factor.(18,202,205)

Another experimental approach, which is not using soot beds, is a two-stage burner. In this experimental set up the soot is generated in a first flame and then oxidized later in a second flame. This approach is taken to decouple the oxidation processes from the formation processes of soot particles. With this approach, soot fragmentation can be investigated as well.(199,200)

Oxidation by O_2, which plays a crucial role in fuel-lean environments, where burn out of the particles and fragmentation occurs, can be investigated using two-stage burners. Under lean conditions, the production of soot particles is reduced. Hence the particles oxidized by O_2 have been formed in fuel-rich regions and pass through fuel-lean conditions due to advection. It is probable that OH radicals also contribute to the fragmentation of particles, but their diffusion inside the particle is unlikely due to their high reactivity.

One of the first empirical kinetic models for soot oxidation via O_2 has been proposed by Nagle and Strickland-Constable in 1962.(206) It assumes two types of reactive sites on the soot particle: a more reactive site A and a less reactive site B. Both react with O_2 to form CO_2, although the oxidation rate for B is slower, and the oxidation of B gives a reactive site A. The thermal conversion of the sites into one another is also included in the model. Although this model is based on oxidation experiments of carbon graphite in an O2 environment over a range of partial pressures, and thus not very representative for flame conditions, it is still widely used. Several updates have

been made to this model ever since showing amongst other things that the model is applicable for flame conditions.(18,198,207)

Table 2: Surface species and reactions for active carbon surface sites.

	C_f+O_2	→	$C(O_2)$ or $C(O_2)_m$		
$C(O_2)_m$	→ C(O) + $C(O)_m$	or/and →	$C(O)_m + C(O)_m$	or/and	→ C(O) + C(O)
	C(O)	→	CO		
	$C(O)_m$	→	CO		
	$C(O)_m + C(O)_m$	→	$C_f + CO_2$		
	$C(O)_m$ + C(O)	→	$C_f + CO_2$		
	CO + C(O)	→	$C_f + CO_2$		
	CO + $C(O)_m$	→	$C_f + CO_2$		
	O_2 + 2 C(O)	→	2 CO_2		

The process of oxidation of a graphitic sheet involves a number of surface intermediates. These intermediates may be lumped to C(O) species as presented in table 2.(208)

Additionally, an Eley-Rideal step may occur: C_f+O_2→C(O)+CO. This process has a higher activation energy but may dominate at higher temperatures [188]. Oxidation on a free carbon site C_F begins with the chemisorption of O_2. The chemisorbed oxygen can be localized or mobile (index m) on the graphitic edge-site and dissociates to give two chemisorbed oxygen atoms.

The process of dissociation is influenced by the chemical functionality of the oxygen on the carbon site since different functionalities show differing desorption energies.(209) For example, common functionalities in carbon oxidation are cyclic anhydrides, lactones, ketones, carboxyls,

semiquinones, quinones, ethers and epoxy groups.(210) As a result of the rearrangements and dissociation of CO and CO_2, these functionalities can also be transformed into one another during the oxidation process. Quinone and ketone structures are most susceptible to nucleophilic addition of oxygen, while carboxyl and lactone structures show the least reactivity.(211) Epoxy groups form on the second row of carbon atoms after the majority of edge carbon sites are occupied and in turn also influence the dissociation of carbon on the edge sites.(210) Cyclic ethers can form after the dissociation of a CO_2 has formed a bay site, where one side is occupied with a ketone. These ethers are rather stable and inert.(211)

Furthermore, the chemisorption and formation of oxygen-functionalities on the graphene plane disturb the planarity of the graphene layer, in contrast to chemisorption on the edge. It breaks up the aromaticity of the layer leading to enhanced reactivity towards further oxidation.(212,213)

Further mitigation of the oxygen and rearrangement of the carbon structure then can lead to the dissociation of CO and CO_2.(214–216) The dissociation can also be initiated by further chemisorption of O_2 or CO to a graphene site, which has already undergone oxidation. Due to the oxidation and rearrangement of the carbon structure defects will arise that will give new edge carbon sites, which in turn increases the specific reactivity of the free carbon site.(213,217,218)

As discussed above, the kinetics of the oxidation of soot are dependent on the nanostructure of the oxidation site. Hence, to describe oxidation with mass action laws one would need to describe the single sites and products individually. This yields an unfeasibly large number of rate equations, and a complex interplay between concentrations and rates. As described above the adsorption and desorption products depend on the amount of oxygen that is already adsorbed. The description of the active carbon site in a mathematically proper form is hence crucial for a complete description of reaction kinetics, since the coverage of the active sites determines further kinetics, as the activation

energy for ads- and desorption changes.(219) Depending on the concentration of the covered sites the subsequent kinetics are then influenced, and the products are formed. A complete description of the conversion mechanism and formation of the oxidation product is again unfeasible, as the variety of reaction mechanisms leads to a large number of reaction rates.

One generally thus tries to postulate a semi-global mechanism that reproduces the major kinetic features and yields kinetic laws with a proper mathematical form in combustion modeling. These mechanisms employ a limited number of reaction steps to capture the kinetics of the oxidation process, with the first being the adsorption of oxygen on the carbon site. It has been shown that a three-step mechanism is capable of describing the global trends in reaction order, the activation energy and the desorption of gaseous carbon species over a wide range of combustion conditions.(194)

A popular approach to model carbon oxidation is the use of Langmuir-Hinshelwood kinetics. This approach assumes a bi-molecular reaction between the two already adsorbed species (oxygenated complex). As under a range of conditions, the coverage of a specific adsorbate is much greater than the other intermediates, Langmuir-Hinshelwood kinetics is usually globalized to power-law kinetics. This allows for a general expression, describing the oxidation process as one step:

$$\omega_{O_2} = k_{O_2} {P_{O_2}}^n \tag{2.1}$$

with k_{O_2} being the reaction rate, P_{O_2} the partial pressure of O_2 and n is the reaction order of oxygen partial pressure. However, power-law kinetics is in general even more limited than Langmuir-Hinshelwood, because it does not correctly account for the poisoning of the active sites by intermediates and products.(201)

The reaction rate is usually fitted to an Arrhenius like expression

$$k_{O_2} = A\, T^{-0.5} \exp\left(\frac{E_A}{RT}\right) \tag{2.2}$$

and the parameters A, E_A and n are fitted to experimental results. The reaction rates found in literature differ up to seven orders of magnitude, however.(198) Also, reaction orders for the Arrhenius equation give mixed results, varying from 0.5 to 0.8 in some cases, while others assume it to be unity.(220) In a recent study, Guo et al. tried to solve this problem, by comparing a large number of measurements and fitting them to a new soot oxidation rate expression. The model does fit experimental data well, but they found an activation energy E_A of 195 $\frac{kJ}{mol}$, which is higher than that of any other previous model.(198)

Neoh et al. showed that OH is the main oxidant of the soot surface in flame environments, while O_2 plays a secondary role, due to the small concentrations relative to OH in fuel-rich environments.(199) They gave a kinetic expression for the oxidation of soot, which is as follows:

$$\omega_{total}(g\ cm^{-2}s^{-1}) = 1.29 \times 10^2 \frac{\Gamma_{OH}}{\sqrt{T}} P_{OH} + \omega_{O_2} \qquad (2.3)$$

where ω is the soot specific oxidation rate, with the index indicating partial rates for the differing oxidants, Γ_{OH} is the collision efficiency of OH, T is the temperature and P_{OH} is the partial pressure of OH. While the oxidation by OH is in most studies approximated to have no activation energy and hence is determined by the collision efficiency, the determination of the soot oxidation rate of O_2 is more delicate, due to adsorption.(198)

The reason for the large difference in soot oxidation rates is likely to be a difference in the soot nanostructure. As discussed in subchapter 1.1 soot nanostructure is dependent on the conditions under which it forms. Vander Wal et al. found that soot with an amorphous structure shows higher reactivity, due to better accessibility of the carbon atoms on the edge sites. They also linked a higher oxidation reactivity to the curvature, due to the strain in the graphitic plane.(20) A study by Ghiassi et al. showed similar results.(221) Alfè, as well as Guerrero, pointed out that the C/H ratio in soot is a good indicator for active sites and hence increase in C/H ratio results in higher

reactivity.(80,82) This can be understood if one considers that larger size of the graphitic layers means less C-H sites and also fewer pores inside the particles giving a larger restriction to diffusion. This means graphitization of soot particles has a direct influence on the oxidation behavior of soot.(222) Additionally, it was found that the oxygen content in fuel has an influence on the oxidative reactivity.(78,82)

In a further study Raj et al. showed that the oxidation rate of soot particles by O_2 is influenced by the size and the structure of the PAHs inside the soot particle, the functional groups of these, the number of active sites and the type of chemical bonding.(223) Other studies showed that the oxidation rates change over time indicating a change in nanostructure during oxidation.(53,76,78,84) The interplay of nanostructure and oxidation of soot particles can thus be seen as a feedback loop, where one influences the other. This was investigated theoretically by Frenklach et al. who showed, that during oxidation of soot five-membered rings emerge on the edge of the graphitic plane due to oxidation of free edge and arm chair sites.(224) These five-membered rings are more robust to oxidation by O_2 and OH radicals. As a result, Frenklach et al. reported that atomistic O radicals are the only species to successfully oxidize these embedded five- membered rings.(225)

Ghiassi et al. showed that so-called “bridges” between particles, meaning the sites where particles are merged during coagulation, are more prone to oxidation by O_2 leading to a breakup of particles.(220) The break-up or fragmentation of particles is a direct result of oxidation as the internal structure gets weakened due to the subsequent removal of C-sites inside the particles. This effect was first proposed by Neoh et al. who observed a rise in particle numbers at the flame tip and explained this finding with fragmentation in this part of the flame.(205) Most predictive models do

not include this process and only recently a few models started investigating this process in premixed laminar flames. (50,200,226)

Implementing these findings into predictive models for combustion engines is hard, however, since the burning conditions inside the engine change spatially due to turbulences. One of the most common approaches to model soot oxidation in computational fluid dynamics models for combustion engines is the one proposed by Appel et al.(93,198) In this model a one-step reaction of O_2 with a radical site is used to describe the oxidation. For OH radicals again a one-step reaction with carbon edge sites is used, using the description of Neoh et al.(36) Reason for the use of these reduced oxidation descriptions is due to the fact that a lot of research results on the influence of nanostructure to the oxidation rates have been made on model systems and hence cannot be directly transferred to combustion engine conditions. Strzelec et al. also correlated the soot reactivity in diesel engines in a study to the local active carbon surface area and found a consistent activation energy for different fuel types and degree of burn out.(227) Jaramillo et al. tried to correlate the oxidation rate to the pressurized conditions in soot from laminar flames, as the pressure is a key difference between model flames and engines. He related oxidation rates to laminar lengths and tortuosity inside soot particles, but could not find a direct correlation between non-pressurized and pressurized conditions, since some of the samples showed no structural differences.(202)

3. Theoretical Approach

In this section, the underlying theoretical approach to this thesis will be explained. First, an introduction to the principles of molecular dynamics simulations will be given and the derivation of macroscopic properties will be explained. Afterwards, the force field used in this work, namely the ReaxFF force field, will be discussed in detail, showing the general structure of the potential. Lastly, the principles of the Chemkin software will be explained for the approach used.

3.1 Molecular Dynamics Simulations

Classical Molecular Dynamics is a simulation method widely used to compute the equilibrium and transport properties of many-particle systems. Geometry optimization allows to model structure properties of novel materials or biological systems. Atomic-level phenomena can be simulated such as thin-film growth, interactions on interfaces, adsorption phenomena or structural changes in proteins due to ligand bonding or novel drugs.(228–232)

A detailed description of the physical and chemical properties of molecules can be calculated by ab initio, perturbation theory or by density functional theory (DFT) methods. In these methods, the Hamiltonian is on electronic interaction and interaction of atomic nuclei. Due to the complex calculations of electron interactions, the computational expenses of these methods scale badly with the number of atoms. In molecular dynamics simulations the Hamiltonian of the investigated system is treated classically, and electrons are not described explicitly. This means that the atomistic motion is treated with classical mechanics and the interatomic interactions are described by a potential, which is modeled based on quantum mechanical potentials, estimating changes in the potential without describing the electronic interactions explicitly.

This significantly reduces the computational cost of the simulations, while still often giving accurate descriptions for the statistical properties of many-particle systems. In the following, the theoretical principles of the molecular dynamics approach will be explained briefly, for a more detailed description of the underlying principles the reader is referred to the literature.(233–235)

The total energy (E_{total}), defined by the Hamiltonian of a system in statistical mechanics, of an N particle system can be expressed as the sum of kinetic and potential energy functions of the set of coordinates r_i and momenta p_i of each particle i.

$$E_{total} = \sum_{i=1}^{N} E_{kin}(p_i) + \sum_{i=1}^{N} E_{pot}(r_i) \tag{3.1}$$

Following classical Newtonian mechanics, the kinetic energy can be described by equation 3.2,

$$E_{kin} = \sum_{i=1}^{N} \frac{p_i^2}{2m_i} = \sum_{i=1}^{N} \frac{1}{2} m_i v_i^2 \tag{3.2}$$

with m_i being the mass and v_i the velocity of particle i. Assuming there is no external potential energy acting on the system, it is governed by the attractive and repulsive interparticle interactions, which give rise to forces that will act on the particles. These forces can be calculated for each particle by

$$f_i = -\nabla_{r_i} E_{pot} \tag{3.3}$$

where ∇_{r_i} is the derivative in all 3 dimensions x, y and z around the particle at coordinate r_i.

With the above-described equations, it is now possible to construct equations of motion for the system, which govern the time-evolution of the system and its mechanical properties. One approach is the velocity Verlet-algorithm, which advances the particle coordinates during one time step Δt like shown in the equations 3.4 and 3.5.

$$r(t + \Delta t) = r(t) + \left(\Delta t / m\right) p(t) + \frac{1}{2}\left(\Delta t^2 / m\right) f(t), \tag{3.4}$$

$$p(t + \Delta t) = p(t) + \frac{1}{2}\Delta t\left(f(t) + f(t + \Delta t)\right). \tag{3.5}$$

Following equations 3.4 and 3.5, one can see how it is possible to simulate the microscopic states of a many-particle system when for a given number of particles, both their positions and momenta are known. These three parameters, i.e., number, position and momenta of particles, can be considered as the first valuable input into a molecular dynamics simulation. The number of particles is usually chosen in a way to represent the system considered. The position coordinates of the particles are then generated according to the system investigated. This can be on a grid for solid phases or in a more random fashion for liquid or gas-phase simulations. The generation of the particle momenta is more delicate but is needed to advance the system in time, as can be seen in the velocity Verlet-algorithm. As the only information at the start of the simulation is the desired temperature or energy of the simulation, the particle momenta are generated in a random fashion, usually following a Maxwell-Boltzmann-distribution, with the restriction that the total momentum of the system cancels out. The distribution of the momenta of the particles is linked to the macroscopic properties of the system, which are the properties one is generally investigating. The link between microscopic states and macroscopic properties is given by statistic mechanics and will be explained briefly in the following paragraphs. Again a complete description exceeds the scope of this work and the reader is therefore referred to literature.(233,235–237)

A thermodynamic state of a system is defined by a small set of parameter like, for example, the number of particles N, the volume V and the temperature T, and not by the positions and momenta of particles, which define the instantaneous mechanical state. These positions and momenta can be thought to span a multidimensional space, the so-called phase space, which has $6N$ dimensions for a system of N particles. The instantaneous value of a property (for example the potential energy) is then a function of the coordinates in the phase space $A(\Gamma)$, where Γ is a particular point in the phase

space, and the macroscopic observable of that property can be assumed to be the time average of all instantaneous values $A(\Gamma)$.

$$A_{obs} = \langle A \rangle_{time} = \langle A\big(\Gamma(t)\big) \rangle_{time} \tag{3.6}$$

$\Gamma(t)$ is here shown as a function of time since the system is assumed to evolve in time.

A macroscopic property in experiments is not a time average, however, but an ensemble average. This brings us to a very important axiom in statistic mechanics, the ergodic hypothesis, which states that the time average equals the ensemble average.

$$\langle A \rangle_{time} = \langle A \rangle_{ens} \tag{3.7}$$

The ensemble is a collection of points Γ in the phase space, which are distributed by a probability density $P_{ens}(\Gamma)$.

$$A_{obs} = \langle A \rangle_{ens} = \sum_{\Gamma} A(\Gamma)\, P_{ens}(\Gamma) \tag{3.8}$$

The probability of a single point Γ in the phase space in the system is given by equation 3.9,

$$P_{ens}(\Gamma) = \frac{w_{ens}(\Gamma)}{Q_{ens}(\Gamma)} = \frac{w_{ens}(\Gamma)}{\sum_{\Gamma} w_{ens}(\Gamma)} \tag{3.9}$$

with $w_i(\Gamma)$ being a 'weight' function, which is basically a non-normalized form of $P_{ens}(\Gamma)$. The normalizing factor $Q_{ens}(\Gamma)$ is called the partition function or the sum of states and is a function of the macroscopic properties defining the ensemble and makes the connection to classical thermodynamics. Hence, the expression for the partition function changes when the expression for the thermodynamic state changes. Different expressions can be used to describe for the thermodynamic state of a system. Four of them will be presented in the following. These are the so-called microcanonical ensemble, the canonical ensemble, the grand canonical ensemble, and the isobaric-isothermal ensemble. The fixed parameters, the description of the probability density, the resulting partition function and the corresponding thermodynamic properties of the ensembles are given in Table 3.

Note that in the canonical ensemble energy fluctuations are non-zero. To solve this by sampling states with the corresponding mechanical equations of motion is not possible since they conserve energy. To avoid this problem one expresses the energy as a sum of kinetic and potential contributions, which factorizes the partition function into a product of kinetic and potential parts.

$$Q_{NVT} = Q_{NVT}^{kin} \times Q_{NVT}^{pot} \tag{3.10}$$

The potential part can now be used to sample the potential states with the assumed interatomic forces, while the kinetic part is solved by fixing the temperature of the system. This is achieved by coupling the system to an isothermal system, a so-called thermostat. A multitude of different approaches for thermostats has been proposed but will not be further discussed here. For more details, the interested reader is invited to consult the literature.(235)

The thermodynamic properties of an ensemble, that are not fixed in advance, can be obtained by ensemble averaging since every state point in phase space will give an instantaneous value of these quantities. These usually deviate from the average, however, and change during time evolution, hence fluctuations occur. Also, one must note that each ensemble produces consistent average properties in the thermodynamic limit (i.e. an infinite system size) as long as phase transitions are avoided. However, as phase transitions do not play a role in this study, we will not further discuss this point.

Table 3: Definition and properties of the different thermodynamic ensembles.

Ensemble	Fixed	Probability density	Partition function	Corresponding thermodynamic property
Micro-canonical	N,V,E	$\delta(H(\Gamma) - E)$	$Q_{NVE} = \frac{1}{N!}\frac{1}{h^{3N}}\int drdp\ \delta(H(r,p) - E)$	Entropy $S = k_B\ lnQ_{NVE}$
Canonical	N,V,T	$\exp\left({}^{-H(\Gamma)}/_{k_BT}\right)$	$Q_{NVT} = \frac{1}{N!}\frac{1}{h^{3N}}\int drdp\ \exp\left({}^{-H(r,p)}/_{k_BT}\right)$	Helmholtz free energy $A = -k_BT\ lnQ_{NVT}$
Grand canonical	μ,V,T	$\exp\left({}^{-(H-\mu N)}/_{k_BT}\right)$	$Q_{\mu VT} = \frac{1}{N!}\frac{1}{h^{3N}}\frac{1}{V_0}\int dV\int drdp\ \exp\left({}^{-(H-\mu N)}/_{k_BT}\right)$	$PV = k_BT\ lnQ_{\mu VT}$
Isobaric-isothermal	N,P,T	$\exp\left({}^{-(H+PV)}/_{k_BT}\right)$	$Q_{NPT} = \frac{1}{N!}\frac{1}{h^{3N}}\frac{1}{V_0}\int dV\int drdp\ \exp\left({}^{-(H+PV)}/_{k_BT}\right)$	Gibbs free energy $G = -k_BT\ lnQ_{NPT}$

3.2 Reactive Force Field Approach

As described above in molecular dynamics simulations the forces experienced by atoms are derived from the space derivatives of the potential used for the MD simulation. The underlying concept of ReaxFF is to model the interactions within a chemical system by using a bond order dependent description of the potential energy functions. This allows for a description of the system kinetics and the atomic interactions which includes bond breakage and formation.(238)

The fundamental assumption of ReaxFF is that the bond order BO'_{ij} between atom i and j can be obtained from the interatomic distance r_{ij} between those atoms. The bond-order term consists of three exponential terms for the σ-bond ($p_{bo,1}$ and $p_{bo,2}$), the first π-bond ($p_{bo,3}$ and $p_{bo,4}$), and the double π-bond ($p_{bo,5}$ and $p_{bo,6}$) between two atoms.

$$BO'_{ij} = BO'^{\sigma}_{ij} + BO'^{\pi}_{ij} + BO'^{\pi\pi}_{ij}$$

$$= exp\left[p_{bo,1}\left(\frac{r_{ij}}{r_0^{\sigma}}\right)^{p_{bo,2}}\right] + exp\left[p_{bo,3}\left(\frac{r_{ij}}{r_0^{\pi}}\right)^{p_{bo,4}}\right] + exp\left[p_{bo,5}\left(\frac{r_{ij}}{r_0^{\pi\pi}}\right)^{p_{bo,6}}\right] \quad (3.11)$$

The bonding terms p_{bo} and the equilibrium distances r_0 are parameterized so that they give bond strengths and distances that agree with *ab initio* calculations. The calculated bond orders need to be corrected for over coordination and for residual 1-3 bond orders in valence angles.(129) The scheme to do so is mathematically rather lengthy and is shown for completion in the appendix. The corrected bond order BO_{ij} is again the sum of the bond order for the σ-bond, the first π-bond, and the double π-bond.

The total potential energy of the system in ReaxFF is described by Chenoweth et al. as a sum of the terms shown in equation 3.12.

$$E_{System} = E_{Bond} + E_{lp} + E_{over} + E_{under} + E_{val} + E_{pen} + E_{coa} + E_{tors} + E_{conj} + E_{C2} + E_{triple} + E_{H-bond} + E_{vdW} + E_{Coulomb}. \quad (3.12)$$

For a complete mathematical description of the potential, the interested reader is referred to the supporting information of the paper by Chenoweth et al.(128) A short description of the single contributions to the potential is given in Table 4.

In the ReaxFF approach, the bonded and non-bonded terms are calculated independently for each atom pair. This is done to avoid energy alterations during bond dissociation. To get a smooth energy transition from non-bonded to bonded conditions, some correction terms need to be included. One of these corrections is the inclusion of a distance-dependent seventh-order polynomial Taper function Tap to avoid energy discontinuities when the distance between atom pairs crosses the cutoff radius.

Another correction is the shielding parameter γ to avoid excessive repulsive or attractive non-bonded interactions at short distances. At short inter-atomic distances this shielding parameter

corrects the potentials to ensure finite values, at longer distances, however, the potentials are the same as for the unshielded case.

Table 4: Description of the terms of the potential energy function of the reactive force field.

Parameter	Meaning	Description
E_{Bond}	Bond energy	The bond energy is described by BO_{ij}, the corrected bond order for the respective bond (see appendix). Bond breaking energies and parameters are dependent on the type of atoms involved in the bond.
E_{lp}	Lone pair energy penalty	Accounts for the rise in energy, if one of the electron lone pairs is broken up and involved in bonding for atoms with lone pairs.
E_{over}	Penalty term for overcoordination	Accounts for a higher total bond order around the atom than the number of bonding electrons of the atom.
E_{under}	Penalty term for undercoordination	Accounts for a lower total bond order around the atom than the number of bonding electrons of the atom.
E_{val}	Valence angle energy term	Total energy contribution due to the valence angle in dependence of the number of π-bond orders on the central atom.
E_{pen}	Valence angle penalty term	Introduced to reproduce the stability of systems with two consecutive double bonds, like allene.
E_{coa}	Valence angle correction term	Introduced to account for the stability of three-body conjugated groups, like in NO_2.
E_{tors}	Torsion rotation barrier correction term	Accounts for the dependence of the torsion rotation barrier on the bond order.
E_{conj}	Conjugation correction term	Accounts for conjugation effects of conjugated π-systems.
E_{C2}	Correction term for C_2-molecules	Introduced to account for an error, which gives very strong double bonds for C_2-molecules.
E_{triple}	CO stabilization term	Stabilizes the triple bond in CO molecules, making CO stable and inert.
E_{H-bond}	Hydrogen bond term	Accounts for X-H—Z systems, in which partial bond orders between H and Z exist and the bond order of X-H is reduced
E_{vdW}	Van der Waals interactions	Non-bond-order-dependent term to describe the Van der Waals interactions containing a Taper-function and a shielding parameter.
$E_{Coulomb}$	Coulomb interactions	Non-bond-order-dependent term to describe the Coulomb interactions containing a Taper-function and a shielding parameter.

To calculate the polarization and charges within molecules ReaxFF uses a method based on the electronegativity equalization method (EEM) of Mortier et al. [216, 217] and the electronegativity equilibration (Qeq) of Rappe and Goddard [218]. This approach uses electronegativity and hardness parameters for each element in the system to determine the polarization.

$$\frac{\partial E}{\partial q_n} = \chi_{eq} = \chi_n + 2 \cdot q_n \cdot \eta_n + \mathrm{C} \cdot \sum_{j=1}^{n} \frac{q_j}{\left\{ r_{n,j}^3 + \left(1/\gamma_{nj} \right)^3 \right\}^{1/3}}, \ \sum_{i=1}^{n} q_i = 0 \qquad (3.13)$$

Here χ_n is the electronegativity of element n, η_n is the hardness of element n and γ_{nj} is the shielding parameter between element n and j. The charge values are generally determined at each simulation step and depend on the geometry of the system. This calculation is computationally the most expensive part of the ReaxFF energy calculations.(239)

As can be seen from the description above, ReaxFF includes a physically sound description of the interatomic interactions based on a bond order description. However, one of the major difficulties of these force fields is the parametrization. This was initially determined through optimization against a training-set obtained from *ab initio* calculations and/or literature by using a single-parameter-based search algorithm or via a Monte Carlo based method, but also other methods for parameter optimization with ReaxFF have been proposed recently.(240–242)

For the single-parameter-based search, an algorithm determines the parameter of interest, as shown in table 4, by minimizing the sum of the squared error for the difference in the ReaxFF and the training set parameter.

$$Error = \sum_{i=1}^{n} \left[\frac{\left(x_{i,QM} - x_{i,ReaxFF} \right)}{\sigma} \right]^2 \qquad (3.14)$$

In the above equation x is a data point in the training set and σ is a weighting factor to account for the relative importance of each data point during the optimization.

3.3 Reaction Kinetics modeling in Chemkin

Chemkin is a proprietary software of Reaction design employed to model complex chemical kinetics in various fields, such as combustion in experimental flames or more complex geometries, chemical processing or atmospheric chemistry.(96–98,243–246) In the following the essential theoretical background of the software to model a closed homogeneous reactor, as described in chapter 4.1, is explained. Furthermore, an outlook for modeling transport with Chemkin is given in the end, but since it is not part of this work, these possibilities with Chemkin are not explained in detail.

3.3.1 Gas-Phase Thermodynamic Properties

In order to describe chemical reaction-flows, several state variables need to be defined in order to define the thermodynamic and chemical state of the gas phase. In the calculations described in the following chapter, the first state variable chosen is the pressure P, as it has been fixed for the total simulation time. The second state variable is the temperature T, as this needs to be chosen as state variable as the thermodynamic properties and the chemical rate constants depend directly on the temperature. The final state variable chosen is the mole fraction X for describing the composition of the gas phase.

With these state variables, it is possible to define the equation of state as an ideal multi-fluid gas as follows.

$$P = \sum_{k=1}^{K} [\mathrm{X}_k] R T_k \tag{3.15}$$

In equation 3.15 P gives the total pressure, with K being the total number of species, $[\mathrm{X}_k]$ being the molar concentration of species k, R being the ideal gas constant and T_k being the specific temperature of species k. The mean mass density is then given as

$$\rho = \sum_{k=1}^{K} [\mathrm{X}_k] W_k \tag{3.16}$$

with W_k being the specific molecular weight and the mean molecular weight is calculated as follows.

$$\bar{W} = \sum_{k=1}^{K} \mathrm{X}_k W_k \tag{3.17}$$

The molar concentration can be converted to the mole fraction with equation 3.18.

$$\mathrm{X}_k = \frac{[\mathrm{X}_k]}{\sum_{j=1}^{K} [\mathrm{X}_j]} \tag{3.18}$$

It is assumed in Chemkin that the standard-state thermodynamic properties are functions of temperature only. In order to model these properties, one must supply thermodynamic data for each species in the system of interest. This data is provided using a tabulated library provided by the user. The tabulated library holds parameters for polynomial fits of thermodynamic properties, such as enthalpy, entropy and specific heat capacity, in dependence on the temperature for each species.

In the gas phase the thermodynamic data is designed in the way described in the NASA chemical equilibrium code.(247) That means seven coefficients are taken for two temperature ranges to describe the polynomial fit of thermodynamic properties. The temperatures are in Kelvin, the fits take the following form:

$$\frac{c_{pk}^0}{R} = a_{1k} + a_{2k} T_k + a_{3k} T_k^2 + a_{4k} T_k^3 + a_{5k} T_k^4 \tag{3.19}$$

$$\frac{H_k^0}{R T_k} = a_{1k} + \frac{a_{2k}}{2} T_k + \frac{a_{3k}}{3} T_k^2 + \frac{a_{4k}}{4} T_k^3 + \frac{a_{5k}}{5} T_k^4 + \frac{a_{6k}}{T_k} \tag{3.20}$$

$$\frac{S_k^0}{R} = a_{1k} ln T_k + a_{2k} T_k + \frac{a_{3k}}{2} T_k^2 + \frac{a_{4k}}{3} T_k^3 + \frac{a_{5k}}{4} T_k^4 + a_{7k} \tag{3.21}$$

with c_{pk}^0 giving the molar heat capacity at constant pressure. The superscript ^{0} refers to the standard-state, which for gas phase species is at one atmosphere. H_k^0 is the standard-state molar enthalpy and S_k^0 is the standard-state molar entropy.

Other thermodynamic properties like the specific heat capacity at constant volume c_{vk}^0, the integral energy U_k^0, the standard-state Gibb's free energy G_k^0 and the standard-state Helmholtz free energy A_k^0 can be given in terms of c_p^0, H^0 and S^0 as follows.

$$c_{vk}^0 = c_{pk}^0 - R \tag{3.22}$$

$$U_k^0 = H_k^0 - RT_k \tag{3.23}$$

$$G_k^0 = H_k^0 - T_k S_k^0 \tag{3.24}$$

$$A_k^0 = U_k^0 - T_k S_k^0 \tag{3.25}$$

The mixture-averaged thermodynamic properties of the feat capacities, the molar enthalpy and the integral energy can be calculated by summing the specific values multiplied by the molar fraction.

For the entropy and the Gibb's and Helmholtz free energy calculation of the mixing properties one must account for the appropriate pressure and entropy-of-mixing terms. Taking this into account the entropy is defined as:

$$S_k = S_k^0 - Rln\mathrm{X}_k - R \ln ({}^{P}/_{P_{atm}}) \tag{3.26}$$

and the mixture-averaged entropies are given as

$$\bar{S} = \sum_{k=1}^{K} (S_k^0 - Rln\mathrm{X}_k - R \ln ({}^{P}/_{P_{atm}}))\mathrm{X}_k. \tag{3.27}$$

The same expression for the entropy can then be used to define the mixture-averaged Gibb's and Helmholtz energies as follows.

$$\bar{G} = \sum_{k=1}^{K} [H_k - T_k (S_k^0 - Rln\mathrm{X}_k - R \ln ({}^{P}/_{P_{atm}}))]\mathrm{X}_k \tag{3.28}$$

$$\bar{A} = \sum_{k=1}^{K} [U_k - T_k (S_k^0 - Rln\mathrm{X}_k - R \ln ({}^{P}/_{P_{atm}}))]\mathrm{X}_k \tag{3.28}$$

3.3.2 Gas-Phase Chemical Reaction Expressions

Gas-phase reactions describe the interactions between gas-phase species. The forward rate constants for each reaction is assumed to be able to be expressed by Arrhenius equations giving the following temperature dependence of the rate constant.

$$k_{fi} = A_i T^{\beta_i} \exp\left(\frac{-E_i}{RT}\right) \tag{3.29}$$

k_{fi} gives the forward reaction rate of the i-th reaction, T refers to the gas temperature, A_i is the pre-exponential factor, E_i is the activation energy and β_i is the temperature exponent. The latter three need to be specified for each reaction in a tabulated form called chemical mechanism. Furthermore, each species in a reaction also needs to be associated with thermodynamic data in order to calculate equilibrium constants and reverse-rate coefficients for a reaction.

The general form to write an elementary reversible or irreversible reaction involving K chemical species is the following.

$$\sum_{k=1}^{K} \upsilon'_{ki} \chi_k \rightleftharpoons \sum_{k=1}^{K} \upsilon''_{ki} \chi_k \tag{3.30}$$

υ_{ki} are integer numbers which give the stoichiometric coefficients of the reactions and χ_k is the chemical symbol of the kth species. The integer i gives the number of the reaction, and the subscript $'$ and $''$ indicate forward and backward stoichiometric coefficients, respectively.

The rate of production of the k-th species $\dot{\omega}_k$ is defined by the sum of the rate-of-progress variables of all reactions involving the k-th species.

$$\dot{\omega}_k = \sum_{i=1}^{I} \upsilon_{ki} q_i \tag{3.31}$$

In equation 3.31 υ_{ki} is defined as the difference between the backward and forward stoichiometric coefficients.

$$\upsilon_{ki} = \upsilon'_{ki} - \upsilon''_{ki} \tag{3.32}$$

The rate-of-progress variable q_i for the i-th reaction is defined by the difference of the forward and reverse reaction rates.

$$q_i = k_{fi} \prod_{k=1}^{K} [\mathrm{X}_k]^{\upsilon'_{ki}} - k_{ri} \prod_{k=1}^{K} [\mathrm{X}_k]^{\upsilon''_{ki}} \tag{3.33}$$

$[\mathrm{X}_k]$ in equation 3.33 is the molar concentration of the k-th species, while k_{fi} and k_{ri} are the forward and reverse rate constants of the i-th reaction. Equation 3.33 is valid when the mechanism is described in elementary reactions and mass-action kinetics are obeyed.

The reverse rate constant k_{ri} and the forward reaction rate k_{fi} are related by the equilibrium constant K_{ci}.

$$k_{ri} = \frac{k_{fi}}{K_{ci}} \tag{3.34}$$

In order to calculate the equilibrium constant from the thermodynamic properties one needs to transpose K_{ci} in pressure units instead of concentration units. This can be done as follows:

$$K_{ci} = K_{pi} \left(\frac{P_{atm}}{RT}\right)^{\sum_{k=1}^{K} \upsilon_{ki}} \tag{3.35}$$

with K_{pi} being the equilibrium constant in pressure units. The equilibrium constant K_{pi} can then be calculated in the following fashion:

$$K_{pi} = exp\left(\frac{\Delta S_i^0}{R} - \frac{\Delta H_i^0}{RT}\right) \tag{3.36}$$

Where the Δ signifies the change of enthalpy or entropy that occurs for a complete passing of reactants to products in reaction i. That is

$$\frac{\Delta S_i^0}{R} = \sum_{k=1}^{K} \upsilon_{ki} \frac{\Delta S_k^0}{R} \tag{3.37}$$

$$\frac{\Delta H_i^0}{RT} = \sum_{k=1}^{K} \upsilon_{ki} \frac{\Delta H_k^0}{RT}. \tag{3.38}$$

3.3.3 Modeling Transport Properties of Chemkin

Since in this study a perfectly stirred closed reactor has been assumed for the modeling of combustion, as described in chapter 4, one major feature of Chemkin that has not been employed is the gas-phase transport properties. This is because in this model perfect homogeneity in the reactor is assumed, hence transport occurs instantly, so that the composition in the gas phase and the temperature can be evaluated by kinetics and transport, and mixing properties can be neglected. It is, however, possible in Chemkin to simulate also injection processes, flame models, stirring and many more, and for these processes, transport properties of gas-phase species are crucial as these determine the rate limits of reactions to occur.

In order to model transport properties, the diffusion coefficients, viscosities, thermal conductivities and thermal diffusion coefficients of pure species are evaluated with standard kinetic theory expressions. The gas mixture properties can then be determined via the pure species properties utilizing a number of approximate mixture averaging rules. As this process is not relevant for the presented work the interested reader is referred to literature.

4. Generation of Precursor Pools using Chemkin

4.1 Introduction

To initiate the ReaxFF MD calculations it is crucial to have a representative description of the gas-phase composition and concentration of the combustion process. For the simulation of the gas phase in combustion systems, we used the Chemkin program.(63) This program combines gas-phase chemistry and thermodynamic data in a mean-field chemical kinetics approach. As described in chapter 3.3 a mass balance equation is utilized, which calculates the change in mass of a certain chemical species due to the given production rate and the system volume. Since the total mass of the system does not change during the calculation, one can express the change in mass as a change in mass fraction and the volume as a specific volume. The kinetics are given as input by the user through reaction libraries, also referred to reaction mechanisms. The program then calculates the reaction products, accounting for a large number of reactions between the gas-phase species to simulate the combustion process.

The combustion was simulated as a closed homogeneous reactor at constant pressure and temperature. The Chemkin simulations were run for 0.2 seconds with a constant pressure of 10 atm to account for in valve conditions of combustion engines. The fuel mixtures were varied from 100 mol% n-decane to 100 mol% toluene, using a stepwise substitution of 20 mol%. The chemical mechanism used to simulate these systems is the one proposed by Raj et al.(96) This mechanism was validated against fuel-rich premixed sooting flames.(96) Especially PAH concentration profiles in this mechanism could be improved in regard to earlier mechanisms. (96,248) There are few other publicly-available mechanisms to predict large PAH formation covering aromatic-containing surrogate mixtures of commercial liquid fuels,(98,120,249) and several newly developed

mechanisms have Raj's mechanism as a basis to predict the formation of larger PAH.(60,243,248,250) As a result, the PAH formation from Raj's mechanism and updated versions of the mechanism have been validated in several experimental studies.(96,243,248,251) Testing updated versions for the generation of the soot precursor pools gave similar results as using Raj's mechanism, hence reassuring the validity of the approach.

The tested temperatures range from 1400 K to 2000 K, with temperature steps of 200 K. The tested equivalence ratio Φ ranged from 2.5 to 5 with steps of 0.5. So, both the temperature range and equivalence ratios were chosen to favor combustion conditions that lie in the sooting region.(252) The temperature is kept constant in the simulation to decouple the thermal and chemical impact of fuel composition by performing the precursor pool generation at fixed temperatures and pressures, allowing a careful comparison of the impact of fuel composition on precursors pool.

In summary, we tested six fuel mixtures, six equivalence ratios and four temperatures, resulting in a total of 144 tested conditions.

4.2 Fuel Mixtures and Equivalence Ratio

The equivalence ratio Φ is the stoichiometric ratio between fuel and air, meaning an equivalence ratio of 1 would be a perfect stoichiometric mixture of the fuel and the air which theoretically leads to complete oxidation. Values of Φ larger than 1 thus match situations where there is not enough oxygen for complete combustion.

$$\Phi = \frac{\left[\frac{n_{fuel}}{n_{Air}}\right]_{given}}{\left[\frac{n_{fuel}}{n_{Air}}\right]_{Stochiometric}} \tag{4.1}$$

The quantity of fuel and oxygen are defined above as the number of atoms, but could also be defined as mass, mole fraction or concentration.

For pure compounds defining the equivalence ratio is straight forward. For mixtures it is more complicated, hence a short example is given for the fuel mixture (n-decane/toluene) used in this study. For this, the stoichiometric formula for the combustion of n-decane (C10H22) and toluene (C7H8) with air is given below.

$$a\ C_{10}H_{22} + b\ C_7H_8 + c\ O_2 + 4c\ N_2 \rightarrow d\ CO_2 + e\ H_2O + 4c\ N_2 \qquad (4.2)$$

a, b, c, d and e may be mole fraction, mole percentages or stoichiometric coefficients. For simplicity, the ratio of nitrogen and oxygen is given as 4/1. In reality, it is 79/21 but the amount of nitrogen does not play any role for the equivalence ratio calculation, hence the simplification.

15.5 oxygen molecules and 9 oxygen molecules are consumed for the complete oxidation of n-decane and toluene, respectively. Therefore, in the complete oxidation shown in equation 4.2 the stoichiometric coefficient c must be $(15.5a + 9b)$. Hence the denominator in the equivalence ratio equation 4.1 has this relation between n_{fuel} and n_{O2}, where $n_{fuel} = a\ C_{10}H_{22} + b\ C_7H_8$ and $n_{Air} = (15.5a + 9b) \times O_2 + 4 \times (15.5a + 9b) \times N_2$. If the enumerator has the same ratio between a, b and c in equation 4.1 the equivalence ratio is 1 and a different ratio between a, b and c in the enumerator yields equivalence ratios different than 1. As in the present study, the equivalence ratios used are larger than one, the calculation of the equivalence ratio for the fuel mixtures is more complicated. The calculation of the equivalence ratio for the different fuel ratios of toluene and n-decane was directly done with the Chemkin software(63). The resulting mole fractions are depicted in Table 5 for all equivalence ratios and fuel mixtures. The mole fractions are consistent over all the tested temperatures.

Table 5.Mole fractions of nitrogen, oxygen, toluene, and n-decane for all tested equivalence ratios and fuel mixtures. The mole fractions for all mixtures are consistent over all temperatures.

Fuel	Mole fraction	Φ=2.5	Φ=3	Φ=3.5	Φ=4	Φ=4.5	Φ=5
0% $C_{10}H_{22}$ 100% C_7H_9	%mol N_2	0.746456	0.738318	0.7303544	0.722561	0.714932	0.707462
	%mol O_2	0.198425	0.196262	0.1941448	0.192073	0.190045	0.188059
	%mol C_7H_9	0.055118	0.065421	0.0755007	0.085366	0.095023	0.104477
20% $C_{10}H_{22}$ 80% C_7H_9	%mol N_2	0.751685	0.744464	0.7373811	0.7304309	0.7236105	0.716916
	%mol O_2	0.199815	0.197895	0.1960127	0.1941652	0.1923522	0.190572
	%mol C_7H_9	0.038799	0.046111	0.053285	0.0603231	0.0672298	0.074008
	%mol $C_{10}H_{22}$	0.009699	0.011527	0.013321	0.015080	0.016807	0.018502
40% $C_{10}H_{22}$ 60% C_7H_9	%mol N_2	0.755793	0.749305	0.742926	0.736656	0.73049	0.724427
	%mol O_2	0.200907	0.199182	0.197486	0.19582	0.194181	0.192569
	%mol C_7H_9	0.025979	0.030908	0.035751	0.040514	0.045197	0.049802
	%mol $C_{10}H_{22}$	0.017319	0.020605	0.023834	0.02701	0.030132	0.033202
60% $C_{10}H_{22}$ 40% C_7H_9	%mol N_2	0.759106	0.753215	0.747414	0.741703	0.736078	0.730538
	%mol O_2	0.201787	0.200222	0.198679	0.197162	0.195666	0.194194
	%mol C_7H_9	0.015642	0.018625	0.021562	0.024454	0.027302	0.030108
	%mol $C_{10}H_{22}$	0.023463	0.027938	0.032343	0.036681	0.040953	0.045161
80% $C_{10}H_{22}$ 20% C_7H_9	%mol N_2	0.761833	0.75644	0.751121	0.745878	0.740707	0.735607
	%mol O_2	0.202512	0.201079	0.199665	0.198271	0.196897	0.195541
	%mol C_7H_9	0.007130	0.008496	0.009842	0.01117	0.012479	0.01377
	%mol $C_{10}H_{22}$	0.028522	0.033985	0.039370	0.044681	0.049917	0.055082
100% $C_{10}H_{22}$ 0% C_7H_9	%mol N_2	0.764118	0.759145	0.754234	0.749388	0.744603	0.739879
	%mol O_2	0.203120	0.201798	0.200492	0.199204	0.197933	0.196676
	%mol $C_{10}H_{22}$	0.032761	0.039058	0.045272	0.051408	0.057464	0.063444

4.3 Point of Extraction of Soot Precursors from the Generated Gas Phase and Influence of the Investigated Parameters

The Chemkin output needs to be post-processed since a one-to-one transfer of the Chemkin output to a ReaxFF input is not feasible due to the very large number of molecules (or atoms *N*) in the system. For example, small non-reactive molecules like molecular nitrogen, need to be filtered out, since they increase the number of atoms considerably, thereby increasing the computation time. The objective is to select a representative onset of soot formation from the chemical kinetic calculations performed. Experimental results show that pyrene mole fraction in the gas phase is closely related to the soot onset.[76, 234] For this reason we identified the pyrene mole fraction as an indicator for the soot inception. Furthermore, analysis of the reactions leading to large PAH in Raj's mechanism(96) indicate that the production of larger-sized PAH, i.e. larger than pyrene, is mainly the result of pyrene consumption. The reaction scheme of the production of PAH from pyrene in Raj's mechanism is given in Figure 4. It can be seen that most of the PAH, with the exception of cyclopenta[1,2]phenalen and fluoranthene (see Figure 9 for their structures), have their major production pathways connected to pyrene through H-abstraction and acetylene addition. Hence, under fuel-rich conditions and temperatures beneath 2000 K, a peak in the pyrene mole fraction indicates a conversion of pyrene into larger species and therefore can be assumed to indicate the onset of soot inception.

To get a consistent description of the gas-phase composition prior to soot inception, we chose the time point at which half of the overall maximum of the mole fraction of pyrene is reached for the first time (see Figure 5). The reason for taking this point is that the maximum of the pyrene mole fraction can be very broad and hence a definite point in time is difficult to make out. A more common approach would be to take a saddle point in this case. However, this approach showed also

difficulties, as the curve of the mole fraction of pyrene can include plateaus or several saddle points, which would make the choice of inception point inconsistent again.

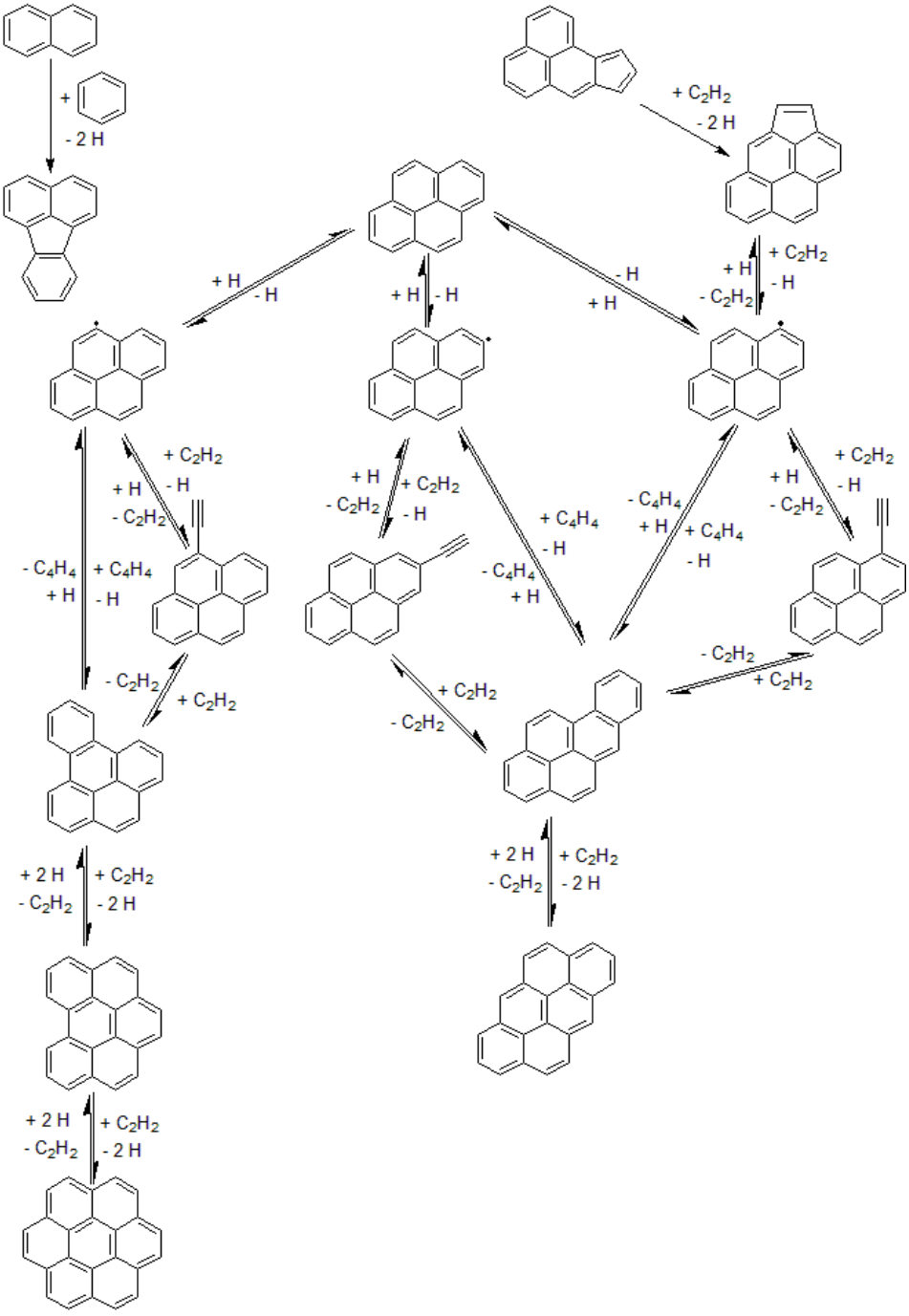

Figure 4. Reaction Pathway scheme for the growth of the PAHs in Raj's mechanism for all PAHs considered in the precursor pool.

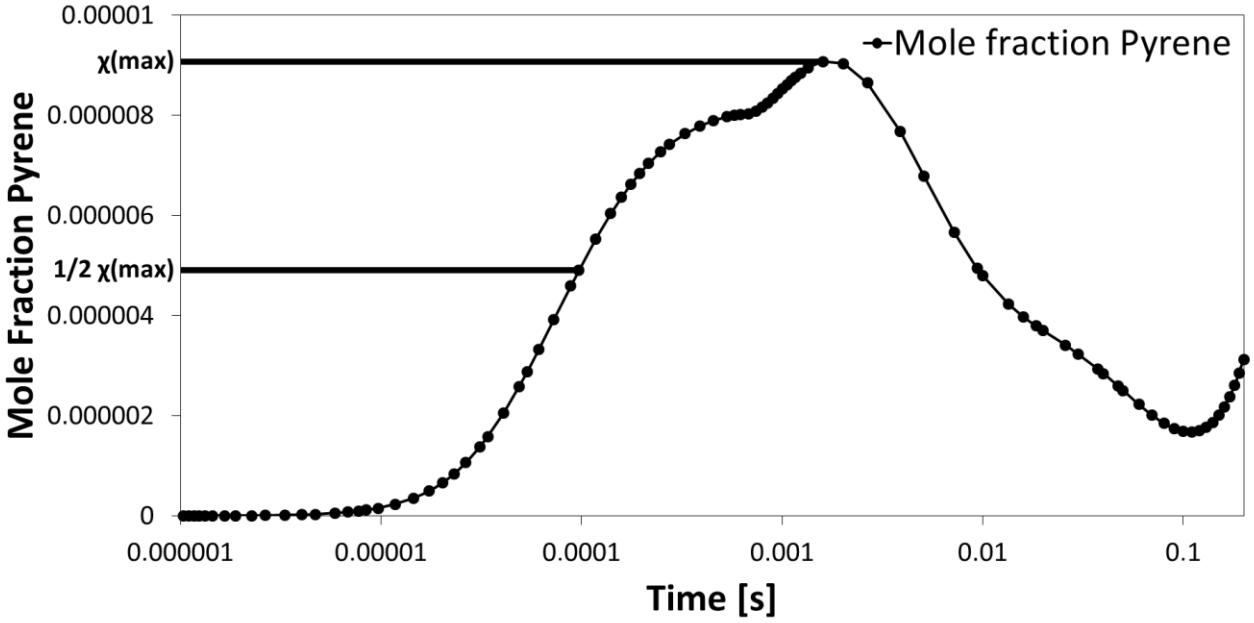

Figure 5. Mole fraction of pyrene for the Chemkin calculation at an equivalence ratio of 3, temperature of 1800 K and a fuel composition of pure n-decane as a function of time. At the time step where 1/2 χ(max) is reached the gas-phase composition is taken for the extraction of the soot precursor pool for the MD simulations.

To further detail our rationale to use this point of extraction the rates of production (ROP) have been analyzed and depicted in Figures 6 - 8 for a number of tested conditions, for all PAH depicted in Figure 4. The vertical lines in Figures 6 - 8 indicate the point of extraction. After the maximum of pyrene is reached, pyrene is consumed more than it is produced in the gas phase. Therefore, the growth of molecules larger than pyrene, as described in the reaction scheme of Figure 4, is starting to take place. This is, an indication for soot inception and as a result, the point of extraction occurs at the start of soot inception.

Nonetheless, it is evident from Figures 6-8 that the tested parameters do have an influence on the rate of production of pyrene and PAH larger than pyrene and in turn on the soot onset. A total of 144 conditions has been tested. Discussing the influence on the rate of production of the PAH for each condition due to the change in parameters individually would be extensive. Thus, the results

are presented in a condensed fashion, by showing the influence of one scanned parameter by keeping the other scanned parameters constant. The discussed trends can be translated to other settings of the two fixed parameters, however, so there is no need to discuss them separately for each condition.

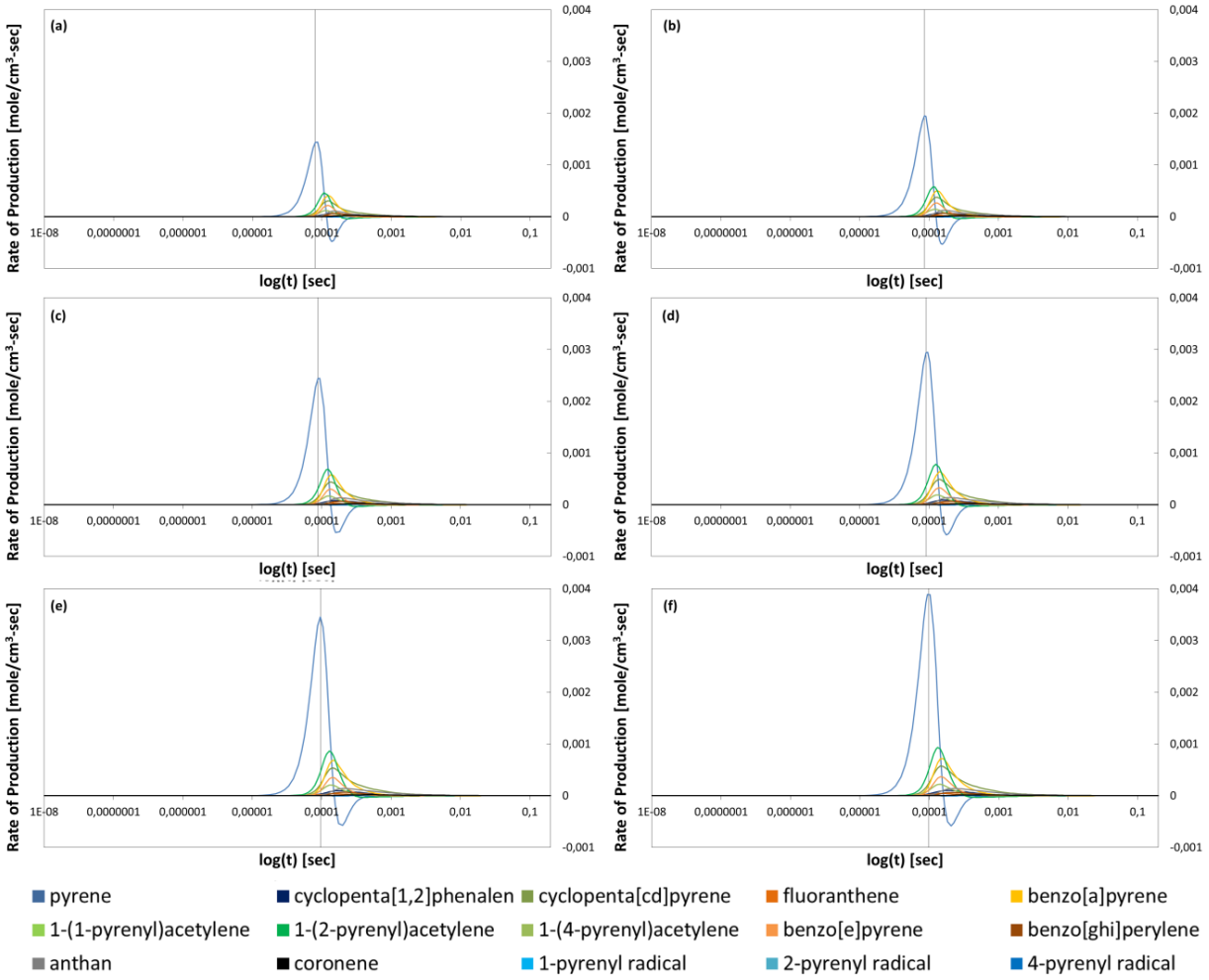

Figure 6. Rates of production of the extracted PAH (shown in Figure 9) over the simulation time for the Chemkin calculations performed with a temperature of 1600K and a fuel mixture of 0 mol% n-decane and 100 mol% toluene, and equivalence ratios of (a) 2.5, (b) 3, (c) 3.5, (d) 4, (e) 4.5, and (f) 5.

Figure 6 shows the extracted ROPS for all PAH of interest for a temperature of 1600 K, a fuel mixture of pure toluene and all tested equivalence ratios. It is evident that the equivalence ratio has

only a minor impact on the PAH ROPs. The only significant influence is a difference in the maximum height of the ROP of pyrene and in turn also a difference in the peak of the total mole fraction of pyrene. With increasing equivalence ratios, the ROP of pyrene rises more steeply and hence also more pyrene is produced during the simulation time. The same holds for PAH larger than pyrene. This can be seen in Figure 6 as no significant change in the shape of the ROP of pyrene or the shape of ROP of PAH larger than pyrene can be observed.

The point of extraction shifts to slightly later times with increasing equivalence ratio. This change is minor, however. The point of extraction for the lowest equivalence ratio (ϕ=2.5) is at 76 ms and continuously shift with increasing equivalence ratio to later times until the point of extraction at the highest equivalence ratio (ϕ=5) is at 98 ms. This is due to the later ignition of the fuel mixtures at higher equivalence ratios and as a result the peak of the pyrene mole fraction, and, in turn, the point of extraction is reached at later times, even though pyrene is produced more rapidly at higher equivalence ratios.

Another minor change is the change in height of the ROP peaks of larger PAH with respect to the peak ROP of pyrene. The height of the ROP peak of pyrene increases with increasing equivalence ratio, but the ROPs of PAH larger than pyrene do not increase accordingly. Hence, the ‘gap’ of the heights of the ROP peak of pyrene and those of larger PAHs grows for larger equivalence ratio. This change can again be related to a change in combustion for the same initial fuel mixture and temperature but a higher equivalence ratio. Due to the different carbon to oxygen atoms ratio, the combustion is more incomplete at higher equivalence ratios and hence the fragmentation of fuel due to combustion is hindered. As a result, fewer smaller molecules are produced that can contribute to the growth of PAH larger than pyrene and consequently the growth of these PAH is hindered.

The reason for the minor influence of the equivalence ratio on the production of pyrene and larger PAH, and therefore also soot, is that the tested fuel-air mixtures are already rich. It is due to this very rich equivalence ratio range tested, that the change of equivalence ratio was not found to have a significant impact as the ratio of oxygen to fuel in the gas mixture is already low. Going to more lean mixtures the equivalence ratio is expected to have an impact of the PAH compositions.(253,254)

A comparison of the found trends to experiment is not straight forward since higher equivalence ratios cohere with different temperatures. Since we especially decoupled these two factors, however, the comparison is not easy. Nonetheless, most studies investigating a change in the structure of soot found that the influence of the equivalence ratio on soot structure is minor. However, the impact of equivalence ratio remains significant on the total particle number.(255–258) Hence, the findings drawn from the simulations are consistent with experimental findings. That is, while the soot nanostructure, and in turn the PAH comprising the soot, remains mostly unchanged when changing equivalence ratio, the amount of soot, and as an equivalent, the amount of PAH has a more significant impact.

Since the amount of PAH used for the ReaxFF calculations is normalized, as described in the following section, the effect of equivalence ratio on the total particle number is not translated to the ReaxFF results, after all. As the main focus of this thesis is to investigate the impact of the varied parameters in the Chemkin calculations on soot structures and the formation of those, this was chosen on purpose, as without a normalization the translation of the Chemkin results to the ReaxFF simulation boxes would have been inconsistent in regard to the number of molecules and size of simulation boxes.

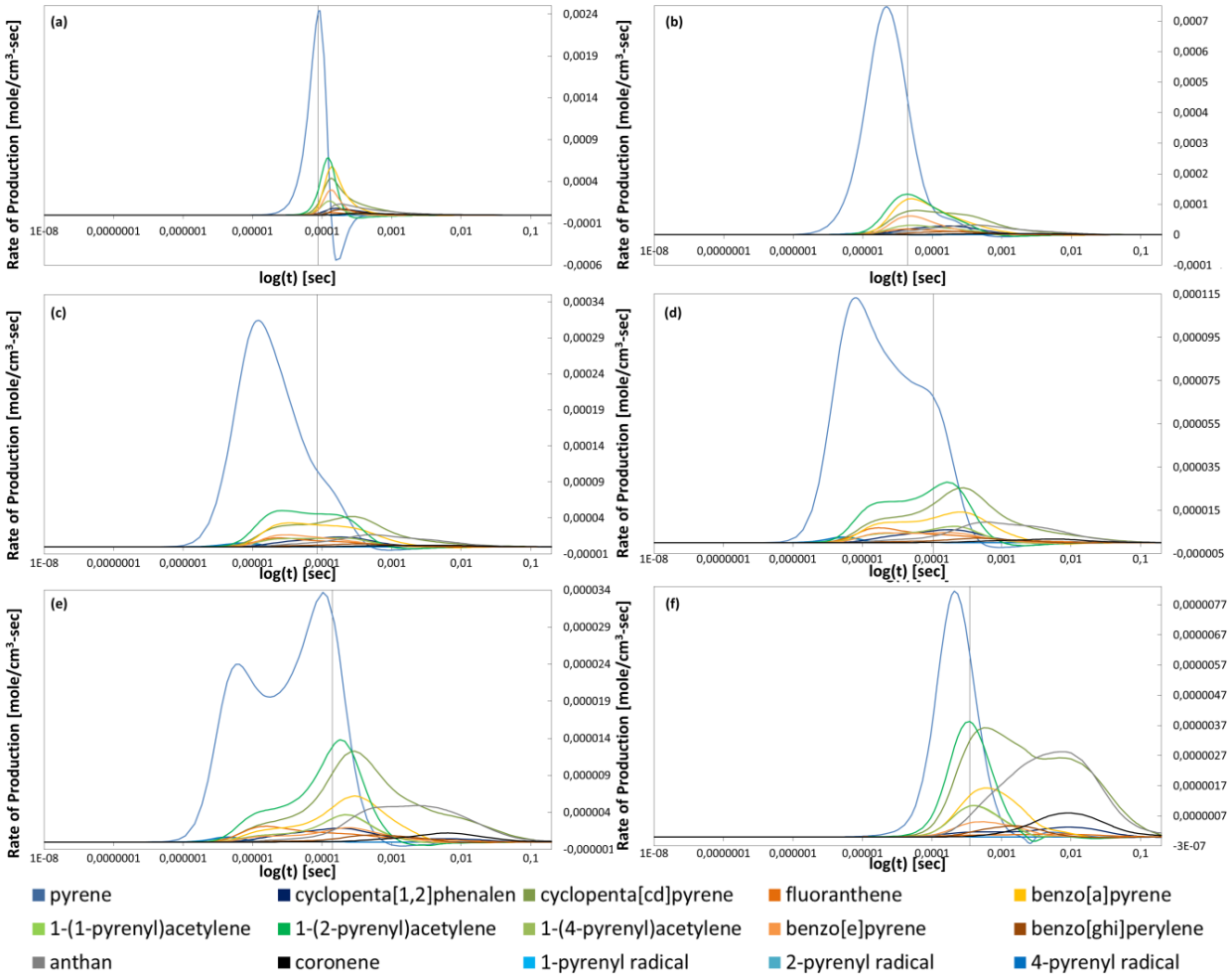

Figure 7. Rates of production of the extracted PAH (shown in Figure 9) over the simulation time for the Chemkin calculations performed with an equivalence ratio of 3.5, a temperature of 1600K and fuel mixtures of (a) 0 mol% n-decane and 100 mol% toluene, (b) 20 mol% n-decane and 80 mol% toluene, (c) 40 mol% n-decane and 60 mol% toluene, (d) 60 mol% n-decane and 40 mol% toluene, (e) 80 mol% n-decane and 20 mol% toluene, and (a) 100 mol% n-decane and 0 mol% toluene.

When investigating the impact of the fuel mixture on the ROP and mole fraction of pyrene, one finds that the impact is much more significant. This is shown in Figure 7, where the ROPs of the PAH of interest are plotted for 1600 K, an equivalence ratio of 3.5 and all tested fuel mixtures. One major influence is the increase in the peak height ROP of pyrene with increasing aromatic fuel content. This led to higher mole fractions of PAH in the gas phase for aromatic fuels and as a result

of more soot. This effect could be shown experimentally as well, where more soot is produced for aromatic fuels than for aliphatic fuels.(259)

Another visible fuel effect is that the ROP for all PAH is broader, meaning the production of PAH is occurring over a longer time, for the fuel mixtures. Thus, the production of PAH over the complete simulation time is longer for mixtures of toluene and n-decane than for the pure compounds due to the broader ROPs, for most tested cases. The synergistic effect of fuel mixtures on the formation of PAH could also be observed experimentally.(51,256–259)

The broadening of the fuel mixtures is due to the different growth pathways from the two investigated fuel components. While the ignition of toluene occurs at a later time than the ignition of n-decane, the growth of pyrene from toluene is much faster than from n-decane in Raj's mechanism. A detailed analysis of this phenomenon is discussed in section 4.4. As a result, the first peak observed in the double peak structures of the PAH ROPs for fuel mixtures must be mainly attributed to the toluene combustion, while the n-decane combustion contributes mostly to the second peak. This is also visible for the fluoranthene ROP, where it gains more significance for fuel mixtures with higher aromatic content. This is due to the different growth pathway of fluoranthene, as presented in Figure 4 since fluoranthene can directly grow from the aromatic fragmentation products of toluene. Hence the growth of PAH from toluene fragments plays a significant role, and the synergistic growth from fragments of toluene and n-decane as well.

Another indication of the difference is the ROPs of PAH that are produced through the HACA mechanism shown in Figure 4. Here one can see an overall expansion of these ROPs with increasing aliphatic content and a rise in relative peak ROP to pyrene peak ROP. This can be explained by considering that acetylene is a typical fragmentation product of n-decane. Hence the HACA pathways are much more pronounced for the aliphatic fuels.

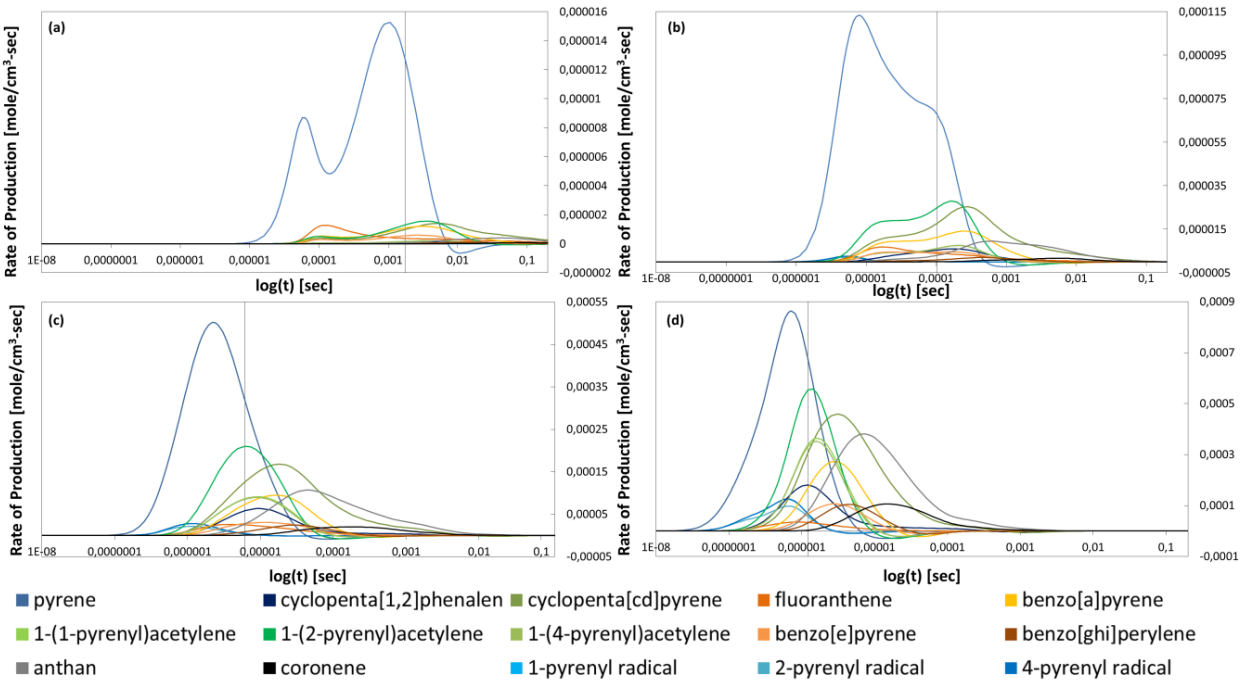

Figure 8. Rates of production of the extracted PAHs (shown in Figure 9) over the simulation time for the Chemkin calculations performed with an equivalence ratio of 3.5, a fuel mixture of 60 mol% n-decane and 40 mol% toluene, and temperatures of (a) 1400 K, (b) 1600 K, (c) 1800 K, and (d)2000 K.

The shift of the point of extraction to shorter times with decreasing aromatic fuel content, except for the pure toluene fuel, can again be mainly attributed to the synergistic effect on PAH growth for fuel mixtures and different ignition times of the fuels. As stated above the aliphatic fuel ignites earlier than the aromatic fuels, but the stepwise growth of PAH from n-decane exhibits many more intermediates than the one from toluene.

One must note, however, that also by fragmentation of toluene similar reaction pathways for the production of PAH can be observed. This brings us to Figure 8, which shows the difference in PAH ROPs for fuel mixtures of 60mol% n-decane and 40mol% toluene, an equivalence ratio for 3.5 and all tested temperatures. In Figure 8 it is clearly visible that the double peak structure is lost with

increasing temperature and the overall ROPs get narrower. Meanwhile, the relative peak ROP of PAH different than pyrene to the peak ROP of pyrene gets smaller, meaning the production of other PAH from pyrene occurs more rapidly. Also, the peak ROP of pyrene, and all other peak ROP rise with increasing temperatures.

Most of the above-mentioned observations can mainly be attributed to a faster and more complete fragmentation of the fuel molecules at higher temperatures. Since the ignition of both fuels occurs at shorter times at higher temperatures, the difference in ignition does not play such a significant role. Furthermore, the more complete fragmentation of the fuels leads to the production of PAH by successive addition of smaller molecules. Hence, the double peak structure is lost, as the direct pathways of PAH production from larger toluene fragments are not as significant anymore, as is the ignition delay of the toluene fuel.

The more complete fragmentation of the fuel is also reason to why PAH larger than pyrene get produced more rapidly at higher temperatures. Firstly, the number of smaller radicals, contributing to HACA mechanism pathways, is higher, and secondly, the overall kinetics are faster at higher temperatures. In turn, the production of PAH larger than pyrene increases. The faster kinetics at elevated temperatures also account for the difference in the peak ROP of all PAH for different temperatures. Since the fuel fragments more rapidly, and the reactions occur more readily, because reaction barriers are easier overcome at higher temperatures, PAHs are formed faster. Increased soot production at higher temperatures has also been found in experiments.(45,260)

4.4 Reduction of the Generated Gas Phase to Soot Precursor Compositions

As the pyrene mole fraction in the generated gas phase is typically on a ppm scale; a corresponding molecular simulation box containing only one pyrene molecule would comprise almost one million other molecules. This yields ensembles where, if one assumes that each

molecule consists of an average of 10 atoms, the number of atoms (N) comes close to tens of millions of atoms. Such systems become too large for daily routine molecular dynamic simulations. Therefore, additional selection criteria for the reduction of the generated gas phase were added. The first criterion ensures that half of the maximum mole fraction of pyrene exceeds the ppm-level in order to assure that enough soot precursors are present. The second criterion is to select only aromatic molecules with four or more rings and discard the mole fractions of smaller molecules in the ReaxFF simulations. This criterion was chosen for several reasons. The first criterion ensures that half of the maximum mole fraction of pyrene exceeds the ppm-level in order to assure that a sufficient number of soot precursors are present. The second criterion is to select only aromatic molecules with four or more rings and to discard the mole fractions of smaller molecules in the MD simulations. This latter criterion ensures the presence of pyrene and PAH of the size of pyrene has been shown crucial in soot formation experiments.(51,52,120,149,156,255) On the other hand, if the smaller-sized aliphatics and aromatics would be included, they would dominate the gas phase composition. However, since their composition hardly changes under the considered thermochemical conditions, the overall gas-phase composition used in the ReaxFF simulations would barely change.

The molecules considered are shown in Figure 9. The presented pool of considered molecules may not necessarily represent the actual gas phase under experimental conditions since it lacks molecules smaller than pyrene and other PAH potentially present in the gas phase. However, the Raj mechanism was chosen as it gives a reasonable distribution of PAH and the chosen PAH include several features whose contribution to the bond formation mechanism between PAH is investigated in this thesis, like aliphatic side chains, five-membered rings, different aromatic sites and radicals.(58,116,261–263)

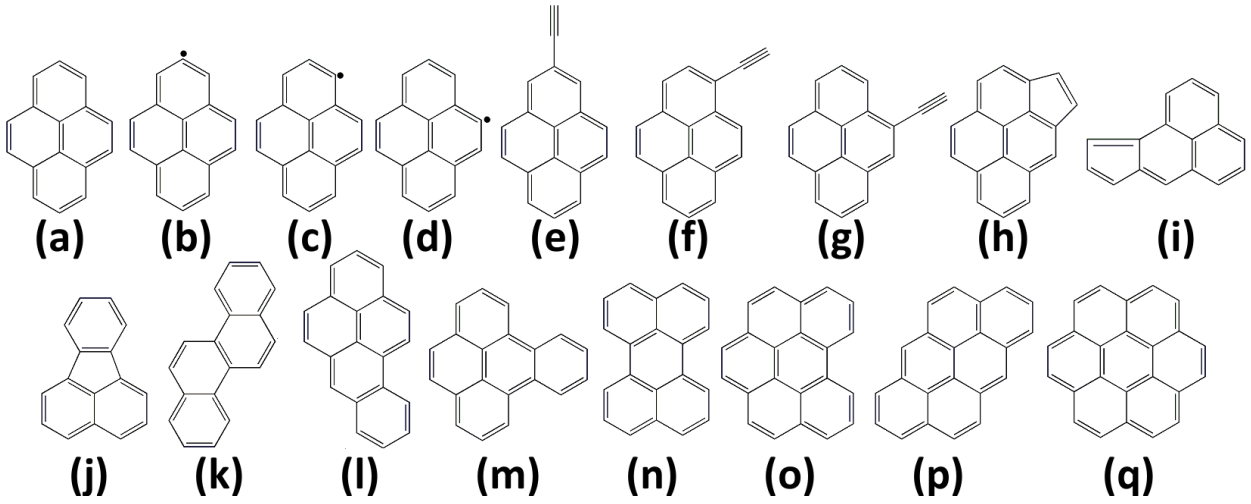

Figure 9. PAH considered for the generation of the precursor pool for the ReaxFF simulations from the Chemkin calculations. (a) pyrene, (b) 1-pyrenyl radical, (c) 2-pyrenyl radical (d) 3-pyrenyl radical, (e) 1-(1-pyrenyl)acetylene, (f) 1-(2-pyrenyl)acetylene, (g) 1-(4-pyrenyl)acetylene, (h) cyclopenta[cd]pyrene, (i) cyclopenta[1,2]phenalen, (j) fluoranthene, (k) chrysene, (l) benzo[a]pyrene ,(m) benzo[e]pyrene, (n) perylene, (o) benzo[ghi]perylene, (p) anthanthrene, (q) coronene.

Based on the above-mentioned selection criteria we generated a ReaxFF-input gas mixture. The total mole fraction of the selected PAH varies when changing the temperature, equivalence ratio and fuel compositions, and amount between 10 and 900 ppm of the total mole fraction of the initial gas phase. The individual PAH mole fractions were summarized and the percentage distributions of the PAH mole fractions in the sum used to account for the number of molecules in the ReaxFF simulation, in order to obtain molecular dynamics boxes of maximum 100 molecules each for the different compositions. The extracted compositions from the Chemkin calculations are given in Figure 10 – 13 and Tables 6 –11.

In the tabular representation, the first four columns from left give the temperature, the equivalence ratio and percentage of n-decane in the n-decane/toluene fuel mixture, and percentage of toluene in the fuel mixture, respectively. The following columns are the number of PAHs of the

respective species given in the first row that are present in the composition at the given conditions. Rows in which for all PAHs an X is marked down, are representing conditions for which the selection criteria for extracting the soot precursor pools have not been met. This is namely the case for compositions at the two temperature extremes, although, the reasons why the selection criteria have not been met differ. At 1400 K no composition could be extracted because there is no maximum of the pyrene mole fraction in the time range of 0.2 seconds for several fuel compositions and equivalence ratios, due to a slower chemical formation of pyrene at lower temperatures. At 2000 K with 100% n-decane and equivalence ratios of 2.5 and 3, as well as 80% n-decane/20% toluene and equivalence ratios of 2.5, the pyrene mole fraction was below the ppm level and hence no composition was extracted.

Another mentionable observation involves the pyrenyl radicals in the soot precursor pool. While the mole fraction of these radicals is very low in the gas phase at lower temperatures (<1800 K), it increases with rising temperature. These radicals affect the extracted soot precursor pools at these temperatures, as they are very reactive. Hence, the precursor pools containing higher numbers of radicals are more reactive and therefore are expected to show faster chemical growth. Furthermore, neither chrysene nor perylene showed high enough mole fractions in the gas phase to be extracted for any soot precursor pool composition.

The change of the extracted soot precursor composition due to the variation of the tested parameters is discussed in the following section.

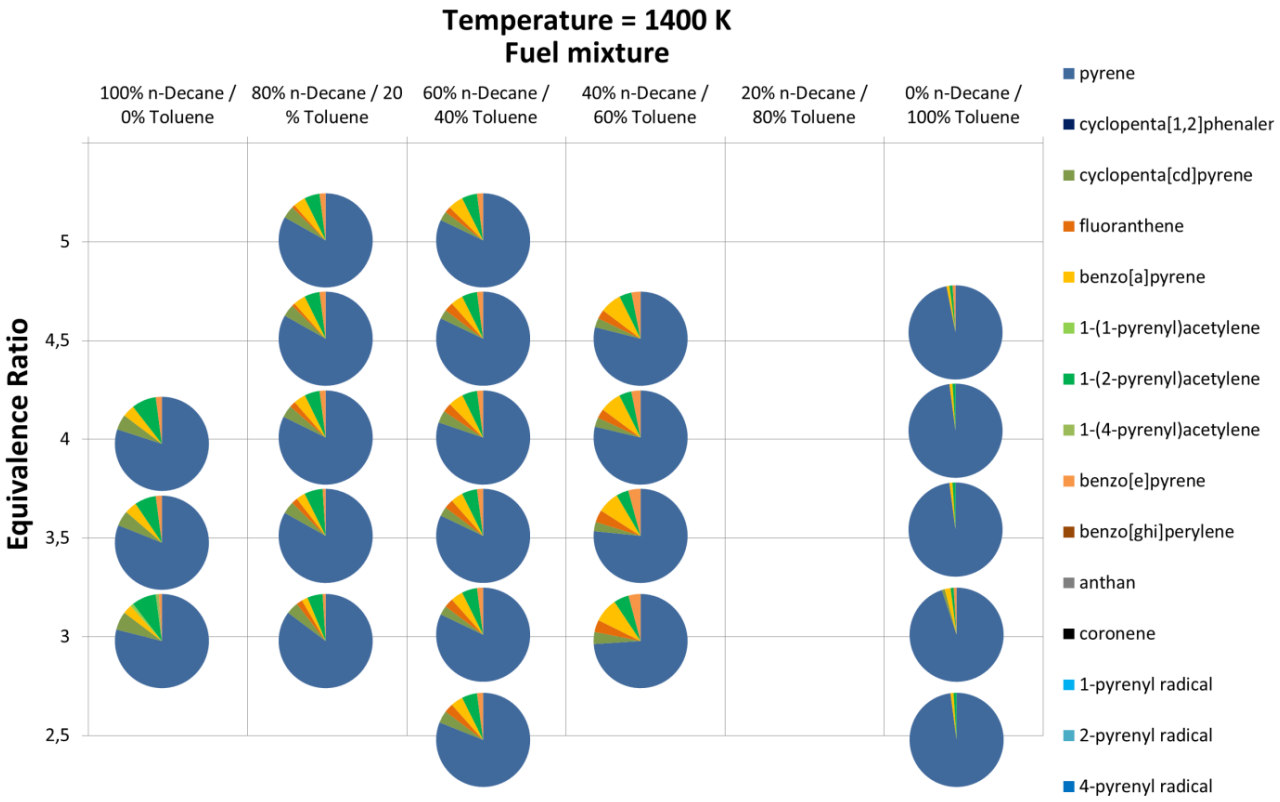

Figure 10. Pie chart of the soot precursor pool compositions at all equivalence ratios and fuel mixtures for a temperature of 1400 K in the Chemkin calculation. The color scheme of the soot precursors included in the compositions is given on the right-hand side. The size of each slice in the pie chart depicts the numerical proportion of the soot precursor of equal color in the composition.

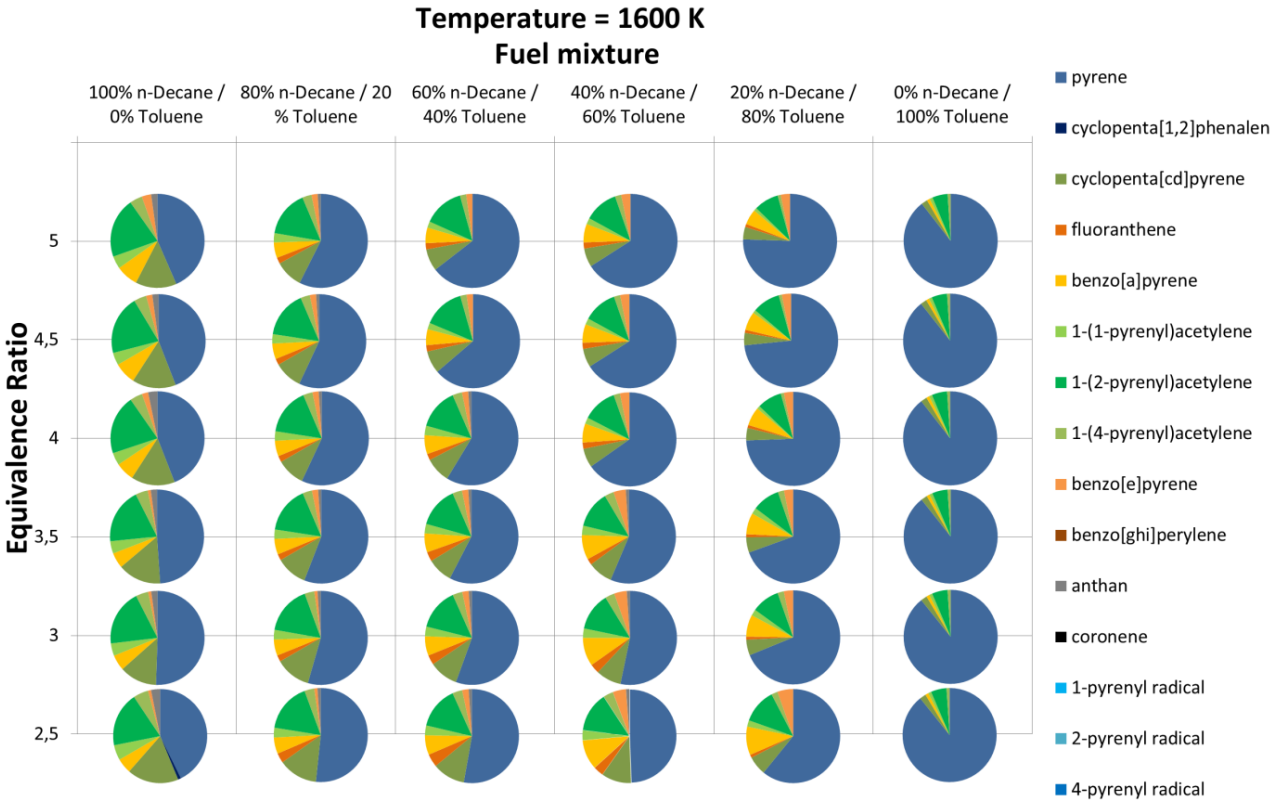

Figure 11. Pie chart of the soot precursor pool compositions at all equivalence ratios and fuel mixtures for a temperature of 1600 K in the Chemkin calculation. The color scheme of the soot precursors included in the compositions is given on the right-hand side. The size of each slice in the pie chart depicts the numerical proportion of the soot precursor of equal color in the composition.

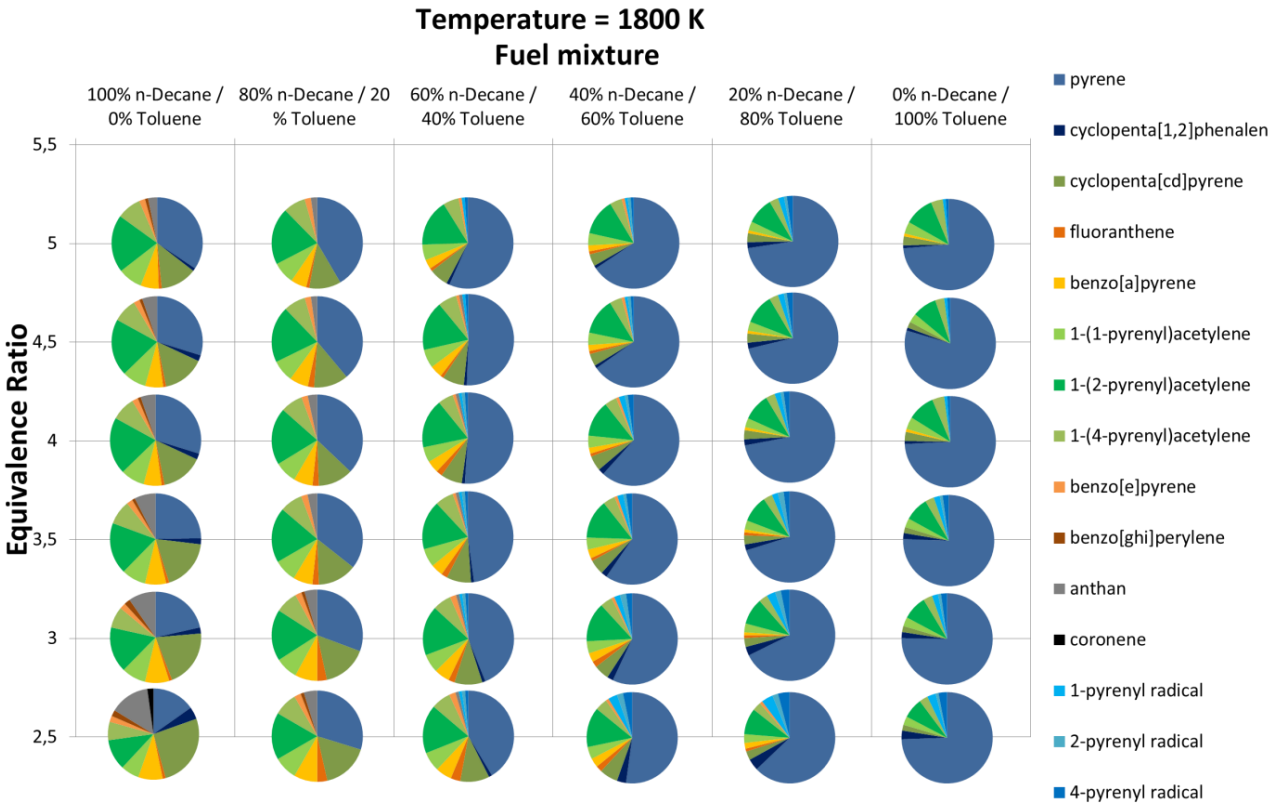

Figure 12. Pie chart of the soot precursor pool compositions at all equivalence ratios and fuel mixtures for a temperature of 1800 K in the Chemkin calculation. The color scheme of the soot precursors included in the compositions is given on the right-hand side. The size of each slice in the pie chart depicts the numerical proportion of the soot precursor of equal color in the composition.

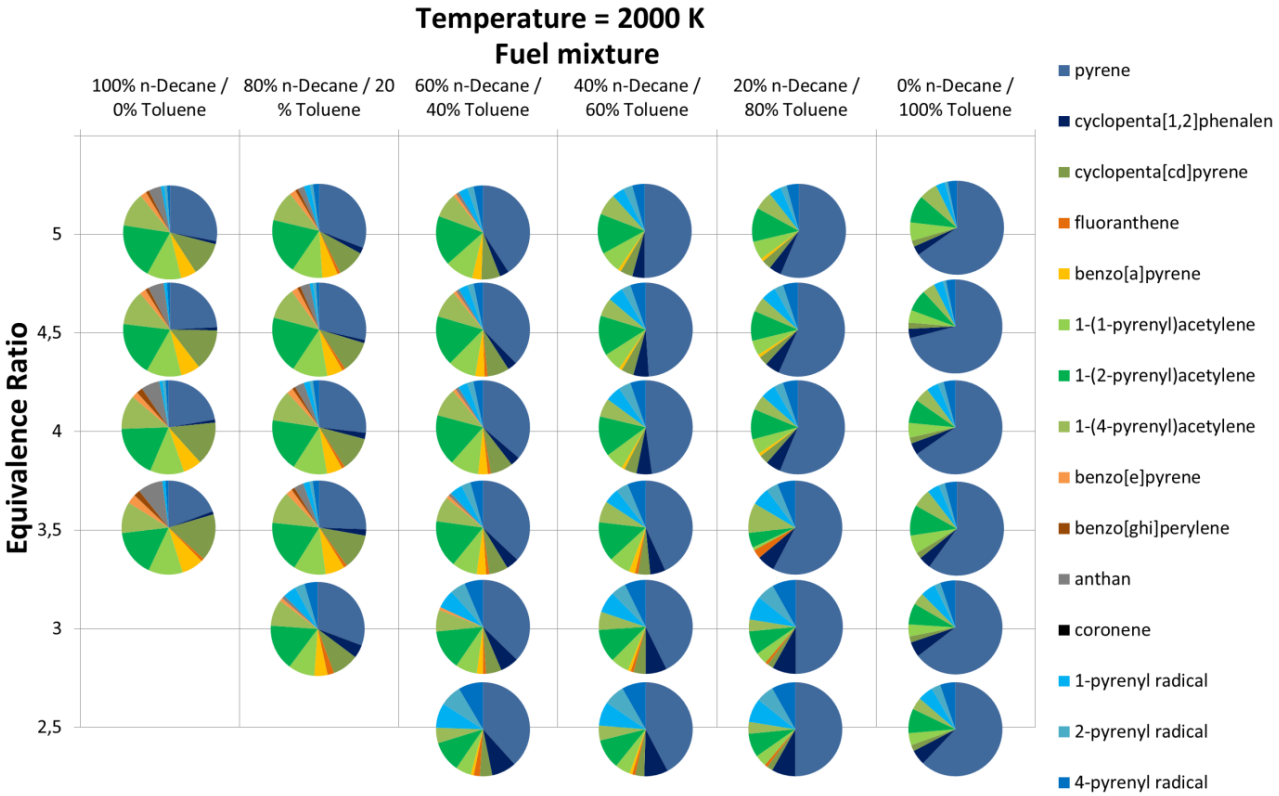

Figure 13. Pie chart of the soot precursor pool compositions at all equivalence ratios and fuel mixtures for a temperature of 2000 K in the Chemkin calculation. The color scheme of the soot precursors included in the compositions is given on the right-hand side. The size of each slice in the pie chart depicts the numerical proportion of the soot precursor of equal color in the composition.

Table 6. Soot precursor pool compositions for the ReaxFF simulations for a fuel composition of 100% n-decane and 0% toluene in the Chemkin calculations.

Temperature (10^3K)	Equivalence Ratio Φ	mol% n-decane	mol% toluene	pyrene	cyclopenta[1,2]phenalen	cyclopenta[cd]pyrene	fluoranthene	benzo[a]pyrene	1-(1-pyrenyl)acetylene	1-(2-pyrenyl)acetylene	1-(4-pyrenyl)acetylene	benzo[e]pyrene	benzo[ghi]perylene	anthan	coronene	1-pyrenyl radical	2-pyrenyl radical	4-pyrenyl radical
1.4	2.5	100	0	X	X	X	X	X	X	X	X	X	X	X	X	X	X	X
1.6	2.5	100	0	41	1	17	0	5	5	18	5	1	0	3	0	0	0	0
1.8	2.5	100	0	14	4	24	1	8	6	10	6	2	2	13	2	0	0	0
2.0	2.5	100	0	X	X	X	X	X	X	X	X	X	X	X	X	X	X	X
1.4	3	100	0	75	0	6	0	3	1	8	1	1	0	0	0	0	0	0
1.6	3	100	0	46	0	14	0	5	4	18	4	1	0	2	0	0	0	0
1.8	3	100	0	20	2	19	1	8	8	15	7	2	2	9	0	0	0	0
2.0	3	100	0	X	X	X	X	X	X	X	X	X	X	X	X	X	X	X
1.4	3.5	100	0	76	0	5	0	4	0	8	0	2	0	0	0	0	0	0
1.6	3.5	100	0	47	0	12	0	5	4	18	4	1	0	2	0	0	0	0
1.8	3.5	100	0	23	2	17	1	7	8	17	8	2	1	7	0	0	0	0
2.0	3.5	100	0	18	1	15	1	7	11	15	10	3	2	8	0	1	0	1
1.4	4	100	0	77	0	5	0	4	0	7	0	2	0	0	0	0	0	0
1.6	4	100	0	41	0	14	0	6	4	19	4	2	0	3	0	0	0	0
1.8	4	100	0	28	2	14	1	6	8	19	8	2	1	5	0	0	0	0
2.0	4	100	0	21	1	14	0	6	11	17	11	2	2	6	0	1	1	1
1.4	4.5	100	0	X	X	X	X	X	X	X	X	X	X	X	X	X	X	X
1.6	4.5	100	0	41	0	14	0	7	4	19	4	2	0	2	0	0	0	0
1.8	4.5	100	0	28	2	14	1	6	8	19	8	2	1	5	0	0	0	0
2.0	4.5	100	0	22	1	13	0	6	11	17	11	2	1	5	0	1	0	1
1.4	5	100	0	X	X	X	X	X	X	X	X	X	X	X	X	X	X	X
1.6	5	100	0	40	0	13	0	7	4	19	4	3	0	2	0	0	0	0
1.8	5	100	0	32	1	12	1	6	8	19	8	2	1	3	0	0	0	0
2.0	5	100	0	26	1	11	0	5	11	18	11	2	1	4	0	1	1	1

Table 7. Soot precursor pool compositions for the ReaxFF simulations for a fuel composition of 80% n-decane and 20% toluene in the Chemkin calculations.

Temperature (10^3K)	Equivalence Ratio Φ	mol% n-decane	mol% toluene	pyrene	cyclopenta[1,2]phenalen	cyclopenta[cd]pyrene	fluoranthene	benzo[a]pyrene	1-(1-pyrenyl)acetylene	1-(2-pyrenyl)acetylene	1-(4-pyrenyl)acetylene	benzo[e]pyrene	benzo[ghi]perylene	anthan	coronene	1-pyrenyl radical	2-pyrenyl radical	4-pyrenyl radical
1.4	2.5	80	20	81	0	4	2	2	0	5	0	1	0	0	0	0	0	0
1.6	2.5	80	20	46	0	12	3	5	3	15	3	1	0	1	0	0	0	0
1.8	2.5	80	20	25	0	14	3	7	7	14	7	2	1	4	0	0	0	0
2.0	2.5	80	20	X	X	X	X	X	X	X	X	X	X	X	X	X	X	X
1.4	3	80	20	80	0	4	2	3	0	6	0	1	0	0	0	0	0	0
1.6	3	80	20	49	0	11	2	5	3	15	3	1	0	1	0	0	0	0
1.8	3	80	20	27	0	14	3	7	7	16	7	2	1	4	0	0	0	0
2.0	3	80	20	27	4	8	2	4	8	14	8	1	0	1	0	4	3	4
1.4	3.5	80	20	79	0	4	2	3	0	6	0	1	0	0	0	0	0	0
1.6	3.5	80	20	52	0	10	2	5	3	15	3	2	0	1	0	0	0	0
1.8	3.5	80	20	31	0	12	2	6	7	17	7	2	0	3	0	0	0	0
2.0	3.5	80	20	23	2	11	1	6	10	16	10	2	1	3	0	2	1	2
1.4	4	80	20	79	0	4	2	4	0	5	0	2	0	0	0	0	0	0
1.6	4	80	20	53	0	9	2	5	3	15	3	2	0	1	0	0	0	0
1.8	4	80	20	33	0	11	2	6	7	18	7	2	0	3	0	0	0	0
2.0	4	80	20	25	2	11	1	5	11	17	10	2	1	3	0	2	1	2
1.4	4.5	80	20	79	0	4	1	4	0	5	0	2	0	0	0	0	0	0
1.6	4.5	80	20	53	0	9	2	5	3	15	3	2	0	1	0	0	0	0
1.8	4.5	80	20	35	0	11	2	6	7	18	7	2	0	2	0	0	0	0
2.0	4.5	80	20	26	1	10	1	5	11	18	10	2	1	3	0	1	1	1
1.4	5	80	20	79	0	4	1	4	0	5	0	2	0	0	0	0	0	0
1.6	5	80	20	54	0	9	2	5	3	15	3	2	0	1	0	0	0	0
1.8	5	80	20	37	0	10	1	5	7	18	7	2	0	2	0	0	0	0
2.0	5	80	20	29	2	9	1	5	10	18	10	2	1	2	0	2	1	2

Table 8. Soot precursor pool compositions for the ReaxFF simulations for a fuel composition of 60% n-decane and 40% toluene in the Chemkin calculations.

Temperature (10^3K)	Equivalence Ratio Φ	mol% n-decane	mol% toluene	pyrene	cyclopenta[1,2]phenalen	cyclopenta[cd]pyrene	fluoranthene	benzo[a]pyrene	1-(1-pyrenyl)acetylene	1-(2-pyrenyl)acetylene	1-(4-pyrenyl)acetylene	benzo[e]pyrene	benzo[ghi]perylene	anthan	coronene	1-pyrenyl radical	2-pyrenyl radical	4-pyrenyl radical
1.4	2.5	60	40	77	0	4	3	4	0	5	0	2	0	0	0	0	0	0
1.6	2.5	60	40	47	0	10	4	6	3	13	3	2	0	1	0	0	0	0
1.8	2.5	60	40	36	1	9	3	5	6	15	6	2	0	1	0	1	1	1
2.0	2.5	60	40	36	8	4	2	1	5	10	5	0	0	0	0	8	7	8
1.4	3	60	40	78	0	3	3	4	0	5	0	2	0	0	0	0	0	0
1.6	3	60	40	50	0	9	3	6	3	13	3	2	0	1	0	0	0	0
1.8	3	60	40	40	1	9	2	5	6	16	6	2	0	1	0	1	1	1
2.0	3	60	40	35	6	5	1	2	7	13	7	1	0	0	0	6	5	6
1.4	3.5	60	40	78	0	3	3	4	0	5	0	2	0	0	0	0	0	0
1.6	3.5	60	40	53	0	8	3	6	3	13	3	2	0	1	0	0	0	0
1.8	3.5	60	40	44	1	8	2	4	6	16	6	1	0	1	0	1	1	1
2.0	3.5	60	40	34	4	6	1	3	8	15	8	1	0	1	0	4	3	4
1.4	4	60	40	77	0	4	3	5	0	5	0	2	0	0	0	0	0	0
1.6	4	60	40	54	0	8	2	6	3	13	3	2	0	1	0	0	0	0
1.8	4	60	40	47	1	7	2	4	5	16	5	1	0	1	0	1	1	1
2.0	4	60	40	33	3	7	1	3	9	16	9	1	0	1	0	3	2	3
1.4	4.5	60	40	78	0	3	3	4	0	5	0	2	0	0	0	0	0	0
1.6	4.5	60	40	58	0	7	2	5	2	13	2	2	0	0	0	0	0	0
1.8	4.5	60	40	46	1	7	1	4	6	16	6	1	0	1	0	1	0	1
2.0	4.5	60	40	35	3	7	1	3	9	16	9	1	0	1	0	3	2	3
1.4	5	60	40	78	0	3	2	5	0	5	0	2	0	0	0	0	0	0
1.6	5	60	40	60	0	7	2	5	2	13	2	2	0	0	0	0	0	0
1.8	5	60	40	51	1	6	1	3	5	15	5	1	0	0	0	1	0	1
2.0	5	60	40	38	3	6	0	3	9	16	8	1	0	1	0	3	2	3

Table 9. Soot precursor pool compositions for the ReaxFF simulations for a fuel composition of 40% n-decane and 60% toluene in the Chemkin calculations.

Temperature (10^3K)	Equivalence Ratio Φ	mol% n-decane	mol% toluene	pyrene	cyclopenta[1,2]phenalen	cyclopenta[cd]pyrene	fluoranthene	benzo[a]pyrene	1-(1-pyrenyl)acetylene	1-(2-pyrenyl)acetylene	1-(4-pyrenyl)acetylene	benzo[e]pyrene	benzo[ghi]perylene	anthan	coronene	1-pyrenyl radical	2-pyrenyl radical	4-pyrenyl radical
1.4	2.5	40	60	X	X	X	X	X	X	X	X	X	X	X	X	X	X	X
1.6	2.5	40	60	43	0	9	3	9	3	12	3	4	0	1	0	0	0	0
1.8	2.5	40	60	48	3	6	2	3	4	13	4	1	0	0	0	3	2	3
2.0	2.5	40	60	41	8	3	1	1	5	10	5	0	0	0	0	8	7	8
1.4	3	40	60	71	0	4	4	8	0	5	0	4	0	0	0	0	0	0
1.6	3	40	60	49	0	8	3	9	3	12	3	4	0	1	0	0	0	0
1.8	3	40	60	53	2	5	2	3	4	13	4	1	0	0	0	2	2	2
2.0	3	40	60	41	7	4	1	1	6	11	6	0	0	0	0	7	5	7
1.4	3.5	40	60	72	0	3	4	7	0	4	0	4	0	0	0	0	0	0
1.6	3.5	40	60	53	0	8	2	8	3	12	3	4	0	1	0	0	0	0
1.8	3.5	40	60	56	2	5	1	3	4	13	4	1	0	0	0	2	1	2
2.0	3.5	40	60	41	5	4	1	2	7	13	7	0	0	0	0	5	4	6
1.4	4	40	60	74	0	3	3	7	0	4	0	3	0	0	0	0	0	0
1.6	4	40	60	60	0	6	2	6	2	11	2	3	0	0	0	0	0	0
1.8	4	40	60	58	2	5	1	2	4	12	4	1	0	0	0	2	1	2
2.0	4	40	60	45	5	4	0	1	6	13	6	0	0	0	0	5	4	5
1.4	4.5	40	60	75	0	3	3	7	0	4	0	3	0	0	0	0	0	0
1.6	4.5	40	60	62	0	6	2	6	2	11	2	3	0	0	0	0	0	0
1.8	4.5	40	60	60	1	4	1	2	4	12	4	1	0	0	0	1	1	1
2.0	4.5	40	60	46	5	4	0	1	6	13	6	0	0	0	0	5	3	5
1.4	5	40	60	X	X	X	X	X	X	X	X	X	X	X	X	X	X	X
1.6	5	40	60	65	0	5	1	5	2	10	2	2	0	0	0	0	0	0
1.8	5	40	60	61	1	4	1	2	4	12	4	1	0	0	0	1	1	1
2.0	5	40	60	47	4	4	0	1	7	13	7	0	0	0	0	4	3	4

Table 10. Soot precursor pool compositions for the ReaxFF simulations for a fuel composition of 20% n-decane and 80% toluene in the Chemkin calculations.

Temperature (10^3K)	Equivalence Ratio Φ	mol% n-decane	mol% toluene	pyrene	cyclopenta[1,2]phenalen	cyclopenta[cd]pyrene	fluoranthene	benzo[a]pyrene	1-(1-pyrenyl)acetylene	1-(2-pyrenyl)acetylene	1-(4-pyrenyl)acetylene	benzo[e]pyrene	benzo[ghi]perylene	anthan	coronene	1-pyrenyl radical	2-pyrenyl radical	4-pyrenyl radical
1.4	2.5	20	80	X	X	X	X	X	X	X	X	X	X	X	X	X	X	X
1.6	2.5	20	80	56	0	6	1	9	2	11	2	5	0	0	0	0	0	0
1.8	2.5	20	80	61	4	3	1	2	3	9	3	1	0	0	0	4	2	4
2.0	2.5	20	80	49	8	2	1	0	4	8	4	0	0	0	0	8	6	8
1.4	3	20	80	X	X	X	X	X	X	X	X	X	X	X	X	X	X	X
1.6	3	20	80	64	0	5	1	7	2	9	2	3	0	0	0	0	0	0
1.8	3	20	80	65	3	3	1	1	3	9	3	0	0	0	0	3	2	3
2.0	3	20	80	46	8	2	0	0	4	9	4	0	0	0	0	8	6	8
1.4	3.5	20	80	X	X	X	X	X	X	X	X	X	X	X	X	X	X	X
1.6	3.5	20	80	66	0	5	1	7	2	9	2	3	0	0	0	0	0	0
1.8	3.5	20	80	66	2	3	1	1	3	9	3	0	0	0	0	2	2	2
2.0	3.5	20	80	56	6	0	3	0	1	5	10	0	0	0	0	6	4	6
1.4	4	20	80	X	X	X	X	X	X	X	X	X	X	X	X	X	X	X
1.6	4	20	80	70	0	4	1	6	1	8	1	3	0	0	0	0	0	0
1.8	4	20	80	67	2	3	0	1	3	9	3	0	0	0	0	2	1	2
2.0	4	20	80	54	5	3	0	1	5	10	5	0	0	0	0	5	3	5
1.4	4.5	20	80	X	X	X	X	X	X	X	X	X	X	X	X	X	X	X
1.6	4.5	20	80	69	0	4	1	6	1	9	1	3	0	0	0	0	0	0
1.8	4.5	20	80	67	2	3	0	1	3	10	3	0	0	0	0	2	1	2
2.0	4.5	20	80	55	5	3	0	1	5	10	5	0	0	0	0	5	3	5
1.4	5	20	80	X	X	X	X	X	X	X	X	X	X	X	X	X	X	X
1.6	5	20	80	71	0	4	1	5	1	8	1	3	0	0	0	0	0	0
1.8	5	20	80	69	2	3	0	1	3	9	3	0	0	0	0	2	1	2
2.0	5	20	80	53	4	3	0	1	6	11	6	0	0	0	0	4	2	4

Table 11. Soot precursor pool compositions for the ReaxFF simulations for a fuel composition of 100% n-decane and 0% toluene in the Chemkin calculations.

Temperature (10^3K)	Equivalence Ratio Φ	mol% n-decane	mol% toluene	pyrene	cyclopenta[1,2]phenalen	cyclopenta[cd]pyrene	fluoranthene	benzo[a]pyrene	1-(1-pyrenyl)acetylene	1-(2-pyrenyl)acetylene	1-(4-pyrenyl)acetylene	benzo[e]pyrene	benzo[ghi]perylene	anthan	coronene	1-pyrenyl radical	2-pyrenyl radical	4-pyrenyl radical
1.4	2.5	0	100	94	0	0	0	1	0	1	0	0	0	0	0	0	0	0
1.6	2.5	0	100	83	0	2	0	1	1	5	1	0	0	0	0	0	0	0
1.8	2.5	0	100	73	3	2	0	0	3	7	3	0	0	0	0	3	1	3
2.0	2.5	0	100	59	5	2	0	0	4	8	4	0	0	0	0	5	3	5
1.4	3	0	100	93	0	1	0	2	0	1	0	1	0	0	0	0	0	0
1.6	3	0	100	83	0	2	0	1	1	5	1	0	0	0	0	0	0	0
1.8	3	0	100	70	2	2	0	0	3	8	3	0	0	0	0	2	1	2
2.0	3	0	100	62	5	2	0	0	4	7	4	0	0	0	0	5	2	5
1.4	3.5	0	100	94	0	0	0	1	0	1	0	0	0	0	0	0	0	0
1.6	3.5	0	100	84	0	2	0	1	1	5	1	0	0	0	0	0	0	0
1.8	3.5	0	100	71	2	2	0	0	3	8	3	0	0	0	0	2	1	2
2.0	3.5	0	100	57	4	2	0	0	6	10	6	0	0	0	0	4	2	4
1.4	4	0	100	94	0	0	0	1	0	1	0	0	0	0	0	0	0	0
1.6	4	0	100	85	0	2	0	1	1	5	1	0	0	0	0	0	0	0
1.8	4	0	100	69	1	3	0	1	4	9	4	0	0	0	0	1	0	1
2.0	4	0	100	64	4	2	0	0	5	8	5	0	0	0	0	4	2	4
1.4	4.5	0	100	94	0	0	0	1	0	1	0	1	0	0	0	0	0	0
1.6	4.5	0	100	84	0	2	0	1	1	5	1	0	0	0	0	0	0	0
1.8	4.5	0	100	74	1	2	0	0	3	8	3	0	0	0	0	1	0	1
2.0	4.5	0	100	66	3	2	0	0	4	7	4	0	0	0	0	3	1	3
1.4	5	0	100	X	X	X	X	X	X	X	X	X	X	X	X	X	X	X
1.6	5	0	100	85	0	2	0	1	1	5	1	0	0	0	0	0	0	0
1.8	5	0	100	70	1	3	0	1	4	10	4	0	0	0	0	1	0	1
2.0	5	0	100	62	3	2	0	0	6	9	6	0	0	0	0	3	1	3

4.5 Discussion of the Change in Combustion Conditions on the generated Precursor Pools

As can be seen in Figures 10 – 13 there are clear tendencies of the precursor pool compositions. For example, the compositions are insensitive with respect to the studied equivalence ratios. Since the equivalence ratio also had only a minor impact on the ROP of PAH in Figure 6, this is not surprising. As a result, the precursor pool compositions only differ in a few molecules when going from the lowest to the highest equivalence ratio for constant fuel compositions and temperatures. This is due to the fact that interactions between oxygen and large precursors are not considered in large for the detailed mechanisms. While there are several oxidations of the large precursors included in the mechanisms, it seems that these are too few to account for the change in the equivalence ratio. Furthermore, the equivalence ratio range comprises only fuel-rich compositions, so the oxygen/fuel ratio in the gas mixture is already low for all tested equivalence ratios and most of the oxygen is consumed before PAH growth reactions take place. Going to more lean mixtures the equivalence ratio is expected to have an impact of the PAH compositions, however.(253,254)

For the compositions at temperatures of 1400 K mixing in of toluene tend to increase the diversity of the extracted precursor pools, but the pure toluene fuel gives almost exclusively pyrene. For the compositions extracted for temperatures above 1400 K, the pure decane fuel yields compositions that are less dominated by pyrene and also show more diversity. It includes, for example, pyrenylacetylene and pyrenyl radicals. However, replacing decane by toluene especially favors the pyrene concentration in the final precursor pools.

The same is observed when increasing the temperature, where compositions at higher temperatures are more diverse than the ones at lower temperatures, for a given fuel mixture and

equivalence ratio. In addition, the impact of the fuel mixture on the composition is increased with increasing temperatures.

In order to investigate these phenomena, one has to take a look at the gas phase compositions at different conditions. This is best expressed with ROP analyses for the molecules of interest, as here one can easily depict the significant molecules contributing to the formation of the molecule of interest. As the ROP analyses of each PAH are too extensive we here give an indicator for the gas phase by discussing the ROP analysis for the pyrene production in Raj's mechanism. Under the tested conditions the production of pyrene occurs by seven distinct reactions in Raj's mechanism. The major reaction pathways observed for the production of pyrene from smaller molecules in Raj's mechanism are shown in Table 12.

Reaction 1 is the addition of a methylene radical to a 4-methylenephenanthrenyl radical. Reactions 2, 3 and 4 can be seen as different intermediates of the H - abstraction - C2H2 – addition (HACA) mechanism. That is, reaction #2 is the direct addition of acetylene to a phenthrenyl radical and subsequent formation of pyrene in one step, reaction #3 is the joined H-addition to an acetylenated phenanthrene and subsequent ring closure to form pyrene, and reaction #4 is the intermediate of reactions #1 and #2, where a phenanthreneacetenyl radical undergoes ring closure to form pyrene. Reaction 5 is the reaction of activated acetylenated naphthalene with cyclobutadiene. Reactions 6 and 7 are addition reactions of a benzyl radical and, respectively, an indenyl radical and two indenyl radicals. Reaction 6 and 7 take resonance-stabilized radicals as reactants. Since these radicals are rather stable, and reaction barriers of the recombination of these species are low, they are known to play a vital role in the production of PAH and soot.(135,264)

The percentage contribution of each reaction to the total positive ROP of pyrene is shown in Figures 14 – 17 for equivalence ratios of 3.5, all tested temperatures and all fuel mixtures. Reactions not shown in one of the graphs did not exceed 1% with respect to the total pyrene ROP.

Table 12. Main reaction pathways for the production of pyrene in Raj's mechanism.

Reaction #1	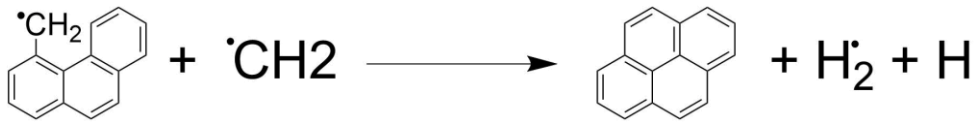
Reaction #2	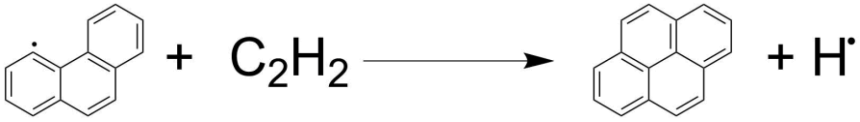
Reaction #3	
Reaction #4	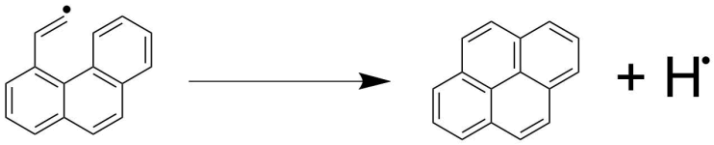
Reaction #5	
Reaction #6	
Reaction #7	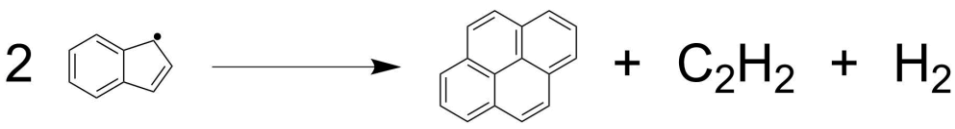

If one is investigating the reactions step by step, we see that reaction #1 is not significant for most of the tested conditions. Only at pure n-decane compositions it is detected for all temperatures and at 1400 K also for the pure toluene composition, but also only at short simulation times and for a short period of time. This is since for reaction #1 the production of methylene-radicals is crucial for the contribution of this reaction. Since n-decane can successively decompose into methylene-radicals its decomposition contributes more towards this reaction as decane is consumed during combustion. Also, toluene can form methylene-radicals by decomposing into a phenyl-radical and a methyl-radical, which in turn by H-dissociation can form methylene-radical. Therefore reaction #1 also slightly contributes to the early stage of pyrene formation at pure toluene mixtures at 1400 K.

Figures 14 – 17 also show that reaction #2 correlates at all tested conditions with reaction #4 for the most part. Only at elevated temperatures and short simulation times, this is not the case. This correlation is due to the fact that the reactant in reaction #4 is an intermediate of the reaction described in reaction #2. Hence also the reactants of reaction #4 can be produced from reaction #2, but since the reactant in reaction #4 is not stable it quickly undergoes ring closure to form pyrene or H-dissociation in order to form a stable product. Furthermore, as described above these two reactions gain significance with increasing aliphatic fuel content, as acetylene can be found in abundance in the gas phase as a fragmentation product of n-decane. It is also observed that the percentage contribution of reactions #2 and #4 rises at the end of each simulation. This can be attributed to the stepwise recombination of acetylene formed from the fragmented fuel molecules, producing larger PAH, in this case, pyrene.

Reaction #3 only contributes at the end of the simulations to the formation of pyrene, as is shown in Figures 14 – 17. This must be attributed to the fact that the formation of acetylenated phenanthrene is closely linked to reactants in reaction #2 and #4. Since only a small margin of these

reactants form the acetylenated phenanthrene and a large part forms other products, such as pyrene, the production of the larger reactant in reaction #3 is not great. Hence, only at a later time, a significant amount is formed, which by H-addition and subsequent H-dissociation can undergo ring closure to form pyrene.

Reaction #5 occurs at fuel mixtures with high aliphatic content, and with increasing temperature also for fuels with more toluene in the mixture. This is due to the fact that neither reactant can be directly formed from toluene at low temperatures. While the acetylinated naphthale can in principle be formed from stepwise addition of small carbon containing radicals to toluene fragments, cyclobutadien cannot. On the other hand, cyclobutadien is the dimerization product of two acetylene molecules, which is one of the major fragments in fragmentation of n-decane. As a result, the fragmentation of n-decane contributes significantly more to reaction #5. Nonetheless, this reaction occurs only at early simulation time, when fuel consumption is high, and only for a short period of time. This is because the cyclobutadien is rather unstable and is only present in the gas phase for short times when the acetylene content is high. The fact that the temperature has an impact on the significance of this reaction at different fuel mixtures shows, however, that the fragmentation of fuels occurs more rapidly with increasing temperature.

Reaction #6 is the recombination of a benzyl radical and an indenyl radical. Since both reactants can be formed from toluene rather easily, benzyl by dissociation of a hydrogen atom from toluene and indenyl by hydrogen dissociation of toluene with the subsequent addition of acetylene, the reaction is dominant at early times . This is also the reason why the reaction occurs for longer times with increasing toluene content in the fuel mixture. Furthermore, since the fragmentation at 1400 K of fuel is low, and larger intermediates are regularly found during combustion, reaction #6 is the dominating reaction for conditions at 1400 K for all fuel mixtures. That said, with increasing

temperature the reactants of reaction #6 are not formed from the aliphatic fuels anymore, which is why the reaction ceases to play a role at higher temperatures and fuel mixtures with high aliphatic content.

Reaction #7 is found at all temperatures and all fuel mixtures. Indenyl is known to be a crucial precursor to pyrene, since it is a resonance stabilized radical, which is highly reactive due to its radical character.(264) Hence the recombination reactions of indenyl and other aromatic molecules do not have a high reaction barrier and form larger PAH readily.(248,264) If one investigates the effect of fuel composition and temperature of the percentage contribution of reaction #7 to the production of pyrene one finds that the reaction becomes more significant with increasing aliphatic fuel content, except at 2000 K, and also shifts to later simulation times with decreasing temperatures. The temperature effect can be attributed to slower fuel consumption at lower temperatures and overall slower kinetics so that the reactions leading to the building of indenyl take a longer time. Furthermore, at 1400 K one observes that reaction #6 is dominant at early simulation times, hence consuming indenyl.The first phenomena, that the indenyl recombination gains significance with increasing aliphatic fuel content, can be attributed to the effect, that fewer benzyl radicals are found with increasing aliphatic fuel content. Since reaction #6 is also consuming indenyl it diminishes the overall indenyl mole fraction in the gas phase and hence reaction #7 is hindered. That can be seen in the graphs in Figures 14 – 17 where reaction #6 and #7 counteract each other and a rise of one of the two reactions leads to a demise of the other. Nonetheless, the significance of the indenyl recombination could possibly be an artifact produced by Raj's mechanism at high equivalence ratios. Since there are only a few non-oxidative indenyl consuming reactions the stability of indenyl is overestimated and as a result is the significance of reaction #7.

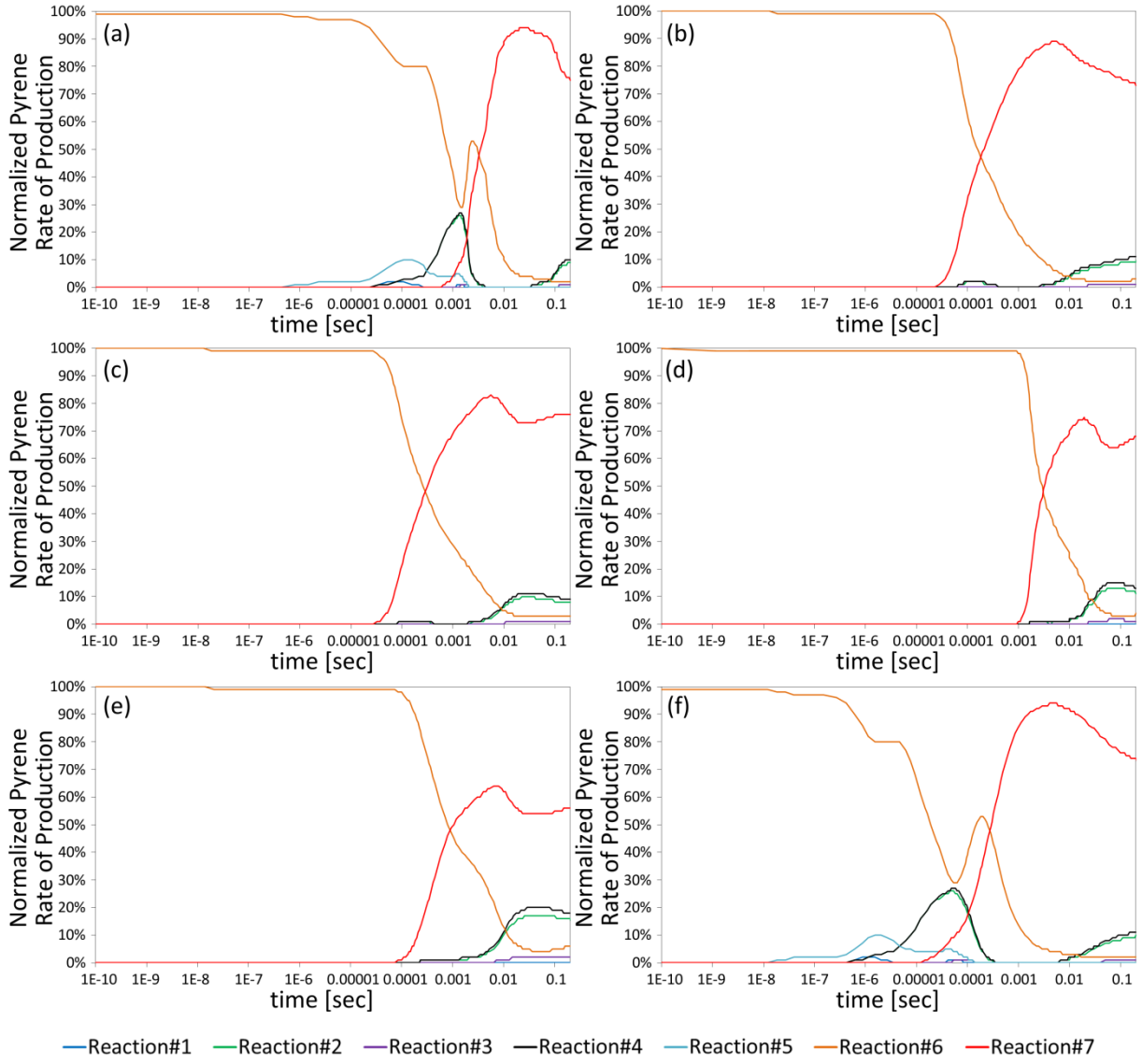

Figure 14. Percentage contribution to the positive ROP of pyrene by each reaction detected to contribute to the growth of pyrene. The numbering of the reactions follows the numbering shown in Table 12. The chosen conditions depicted are taken at an equivalence ratio for 3.5, a temperature of 1400K and a fuel mixture of (a) 100 mol% n-decane, (b) 80 mol% n-decane and 20 mol% toluene, (c) 60 mol% n-decane and 40 mol% toluene, (d) 40 mol% n-decane and 60 mol% toluene, (e) 20 mol% n-decane and 80 mol% toluene, and (f) 100 mol% toluene, to show the impact of fuel composition on the percentage contribution of each reaction. Reactions not shown in one of the graphs did not exceed 1% with respect to the total pyrene ROP.

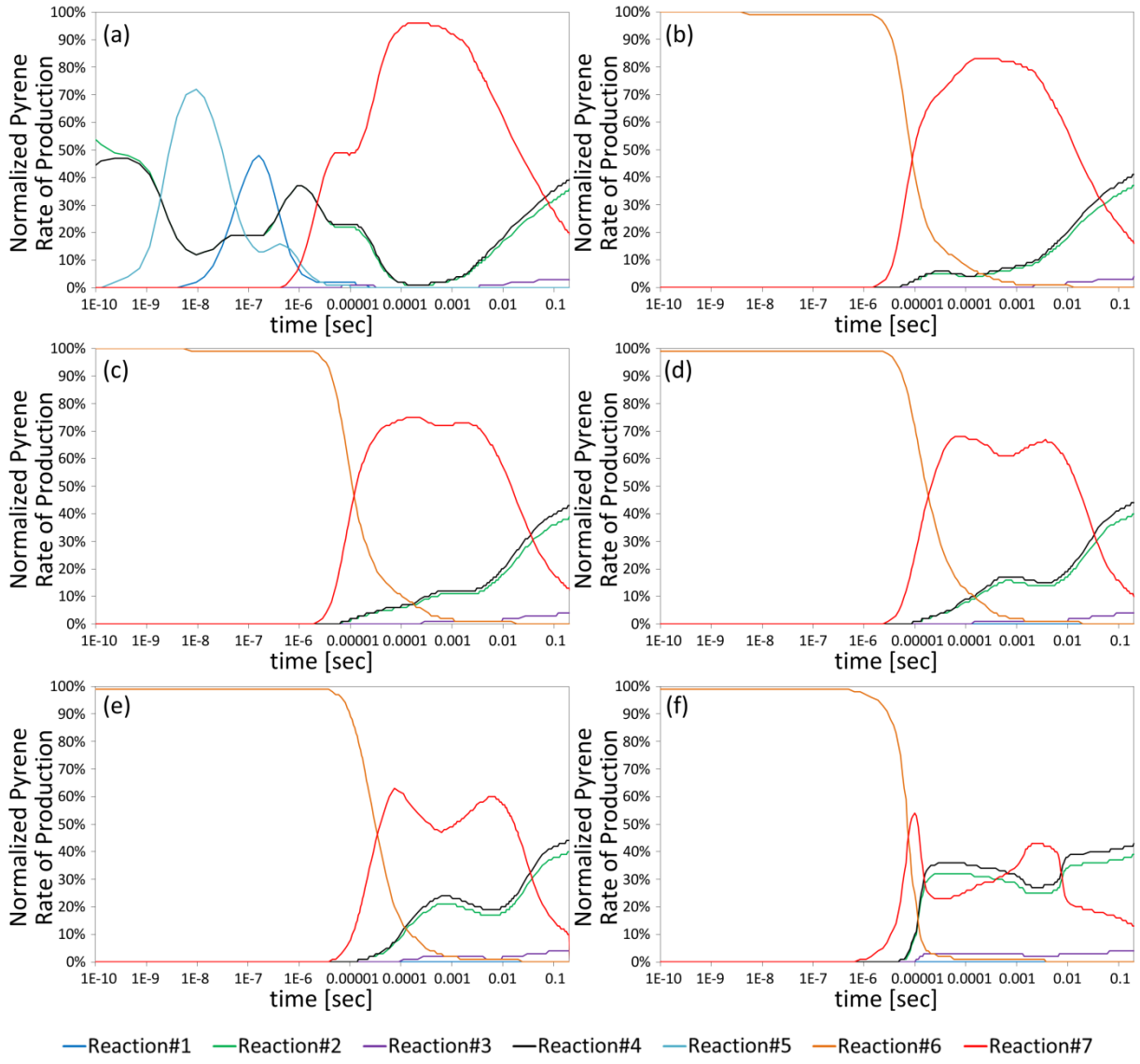

Figure 15. Percentage contribution to the positive ROP of pyrene by each reaction detected to contribute to the growth of pyrene. The numbering of the reactions follows the numbering shown in Table 12. The chosen conditions depicted are taken at an equivalence ratio for 3.5, a temperature of 1600K and a fuel mixture of (a) 100 mol% n-decane, (b) 80 mol% n-decane and 20 mol% toluene, (c) 60 mol% n-decane and 40 mol% toluene, (d) 40 mol% n-decane and 60 mol% toluene, (e) 20 mol% n-decane and 80 mol% toluene, and (f) 100 mol% toluene, to show the impact of fuel composition on the percentage contribution of each reaction. Reactions not shown in one of the graphs did not exceed 1% with respect to the total pyrene ROP.

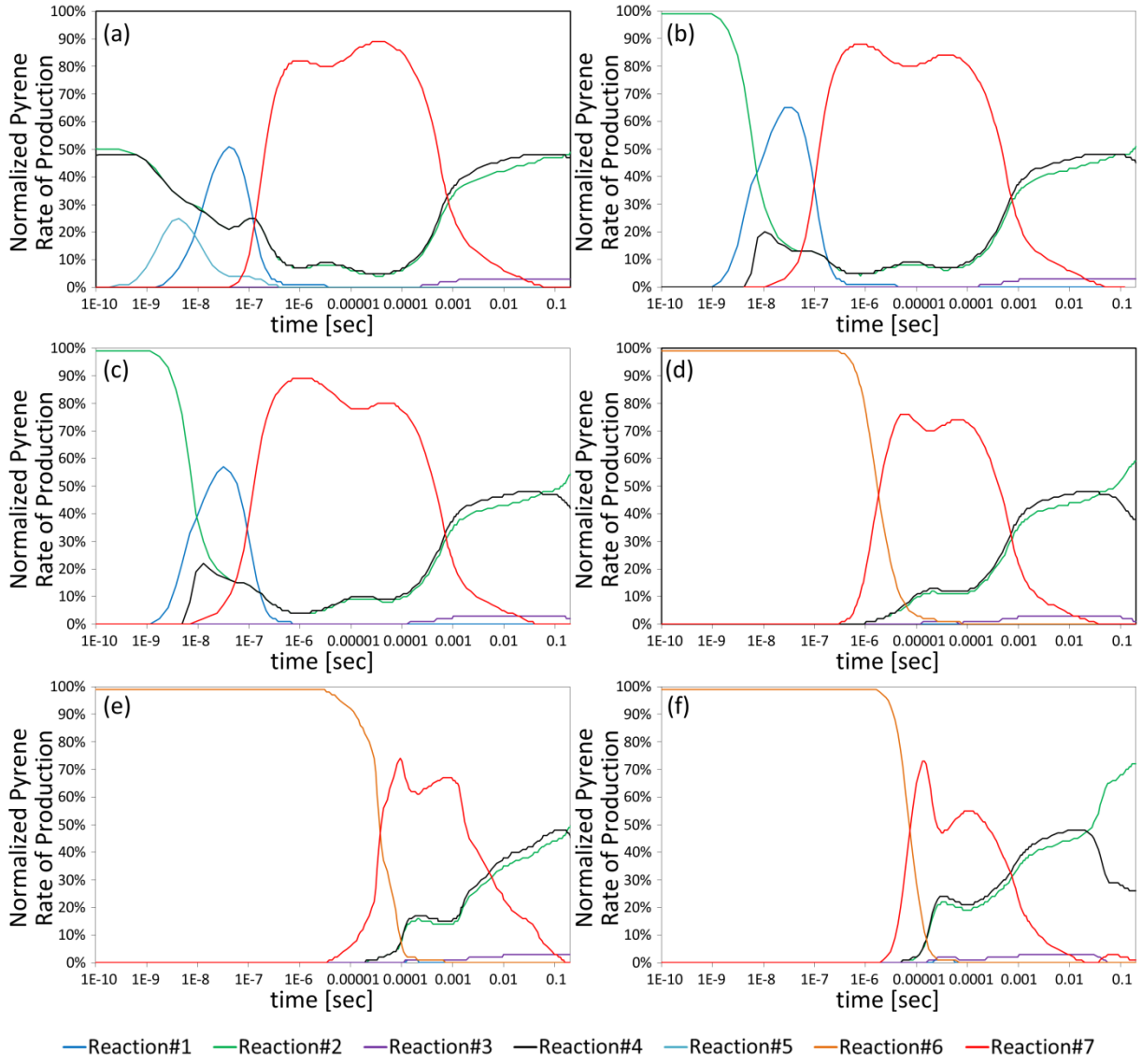

Figure 16. Percentage contribution to the positive ROP of pyrene by each reaction detected to contribute to the growth of pyrene. The numbering of the reactions follows the numbering shown in Table 12. The chosen conditions depicted are taken at an equivalence ratio for 3.5, a temperature of 1800K and a fuel mixture of (a) 100 mol% n-decane, (b) 80 mol% n-decane and 20 mol% toluene, (c) 60 mol% n-decane and 40 mol% toluene, (d) 40 mol% n-decane and 60 mol% toluene, (e) 20 mol% n-decane and 80 mol% toluene, and (f) 100 mol% toluene, to show the impact of fuel composition on the percentage contribution of each reaction. Reactions not shown in one of the graphs did not exceed 1% with respect to the total pyrene ROP.

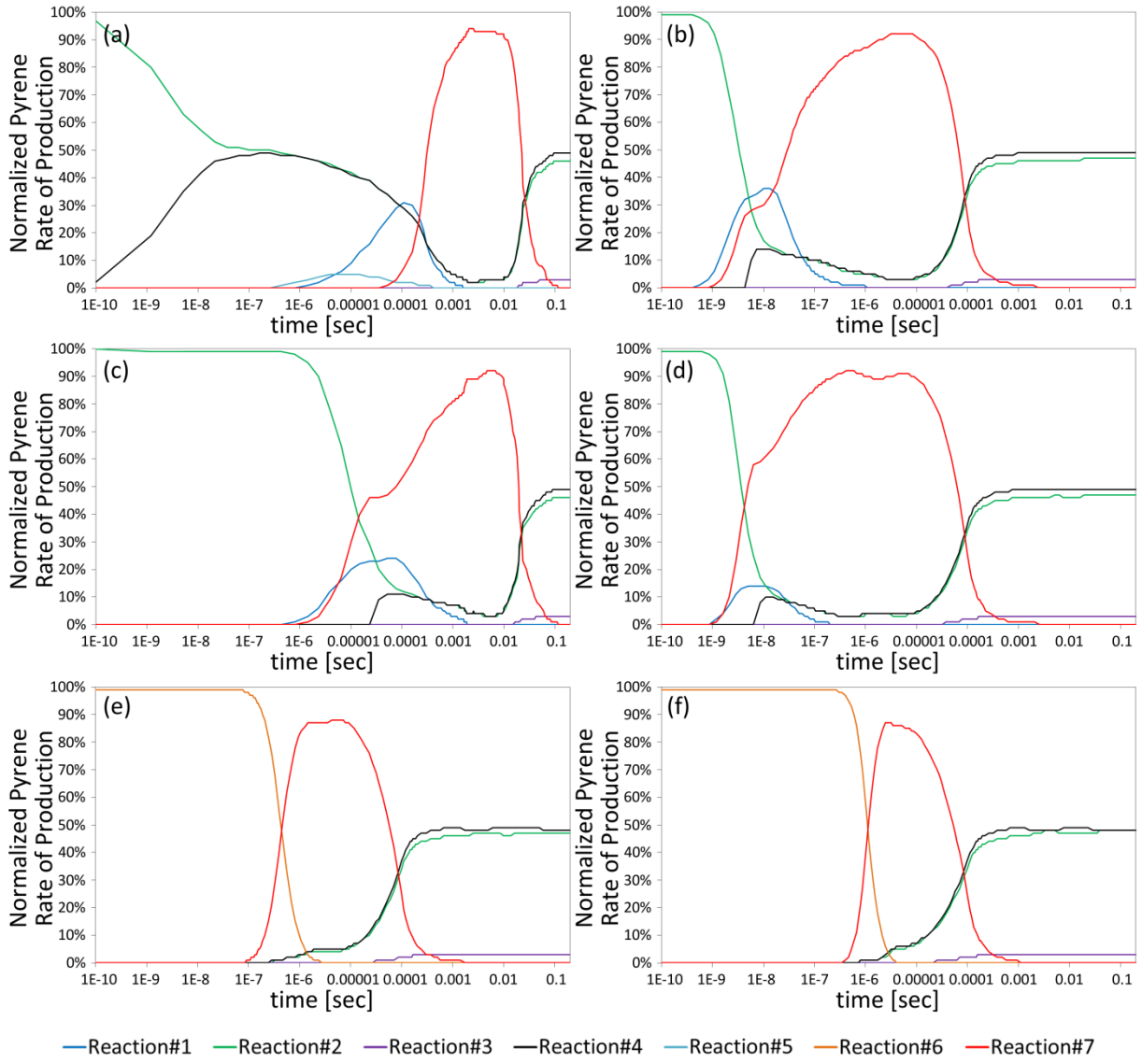

Figure 17. Percentage contribution to the positive ROP of pyrene by each reaction detected to contribute to the growth of pyrene. The numbering of the reactions follows the numbering shown in Table 12. The chosen conditions depicted are taken at an equivalence ratio for 3.5, a temperature of 2000K and a fuel mixture of (a) 100 mol% n-decane, (b) 80 mol% n-decane and 20 mol% toluene, (c) 60 mol% n-decane and 40 mol% toluene, (d) 40 mol% n-decane and 60 mol% toluene, (e) 20 mol% n-decane and 80 mol% toluene, and (f) 100 mol% toluene, to show the impact of fuel composition on the percentage contribution of each reaction. Reactions not shown in one of the graphs did not exceed 1% with respect to the total pyrene ROP.

In summary, the temperature and fuel effect on the soot precursor pool compositions can be explained by looking at the change of percentage contribution of each reaction over the different temperatures in Figures 14 – 17 and the nature of these reactions. One can group the presented reactions into two groups. The first group is the production of pyrene by subsequent addition of small aliphatic molecules to aromatics smaller than pyrene. This group consists of reactions 1 to reaction 4. The second group is the production of pyrene by recombination of two aromatic molecules smaller than pyrene. This group consists of reaction 5 to reaction 7.

By regrouping the seven reactions on observes that reactions in which small molecules are involved, i.e. reactions 1 to 4, gain significance with increasing temperatures. This is due to the increased fuel consumption and faster fragmentation of fuel molecules with increasing temperatures. As a result, at higher temperatures, the number of small radicals increases and the pathways leading to pyrene and larger PAH by the addition of smaller radicals to aromatics are favored. Therefore, at elevated temperatures also more PAH other than pyrene are present. As the growth pathways of these PAH in Raj's mechanism are largely due to the HACA mechanism the increased mole fraction of acetylene due to faster fuel fragmentation at increased temperatures is the reason for a higher diversity of the soot precursor pool compositions with increasing temperature.

The influence of the fuel mixture on the diversity of the extracted precursor pools follows the same trends. In Raj's mechanism, the growth of pyrene and larger aromatics from n-decane is ascribed to the fragmentation of n-decane into smaller radicals followed by the recombination to form aromatic species. For toluene-rich fuels, pyrene growth is significantly different, since toluene and its fragmentation products already consist of an aromatic ring. As a result, the formation of pyrene from toluene follows a more direct path in Raj's mechanism and a significant amount of toluene directly forms pyrene, without first being decomposed into smaller radicals. Hence, for

more aromatic fuels, the growth of pyrene via larger fuel fragments is favored, while there is less acetylene present thereby slowing down the HACA-mechanism in the synthesis of PAH larger than pyrene. Inversely, with more aliphatic fuel mixtures, the HACA-mechanism gains significance again and in turn, a more diverse PAH composition is present in the gas phase.

Hence the changes in combustion condition due to a change in temperature and fuel mixture are well translated to the extracted soot precursor pool compositions. The impact of the equivalence ratio on the production of soot precursors, that is that with higher equivalence ratios more soot precursors form in the gas phase, was not translated due to the normalization of the extracted compositions. The relative ratios of PAH did not vary a lot for different equivalence ratios, hence a structural change due to different soot precursors is not expected. Instead, the amount of soot formed would be influenced.

4.6 Conclusion

We have shown in this chapter the results of Chemkin calculations with the mechanism presented by Raj et al. for various conditions. These calculations have been performed with the aim of modeling the changes in the chemical compositions of the gas phase during combustion, in order to be able to translate these chemical changes to the ReaxFF calculations.

Following this intention, a range of temperatures, equivalence ratios, and fuel mixtures was scanned. The equivalence ratios and temperatures have been chosen to lie in the sooting regime. Furthermore, the temperature has been kept constant over the simulation time in order to decouple the thermal effects of fuel mixture and equivalence ratio on the chemical compositions. As fuel, mixtures of toluene and n-decane have been taken, in order to investigate the impact of aliphatic and aromatic fuel on the chemical composition of the combustion gas phase.

The impact of the scanned parameters on the production of soot precursor molecules was investigated, and it was found that while the equivalence ratio mainly influences the number of soot precursors produced, the temperature also affects the diversity of the molecules found. The fuel mixtures showed a synergistic effect, that is in gas phases of mixtures of n-decane and toluene, more soot precursors were detected than for the pure components. The changes in the combustion gas phase due to the parameter changes compare well to experimental findings and could be rationalized.(45,96,243,254,256)

In order to extract the molecules relevant for the soot inception process, so that one may generate input for ReaxFF simulations, we presented an approach to reduce the gas phase of the Chemkin calculations. In order to do so, two selection criteria were introduced. First that the size of molecules selected must lie over a certain threshold, and secondly that the concentration of these molecules, relevant for the soot inception process, must be above the ppm-level. Furthermore, it was shown that the point of extraction has been chosen in a fashion that is consistent over all conditions and occurs before soot inception. To have this extraction point prior to soot inception is crucial, as the aim of this thesis is to model the processes at soot inception and structural differences of the formed structures due to dimerization and bond formation.

Applying this technique 128 different soot precursor pool compositions have been extracted from the tested 144 conditions. The extracted soot precursor pools show the impact of the equivalence ratio, the temperature and the fuel composition on their composition.

These trends for the three parameters tested have been rationalized and it has been shown that the impact of variation of one of the parameters translates well to the extracted soot precursor pool compositions. This reassures that the extracted molecules are representative of the tested conditions and hence provide a reasonable input to model the soot inception process with ReaxFF simulations.

5. Evaluation of ReaxFF Force Field Parameter Sets and the Influence of Simulation Parameters

5.1. Introduction

The reactive force field approach has been employed to model several phenomena. For example, ReaxFF studies have been done in the field of catalytic studies(65,265–267), the study of molecular depositions on surfaces(267–270), interactions of non-organic atoms in aqueous phases(269,271), proton transfer of water through graphene layers(272), biochemical systems(273,274), energetic materials(273,275,276), combustion of hydrocarbons(66,124,277,278), pyrolysis of coal(217,267,279–282), and formation of soot (66,127,147) amongst others. In order to model the presented studies no uniform force field was employed, however. Instead, target force fields have been developed in most of the cases. This is due to the fact, that the original reactive force field published by van Duin et al. was modeled to describe only the interactions between carbon and hydrogen atoms. The description of parameters has later been updated to also include silica and with the introduction of nitroimines and oxidation of hydrocarbons the description of parameters has been stable, allowing to introduce other atoms without modifying the nature of parameters.(65,276) Hence, if a study targets another type of atom, parameter values for this kind of atom need to be introduced in order to describe its interaction with the remaining atoms of interest. This has been done for several atoms on the periodic table, so far.(238) Furthermore, parametrization in ReaxFF often leads to a trade-off if interactions of more than two atomistic species are investigated. Tuning of the universal parameters of the force field can result in the improvement of one phenomenon, while the description of other phenomena is captured worse.

The first force field parameters sets that enabled hydrocarbon oxidation by updating the original reactive force field parameter set published by van Duin et al. by introducing oxygen is the one published by Chenoweth et al.(277). Since then a number of force field parameter sets for carbon, hydrogen and oxygen atoms have been published. Most of them are based on the Chenoweth force field parameter set and have been developed in order to improve certain phenomena better. For example, Srinivasan et al. took this force field as a base to develop a force field parameters set for carbon condensed phases(283), Müller et al. went from the Chenoweth force field to develop a force field suited to describe hydrocarbon catalysis by nickel surfaces(284), Ashraf et al. developed a force field for syngas combustion based on the Chenoweth force field(124), and Mao et al. modified the Chenoweth force field to better describe the Van der Waals interactions between PAH molecules.(147)

As said above since an improvement of description in the force field could incite with diminishing results of other phenomena, the most relevant force fields have been tested in order to test their capability to describe the bond formation between soot precursors. This chapter presents the results of this study. In the second subchapter, the force field parameter sets chosen are compared to density functional theory calculations. In the third section, the capability of the force field to form clusters of PAH in the gas phase at different temperatures is investigated. In the following section the impact of simulation parameters independent of the force field, i. e. temperature and time step, is examined. Finally, the main conclusions are drawn.

5.2. Comparison of Bond Dissociation Energies in ReaxFF and DFT calculations

As has been presented above, there is a multitude of ReaxFF force fields published in the literature. Three force fields have been selected to test the modeling of bond formation between soot precursor molecules. The force fields chosen to do so are the following: the force field published by

Chenoweth et al., which has been developed in order to model hydrocarbon oxidation kinetics.(278) The force field of Chenoweth et al. is in the following referred to as CHO08. Secondly, we chose the force field developed by Ashraf et al.(124). This force field has been developed in order to model syngas combustion, with an emphasis on better describing the interaction of small hydrocarbons and oxygen in the gas phase. During development the authors used the force field of Chenoweth et al. and a force field developed by Srinivasan et al. as a basis.(283) The force field of Ashraf et al. is in the following referred to as CHO16. The third force field that was investigated in this study is the one developed by Mao et al.(147). This force field has been developed to model dimerization between PAH in the gas phase. The target has been to better describe the π-π-interactions of larger polyaromatic hydrocarbons, by fitting them to dispersion corrected DFT calculations. The force field of Mao et al. is in the following referred to as CHOPAH.

In order to evaluate the three force fields described above, comparison of the performance of simulations using ReaxFF with density functional theory (DFT) calculations have been done. The DFT approach, developed by Hohenberg, Kohn, and Sham (285,286), is a quantum mechanical modeling approach to describe the electronic and nuclear structure of molecular systems. In this approach, the electronic energies of many-electron systems in the ground state are assumed to be dependent on the electron density. The spatially dependent electron density is described as functional, which is a function of electron functions. With this description of the electron density the properties of the molecular systems can be determined. Due to the non-explicit description of electrons, the computational effort of DFT scales much better than wave function methods with increasing system size. Therefore, DFT is a quantum mechanical approach able to model larger systems, such as proteins and enzymes, and thus has been widely popular.

For the comparison of the ReaxFF force fields to the DFT calculations, several bond dissociation energies for reactions on single molecules have been modeled. A nudge elastic band approach was employed for the ReaxFF calculations. For this methodology the initial and final state of a system is given, in the current case the bonded and dissociated system. The system is then iteratively moved along a coordinate to give the transition from the initial to the final state. This is achieved by bonding the initial, final and current state of the system together with springs, so that the current state is constrained between the initial and final state. Since energy relaxations of the intermediate states are allowed, however, the energy surface between the initial and final state can be determined and the minimum energy path determined.(287)

A reactive coordinate scan is used for the DFT calculations. This approach is slightly different to the nudged elastic band. The difference is that only the initial state is known, and the system is iteratively moved along a reaction coordinate. For the presented cases the chosen reaction coordinate is the distance between the two atoms involved in the bond for which the dissociation is investigated. Hence the energy is optimized for different distances, giving an estimate of the energy surface of the scanned reaction coordinate.

The result is comparable to the nudged elastic span, only that the final state might differ. The reaction coordinate scan was performed in a fashion so that the distance between the atoms is decreased, moving from the dissociated to the bonded system. Like this, the difference in energy path is minimized between the two approaches.

The reactions chosen to investigate have been hydrogen dissociation of benzene, the hydrogen dissociation of pyrene, the methyl dissociation of toluene and dissociation of biphenyl into two phenyl radicals. The first two reactions have been chosen in order to investigate hydrogen dissociation from aromatic carbons, as this is a crucial reaction in the soot growth process. The

latter two reactions have been chosen in order to model the carbon-carbon bond breaking between an aromatic and an aliphatic carbon atom, as well as two aromatic carbon atoms.

The results of the calculation of the bond dissociation energy (BDE) calculations for the three ReaxFF force fields, as well as the DFT calculation are shown in Figure 18. In order to get the transition of the nonbonded singlet state to the unbound triplet state with DFT, both states have been calculated for several interatomic distances. In Figure 18 only the energy of the lowest energy curve as a function of bond distance and spin state is depicted, however, as the system transits from the singlet to the triplet state during dissociation. The exchange-correlation functional employed for the DFT calculations is the combination of the Becke 88 exchange functional (288) and the correlation functional of Lee, Yang and Parr (289), which is commonly referred to as B3LYP. The employed basis set is 6-311G(d,p), that is six Gaussian functions to describe the inner shell electrons, three Gaussian functions summed to give the first slater type orbitals for the valence shells, and one more gaussian function summed each to give the second and third slater type orbitals. The (d,p) in the description of the functional indicates that an additional polarization function for d-orbitals in non-hydrogen atoms and polarization functions for p-orbitals in hydrogen atoms is added.(288)

For the hydrogen dissociation from benzene, the experimental value found in literature is 112 kcal/mol.(290) The calculated BDE employing the DFT B3LYP 6-311G(d,p) approach is 117.23 kcal/mol for a carbon-hydrogen distance of 5 Å. A deviation of 5 kcal/mol is reasonable and hence assures the accuracy of the DFT approach

From Figure 18 one observes that the bond breaking distance for all the tested cases occurs at shorter distances in the ReaxFF calculations compared to the DFT calculations. This is indicated by

the ReaxFF calculations reaching the energy plateau of the dissociated species at shorter distances than the DFT calculations.

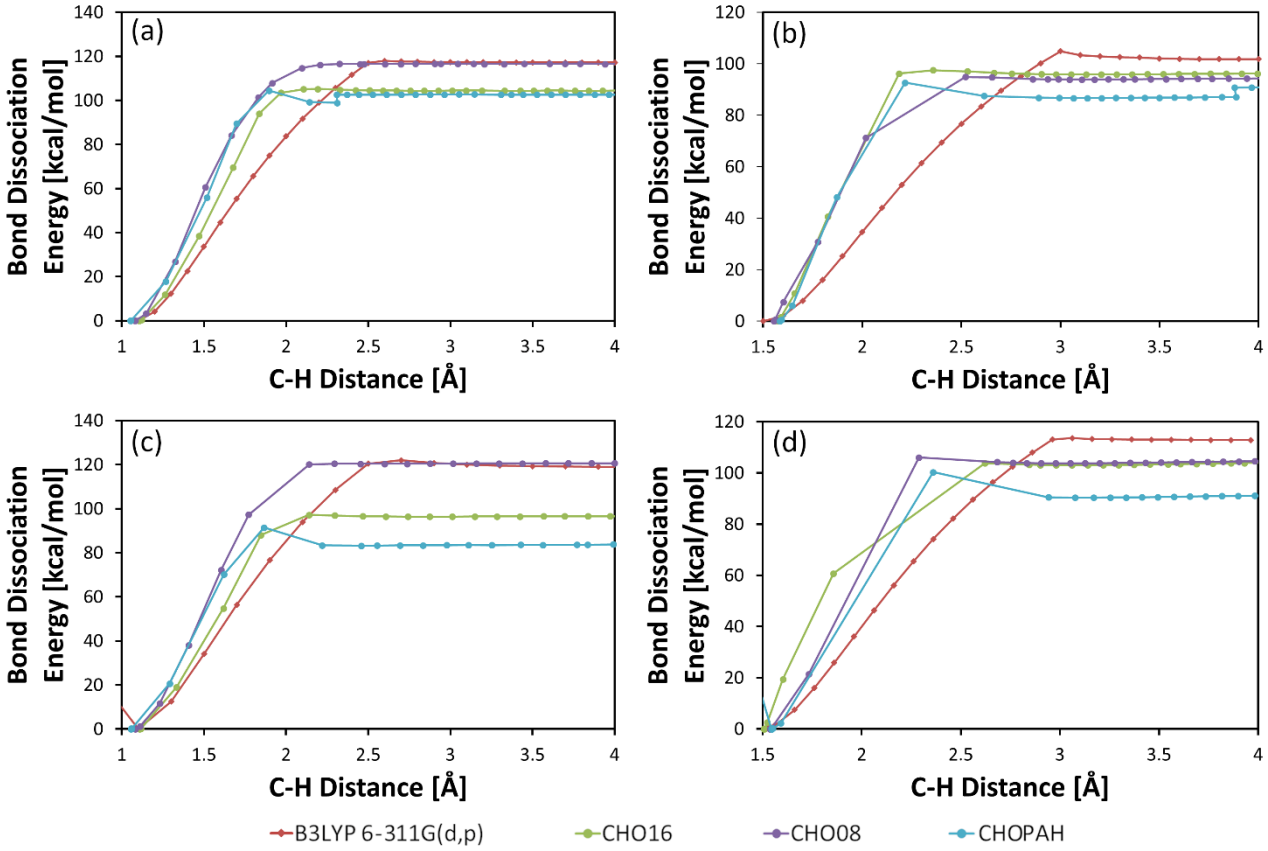

Figure 18. Bond dissociation energy calculations utilizing DFT and ReaxFF calculations for (a) hydrogen dissociation from benzene, (b) methyl dissociation from toluene, (c) hydrogen dissociation from pyrene, and (d) dissociation of biphenyl into two phenyl radicals. The energy of the relaxed bond distance has been normalized to 0 kcal/mol for all calculations.

While the selected ReaxFF force fields do not differ largely for the bond breaking distance, they show more significant differences in the bond dissociation energy. While the CHO08 force field achieves to meet almost the exact dissociation energy for hydrogen dissociations from the tested aromatics, the other force fields perform worse. The difference between BDE for the DFT and the CHO08 calculation amounts merely 2.25 kcal/mol, with CHO08 being closer to the experimental value. The difference between the DFT and CHO16 calculation is 14.48 kcal/mol, and 16.13

kcal/mol for the DFT CHOPAH calculations. Furthermore, the CHOPAH calculation shows a jump in energy at 2.3 Å. This is due to a sudden change in bond angles and will be discussed in detail later. The BDE differences for the DFT calculations of the methyl toluene dissociation and the ReaxFF calculations are 7.28 kcal/mol for CHO08, 4.45 kcal/mol for CHO16, and 10.8 kcal/mol for CHOPAH. The CHOPAH again jumps, this time at 3.9 Å, before this jump the difference in energy to the DFT calculations is 14.74 kcal/mol. For the hydrogen abstraction from pyrene the differences in BDE for the DFT and ReaxFF calculation are even more significant. For CHO08 it is only 1.7 kcal/mol, for the CHO16 and CHOPAH the BDE energy differences are 22.26 kcal/mol and 35.21 kcal/mol, respectively. Lastly, the BDE energy differences for the biphenyl dissociation, between the DFT and ReaxFF calculations are 8.57 kcal/mol for CHO08, 7.87 kcal/mol for CHO16, and 21.22 kcal/mol for CHOPAH.

For the chosen test cases the CHO08 retained the most accuracy compared to the DFT cases, as it gave nearly the same BDE for the hydrogen dissociation reactions and good results for the carbon-carbon dissociation in aromatic hydrocarbons. CHO16 performed slightly better for the carbon-carbon dissociation in aromatic hydrocarbons than CHO08 but showed an underestimation of the BDE of the hydrogen dissociation. CHOPAH performed the worst overall, as it did underestimate all BDE significantly. In addition, there is an energy stabilization occurring in the aromatic hydrocarbons in CHOPAH, leading to a distortion of bond angles and a slight decrease in energy after the dissociation. This distortion has been found for each ReaxFF force field, where the angle in the ring on the carbon at which the dissociation occurred showed an increase. The CHOPAH force field has been the force field to show the biggest effect on this, however, almost giving C-C-C bond angles of 160° on the carbon where the radical is located. Furthermore, the energy stabilization due to this ring distortion was observed as well as other slight distortions in the bond angles. Why this

distortion occurs has not been clear, but it can be assumed that the valence angle penalty term in the force field is overshadowing the conjugation correction term. Since both terms are dependent on several parameters in the force field this assumption could not be confirmed, however.

In summary, the CHO08 force field performs best for reproducing the BDE of the DFT calculations for the reactions considered to be most relevant. Even though it fails to give the exact bond-breaking distance. This is common for all tested force field, however. The CHO08 forcefield is hence the most suitable force field to reproduce the reactions under investigation.

5.3. Evaluation of ReaxFF Force Fields on their Abilitiy to form PAH Trimer Structures under Different Temperatures.

Since the aim of this thesis is to investigate the formation of incipient soot structures, for which dimerization of PAH due to van der Waal is considered to play a role, we investigated the formation of dimers and trimers in the ReaxFF calculations. It must be said, however, that using ReaxFF to model physical dimerization is difficult, as most force fields are not specially trained against physical di/trimerization reactions, but rather trained against chemical reactions, with the exception of the force fields proposed by Mao et al. and Liu et al.(65,124,129,147,273,276) In recent years, development of classical non-reactive molecular dynamics force fields to investigate physical nucleation, namely by the Kraft group in Cambridge, has been done, proposing several improvements to describe physical nucleation of PAHs, and therefore these approaches seem more promising than using ReaxFF in order to describe physical nucleation.(160,291)

The interactions resulting from to Van der Waals forces in ReaxFF are described by a parameter independent from the bond-order, unlike most parameters are in ReaxFF. Only a few ReaxFF force field have been trained specifically to improve this parameter.(147,273) This was achieved by training the force field against calculations of dispersion corrected DFT(147) with Grimme's

empirical corrections to better describe Van der Waals forces.(292) Other ab-initio methods, such as perturbation theory or coupled cluster methods, are more suited to describe the Van der Waals forces. Since these methods scale badly with increasing electron systems the calculation of Van der Waals forces for large PAH is expensive, however.

The lacking description of Van der Waals forces in DFT and the expense of other ab-initio methods are the reasons why in this study the evaluation of the three force fields under investigation is not achieved by comparison to ab-initio methods. Instead, we simulated one soot precursor pool extracted from the Chemkin calculations at different temperatures and investigated the formation of trimer structures. For this, we developed a post-processing code, which calculates the centers of mass (COM) of the molecules in order to calculate the distance between molecules. This approach was chosen as the calculation of molecular planes, their orientation, and their distances is a difficult task in molecular dynamics. Since in ReaxFF no bonding-library of the atoms exist, that is a fixed bond for each atom over the complete simulation time, a check of a molecular structure has to be performed in ReaxFF at each time step and for every molecule, before being able to perform the calculation of a molecular plane. The coordinates of the atoms in each molecule could then give a molecular plane. This calculation is difficult, however, since the check of the molecular structure has to be performed prior to calculation of the plane and calculation of the orientation and distance between planes. The check for the molecular structure must be performed for the calculations of COMs as well, but since the COM can be calculated rather easily this approach was chosen to calculate the intermolecular distances. Furthermore, the COMs of two PAHs is closest, when the orientation of the molecular plane is parallel. Hence, the calculation of distances of COMS gives comparable results to the calculation of distance and orientation of molecular planes.

The choice to focus only on trimer structures has been taken since the detection of dimers occurs frequently. Often the detected dimers are not bound for longer times due to Van der Waals forces, however, but are two molecules in vicinity of each other and hence exhibit short lifetimes. The addition of a third molecule indicates more clearly that the detected structures are bound by Van der Waals forces and not just a product of close vicinity.

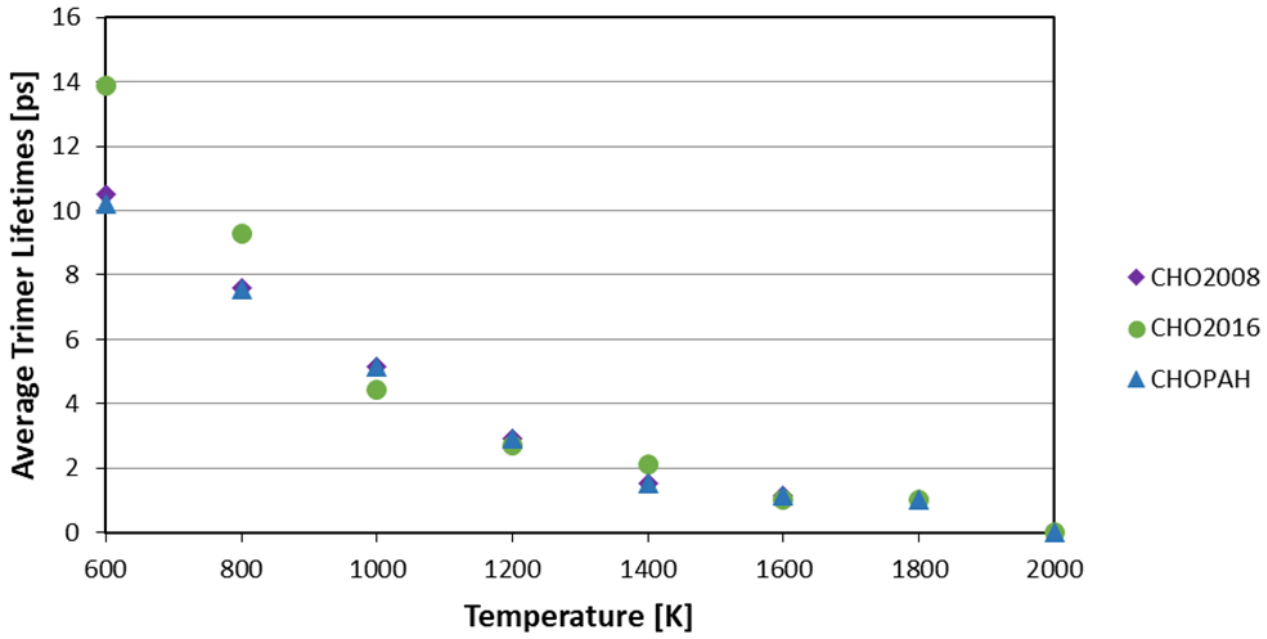

Figure 19. Average lifetimes of trimer structures detected during ReaxFF calculation performed for 2 ns at different temperatures for the three force fields investigated.

To test the physical dimerization of PAHs with the different force fields, we tested the presented three force field parameter sets in a temperature range from 600 K to 2000 K with steps of 200 K. The precursor pool with an initial temperature of 2000 K, equivalence ratio of 5 and fuel composition of 80% n-decane and 20% toluene was used to run the simulations and compare the force fields. The average lifetime of trimers for the different calculations can be seen in Figure 19.

These trimers include every physical agglomeration of precursor molecules regardless of the chemical composition.

In general, all force fields showed similar results. CHO16 gave longer lifetimes at low temperatures, but lifetimes comparable to the other two force fields for temperatures above 1000 K. Especially for temperatures above 1400 K a very low number of stable trimers was produced in all force fields. Surprisingly the CHOPAH force field showed no significant improvement for the trimer lifetimes over the other two force fields, but in fact, gave similar results than the CHO08 force field. This has not been expected since Mao et al. trained the force field against Grimme corrected DFT calculations specifically to better describe the Van der Waals interactions. As can be seen in Figure 19 no improvement could be detected in this study, however.

The results of these comparisons show that physical nucleation of the PAHs is strongly temperature-dependent. At high temperatures, formation of trimers could not be detected with the tested force fields. Comparison to other MD studies shows that our results are in general comparable to other molecular dynamics studies on this topic which confirm that the physical dimerization products of precursor molecules of the size of pyrene are not stable at temperatures of 1400 K and higher.(142,159,160,293) We can conclude that dimerization of 4-ring-PAHs, which are the most present in the generated precursor pools, do not form stable trimers at temperatures above 1000 K. Hence soot inception by dimerization of PAHs with the size of pyrene due to Van der Waals forces under combustion conditions is unlikely to play a role in the ReaxFF calculations and the chemical route probably is expected to have a more significant impact on soot formation.

5.4. Impact of Simulation Parameters on the ReaxFF Calculations

In ReaxFF a number of different simulation parameters must be given before the start of the calculation. These are for the NVT calculations employed, the volume of the model and the number

of atoms in the system, which are both kept constant for the complete simulation times, the time step for which the system is progressed at each iteration, the targeted temperature and the temperature damping frequency at which the system is coupled to the thermostat.

As a range of temperatures is tested in the Chemkin calculations, the temperature setting of the ReaxFF calculations is crucial to the development of the presented approach. Initially a direct transposition of the temperatures employed for the generation of each soot precursor pool and the ReaxFF calculations was tested. At the employed temperatures no bond formation between PAH could be detected, however, only for the compositions at 2000 K growth of a single growth product was detected within simulation times shorter than 5 ns. This finding is similar to the one of Mao et al. (147), who found that chemical bond formation in ReaxFF within reasonable simulation times is only observed at elevated temperatures. Hence, in order to accelerate the production of growth structures the temperatures have been increased.

This approach is common practice in ReaxFF as it allows to artificially speed up the kinetics of the reactions without significantly altering the reaction pathway(217,281,282,294–296). As a result, the computational expense of the simulations is reduced while giving the same results. Figure 20 shows the comparison of the maximum molecular weight and the number of molecules for the initial PAH, C_2H-radicals and the growth species produced during simulation for a simulation at 2000 K executed for up to 8ns and the same system modeled at 2500 K run for 2 ns. The molecular composition for both calculations corresponds to the precursor pools generated with Chemkin calculations at a temperature of 2000 K, an equivalence ratio of 3.5 and a fuel mixture of pure n-decane. One can see that the results are similar, the main species consumed are the acetylenated pyrene and the pyrenyl radicals. The consumption occurs much faster at 2500 K, however. Both systems produce one growth structure after the complete calculation time.

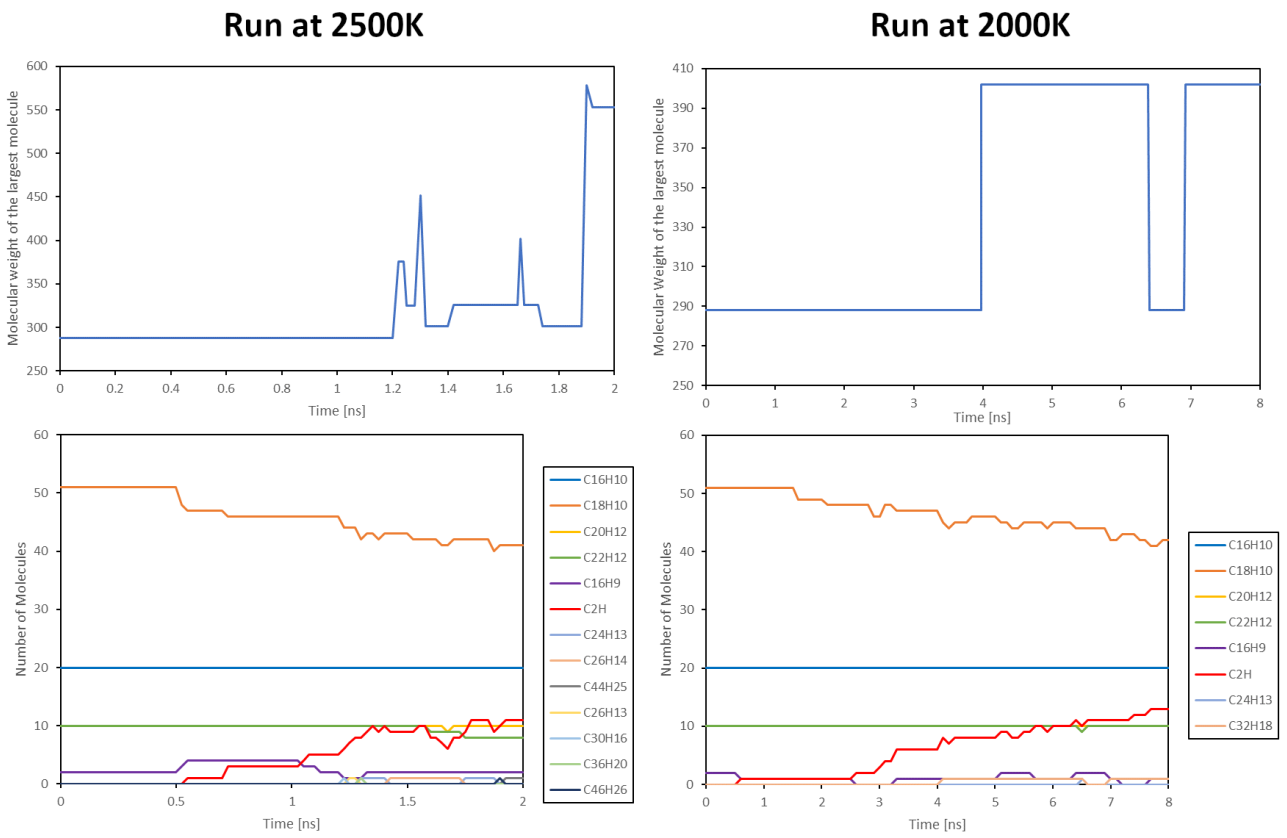

Figure 20. Graphs of the molecular weight of the largest molecule and the number of relevant molecular species found during the ReaxFF calculations over the simulation time. The calculations are performed with the precursor pools generated with Chemkin for a temperature of 2000 K, an equivalence ratio of 3.5 and a fuel mixture of pure n-decane. The ReaxFF calculation is performed at 2500 K (left side) and 2000 K (right side) to show the impact of temperature on the reactivity in the ReaxFF calculations.

Even though the fragmentation of molecules at 2500 K is faster and an increased number of species has been found in total during the simulation time, the outcome of the simulation, that is the growth structure and number of growth structures that are produced are similar. The growth reactions differ slightly, as bond formation and dissociation occur faster for the calculations at 2500 K, while at 2000 K the bond formation is more stable. The type of reaction, that is bond formation

between PAHs, is sufficiently similar, however. This is reassuring the approach and supporting the assumption that the increase in temperature only influences the kinetics of the reactions.

However, further temperature increase, inevitably results in the dissociation of more molecules. This is depicted in Figure 21, in which the molecular weight of the largest molecule found during the ReaxFF simulation is depicted for temperature ranges above 2000 K. The calculations were performed using the precursor pool corresponding to the Chemkin calculations performed at a temperature of 1400 K, an equivalence ratio of 2.5 and a fuel composition of 60% n-decane and 40% toluene. One observes that for temperatures between 2000 K and 3000 K the growth of molecules is similar, all ending at a molecular mass of around 450 a.m.u. after 2 ns. At temperatures above 3000 K one can see that the maximum molecular weight drops again after growth occurred around 800 ps. At 3500 K, dissociation reactions immediately take place and the maximum molecular weight continuously diminishes, corresponding to the fragmentation of the PAH.

This fragmentation of molecules at temperatures above 3000 K is connected to the time step. All graphs depicted in Figure 21 are extracted from simulations run with a uniform time step of 0.1 fs. In classical molecular dynamic simulations, the choice of the time step is usually taken to be one order of magnitude larger than the shortest vibrational motion in the simulated system (277), which is typically 1 fs. These are harmonic bond C–H stretching vibrations in hydrocarbon systems.(297,298) However, since ReaxFF calculations do not have a fixed topology, but allow for bond formation and breaking, a shorter time step must be applied to account for the recalculation of charges and bond orders.(65)

With increasing temperature, the velocities and momenta of atoms during the ReaxFF calculation changes. As a result, the time step needs to be adjusted to avoid falsely predicted bond ruptures,

when two atoms move too far apart from each other. Consequently, too large time steps severely impact the outcome of the ReaxFF calculations.(297,298)

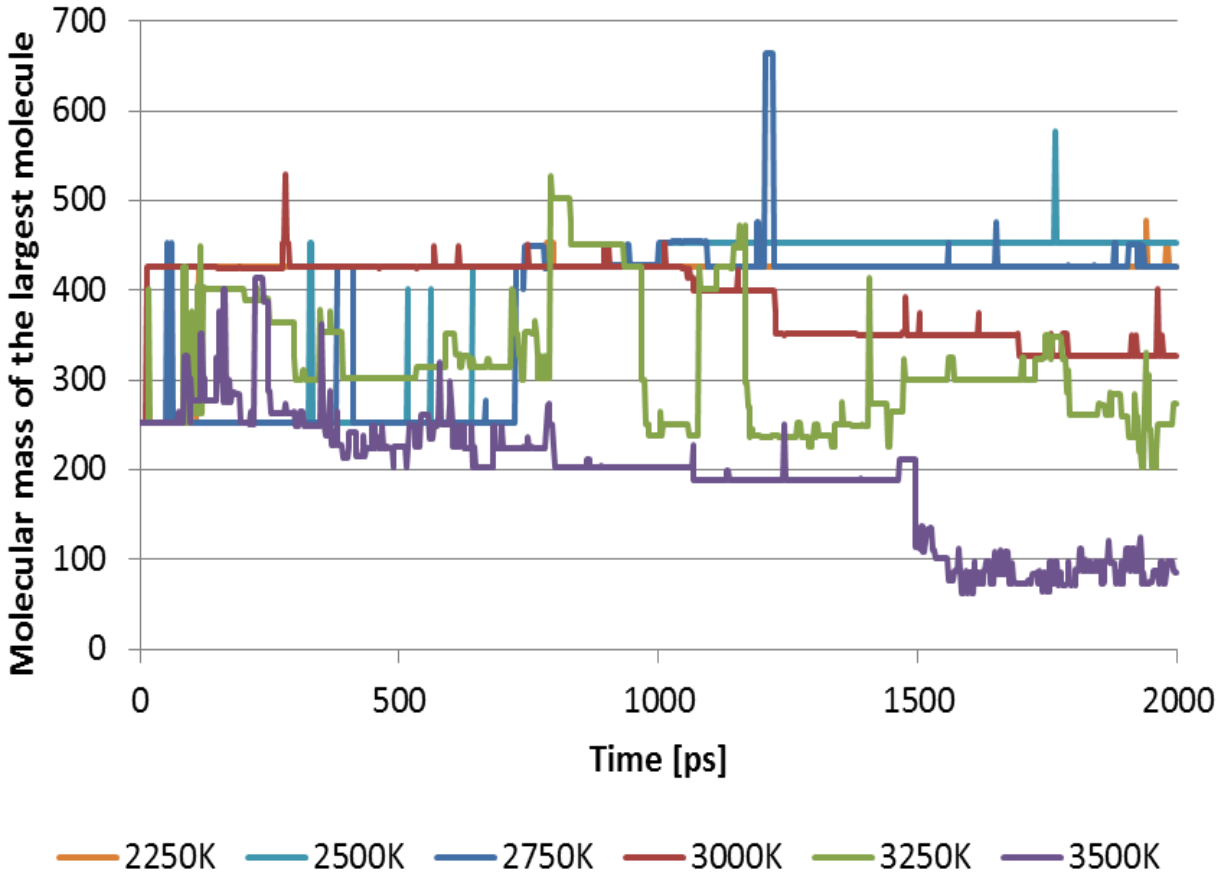

Figure 21. Molecular mass of the largest molecule found during ReaxFF calculations over the simulation time at different temperatures. The molecular composition used for simulation is the precursor pool composition extracted from the Chemkin simulated at a temperature of 1400 K, an equivalence ratio of 2.5 and a fuel composition of 60% n-decane and 40% toluene. While the reactivity is initially accelerated with increasing temperatures for temperatures >3000 K, fragmentation of the molecules takes over for temperatures <3000 K.

For this reason, the time step must be carefully chosen when increasing temperature to accelerate the kinetics in the system under investigation in order to save computational expenses. On the one hand, one can increase the kinetics by elevating the temperature, on the other hand, one must

decrease the time step if this increase is passing a certain threshold, hence leading to more iterations during the simulation of a certain time range and in turn increasing computational expense by calculating forces and charges for each iteration.

As one can find several parameter choices for ReaxFF simulations in the literature (66,147), we performed a test of simulation parameters to evaluate the right choice of parameters. A similar study has been conducted by Jensen et al.(297,298) To verify the time step, simulations with identical systems and identical conditions were performed with varying time steps to determine a critical time step. Larger time steps than the critical time step will fail to reproduce the results and hence cannot be deemed suitable for the used system.(297,298) To verify the time step, simulations with identical systems and identical conditions were performed with varying time steps to determine a critical time step. Larger time steps than the critical time step will fail to reproduce the results and hence cannot be deemed suitable for the used system.

The calculations were performed with an NVT ensemble at 2500 K with a Nose-Hoover thermostat and a damping constant of 10 fs, for 3 ns with the molecular composition of the precursor pool generated with Chemkin for an initial temperature of 1400 K, an equivalence ratio of 2.5 and a fuel composition of 60% n-decane and 40% toluene. The time steps tested are 0.05 fs, 0.075 fs, 0.1 fs, 0.11 fs, 0.12 fs, 0.13 fs, 0.14 fs, 0.15 fs, 0.2 fs and 0.25 fs. The total energies of the simulations are displayed in Figure 22.

As can be seen in Figure 22, time steps larger than 0.13fs fail to reproduce the results of the simulations with smaller time steps. During the investigation we found that the reactions occurring during the simulation time one finds that for the largest time steps the decomposition of the PAH molecules is substantially more present than for the systems with a time step of 0.1fs or smaller.

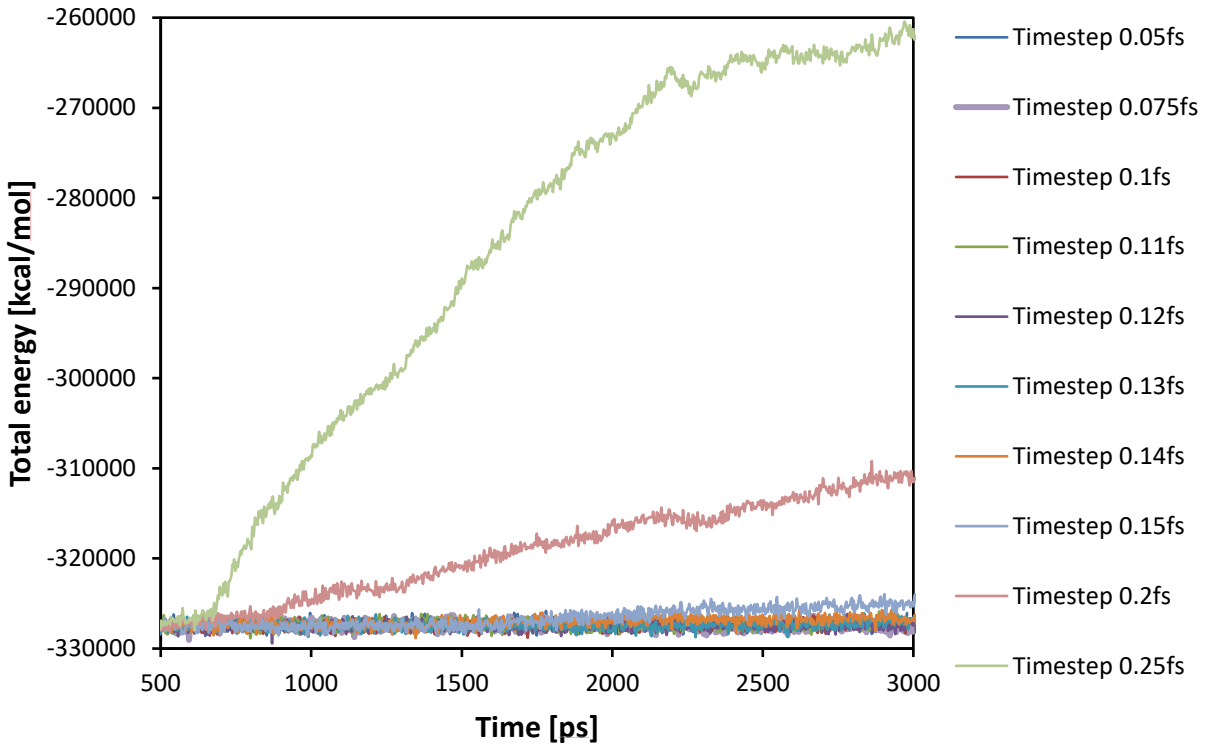

Figure 22. The total energy of the ReaxFF calculations over time for different time steps employed during the calculation for a simulated temperature of 2500 K. Failing to reproduce the results of smaller time steps indicates that the time step chosen is too large.

To test also the temperature dependence of the time step we simulated the respective systems in a temperature range from 600 K to 2000 K with temperature steps of 200 K at timesteps of 0.1 fs, 0.15 fs, 0.2 fs and 0.25 fs. The results for 2000 K and 1800 K are shown in Figure 23. At temperatures beneath 1800 K, the timestep does not impact the chemistry outcome and thus the largest timestep, i.e. 0.25 fs, is suitable to describe the system. However, as soon as the simulation is run at higher temperatures and a reasonable amount of chemical decomposition and bond formation can be expected, shorter time steps need to be applied. This finding is similar to the study of Jensen et al.(297,298).

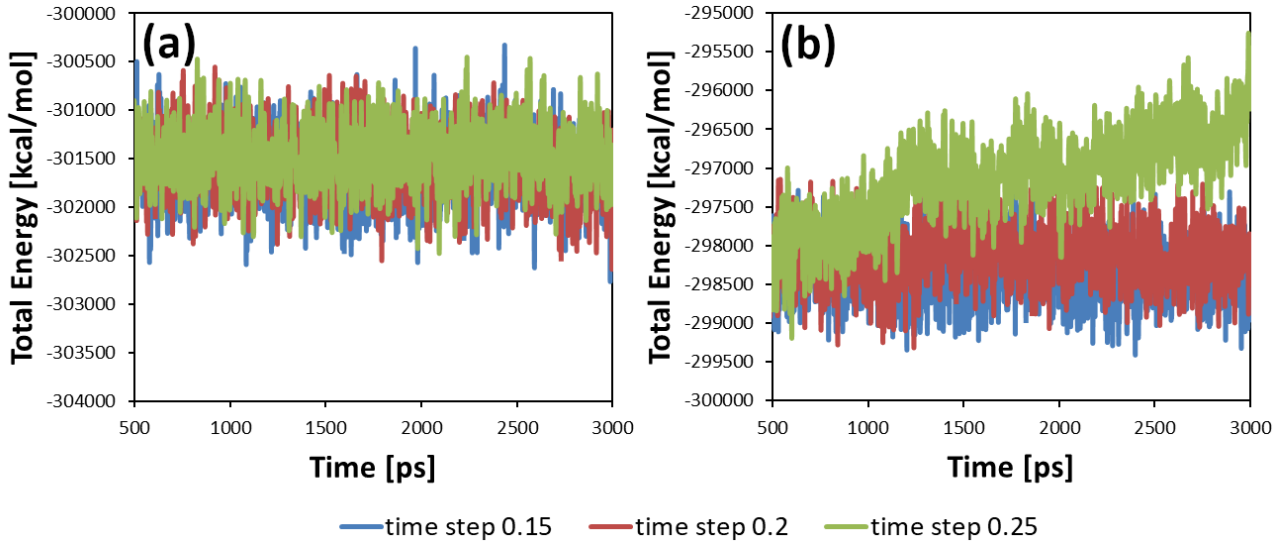

Figure 23. The total energy of the ReaxFF calculations over time for different time steps employed during the calculation for temperatures of (a) 1800 K and (b) 2000 K simulated in the ReaxFF calculations.

From the investigation of the simulation parameters, we determined that a temperature of 2500K is suitable, to accelerate the kinetics in the soot precursor pool enough, so that bond formation and growth of incipient soot structures could be observed during reasonable simulation times. The critical timestep at this temperature has been found to be 0.13fs. As a timestep of 0.13fs is rather unfeasible in terms of output frequency, the chosen time step for the calculations at 2500 K is safely reduced to 0.1 fs.

One factor that is also crucial to the occurring reactions is the density of the modeled system. Increasing the density can lead to an increase in reaction events, since the collision rate is higher. However, since in this study the aim was to generate reasonably sized growth structures, we chose to calculate the density based on an ideal gas assumption, the pressure and temperature of the Chemkin calculations, and the number of molecules. This gave densities in the range of 0.013-0.015 g/cm^3.

Higher densities lead to more collisions during the calculations and in turn to more reactions between PAHs, which consequently results in an increase in the molecular weight of the growth structures found. The resulting growth structures further graphitized and gave fullerene like structures. The differentiation of structural features due to the different precursor pools generated under varying conditions in the Chemkin calculations could not be detected any more. This is due to the ongoing graphitization during the simulation, indicating that at the modeled simulation times the soot inception zone has been fully passed. It is probable that the chemical growth through bond formation proceeds to occur during soot growth after the inception phase and it has been shown that graphitization occurs at later stages of soot growth.(55) At some point other phenomena, like interactions due to Van der Waals forces and particle phenomena, start to play a role, however, which could not be observed since the number of larger structures formed was small due to the limited number of atoms. Since the aim of this thesis is to capture processes at the soot inception stage of combustion, lower densities have been employed, in order to be able to observe the inception process by bond formation of PAHs better.

5.5. Conclusion

In this chapter we presented the evaluation and optimization of different force field parameters to objectives of this thesis. In order to do so the BDE calculated with three force field parameter sets have been compared to DFT calculations of the same reactions. In this comparison the CHO08 force field parameter set developed by Chenoweth et al. yielded the best results for the conditions tested.

Furthermore, the ability of the three force fields to form trimer structures of PAH at different temperatures has been investigated. The results for the three force field parameter sets are very similar and hence no decision on the performance of the force field parameter sets could be taken.

As a result, the CHO08 has retained as the force field parameter set most suitable to describe the bond formation between soot precursor molecules in order to describe soot inception.

In addition, different input parameters for the ReaxFF simulations, i.e. the temperature and the time step, have been investigated. It could be shown that an increase in temperature can lead to an acceleration of the ReaxFF simulations. This means that the general reaction pathways and behavior of the molecules remain the same, but the speed at which reaction events occur increases. That leads to an artificial speed-up of the ReaxFF calculations and an overall saving of computational expense.

However, it was found that the temperature effects the performance of the ReaxFF calculations if the time step is not adjusted. The results for the ReaxFF calculations indicate that increasing temperatures lead to a faster fragmentation of molecules. This faster fragmentation could be linked to the choice of time step by investigating the same system at varying temperatures and varying time steps. It was shown that for each temperature a critical time step exists, at which the ReaxFF calculations fail to reproduce the results at smaller time steps. Above these so-called critical temperatures, the system's temperature can no longer be controlled, and unwanted dissociation reactions occur.

For the modeling of bond formation between soot precursors using systems of soot precursor pools extracted from Chemkin calculations it was found that at temperatures of 2500K and time steps of 0.1 the results with the least computational expenses are reached. A temperature increase to 2500K gives an artificial acceleration of the reactions of a factor of around four, while the decrease from 0,25 to 0,1 fs causes a deceleration of a factor of 2,5. Hence, there is an overall gain of 1,6 in computation time for a given simulation run.

6. Modeling Soot Inception with ReaxFF

6.1. Introduction

Soot inception, that is the step from the gas phase towards the particle phase during combustion, is to date a phenomenon that is poorly understood.(13,45,90,299) The most widely accepted mechanism for modeling soot particle inception is the irreversible dimerization of two PAH due to π-π interactions, with the smallest dimerizing PAH being pyrene, due to its thermal stability.(93,149–151) Experiments have shown that the size distribution of soot particles in flames exhibits a bimodal behavior,(121) which may be well reproduced by assuming physical dimerization as the soot inception step.(13,134) Furthermore, experimental evidence of excimers of aromatic aggregates in flames suggests that physical dimerization plays a role.(52)

The dimerization of PAHs of the size of pyrene due to π-π interactions under combustion conditions has been under debate, however.(13,149,156–159) From dimerization equilibrium constants(160,161) it appears that pyrene dimerization due to Van der Waals forces is unlikely to play a role in nucleation at combustion temperatures, and an investigation of the potential energy surface (PES) by Violi et al. supports this finding.(159)

Nonetheless, species larger than pyrene like ovalene and hexacoronene may be involved in the nucleation step by dimerization due to Van der Waals forces as the polarizability increases due to the larger aromatic plane.(158,159) The concentration of these species in the gas phase during combustion is low,(13) however, and soot inception was shown to occur before the peak concentration of these species.(300) Additionally, Violi et al. showed that smaller PAH substituted with aliphatic chains are more likely to form dimers.(159,300)

Since small PAH have too weak Van der Waals interactions to account for the irreversible dimerization, Eaves et al. introduced reversibility to the physical dimerization term in a nucleation study.(152,153) In order to reproduce experimental findings a chemical bond formation term, describing chemical bonding of PAHs and hence soot inception, was introduced to reduce the reversibility and thereby accounting for the soot inception. The formation of chemical bonds is also assumed in other models(49,117,144,154) to account for the high temperature soot inception and recent experimental studies support these findings.(56,301) Despite all these previous studies, several issues remain to be worked out and bond formation between soot precursors is not well understood.

In order to derive expressions for these chemical bond formations theoretical molecular modeling studies need to be performed. *Ab initio* methods are to date computationally too expensive to get accurate kinetics of the chemical bond formation between larger PAH due to the large number of electrons involved. As a result these rates are usually extrapolated from calculations on smaller aromatics.(302) Another molecular modeling approach to study the chemical growth on large PAH is based on kinetic Monte-Carlo calculations where chemical growth of a seed molecule is considered and was developed by Violi et al.(92,303) In this approach it is possible to differentiate nanostructures of soot particles based on different fuels, suggesting that aromatic fuels tend to produce more bent aromatic structures than aliphatic fuels.(30,113,304) Another recent approach used for modeling soot inception and combustion processes is based on reactive force field molecular dynamics.(129) Using this methodology, soot formation has been investigated in several studies. Zhang et al. modeled carbon black formation from acetylene and methane pyrolysis under high pressures using ReaxFF.(131,132) They found that during the pyrolysis small radicals first polymerize into longer chains, which in turn form ring-structures and finally coalesce into one large

particle. Han et al. modeled the combustion of a 24-component fuel to investigate the soot inception process using ReaxFF.(66) They interestingly showed that soot formation followed three distinct stages: the formation of the first ring, coalescence of smaller molecules into bigger structures and finally a graphitization stage. Furthermore, Mao et al. modeled physical and chemical soot nucleation of intermediate-sized PAH using ReaxFF by modeling homo-molecular dimerization at different temperatures, producing dimerization kinetics of physically and chemically bound PAH in dependence of the temperature.(125,147) They showed that in dependence of the size of the PAH the temperature at which physical dimerization occurs differs, while homo-molecular bond formation only occurred at elevated temperatures independent of the PAH size.(147) In a further study they investigated the kinetics and lifetime of homobinary collision of PAH molecules and radicals.(126) They revealed an influence of molecular size, the number of radical sites in the molecule and the temperature on the dynamics of the dimerization process. Additionally they showed that metal atoms could assist bond formation between PAH.(127) Yuan et al. showed that an estimated mixture of small PAH and smaller radicals, which are found in abundance during combustion, produces large molecules using ReaxFF at experimental flame temperatures.(148) They showed that with different mixtures of PAH and radicals the polymerization process between PAH follows different pathways. They notably found that at low temperatures the soot formation mechanism is governed by physical forces and direct carbon addition, while at higher temperatures radical reactions play a more dominant role.(148)

Wang categorized the soot nucleation process into three pathways, the first being the stepwise growth of soot from addition of smaller molecules, the second being dimerization of soot precursor molecules due to π-π-interactions and the third being the reactive bond formation (also called coalescence) between soot precursor molecules.(13) In the present chapter the third pathway is

investigated and chemical bond formation between soot precursor molecules is modeled in order to understand structural differences of nascent soot particles. For this, the extracted soot precursor compositions from the Chemkin calculations, as presented in chapter 4, are used in order to investigate the effects of the differences in molecular composition due to the different combustion conditions. It is expected that due to the compositional differences in the soot precursor pool, the growth and as a result the nanostructure of the soot will differ. Here, we propose a way to rationalize the expected correlation between the initial conditions and the resulting soot nanostructure.

First the results of the ReaxFF calculations are presented and the monitoring of the simulations and the conclusions drawn are discussed. Secondly, the common features to all detected soot growth structures are discussed and compared to experimental studies. In the fourth subchapter the impact of soot precursor composition due to the different parameters used for the Chemkin calculations is analyzed. The generated growth structures can be structurally distinguished in directly linked, aliphatically linked and pericondensed polycyclic hydrocarbons. Based on this structural differentiation the impact of soot precursor composition is discussed. Lastly, a number of example reaction pathways that was observed for each structural group is given, before drawing a conclusion on the results of the ReaxFF calculations.

6.2. Details on the Methodology of the ReaxFF Calculations to Model Nascent Soot Structures through Bond Formation between Soot Precursors

The ReaxFF calculations were performed using the SCM ADF modeling suite(305) within the NVT ensemble at 2500 K with a Nosé-Hoover thermostat, a damping constant of 10 fs and a time step of 0.1 fs and employing the force field published by Chenoweth et al.(277) The simulation choices are based on the evaluation of the ReaxFF approach in chapter 4.

The density of the simulation boxes was chosen to correspond to the pressure of 10 atm used in the Chemkin calculations which correspond to densities representative of real engine conditions.(306) Hence, the densities of the different soot precursor mixtures vary from 0.013 to 0.015 g/cm^3. The statistics of the molecular dynamics simulations were improved by using three different initial starting geometries for each condition. The different initial geometries, i.e. different initial atomic coordinates and initial velocities are used in order to limit a bias towards a certain reaction due to an immediate vicinity of two molecules at the beginning of the calculation.

All systems were thermochemically equilibrated for 100ps at 2500K with the reactivity turned off by preventing bond orders to change between atoms. After equilibration of the temperature, the bond order algorithm of ReaxFF was turned on, to allow for bond breaking and formation. The simulations were run for 2 ns. At the end of each calculation, every structure which molecular weight exceeded the initial maximal mole mass of the starting composition, was detected as a growth-structure. Thereafter, the structural features and reaction pathway of each growth structure detected have been investigated. A total of 449 individual growth structures was obtained from all calculations run for the tested 128 soot precursor compositions.

6.3. Results from the ReaxFF calculations

The ReaxFF simulations were monitored, all structures that underwent some kind of growth reaction were analyzed. In Figure 24 the averaged molecular weight of the largest molecule during the calculation for all tested temperatures, all fuels and the median equivalence ratio (φ=3.5) are shown. The same graphs for other compositions are not shown as they follow similar trends.

It is to note that the average of the three calculations at each condition is usually smaller than the molecular weight found at the end of one calculation, since the formation of a growth species is a rare event. As a result, the highest molecular weight detected in some cases did not increase, and

consequently the change in molecular weight depicted in Figure 24 is decreased due to these smaller molecular weights contributing to the average. This is also the reason why it appears, the molecular weight at elevated temperatures is bigger compared to lower temperatures. This is due to the fact that the formation of a bond between PAH leading to a growth structure appeared more often in these calculations.

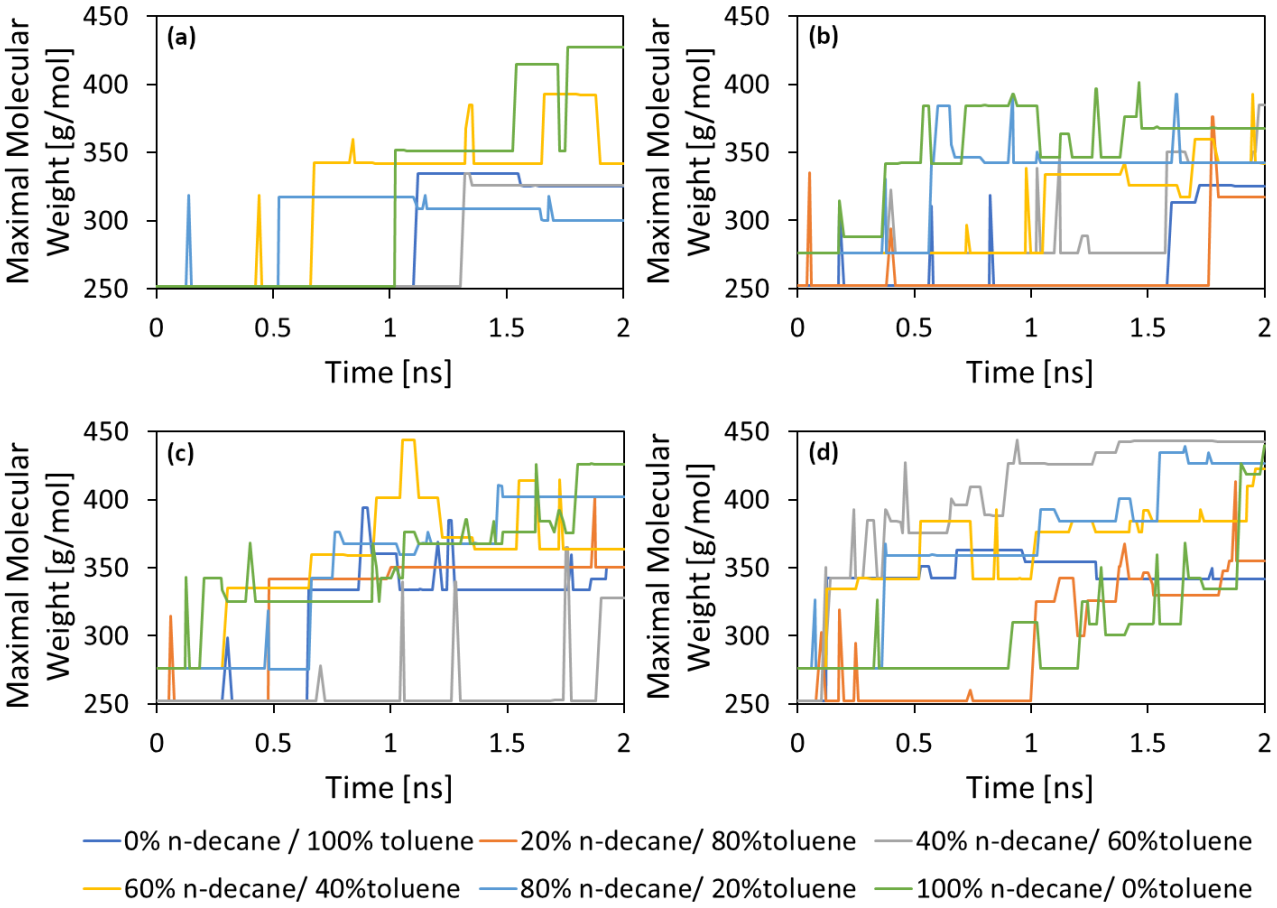

Figure 24. Molecular weight of the largest molecule detected during the ReaxFF simulation averaged over all simulations of one condition and plotted over the calculation time. The soot precursor compositions correspond to the Chemkin calculations performed with an equivalence ratio of 3.5, all fuel mixtures and (a) 1400K, (b) 1600K, (c) 1800K and (d) 2000K.

The different reactivity of species is shown in Figure 25, where consumption of the PAH during the ReaxFF calculation for some example conditions is monitored. The conditions presented are the

ReaxFF Calculations for the precursor pools at 1) equivalence ratio of 2.5, temperature of 1800 K and a fuel mixture of pure-n-decane and 2) equivalence ratio of 2.5, temperature of 2000 K and a fuel mixture of 60 mol% n-decane and 40 mol% toluene. These conditions have not been chosen in order to portray the change of reactivity due to the change in Chemkin parameters. The change in reactivity is a result of the change in composition due to the parameter change in the Chemkin calculations, as all ReaxFF calculations are run at the same temperatures and comparable densities. The change of soot precursor pool composition due to the change in Chemkin parameters has been discussed in chapter 4.4. Instead the displayed compositions have been chosen to show the change in reactivity by highlighting certain features of the soot precursor compositions, such as a large amount of diversity of the PAH compositions or a large number of pyrenyl radicals. This gives an estimate of the species contributing most to the growth. Other compositions follow the same trends as presented in these two compositions for the consumption of species and thus are not shown.

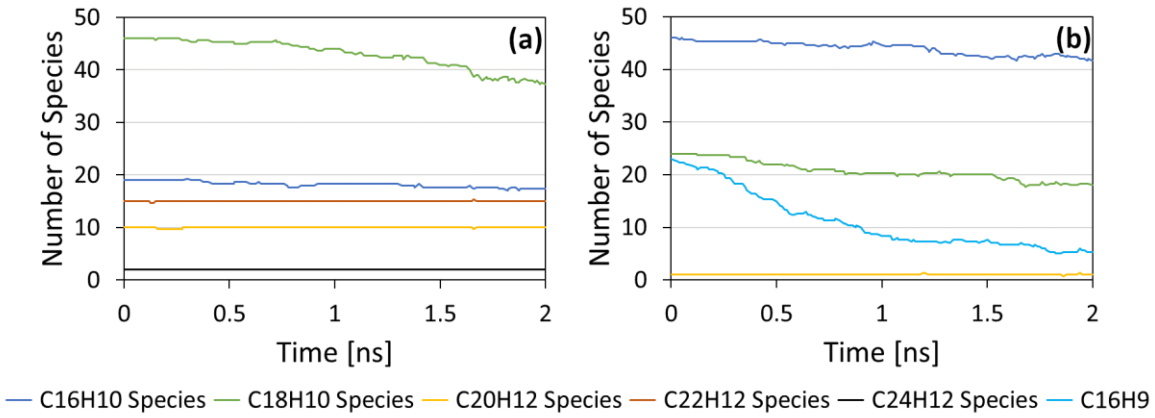

Figure 25. Consumption of the initial species present in the ReaxFF calculations plotted over the calculation time. The precursor pool compositions depicted represent the Chemkin calculations at (a) an equivalence ratio of 2.5, temperature of 1800K and a fuel mixture of pure-n-decane and (b) an equivalence ratio of 2.5, temperature of 2000K and a fuel mixture of 60 mol% n-decane and 40 mol% toluene.

Unfortunately, in ReaxFF species are distributed by their sum formula, making a monitoring of isomers difficult. Hence the isomers pyrene, cyclopenta[1,2]phenalene, and fluoranthene, molecules (a), (i), and (j) shown in Figure 9 respectively, are drawn together under the sum formula $C_{16}H_{10}$. The pyrenyl radicals, species (b), (c), and (d) in Figure 9, are all shown as the sum formula $C_{16}H_9$. The sum formula $C_{18}H_{10}$ groups the molecules 1-(1-pyrenyl)acetylene, 1-(2-pyrenyl)acetylene, 1-(4-pyrenyl)acetylene, and cyclopenta[cd]pyrene, depicted as molecules (e), (f), (g), and (h) in Figure 9, respectively. The molecules benzo[a]pyrene and benzo[e]pyrene are grouped under the sum formula $C_{20}H_{12}$, depicted as molecules (l) and (m) in Figure 9. Perylene would normally be also grouped under the sum formula $C_{20}H_{12}$, but since it is not present in any of the soot precursor compositions it is not represented in Figure 25. The sum formula $C_{22}H_{12}$ gives benzo[ghi]perylene and anthanthrene, molecules (o) and (p) in Figure 9, respectively, and the sum formula $C_{24}H_{12}$ is coronene, molecule (q) in Figure 9.

From Figure 25 one can now draw conclusions on the stability of the species and which species tend to be more reactive. Figure 25a, which depicts the simulation for the soot precursor pool generated with Chemkin at a temperature of 1800 K, an equivalence ratio of 2.5 and a fuel composition of pure n-decane, shows that with increasing molecular weight the molecules appear to be more stable, meaning species with more than twenty carbon atoms appear to be less reactive . This effect is due to two reasons. The first is the abundance of species. Since the larger species are present during the simulation in smaller numbers, the probability of them reacting with other species is smaller, if one assumes that each molecule in the box has the same probability to react.

The second reason for why the larger species are less reactive is because of their ratio of hydrogen to carbon atoms, the H/C-ratio. The single bond between hydrogen and carbon atoms found in the PAH is much weaker than the aromatic bonds between carbons in the PAH.(307–309)

Hence a C-H site is usually seen as a reactive site. Since the H/C-ratio is increasing with increasing molecular size of the PAH, the molecules possess less reactive sites compared to non-reactive sites as a result.

The species with the sum formula $C_{16}H_{10}$ are more reactive compared to the species with twenty carbon atoms or more, since a reasonable amount of these species are consumed during the ReaxFF simulation. This is due to the abundance of these species. Compared to the acetylenated pyrenes, which are represented under the sum formula $C_{18}H_{10}$, the $C_{16}H_{10}$ are less reactive, however. This is due to the additional sidechain in most of the $C_{18}H_{10}$ species. During the simulation it was found that reactions at the sidechain or the dissociation of the C_2H-sidechain occurred frequently. Due to the presence of an acetylene sidechain, a radical addition at the end of the sidechain is sterically less hindered than in the absence of a sidechain. The dissociation of the sidechain can be attributed to an increased stabilization of the formed radicals. Furthermore, it was observed that the aromatic 5-ring in cyclopenta[cd]pyrene is prone to ring opening reactions, leading to a PAH with a sidechain and dual radical character. This species hence is also rather reactive, compared to the $C_{16}H_{10}$ species.

The species most reactive are the pyrenyl radicals, as can be seen in Figure 25b, where these species are quickly consumed. This can mainly be attributed to the radical character of these species. Due to the radical site, reactions including the pyrenyl radicals occur more readily. Furthermore, it could be observed that fragmentation of the pyrenyl radicals occurs often. The reason for this is that the system is aiming to stabilize the radical, due to the undercoordination of the carbon atom at which the radical site is present. As a result, increasing bond order towards a neighboring carbon atom, as the ReaxFF force field tries to minimize the undercoordination penalty term, can lead to bond breakage of the opposite bond. This can lead to a chain reaction that results in fragmentation of the pyrenyl radicals to smaller resonance-stabilized radical species, which in

turn can produce PAH radicals through H-abstraction. The latter can then react with each other or be involved in additional reactions with another PAH. This kind of fragmentation is also observed in the $C_{18}H_{10}$ species after dissociation of the sidechain, or in other species as a result of a bond formation with other molecules, leading to radical character.

6.4. Common Properties to all Detected Growth Structures.

At the end of the ReaxFF simulations, all structures that underwent growth reaction leading to a molecular weight higher than the initial maximal molecular weight were analyzed. The abundance of each generated structure was plotted against its molecular mass for all fuel mixtures, equivalence ratios and temperatures in Figure 26. This plot is similar to experimental mass spectra distributions measured in the soot inception zone. Experiments have shown that species with similar molecular masses can be detected in the soot inception zone. (51,302,310,311)

The main peak at a molecular mass of 402 g/mol notably matches the molecular formula of $C_{32}H_{18}$, which corresponds to the product of two pyrenyl radicals. As pyrene is the most abundant species in the compositions, it is not surprising that the most prominent product corresponds to the reaction of two pyrene molecules. In fact, over 50% of the total structures generated had pyrene as a reactant and 100% of these structures had either pyrene, pyrenyl radical or acetylenated pyrene as a reactant. This leads to the assumption that the precursor pool extracted from Raj's mechanism is missing possible other PAH than pyrene that can form in the gas phase. This is taken into account, but since pyrene is a good substitute for the general properties of PAH the results obtained can nonetheless be considered to be representative.

Furthermore, it is noticeable that the main peaks are each separated by a molecular mass of 24 g/mol or 26 g/mol, corresponding to two carbon atoms or two carbon and two hydrogen atoms. This is a spacing often found also in experimental results and is usually related to the so-called

stabilomer grid.(136,312–314) That grid is a number of isomers of PAH with certain molecular masses proposed due to their thermodynamic stability by Stein an Fahr. (87)

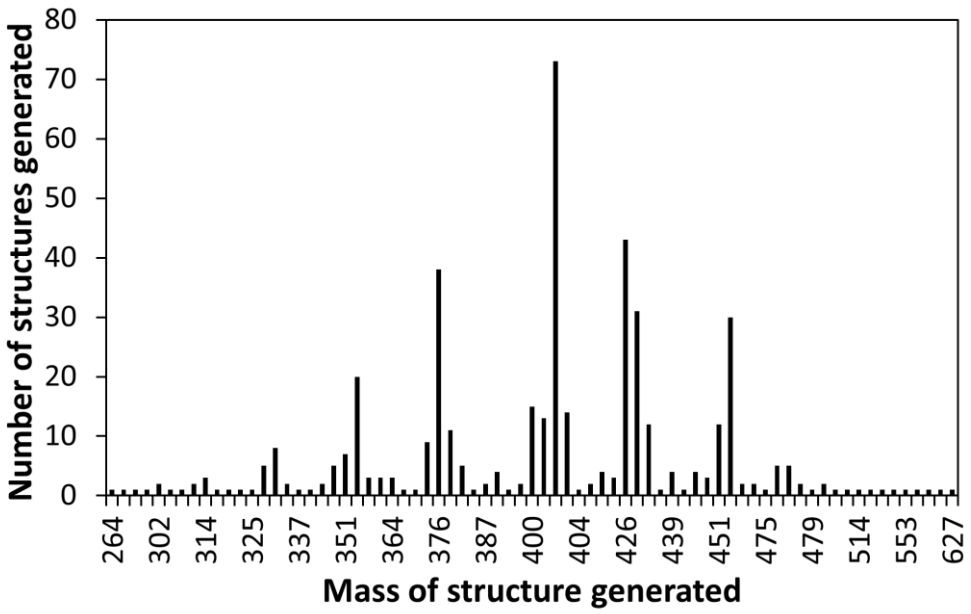

Figure 26. Mass distribution of all detected structures grown from soot precursors for all fuel mixtures, equivalence ratios and temperatures. The main peaks correspond to the following sum formula: $C_{26}H_{15}$ = 327 g/mol; $C_{28}H_{16}$ = 352; $C_{30}H_{16}$ = 376 g/mol; $C_{32}H_{18}$ = 402 g/mol; $C_{34}H_{18}$ = 426 g/mol; $C_{36}H_{20}$ = 452 g/mol.

In this study the reason for this spacing for species with molecular masses higher than 402 g/mol is a result of the dominance of the HACA-mechanism for growth of PAH in RAJ's mechanism. That is the molecular masses of the species present in the soot precursor pools are also separated by a molecular mass of 24 g/mol or 26 g/mol, i.e. the next largest species either possesses two more carbon atoms or two more carbon atoms and two more hydrogen atoms. Hence, if the peak at 402 g/mol represents the reaction of two species of the weight of pyrene with each other, the peak at 426 g/mol represents the product of a reaction of a pyrene and a species of the weight of the

acetylenated pyrene, while the peak at 452 g/mol corresponds to the product of the reaction of two species of the weight of the acetylenated pyrene found in the precursor pools.

For molecules with lower masses mass than 402 g/mol the explanation of the spacing between the main peaks is slightly more complicated. Here the effect of stabilization of fragmentation products plays a role. The fragmentation of pyrene often leads to the formation of a phenanthryl radical and an acetylenyl radical, since phenanthrene is the next stable aromat on the stabilomer grid smaller than pyrene. Hence, the formation of phenanthrene is more favorable than other fragmentation products due to its increased stability. As a result, the peak at 376 g/mol represents products of a reaction of a molecule with the weight of pyrene and a molecule with the weight of phenanthrene and the peak at 351 g/mol represents products of a reaction of two molecules with the weight of phenanthrene.

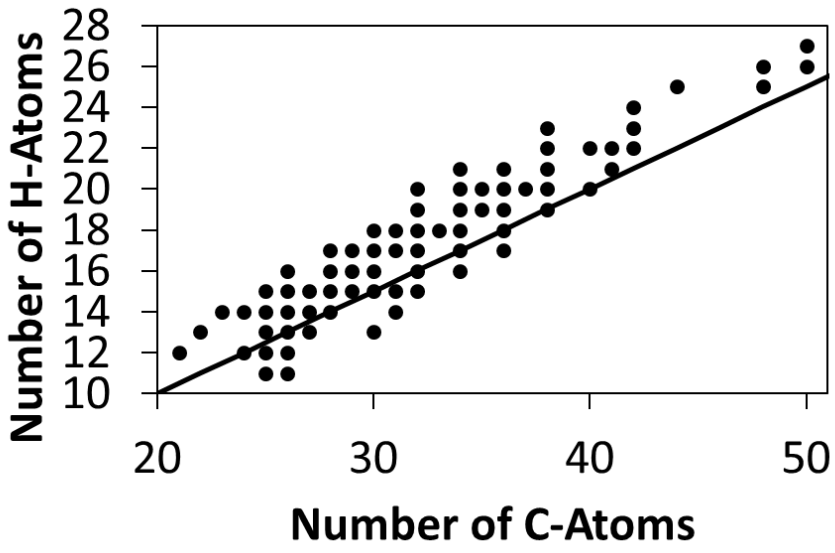

Figure 27. Number of H-atoms over the number of C-atoms found for all detected structures grown from soot precursors for all fuel mixtures, equivalence ratios and temperatures. The solid line depicts the values for an H/C ratio of 0.5.

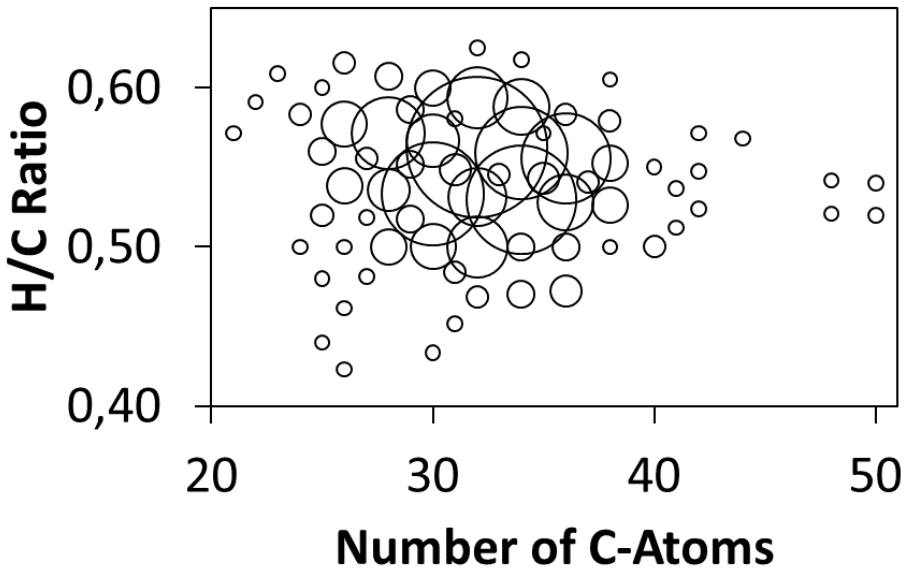

Figure 28. Number of species with a certain H/C-ratio over the number of C-atoms found for all generated structures grown from soot precursors for all fuel mixtures, equivalence ratios and temperatures. The size of the circles gives the amount of species found for a H/C-ratio and a number of carbon atoms. The smallest circles stand for a count of one species, while the biggest circle represents the amount of 73 species found with that H/C-ratio and that number of carbon atoms.

Figure 27 shows the number of H-atoms present in the product molecule as a function of the number of C-atoms. This figure puts forward that upon increasing carbon content (and thus molecular mass), the H/C ratio converges to a value larger than 0.5. Figure 28 depicts the number of species found with a certain H/C-ratio over the number of carbon atoms in the species. The size of the circles gives the amount of species found for a C/H-ratio and a certain number of carbon atoms. One can see that the majority of species lies well above an H/C ratio of 0.5. Again one can find that these plots are comparable to experimental studies in which H/C ratios around 0.5 were found in the soot inception zone in experimental flames for the largest species.(51,302,310,311)

Figure 29 shows the number of detected growth structures over the number of aromatic rings found in the structures. The majority of the generated structures possess between six and nine aromatic rings. This finding is consistent with a HRTEM analysis by Botero et al., who estimated the number of rings of a fringe found in soot particles based on the fringe length.(315) Furthermore, 18% of the structures include one or more rings with an odd number of C-atoms, leading to a stress in the graphitic plane and as a result of a more bend structure. This finding is consistent with other modeling studies,(114,115,145) as well as a recent atomic force microscopy study by Schulz et al.(56) on soot precursors in the inception regime, showing that odd-numbered rings are found in nascent soot particles. In general, all features observed by Schulz et al., i.e., linked aromatic moieties, aromatic moieties with sidechains and large PAH with six or more rings were reproduced by the present study. Furthermore, Adamson et al. showed in a recent mass spectra study that aliphatic links between aromatic moieties and also aliphatic sidechains are found in nascent soot particles.(301) These features are also found in the structures created with our coupled Chemkin ReaxFF approach as 47% of the total structures generated exhibit sidechains, 36% of the total structures are aliphatically linked and 32% are directly linked.

6.5. Impact of the Soot Precursor Pool Compositions on the Structural Differences

The number of growth structures detected at the end of the ReaxFF calculations are averaged for the whole range of two parameters and varying the third parameter in Figures 30 – 32 This is done in order to show the influence of the third parameter on the growth through, e.g. chemical dimerization or fragment addition. For example, Figure 30 reports the detected growth structures averaged for the whole range of fuel mixtures and equivalence ratios, at distinguished steps of temperature. This better illustrates the impact of soot precursor composition change resulting from one of the tested parameters and subsequently the bond formation between PAH.

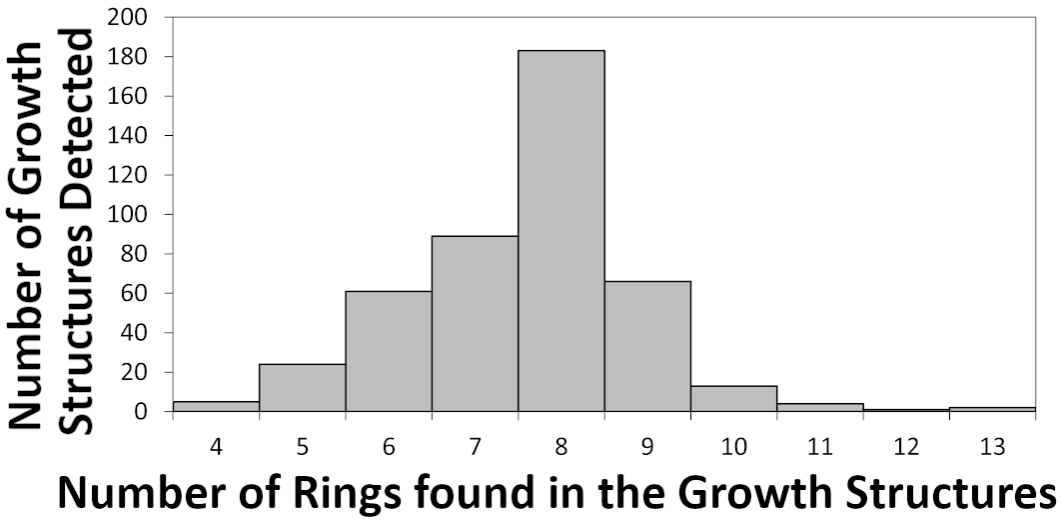

Figure 29. Bar diagram of the number of detected growth structures for all calculations at all temperatures, equivalence ratios and fuel mixtures over the number of pericondensed rings found in the structure.

While the average number of detected growth structures remains rather constant over the range of tested fuel mixtures and equivalence ratios, one can distinguish a linear increase of the growth structures detected with increasing temperature used in the Chemkin calculations. Since all molecular dynamic simulations are realized at 2500 K, this increase must be attributed to changes in the composition resulting from the Chemkin calculations. Indeed, higher radical concentrations, e.g. pyrenyl radicals, are found with increasing temperatures, in line with the higher radical concentration found in precursor pools in experiments, thereby enhancing chemical growth.(45,260)

As discussed in chapter 5.3, a group of species that proved to contribute largely towards the reactivity are the acetylenated pyrenes. These species may account for the difference between structures generated at 1400 K and 1600 K. While the compositions obtained at 1400K are dominated by pyrene, the compositions obtained at 1600 K are more diverse and have higher numbers of acetylenated pyrene entities.

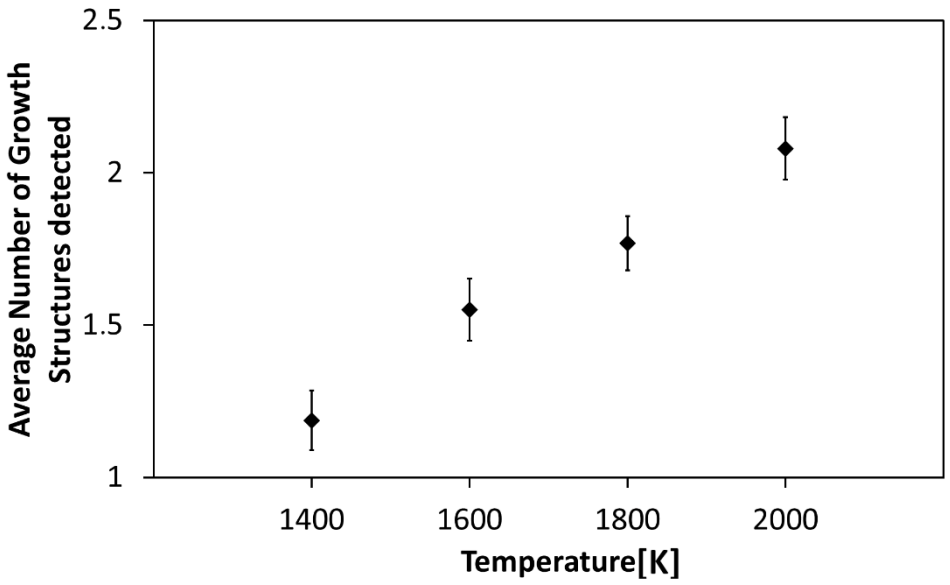

Figure 30. Number of all detected growth structures through bond formation as a function of temperature. The number of structures is averaged for all equivalence ratios and fuel mixtures and distinguished by temperature. The vertical bars represent error bars.

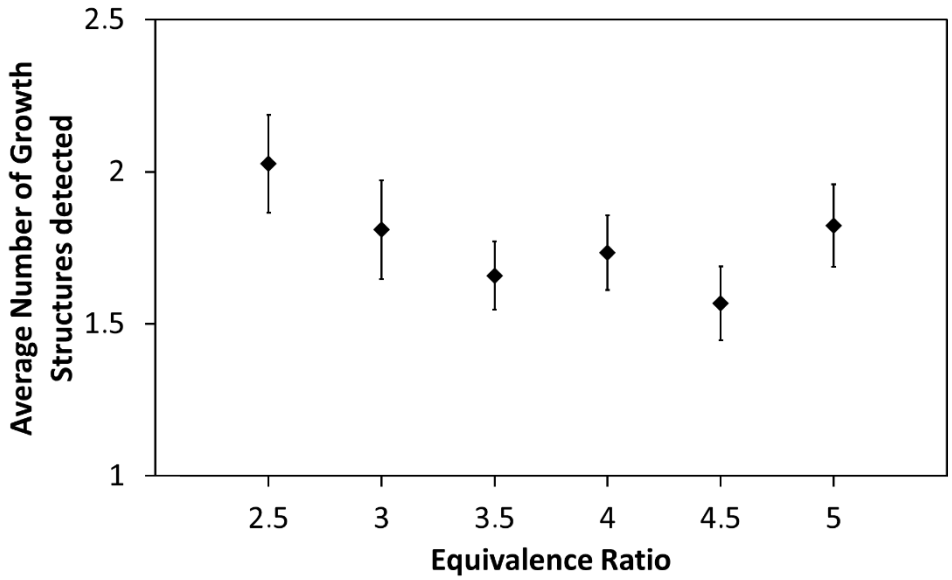

Figure 31. Number of all detected growth structures through bond formation as a function of equivalence ratio. The number of structures is averaged for all temperatures and fuel mixtures and distinguished by equivalence ratio. The vertical bars represent error bars.

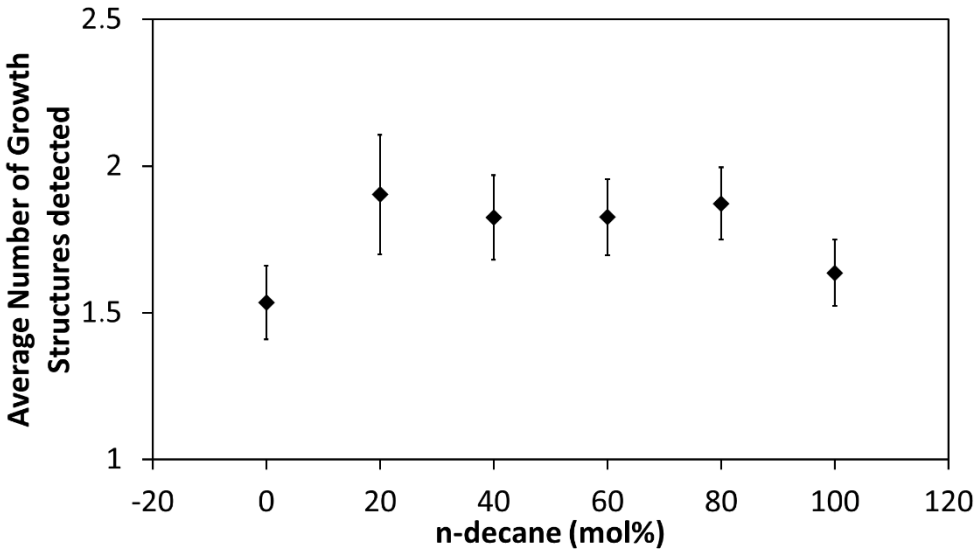

Figure 32. Number of all detected growth structures through bond formation as a function of n-decane mol fraction in the fuel mixture. The number of structures is averaged for all temperatures and equivalence ratios and distinguished by fuel mixture. The vertical bars represent error bars.

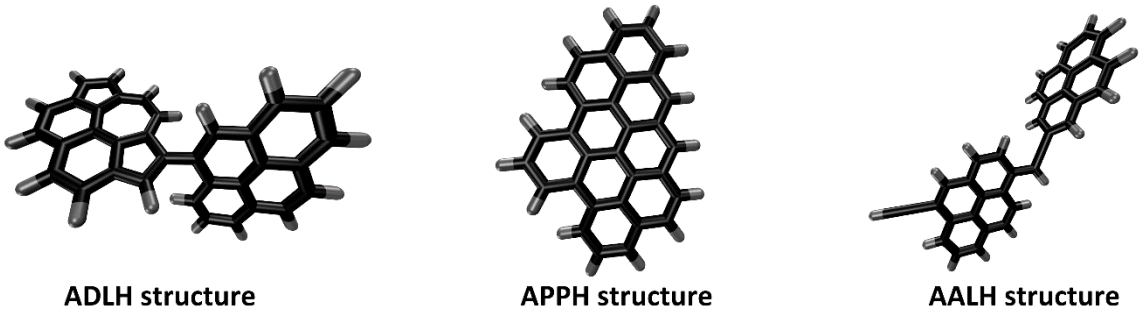

Figure 33. Representative structures of the three groups used to show their structural differentiation. Left: aromatic directly linked hydrocarbon structure; middle: aromatic pericondensed polycyclic hydrocarbon structure; right: aromatic aliphatically linked hydro-carbon structure.

All generated species from our ReaxFF simulations could be categorized into three main classes on the basis of their chemical structure. The first class envelopes all structures with directly linked aromatic moieties. Structures exhibiting this feature are in the following referred to as aromatic directly linked hydrocarbon structures (ADLH). This means that the two aromatic pericondensed

planes are directly linked to one another, without additional C-atoms between the aromatic moieties. The second class assembles the molecules that exhibit one pericondensed polycyclic plane as the main feature and are termed aromatic pericondensed polycyclic hydrocarbon structures (APPH). The third class comprises molecules exhibiting two or more aromatic moieties linked by aliphatic chains, in the following referred to as aromatic aliphatically linked hydrocarbons (AALH). Representatives of the structural different groups are depicted in Figure 33.

The influence of the parameters varied in the Chemkin calculations on the three structural different groups has been analyzed. The average number of structures for each group as a function of one parameter is shown in Figures 34 – 36. Like in Figures 30 – 32 this is achieved by averaging for the whole range of two parameters and varying the third parameter.

From Figures 34 – 36 one can deduct that the equivalence ratio as a parameter had the least influence on the generation of structures of one specific group. Only the number of APPH structures appears to be decreasing slightly with increasing equivalence ratio. However, since this decrease is well within the error bars of the measurement points this finding is not statistically significant. This is not surprising since the equivalence ratio also had very little impact on the soot precursor pool compositions.

The temperature, on the other hand, shows the same trend as for all structures. This is that with increasing temperature the number of growth structures formed for one structural group increases as well. This trend is similar for all three classes and is due to the overall increase in detected structures with increasing temperatures.

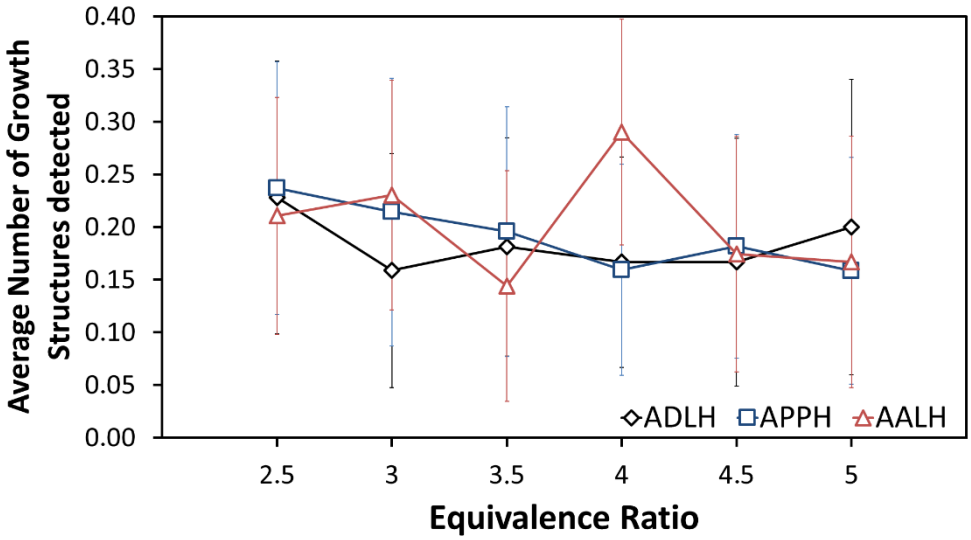

Figure 34. Number of detected growth structures through bond formation with different structural features plotted as a function of the equivalence ratio. The number of structures of each structural group are averaged for all temperatures and fuel mixtures and distinguished by equivalence ratio. The vertical bars represent error bars.

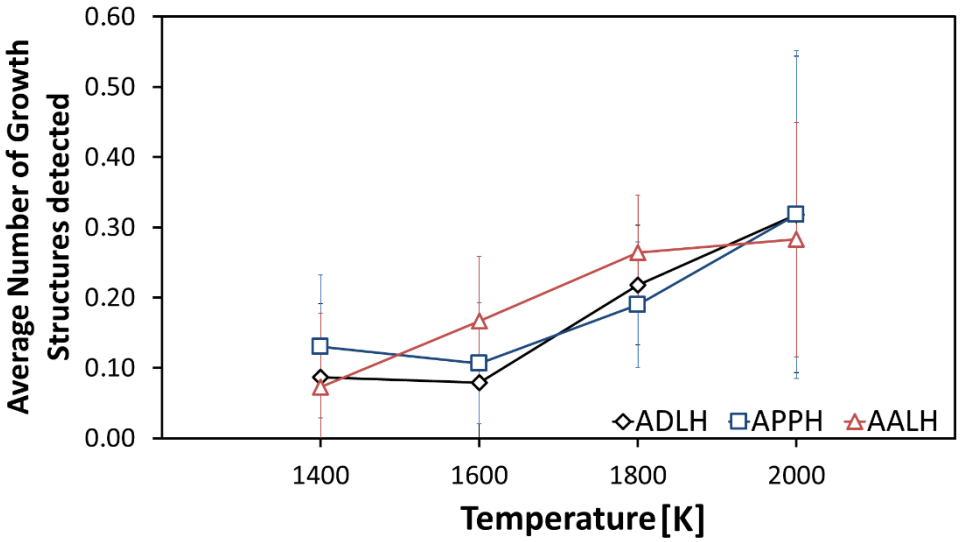

Figure 35. Number of detected growth structures through bond formation with different structural features plotted as a function of the temperature. The number of structures of each structural group are averaged for all equivalence ratios and fuel mixtures and distinguished by temperature. The vertical bars represent error bars.

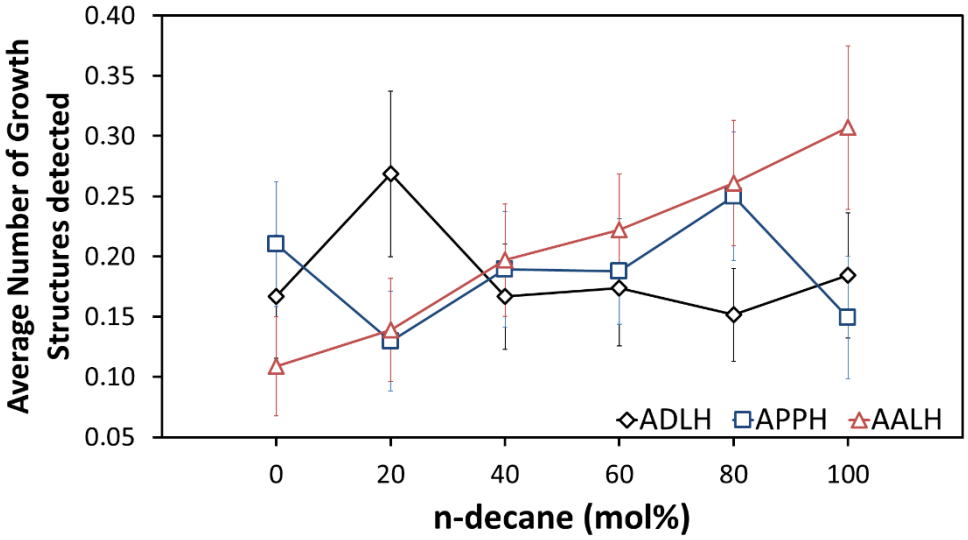

Figure 36. Number of detected growth structures through bond formation with different structural features plotted as a function of the n-decane mol fraction in the fuel mixture. The number of structures of each structural group are averaged for all equivalence ratios and temperatures and distinguished by fuel mixture. The vertical bars represent error bars.

This is different for the evolution of the three classes as a function of the fuel mixture, as shown in Figure 36. While there is no clear trend for the ADLH and APPH structures, there is a clear linear trend for the AALH structures. The formation of AALH structures increases with the aliphatic content of the fuel mixture.

The generated structures can also be classified according to the presence of aliphatic sidechains. The occurrence of aliphatic sidechains as a function of the parameters varied as input for the Chemkin calculations are shown in Figures 37 – 39. The atomic force microscopy study of Schulz et al. shows that sidechains commonly occur in early soot structures.(56) In addition, Adamson et al. found aliphatic sidechains in soot precursors using mass spectrometry.(301)

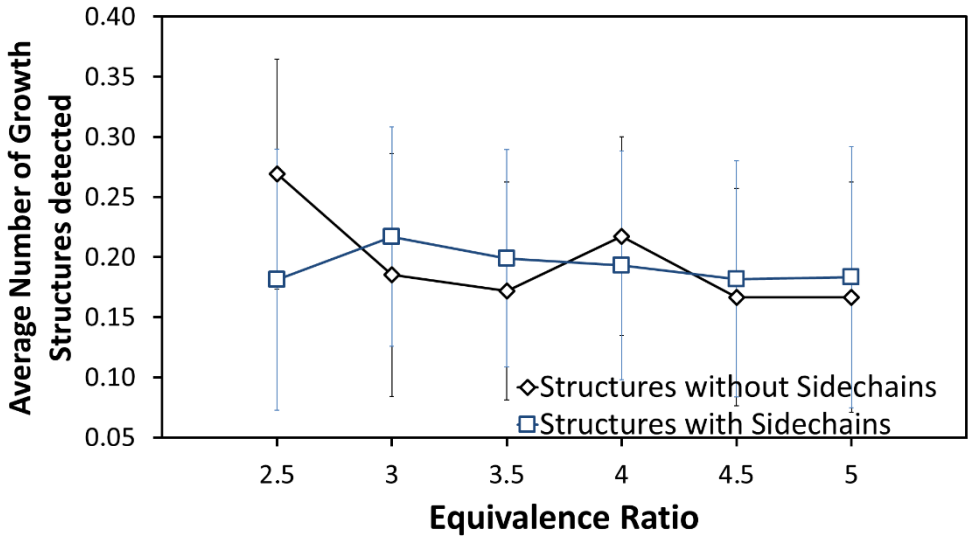

Figure 37. Number of detected growth structures through bond formation with and without sidechains plotted as a function of the equivalence ratio. The number of structures of each structural group are averaged for all temperatures and fuel mixtures and distinguished by equivalence ratio. The vertical bars represent error bars.

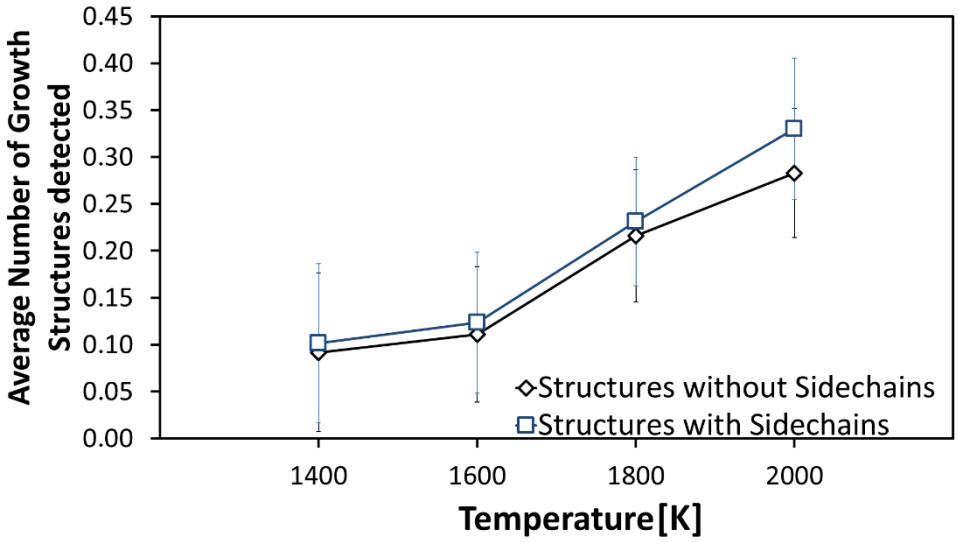

Figure 38. Number of detected growth structures through bond formation with and without sidechains plotted as a function of the temperature. The number of structures of each structural group are averaged for all equivalence ratios and fuel mixtures and distinguished by temperature. The vertical bars represent error bars.

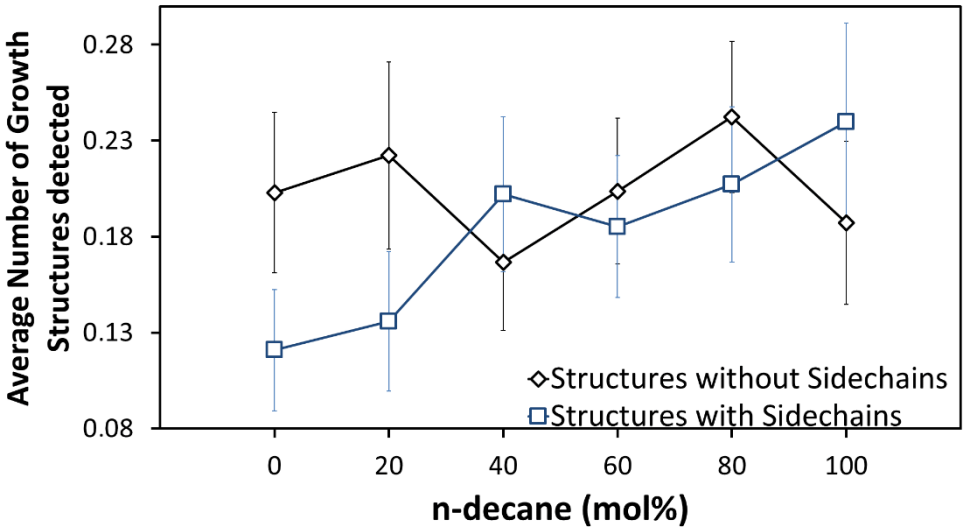

Figure 39. Number of detected growth structures through bond formation with and without sidechains plotted as a function of the n-decane mol fraction in the fuel mixture. The number of structures of each structural group are averaged for all equivalence ratios and temperatures and distinguished by fuel mixture. The vertical bars represent error bars.

In Figures 37 – 39 similar trends compared to those found in Figures 34 –36 can be seen. While the equivalence ratio does not show an impact over the tested range for the generation of structures with or without sidechains, the temperature gives a general increase of both types of structures with increasing temperatures. The average number of growth structures detected with and without sidechains plotted over the range of tested fuel mixtures gives again a differentiation. While there is no trend for structures without sidechains over the tested range, the number of structures with sidechains is increasing with increasing aliphatic fuel content.

To study functional groups on soot surfaces experimentally, FT-IR spectroscopy has been previously used to probe the nature and content of C-H functional groups. Using this approach Jaramillo et al. found that soot formed from pure aromatic fuels has a higher sp2/sp3 ratio (i.e. it contains less aliphatic C-H groups) than soot formed from aliphatic fuels.(202) Interestingly, they also found that soot formed from mixtures of aliphatic and aromatic fuels have a sp2/sp3 ratio that

is even smaller than the ratio for pure aliphatic fuels, and thus even contains more aliphatic C-H groups than soot formed from pure aliphatic compounds, which has also been confirmed in a study by Liu et al.(316)

The average ratio of carbon atoms present in a sidechain or bridge to carbon atoms in pericondensed rings is shown in Figure 40. One finds that the growth structures formed from pure n-decane exhibit a higher ratio of "sidechain/bridge" carbon to "pericondensed ring" carbon than the structures found for pure toluene. Mixtures of n-decane and toluene with a n-decane fraction of more than 50 percent show even higher ratios of "sidechain/bridge" carbon to "pericondensed ring" carbon than the pure n-decane. This ratio decreases with increasing aromatic fuel content, and was found to be the lowest for fuel mixtures of 20% n-decane and 80% toluene.

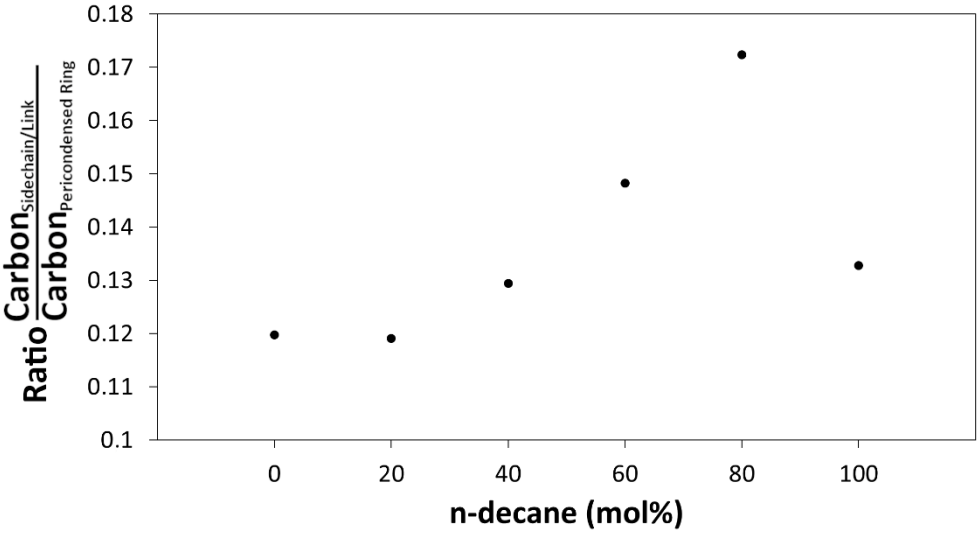

Figure 40. The ratio of carbon atoms found in a sidechain or ring of the growth structures detected to carbon atoms found in pericondensed rings of the growth structures detected as a function of the n-decane mol fraction.

Hence, our results are in line with the FT-IR studies of Jaramillo et al. and Liu et al. Yet, a direct comparison of our results with the FT-IR studies is not straightforward. In the FT-IR studies the ratio of sp3 (aliphatic) carbon to sp2 carbon in pericondensed rings is measured by comparing the

relative peak heights of the C=C stretching mode and the aliphatic C-H stretching mode, since the aromatic C-H stretching modes and the acetylenic C-H stretching modes are “hidden” behind the broad O-H stretching mode.(317) However, the sidechains in this study generally contain unsaturations and these could not be distinguished from the aromatic vibrations in the FT-IR studies. Interestingly, in Raman spectroscopy studies, Le et al. found a peak corresponding to sp-hybridized carbon structures in soot formed from low pressure ethylene soot, indicating the presence of such polyene sidechains,(318) which were also detected in our theoretical study.

In the present study, the correlation between the fuel composition and the growth structures containing aliphatic links and/or sidechains is related to the soot precursor compositions extracted from Chemkin being more diverse for aliphatic-rich fuels than for aromatic-rich fuels (see chapter 4.4). As a result of the higher diversity and the higher amount of PAH possessing a sidechain, reactions occurring on carbon atoms in a sidechain become more probable. Furthermore, after a bond formation between two PAH has occurred the growth structure is more likely to possess a sidechain, because one of the reactants already possessed a sidechain.

This conclusion can be drawn from Figure 41. There the amount of carbon atoms found in links (Figure 41a) and the amount of carbon atoms found in sidechains (Figure 41b) are depicted. It is evident that the links and sidechains are mostly consisting of two carbon atoms, corresponding to an ethyl bridge or an acetylene sidechain. This is due to the fact, that the introduced sidechains from the soot precursor compositions are only acetylene sidechains.

The established correlation between the (aliphatic) decane content in the fuel mixture and the detected number of growth structures containing aliphatically linked structures and/or sidechains seems plausible none the less, since the concentrations of aliphatic molecules and aliphatic radicals

are higher for aliphatic fuels than for aromatic fuels in the gas phase during combustion. Hence, the addition of these species to PAH radicals occurs more frequently.

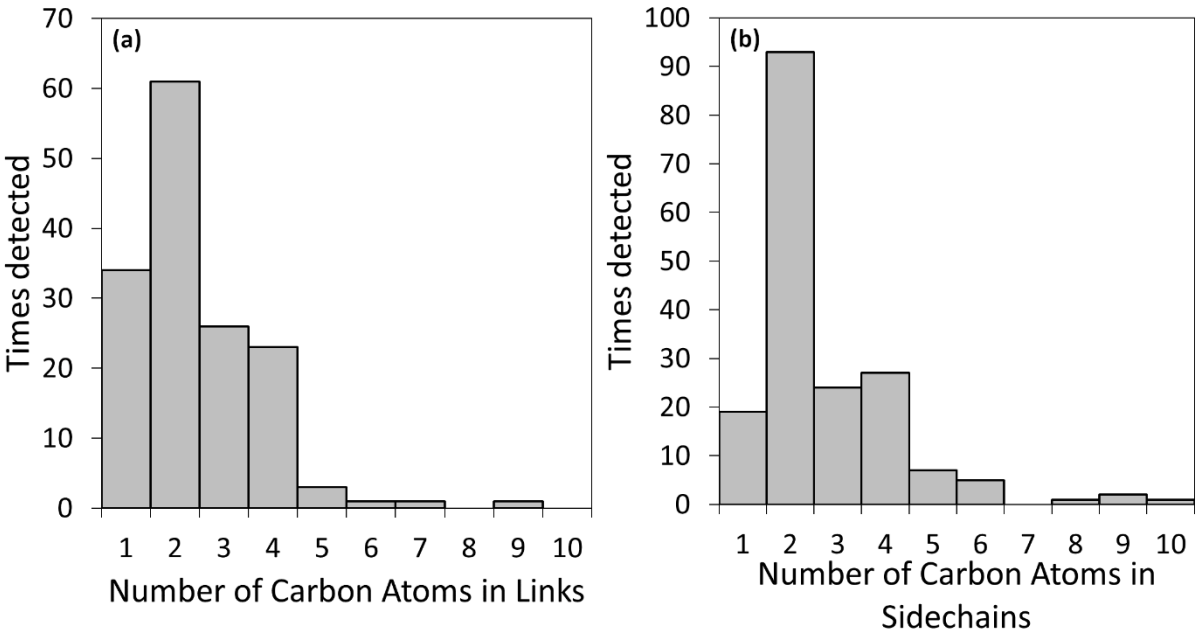

Figure 41. Bar diagram of the number of carbon atoms found in (a) links between aromatic moieties of the detected growth structures and (b) in sidechains attached to the detected growth structures.

6.6. Reaction Pathways

Based on the above described structural differentiation of ADLH, APPH and AALH structures, one can investigate the most common reaction pathways that lead to these structures. In this context it is important to note that all three structure types have a common initiation reaction, i.e., the production of radicals through the dissociation of smaller species from the PAH, thereby stressing its importance. Apart from C-H dissociation, the dissociation of an acetylenyl-radical from an acetylenated PAH also occurs frequently. Furthermore, resonance stabilized radicals, which have been shown to play a crucial role in PAH and soot formation,(135) have been detected during the bond formation between PAH. However, in this. study no increased reactivity from these species could be detected in comparison to non-stabilized radicals.

The ADLH structures are created by a direct addition of one PAH radical to either another PAH radical or a non-radical PAH, usually followed by an H-dissociation, or occasionally by a C_2H-dissociation. A general representation of the common reaction pathway is depicted in Figure 42, where the ADLH structure is highlighted in red. In some cases, an addition to a PAH with a sidechain at the position of the sidechain could be observed. However, this pathway is far less common due to steric hindrance.

Under the conditions investigated, the most commonly encountered reaction pathways for AALH structures are twofold. The pathway is either initiated by the addition of a PAH radical to the sidechain of another PAH or a direct addition of a PAH radical to another PAH followed by a ring opening, hence leading to an aliphatic link between the two aromatic sheets. Since the presence of PAH with aliphatic side chains in the initial compositions is less marked, the ring openings of ADLH structures are more frequently observed than direct addition to the aliphatic side chain of another PAH. For this reason, one of the aromatic moieties of the AALH structures consists of fewer than 4 rings. A general schematic representation of the two pathways observed is depicted in Figure 42, where the AALH structure is highlighted in green.

The unstable AALH structures further evolve into APPH structures through rearrangement, leading to ring closure and the production of one pericondensed plane. Ring opening and rearrangement reactions have been known to play a role in the growth and stabilization on graphene and PAH surfaces.(114,319) For a better understanding a general diagram of the growth pathways of APPH structures is depicted in Figure 42, in which the APPH structure is highlighted in blue. In principle, a direct transition from an ADLH structure to an APPH structure is also possible in some cases. This was also observed during the simulations. This reaction was less frequent, however, compared to the route through a ring opening leading to an AALH structure first.

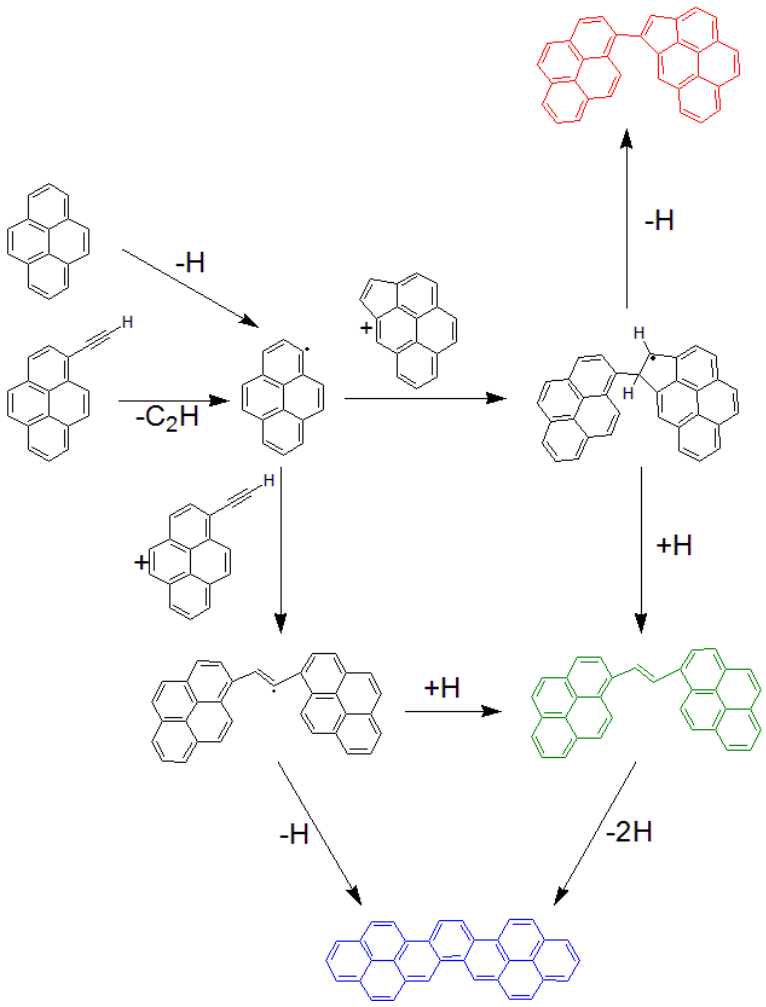

Figure 42. A schematic depiction of the most representative reaction pathways for the three structural groups found. The product for each structural group is highlighted in color. In order to help comprehension only forward reactions are shown.

As shown in Figure 26 the range of molecular masses is broad, ranging from 264 to 627 g/mol. Hence, also the growth through smaller species would have to take place and was observed during the simulations. These species were generated by the dissociation of small, aliphatic species from PAH that either already possesses a side chain or where the side chain is formed after a ring opening. The latter route also leads to smaller-sized radicals and resonance-stabilized radicals. These species influence the growth by the addition to PAH leading to growth products of different structures and masses. Figure 42 hence generalizes the most common reaction pathways. It is also

important to note that each reaction is in principle reversible in the molecular dynamics simulations, but they are depicted only as forward reaction for better comprehension in Figure 42. Therefore, a ring opening can be followed by a ring closure or a dissociation reaction by recombination and vice versa. Furthermore, it was found that H-migration plays a significant role in the bond formation process. Rapid migrations of hydrogen atoms on the PAH and assisted ring opening and rearrangement reactions could be observed. This finding is consistent with earlier findings of Frenklach et al.(320) who observed that similar migration reactions also assist the growth of PAH through addition of smaller species.

6.7. Conclusions

In this chapter the generation of growth structures through bond formation between PAH modeled with ReaxFF has been discussed. ReaxFF has proven to be a valuable approach to model soot formation.(66,125–127,131,132,147,148) By linking the molecular composition of the ReaxFF calculations to simulation conditions in Chemkin we here present an approach to link the formation of incipient soot structures and their structural differences to the combustion conditions.

We first presented the simulation details that have been derived from the evaluation of the ReaxFF approach in chapter 4 and the fashion in which the reaction products are detected as growth structures from bond formation between PAH. In consequence the results of the modeling of bond formation between the generated soot precursor pools and discussed the impact certain species have on the process of bond formation. Especially two species have shown to aid bond formation between PAH. That is PAH possessing a sidechain and PAH radicals. These two species have shown to be consumed the fastest during the simulations indicating their reactivity. The reason for this increased reactivity is the additional reaction sides that are sterically less hindered due to the

sidechain in PAH possessing sidechains, and the radical character leading to an overall higher reactivity in the PAH radicals.

Another conclusion drawn from the analysis of the reactivity of species during the ReaxFF calculations is, that the reactivity of species decreases with increasing molecular size. This effect could be explained by the decreasing ratio of reactive sites to non-reactive sites with growing size of species.

Analysis of the molecular weight of the detected species showed peaks indicating an increased number of species for certain molecular weights separated by 24 – 26 a.m.u.. This spacing between molecules found in the soot inception zone is also detected in mass spectra experiments. In the presented study, this result is, on the one hand, due to the PAH in the generated soot precursor pools being separated by a certain molecular weight, and hence the product of a reaction of two of those PAH is limited to certain molecular weights. On the other hand, this is a product of the PAH fragmentation following to some extent the stabilomer grid, that is the fragmentation of one PAH usually gives a small aliphatic radical and the next smallest PAH radical on the stabilomer grid.

In addition to weight analysis of the products of bond formation between PAH their ratio of hydrogen to carbon atoms was investigated. It was found that with increasing number of carbon atoms this ratio rises and most products found have a H/C-ratio larger than 0.5. This result corresponds well to experimental results of molecules found in the soot inception zone. Furthermore, the size, that is the number of rings, and structural features present in the detected structures, that is odd numbered rings, aliphatic sidechains and aliphatic links, compare well to experiments. The results for the properties of the detected structures and the comparison to experiment reassures the presented approach.

We also could show that the soot precursor pool composition, which is influenced by the variation of the temperature, the equivalence ratio and the fuel mixture in the Chemkin calculations, has an influence on the detected structures in the ReaxFF calculations. It was found that the number of detected structures increases for the soot precursor pools generated at higher temperatures with Chemkin. This is due to higher diversity of the soot precursor pools and an increased amount of acetylenated pyrene and pyrene radicals.

Analysis of structural differences of the generated species gave that all structures could be assigned to one of three structural groups. These are aromatic directly linked hydrocarbons, aromatic pericondensed polycyclic hydrocarbons and aromatic aliphatically linked hydrocarbons. While the change in soot precursor pool due to temperature and equivalence ratio change in the Chemkin calculations did not show any tendency for structurally different species, increasing aliphatic content in the fuel mixture taken for the Chemkin calculations resulted in an increase in aromatic aliphatically linked hydrocarbon structures detected at the end of the ReaxFF calculations. These aliphatically linked species have been found in the soot inception zone and are believed to aid soot inception.(301)

In addition, also an effect of the fuel mixture taken as input for the Chemkin calculations on the occurrence of sidechains in the species detected at the end of the ReaxFF calculations was found. Soot precursor pools generated from fuel mixtures with elevated aliphatic fuel content produced more species with sidechains than those for aromatic fuels. Comparison to experiment showed again that this effect can be found during combustion reassuring the presented coupled Chemkin ReaxFF approach.(202,316,318) Other studies have found that these species including sidechains aid the soot inception (159) and in the presented study it was found that sidechains lead to increased

reactivity of soot precursors, making bond formation between PAH more likely and in turn leads to increased soot inception.

In addition to an influence of the conditions taken for the Chemkin calculations on the bond formation between PAH and the structural differences, certain main reaction pathways for the three presented structural group were identified. The reaction pathway analysis showed that radical formation by hydrogen dissociation from PAH is usually the first step to occur during the bond formation between soot precursor. Moreover, it could be shown that ring opening and rearrangement reactions occur after bond formation between PAH in order to stabilize the reaction product. These reactions have been found to be assisted by rapid hydrogen migration reactions.

Due to the above-mentioned reasons the approach of coupling the macroscopic reaction kinetics approach with reactive molecular dynamics proved that structures could be generated that correspond well to experimental results. In turn that strengthens the point, that bond formation between larger aromatics need to be taken into account during the soot inception process. Furthermore, the correlation of structural differences of the generated nascent soot species appears to be interesting and compare well to experimental findings. Hence reassuring that the presented multiscale approach can aid to achieve a better understanding on how conditions under which soot is formed influence its structural features.

7. Impact of Oxidation on the Nascent Soot Structures

7.1. Introduction

As described in chapter 1.4, soot oxidation is also a process that is influenced by the soot nanostructure.(79) Experiments have shown that during oxidation soot structures are changing due to the oxidation process.(54,55,81,321) Most experiments performed on the soot oxidation process are accomplished by thermogravimetric analysis or two-stage burners, and hence deal with fully-grown soot particles, that already underwent process of coagulation and further soot growth. Therefore only the impact of O_2 and OH radicals is considered for the oxidation process of soot particles as these are relevant oxidizers on the flame edge and in non-combusting conditions.(18,198–200,206,322)

In this chapter the influence of different oxidizers on the structural differences of the molecules generated in chapter 5 is investigated. Since these species cannot be considered as fully-grown soot particles but must be seen as nascent soot structures at most, oxidation by O_2 is not investigated. The reason for this is that the generated molecules are considered to occur during combustion of rich fuel mixtures due to the set of parameters tested. Under these conditions the concentration of molecular oxygen is very low. This is coherent with the analysis of the Chemkin calculations, which showed that at the point of extraction of the soot precursor pools little to no molecular oxygen was present in the calculations. That is due to consumption of molecular oxygen by oxidation of the fuel. As a result, other oxygen containing species are present during combustion, however.

In the last decades the understanding of flame chemistry has been evolved from an empirical, phenomenological description to quantitative modeling of chemical processes.(13) Consequently

there are several mechanisms proposed for the oxidation pathways of aromatic structures at combustion conditions.(36,197,323,324) Description of these processes and determination of reaction rates and species involved are calculated with ab initio methods and compared to experiments. Also ReaxFF has been proven to be a valuable tool to investigate oxidation pathways during combustion of hydrocarbons.(124,130,217,278,296)

The impact of oxidation on the soot formation process has also been investigated.(40,51,54,55,205,315) An influence of oxygenated fuels on the soot formation has been shown experimentally.(27,253,325–328) Furthermore, the nanostructure, which is influenced by the conditions under which the soot has formed, shows to have a significant impact on the oxidation kinetics.(19,54,55,79,202) In addition, the oxidation of aromatic structures or insertion of oxygen into the aromatic structures during soot inception can play a role and has been reported to assist the soot inception process.(145)

As the soot inception process in chapter 5 has been investigated for pyrolytic conditions, in this chapter the interaction of the generated nascent soot structures in chapter 5 is investigated for four different oxidizers with ReaxFF in order to test a possible impact on the soot structures. The main goal is to study the difference in chemical reactivity and kinetics for different oxidizers with respect to the different soot precursors structures.

First the influence of the different structural groups, as well as the presence of sidechains in the detected nascent soot structures are investigated. In order to do so, the oxidation reactions of each species are simulated for four different oxidizer radicals. These oxidizer species are atomic oxygen, hydroxyl, hydroperoxyl and methoxyl radicals. These oxidizers have been selected as they occur during combustion in the gas phase as products of oxidation of fuel by molecular oxygen.(89,96,329) The formation of oxidation products and the respective reaction pathways are

investigated and differences between different structural groups identified. Following the reaction pathway analysis, the kinetics of the reactions of atomic oxygen with the different species are attempted to be unraveled. In order to do so two approaches are presented. The first being a generalization of the structures for each species, investigating if the kinetics of the oxidation process by atomic oxygen can be unraveled using the ChemTrayZer package.(330) The second is a graphical analysis of the consumption of atomic oxygen during the simulations and determination of kinetic constants and activation energies by fitting the decay. (330)

7.2. Details on the Methodology of the ReaxFF Calculations to Model Oxidation of the Nascent Soot Structures generated with the Multiscale Approach

In order to model oxidation in dependence on the structural differences of the soot structures generated in Chapter 5, the structures have been separated into six individual groups. The three classes presented in chapter 6.5 and for each class separation of species with and without sidechains. Hence the groups are aromatic directly linked hydrocarbons without sidechains, aromatic directly linked hydrocarbons with sidechains, aromatic pericondensed polycyclic hydrocarbons without sidechains, aromatic pericondensed polycyclic hydrocarbons with sidechains, aromatic aliphatically linked hydrocarbons without sidechains, and aromatic aliphatically linked hydrocarbons with sidechains. As oxidizers four different oxygen containing radicals have been chosen, that being the atomic oxygen, the hydroxyl radical, the hydroperoxyl radical and the methoxy radical.

The number of molecules is 84 for the ADLH with sidechains, 62 for ADLH without sidechains, 79 for APPH without sidechains, 66 for APPH with sidechains, 82 for AALH without sidechains, and 76 for AALH with sidechains. Hence the number of molecules for each group varies. Furthermore, the number of oxidizer radicals has been kept constant to 100 molecules per

simulation. This choice of relatively low oxidizer concentrations is taken, since the interaction of oxidizers with the generated molecules is investigated. Thus, recombination of oxidizers is unwanted and hence the concentration of oxidizers is kept artificially low. The amount of oxygen with respect to the number of carbon atoms found in the simulation boxes is still high for all compositions, however. The ratio of carbon to oxygen radicals is 29 for the ADLH with sidechains, 19 for ADLH without sidechains, 24 for APPH without sidechains, 21 for APPH with sidechains, 29 for AALH without sidechains, and 25 for AALH with sidechains. Consequently, the change of carbon atoms, as a result of the change in the number of soot structures, for each group is deemed to be negligible with regard to the reaction pathways since the oxygen concentration is low compared to the carbon concentration.

The systems have then been run for 500ps for the OH, OOH and methoxy radicals, and 50ps for the oxygen radical due to the faster dynamics in comparison to the other oxidizer species, at a temperature of 2500K and a timestep of 0.1 fs in an NVT ensemble with a Nosé-Hoover thermostat and a damping constant of 100fs using the SCM ADF modeling suite.(305) The systems have been geometry optimized with the ReaxFF force field and equilibrated for 10000 iterations at the respective temperature with the bond orders kept constant between atoms. To first test the interactions of these oxidizer species with the soot structures, all structures of one group and 100 oxidizer molecules have been put into a simulation box with a total density of 0.1 g/cm^3.

The high density and temperatures have been employed to accelerate the dynamics and the collision rate, in order to increase the reactivity as described in chapter 5.5. This artificial speed up has been tested for lower temperatures and densities and revealed that the general reactions are not influenced, but the occurrence of those are, resulting in less computational expenses while giving similar results.

Table 13. Representative structures chosen for the three main sum formulas detected at the end of the ReaxFF calculations on bond formation between soot precursors.

Group	Sum Formula	$C_{30}H_{16}$	$C_{32}H_{18}$	$C_{34}H_{18}$
ADLH	Without Sidechain	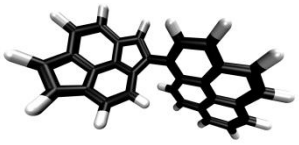	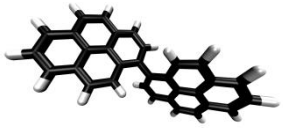	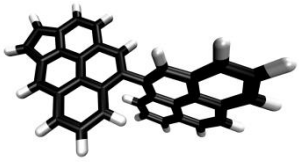
	With Sidechain	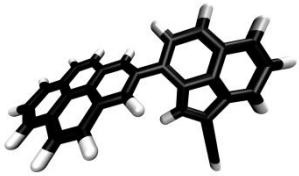	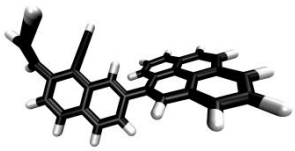	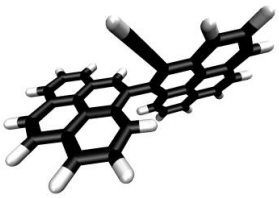
APPH	Without Sidechain	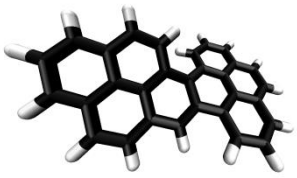	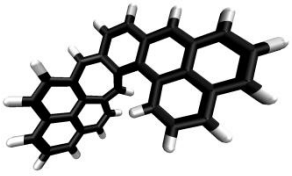	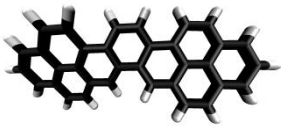
	With Sidechain	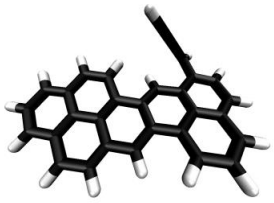	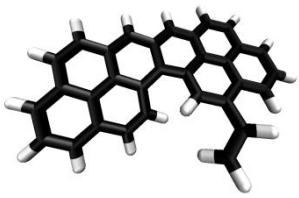	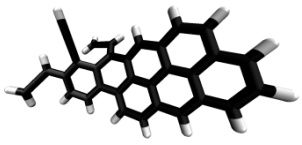
AALH	Without Sidechain	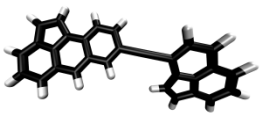	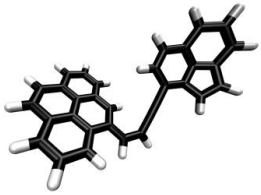	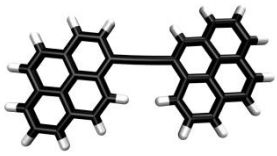
	With Sidechain	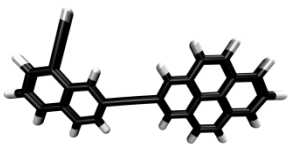	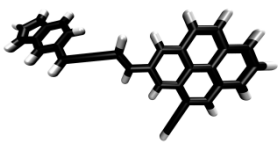	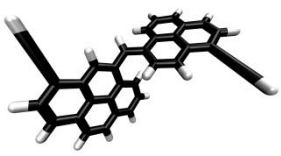

To investigate the oxidation kinetics by atomic oxygen or hydroxyl for the representative structures for each group, three structures have been chosen with a molecular weight equal to the main peaks in Figure 26. This has been done in order to correct the slight variations of molecule numbers for each group. Table 13 shows the selected structures for each group.

Three simulations for each of the three structures have been performed. The systems have then been run for 150 ps for the OH, and 50ps for the oxygen radical in an NVT ensemble and a timestep of 0.1 fs using the SCM ADF modeling suite.(305) The simulated temperatures are 1500 K, 1665 K , 1874 K, 2145 K, and 2500K with a Nosé-Hoover thermostat and a damping constant of 100fs. Box sizes have been chosen to give a total density of 0.1 g/cm$^{3.}$ Furthermore, as with the prior simulations, all systems have been geometry optimized and equilibrated for 10000 iterations at the respective temperature.

7.3 Results and Discussion

In this chapter the results of the calculations with the aromatics hydrocarbons are presented. First the reactions of the four different oxidizers are discussed, by showing the consumption of the oxidizers, the main reaction products and highlighting the most common reaction pathways. Secondly, the kinetics of the consumption of the atomic oxygen and the hydroxyl radicals is investigated by fitting.

7.3.1. Investigation of the Main Reaction Pathways of Oxidation by Atomic Oxygen

Atomic oxygen is known to be a strong oxidizer which occurs in the gas phase during combustion due to dissociation of molecular oxygen.(329) The reaction pathways of atomic oxygen with aromatic molecules have been studied multiple times.(331–337) Due to its high reactivity, atomic oxygen is prone to attack on the aromatic ring. The chemisorbed oxygen can then oxidize

the aromatic ring in several ways. In smaller aromatics this leads to a fragmentation of the aromatic ring.(338) Also insertion of atomic oxygen into the aromatic ring has been found to be possible. Recently Frenklach et al. found that the oxidation of aromatic 6-membered rings creates 5-membered ring structures on the edge of aromatic planes. Since these 5-ring structures are more robust to oxidation by molecular oxygen or hydroxyl the oxidation behavior of the soot changes. Frenklach et al. argue that the most effective oxidizer for these embedded five-membered rings is atomic oxygen, hence stressing its importance in the oxidation of soot oxidation.(224)

For the simulations of the nascent soot structures with atomic oxygen the relevant oxidation species are depicted in Figure 43 for all structurally different species. It is observed that the oxygen radicals are consumed rapidly. The main species found at the end of the calculation are oxygenated hydrocarbons, i.e., PAH containing oxygen due to bond formation, and carbon monoxide. The latter is produced in a multi-step reaction through oxidation of the PAHs with atomic oxygen. The atomic oxygen first adds to one of the hydrocarbons, forming an oxygenated species, and through several rearrangement pathways carbon monoxide is ejected, and the initial hydrocarbon molecule is oxidized. This is indirectly visible in Figure 43, where first the decline of oxygen radicals in the box is ensued by a fast rise in oxygenated species. This rise starts decreasing with a rise in carbon monoxide, hinting at the transformation of oxygenated hydrocarbons to carbon monoxide and an oxidized hydrocarbon.

The consumption of atomic oxygen is similar for all the structural different species. Only the speed of consumption is slightly different for species with and without sidechains. This is shown in Table 14 where the halftimes for the consumption of atomic oxygen is given, i.e., the time point at which half of the oxygen radicals are consumed.

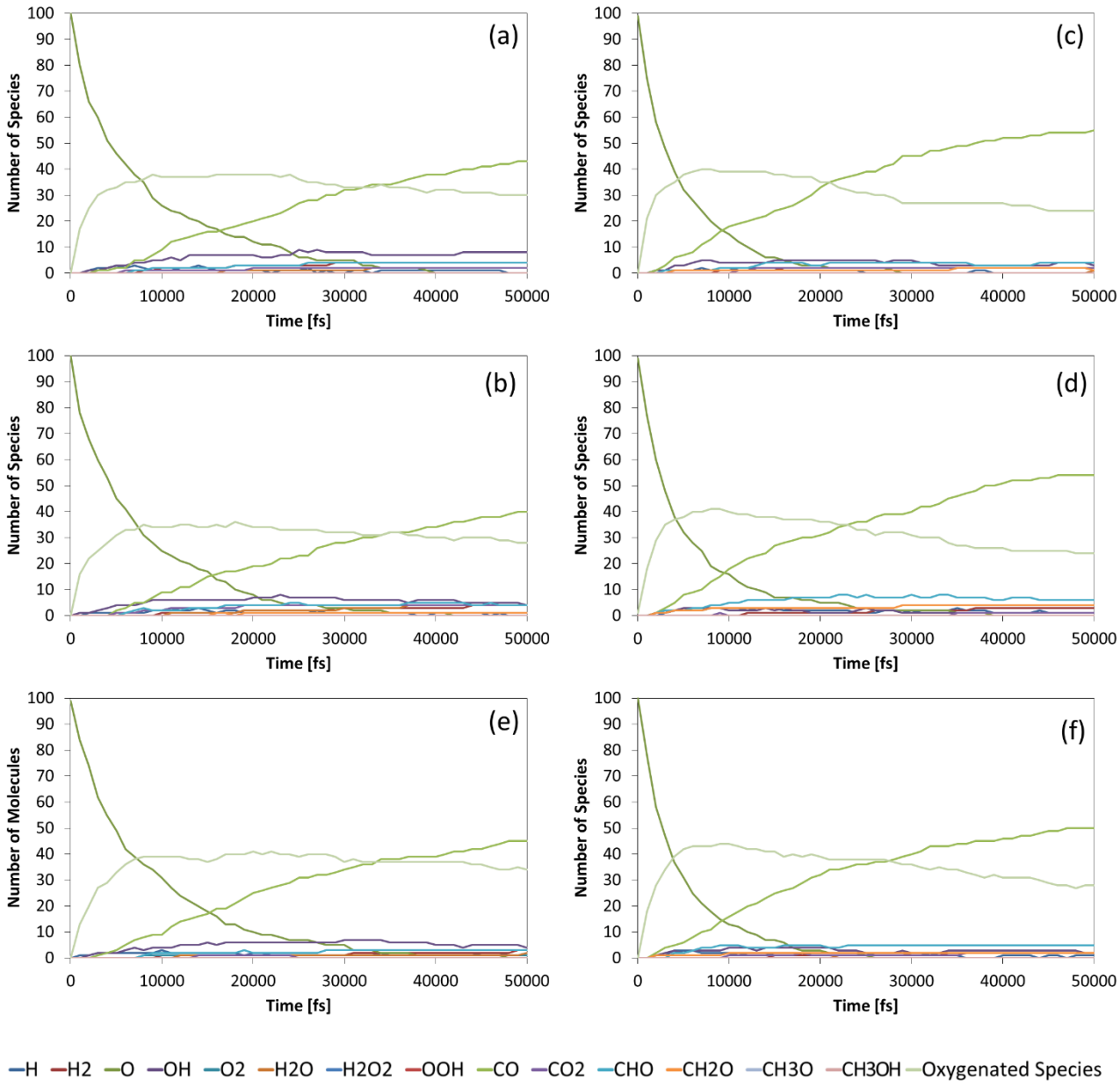

Figure 43. Number of oxygen containing molecules over time for the reactions of the nascent soot structures and atomic oxygen. The results have been averaged over the three calculations performed at each condition. The corresponding calculations contain 100 atomic oxygen radicals and (a) all ADLH species without sidechains, (b) all ADLH species with sidechains, (c) all APPH species without sidechains, (d) all APPH species with sidechains, (e) all AALH species without sidechains and (f) all AALH species with sidechains.

Table 14. Computed halftimes for the consumption of atomic oxygen.

Species	ADLH without Sidechains	APPH without Sidechains	AALH without Sidechains	ADLH with Sidechains	APPH with Sidechains	AALH with Sidechains
Halftime(O)[fs]	5520	6560	6121	4148	2952	2781

One finds that the halftime for the cases in which the nascent soot structures possess a sidechain are shorter than for the cases when the soot structures do not possess a sidechain. The halftimes for all the structures are rather short, however. This is due to the high reactivity of the atomic oxygen.

In all cases the decline of atomic oxygen coincides with a steep rise of oxygenated hydrocarbons, indicating a fast addition of the atomic oxygen. This trend is the same for all investigated structures. The only change in reactivity due to structural differences is that species with sidechains show a faster decline of the oxygen radical, and a steeper decline of the oxygenated hydrocarbons at longer simulation times. As a result, the amount of carbon monoxide formed for the simulations of the species containing sidechains is higher compared to the species containing no sidechains. This difference in the speed is a result of the better accessibility of the sidechains. Due to this an oxygen addition on a sidechain occurs more rapidly.

The most frequent detected reaction pathway for the oxidation of a sidechain by atomic oxygen is depicted in Figure 44. It is to note that due to the mostly unsaturated nature of the sidechains the depicted reactions are postulated for unsaturated sidechains. The oxidation of saturated sidechains probably follows a different route. In the depiction of the reaction pathways the sidechain is assumed to be an ethylene sidechain, since it is the most prominent sidechain found.

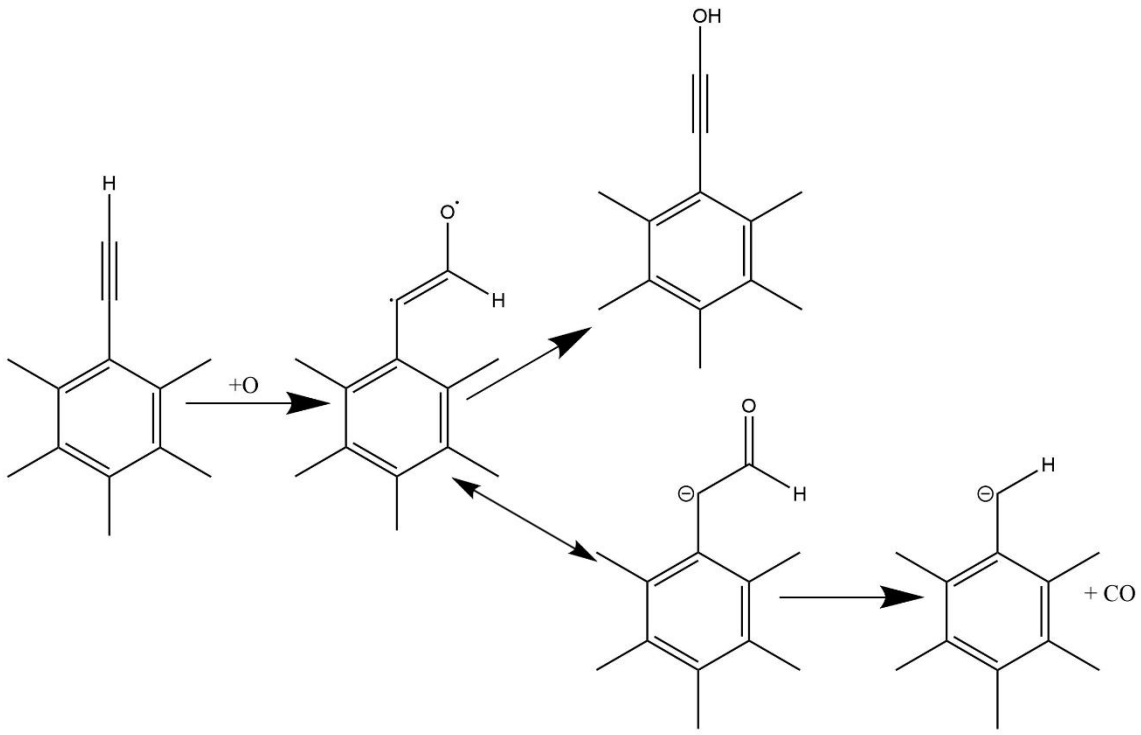

Figure 44. Detected reaction pathways for the addition of atomic oxygen to terminal sidechain carbon.

It was found that the addition of oxygen is usually followed by a hydrogen migration. Hydrogen abstraction by atomic oxygen on a sidechain was rarely found, on the other hand. The migration of the hydrogen leads to the formation of either a ketone group or an alcohol group. Due to the radical character after oxygen addition a bond rupture between the two carbon atoms occurs and carbon monoxide is emitted. The remaining hydrocarbon retains radical character. The radical is delocalized by the aromatic plane, however.

In the case of an attack of oxygen on a non-terminal carbon atom in a side chain, also larger carbonyl radicals can be emitted via oxidation of the hydrocarbon structures possessing sidechains. These are not explicitly tracked and hence do not show in Figure 43 but are grouped with the oxygenated hydrocarbon species.

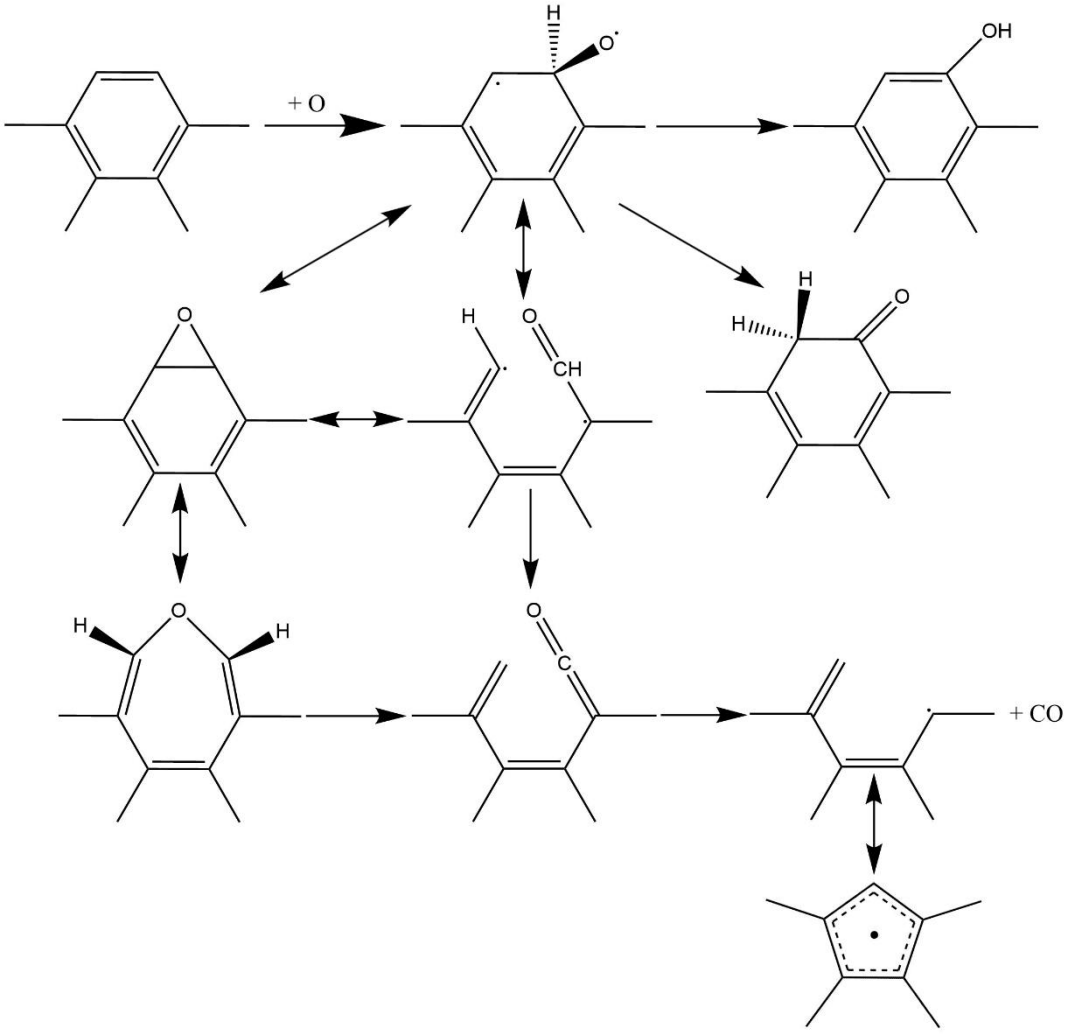

Figure 45. Detected reaction pathways for the addition of atomic oxygen to free edge sites of aromatic hydrocarbons.

The reaction pathways for the oxidation of carbon atoms in the aromatic plane are given in Figures 45 and 46. After addition of the oxygen radical on the aromatic carbon a number of reactions may occur. One is the formation of an alcohol group resulting in the insertion of the oxygen radical. This alcohol group is in most cases stable as it has lost all radical character. The formation of a carbonyl group is also possible. The formation of the carbonyl sometimes results in a bond rupture between the α- and β-carbon. Additionally, a hydrogen migration from the α- to β-carbon could be observed in some cases. The formation of the carbonyl can then either lead to the

fragmentation of the aromatic ring aided by hydrogen migration or stabilization of the carbonyl by hydrogen dissociation. A fragmentation of the ring can then result in the ejection of carbon monoxide, this is in some cases followed by formation of an aromatic 5-ring by bond formation between the ruptured part of the ring and the β'-carbon. Furthermore, an insertion of the oxygen radical into the aromatic ring could be observed.

One also finds that some amount of hydroxyl radicals is formed for species without sidechains, as a result of hydrogen abstraction from the hydrocarbons. The observed difference for this hydrogen abstraction between species with and without sidechains indicates the lower energetic barrier of the atomic oxygen addition to the sidechains, compared to the addition of an aromatic reaction site.

Hence it is evident that the reactivity of sidechains is different from those of aromatic planes. Furthermore, stabilization of radical character due to the aromatic plane after oxidation seems to play an important role. The detected reaction pathways are in good agreement with *ab initio* studies and other proposed reaction pathways found in literature.(331,332,335,339,340)

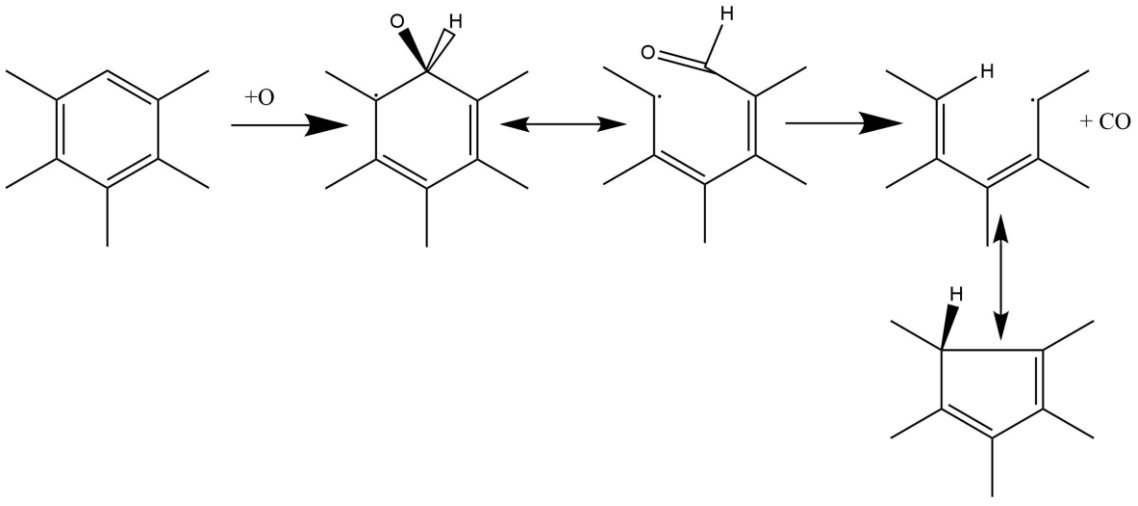

Figure 46. Detected reaction pathways for the addition of atomic oxygen to zigzag sites of aromatic hydrocarbons.

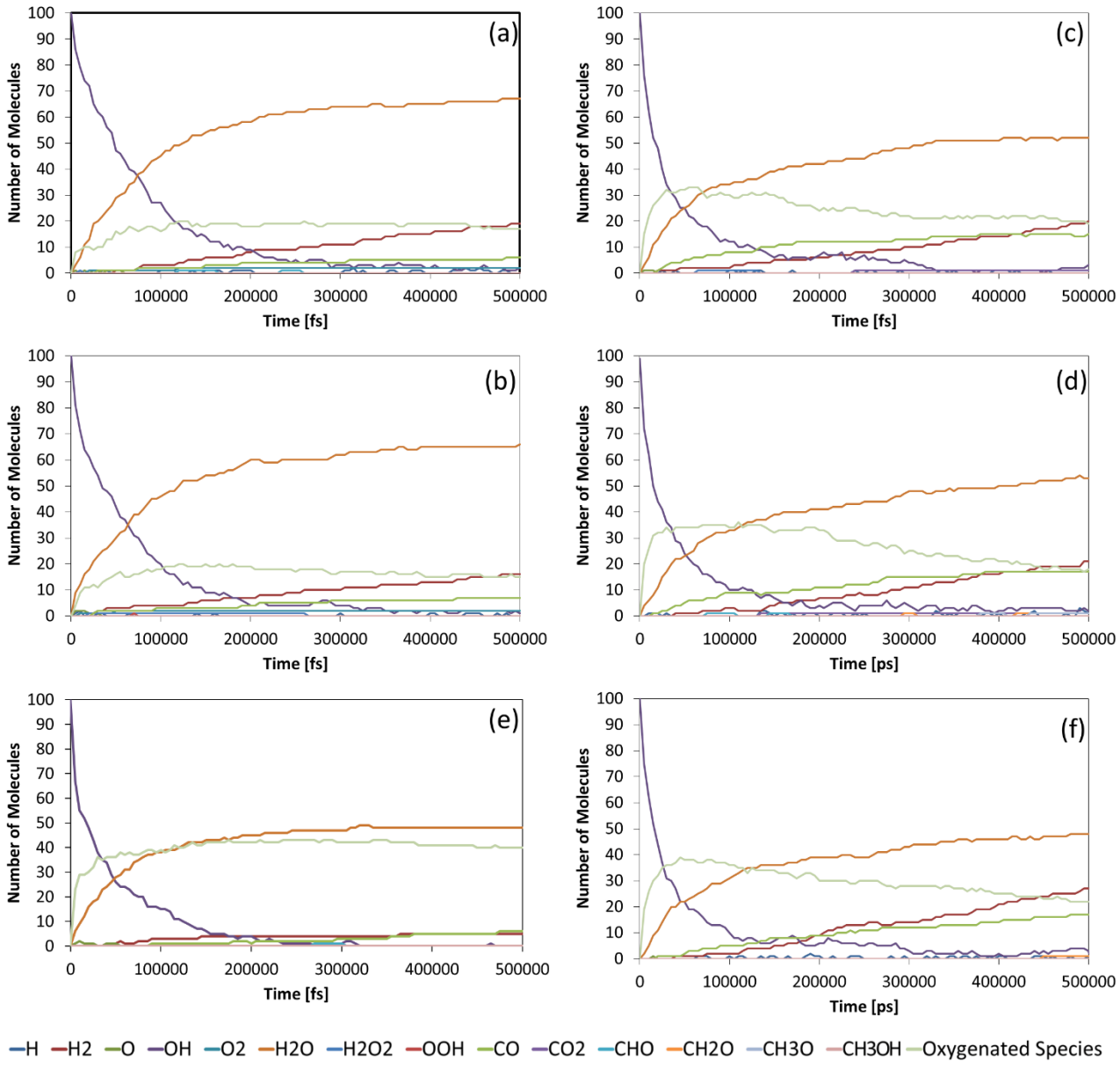

Figure 47. Number of oxygen containing molecules over time for the reactions of the nascent soot structures and hydroxyl radicals. The results have been averaged over the three calculations performed at each condition. The corresponding calculations contain 100 hydroxyl radicals and (a) all ADLH species without sidechains, (b) all ADLH species with sidechains, (c) all APPH species without sidechains, (d) all APPH species with sidechains, (e) all AALH species without sidechains and (f) all AALH species with sidechains.

7.3.2. Investigation of the Main Reaction Pathways of Oxidation by Hydroxyl Radicals

The hydroxyl radical is known to be a potent oxidizer of soot structures.(198,199,274,323) Due to the also high reactivity in most macroscopic soot models the limiting reaction step is diffusion. The activation energy of the reaction of oxidation by hydroxyl is assumed to be negligible.(198) In Figure 47 again the amount of oxidation species is plotted over time. One can see that the interactions of OH with the nascent soot structures is inherently different by comparing Figures 43 and 47. The hydroxyl radical produces water as the main oxidation product in all cases by abstraction of hydrogen from one of the hydrocarbons. The difference in reactivity due to different structural features is comparable to the trends found for the reactivity of atomic oxygen. That is, while the ADLH and APPH structures without sidechains show similar consumption of hydroxyl radicals and production of oxygenated species, all species possessing sidechains show a different behavior. AALH structures without additional sidechains show a production of oxidation products that is not comparable to any of the other structures.

It is also to note that the hydroxyl radical shows a decrease in reactivity compared to the atomic oxygen radicals. This is shown in Table 15, which gives the halftimes of the consumption of hydroxyl radicals during the calculation. By comparison with Table 14 it is evident that the hydroxyl radical has a much longer halftimes hence denoting that the atomic oxygen radicals have a higher tendency to react.

Table 15. Computed halftimes for the consumption of hydroxyl radicals.

Species	ADLH without Sidechains	APPH without Sidechains	AALH without Sidechains	ADLH with Sidechains	APPH with Sidechains	AALH with Sidechains
Halftime(OH)[fs]	62836	54345	36736	15871	15098	14542

For the investigation of the main reaction pathways the differentiation of structures with sidechains and structures without sidechains holds. For the structures without sidechains the main oxidation product is water as a result of hydrogen abstraction by one hydroxyl radical from a hydrocarbon, like said before. Nonetheless, the addition of hydroxyl radicals to the soot structures is observed as well, as concluded from the increasing concentration of oxygenated hydrocarbons in time. This addition reaction results in the formation of molecular hydrogen, as can be seen in Figure 47, as the formation of molecular hydrogen coincides with the formation of oxygenated hydrocarbons. This is a result of the transformation of the added hydroxyl, giving an alcohol group, to a carbonyl group on the aromatic hydrocarbon by dissociation of the hydrogen on the oxygen atom and the hydrogen on the α-carbon, giving molecular hydrogen. After the dissociation of the molecular hydrogen the radical remains on the hydrocarbon and is resonantly stabilized by the aromatic plane.

Only small amounts of carbon monoxide are formed for the structures without sidechains. The reaction pathway follows the reaction pathway for the production of carbon monoxide with terminal sidechain carbons, but for the addition of hydroxyl to the terminal sidechain carbon the transfer of the hydrogen on the hydroxyl precedes the dissociation of carbon monoxide. This hydrogen transfer occurs either to the β-carbon, or by reaction with another radical in the gas phase.

The decline of the hydroxyl radical concentration is again faster for the species containing sidechains as shown in Table 15. Furthermore, the formation of oxygenated hydrocarbons is faster, indicating that addition of hydroxyl radicals to hydrocarbons occurs more rapidly for the species containing sidechains. Moreover, this faster addition of hydroxyl to hydrocarbons results in a more pronounced formation of carbon monoxide for the species containing sidechains over the species that do not, which coincides with the decrease of oxygenated hydrocarbon species. The formation of

carbon monoxide by addition of the hydroxyl radical to the terminal carbon of the sidechain is shown in Figure 48.

Also, addition to non-terminal carbon atoms was found to occur in some cases. In these cases, the reaction pathway is similar to those on aromatic hydrocarbons for the most part, that is a formation of a carbonyl group occurs after addition of the hydroxyl radical and dissociation of molecular hydrogen. In some cases, a breaking of the sidechain was observed, however, leading to an aliphatic hydrocarbon with a carbonyl group.

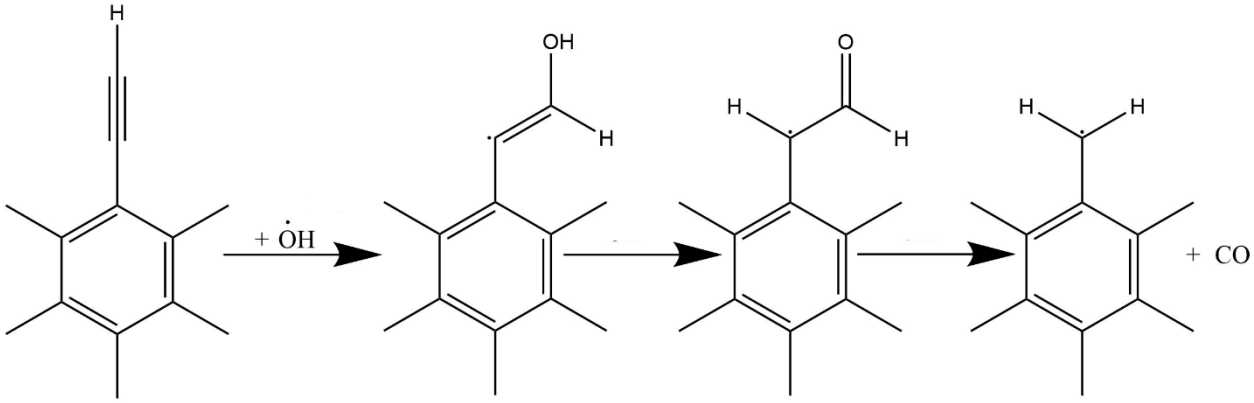

Figure 48. Detected reaction pathway for the addition of hydroxyl radicals to terminal sidechain carbon.

For the AALH structures the oxidation products are significantly different compared to the other structures, as shown in Figure 47. For these species a higher number of oxygenated hydrocarbons are produced compared to the other species that do not possess sidechains. However, a decline of the oxygenated hydrocarbons coinciding with the production of carbon monoxide, like in the structures possessing sidechains, can also not be observed. This is due to the fact that the addition of hydroxyl radicals on the aliphatic link in the AALH structures occurs more easily, like on the sidechains for structures with sidechains. However, since the link has no terminal carbon atom the production of carbon monoxide is hindered. Consequently, also formation of a carbonyl group is

hindered, since the majority of links in the AALH structures are ethyl bridges and as a result do not possess hydrogen atoms on the α-carbon. A small amount of carbon monoxide and molecular hydrogen is produced for the AALH structures, nonetheless. The production of these species follows the same route as for the other species without sidechains for the most part.

7.3.3 Investigation of the Main Reaction Pathways of Oxidation by Hydroperoxyl Radicals

Hydroperoxyl (OOH) radicals can form during combustion by addition of a hydrogen radical to molecular oxygen.(329) Especially the interactions of hydroperoxyl and smaller molecules, like methanol, formaldehyde, and methane, have been investigated for high temperatures.(341–345) But also hydrogen abstraction from aromatics by hydroperoxyl has been reported.(329,346) In this subchapter the interactions of hydroperoxyl radicals with the detected hydrocarbon species in chapter 5 are investigated.

Figure 49 shows a different reactivity than the two previously investigated systems. The main products at the end of the calculations are molecular oxygen and water. This is due to dissociation of the hydroperoxyl radicals. The hydroperoxyl radical quickly detaches a hydrogen atom thereby forming molecular oxygen. The detached hydrogen atom is very reactive and as a result is prone to add to another hydroperoxyl radical, forming hydroperoxide, which in turn dissociates into two hydroxyl radicals. These hydroxyl radicals can further react with another hydroperoxyl radical to give water and molecular oxygen or dissociate a hydrogen from another hydrocarbon to form water. Also, addition of the dissociated hydrogen atoms to hydrocarbon species was observed. These hydrocarbons have not been depicted as a species in Figure 49, since only oxygen containing species are shown.

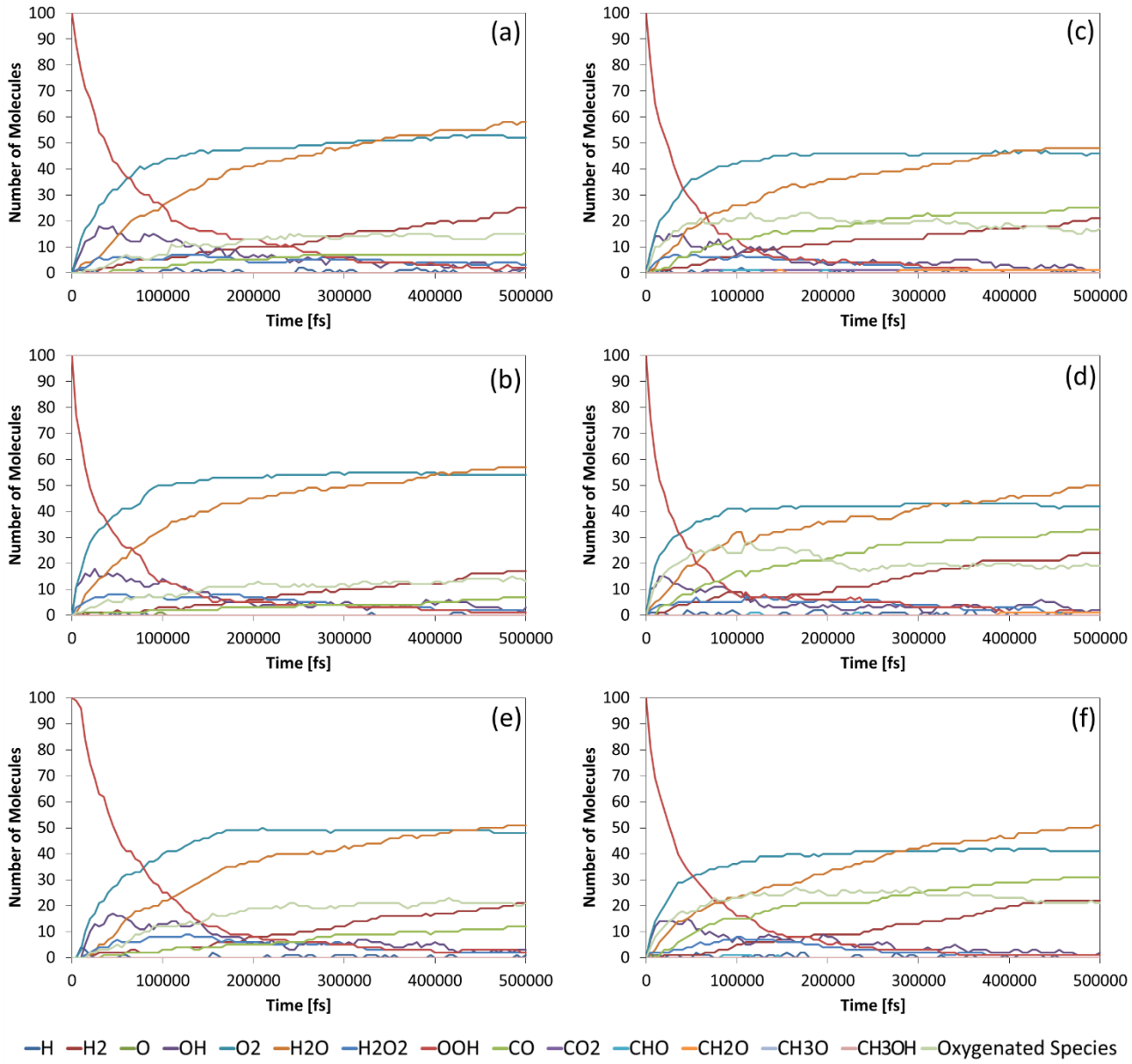

Figure 49. Number of oxygen containing molecules over time for the reactions of the nascent soot structures and hydroperoxyl. The results have been averaged over the three calculations performed at each condition. The corresponding calculations contain 100 hydroperoxyl radicals and (a) all ADLH species without sidechains, (b) all ADLH species with sidechains, (c) all APPH species without sidechains, (d) all APPH species with sidechains, (e) all AALH species without sidechains and (f) all AALH species with sidechains.

Another dissociation reaction that has been observed with the hydroperoxyl radicals is the formation of atomic oxygen and hydroxyl radicals. Even though this dissociation is less favored than the dissociation into molecular oxygen and atomic hydrogen.

The main hydroxyl producing channel is the result from the addition of hydrogen, that has dissociated from another hydroperoxyl radical, to a hydroperoxyl, leading to HOOH, which in turn dissociates into two hydroxyl radicals. This reaction is reflected in Figure 49 as a peak in the amount of the hydroxyl radical in the first 200 ps. Furthermore, water molecules are formed as one of the main products, but at a slower rate than the formation of molecular oxygen. This is mostly attributed to the recombination of hydroxyl with atomic hydrogen or hydrogen abstraction by the hydroxyl radical from one of the hydrocarbons.

The described dissociation reactions of hydroperoxyl radicals in the ReaxFF simulations are the main channels of its consumption. As a result, pathways of oxidation of the hydrocarbon species are similar to those described by atomic oxygen and hydroxyl radicals. The resulting oxygenated hydrocarbons at the end of the simulations can mainly be attributed to the transfer of an oxygen radical from hydroperoxyl, forming an oxygenated hydrocarbon and hydroxyl radical. Further oxidation of hydrocarbons by the produced hydroxyl radicals has also been observed. The oxygen transfer is mainly observed on sidechains, however, and the reaction pathways follow the addition of atomic oxygen on the sidechain. Also, for the hydroxyl radicals the differences observed between species with and without sidechains follow the same reactivity as in the previous section. That is a faster production of oxygenated hydrocarbons and carbon monoxide for species containing sidechains, in the hydroperoxyl radical reactivity simulations.

7.3.4. Investigation of the Main Reaction Pathways of Oxidation by Methoxyl Radicals

Methoxyl radicals are direct products of the O–H bond dissociation from methanol or fragmentation of saturated fuel molecules. Since alcohols and poly(oxymethylene)ethers became interesting as fuel additives in recent years the interest in the oxidative capabilities of these species has gained interest.(253,327,328,345,347–350) Also during combustion methoxyl radicals can be detected in the gas phase.(351) Hence, the interactions of the detected nascent soot species with methoxyl radicals has been investigated and is presented in this section.

The simulations with methoxyl radicals show that the main products formed are formaldehyde and molecular hydrogen, as can be seen in Figure 50. This is, as for the hydroperoxyl calculations, mainly attributed to fragmentation of the methoxyl radicals. A hydrogen atom dissociates from the methoxyl radical producing fromaldehyde. The fact that molecular hydrogen is steadily produced in the simulations supports this finding, as two dissociated hydrogen atoms recombine. Also, hydrogen dissociation from one methoxy radical and subsequent hydrogen addition to another methoxy radical, forming methanol, is observed, as the amount of methanol also rises and plateaus almost at similar times as the number of formaldehyde molecules found in the simulation boxes. This plateau is reached due to further dissociation of formaldehyde, producing formyl radicals and subsequently carbon monoxide. Additionally, a C-O bond breaking can occur, and water is formed by the initial methoxy radical in some cases.

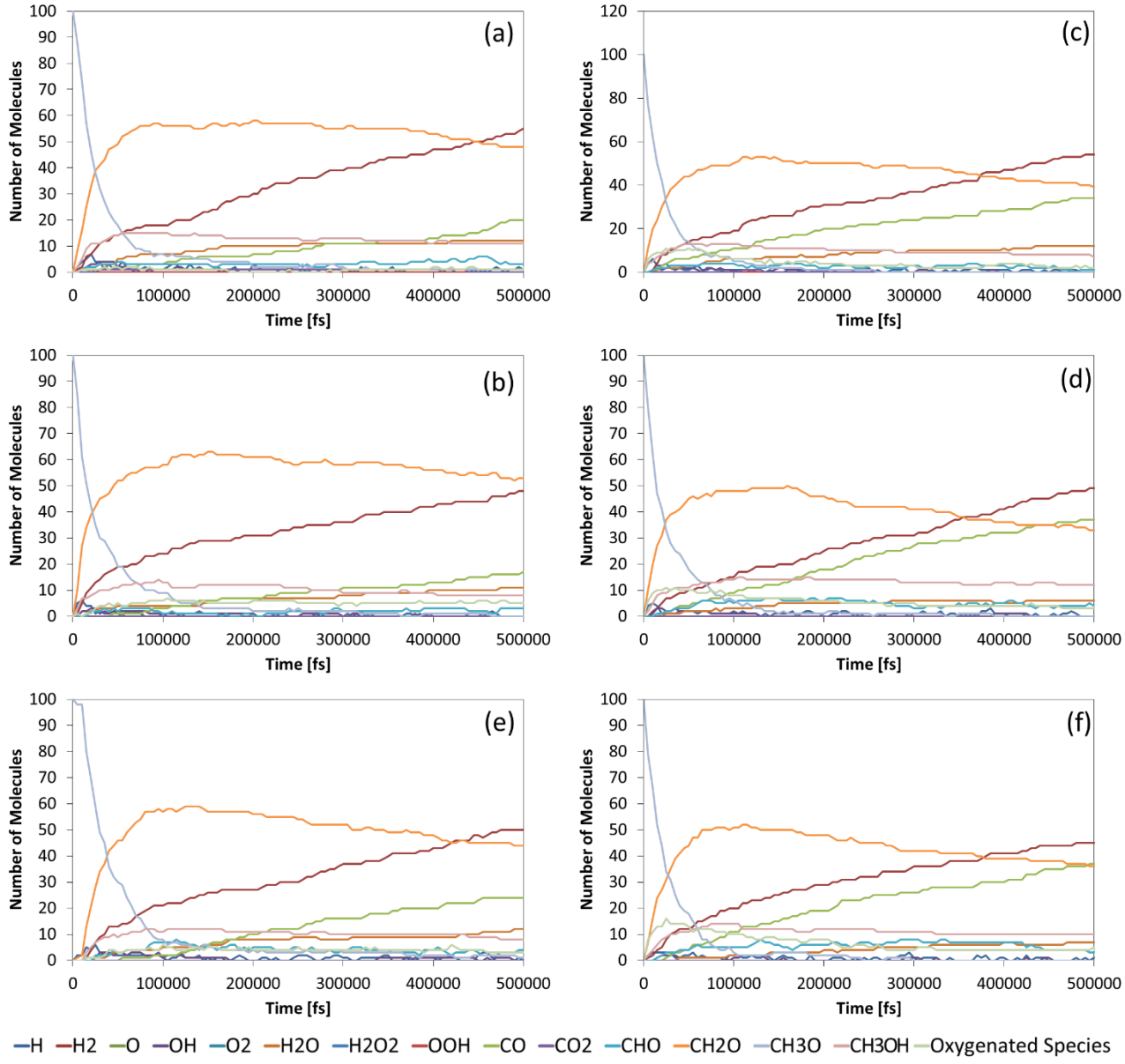

Figure 50. Number of oxygen containing molecules over time for the reactions of the nascent soot structures and methoxyl radicals. The results have been averaged over the three calculations performed at each condition. The corresponding calculations contain 100 methoxyl radicals and (a) all ADLH species without sidechains, (b) all ADLH species with sidechains, (c) all APPH species without sidechains, (d) all APPH species with sidechains, (e) all AALH species without sidechains and (f) all AALH species with sidechains.

Only small differences are observed for species possessing sidechains compared to those that do not. That is a rise of oxygenated hydrocarbons occurs at early simulation times. The amount of these species peaks around 30 fs and then decreases slowly with continuing simulation time. Investigation of this phenomena gave, that addition of methoxyl radicals to the sidechain does occur to some amount. The formed oxygenated sidechain structures are not stable in most cases, however. As the sidechains are, as discussed, of unsaturated nature, the addition of the methoxyl radical leads to a radical on the β-carbon. This incites a transfer of hydrogen from the carbon atom initially belonging to the methoxyl radical, localizing the radical on that carbon atom. Subsequently either a second transfer of hydrogen can occur from the methoxyl α-carbon to the sidechain α-carbon leading to dissociation of formyl, or the bond breakage between the oxygen and the sidechain α-carbon occurs without hydrogen transfer, leading to dissociation of formaldehyde and a radical on the oxidized sidechain. Both reaction pathways are represented in Figure 51.

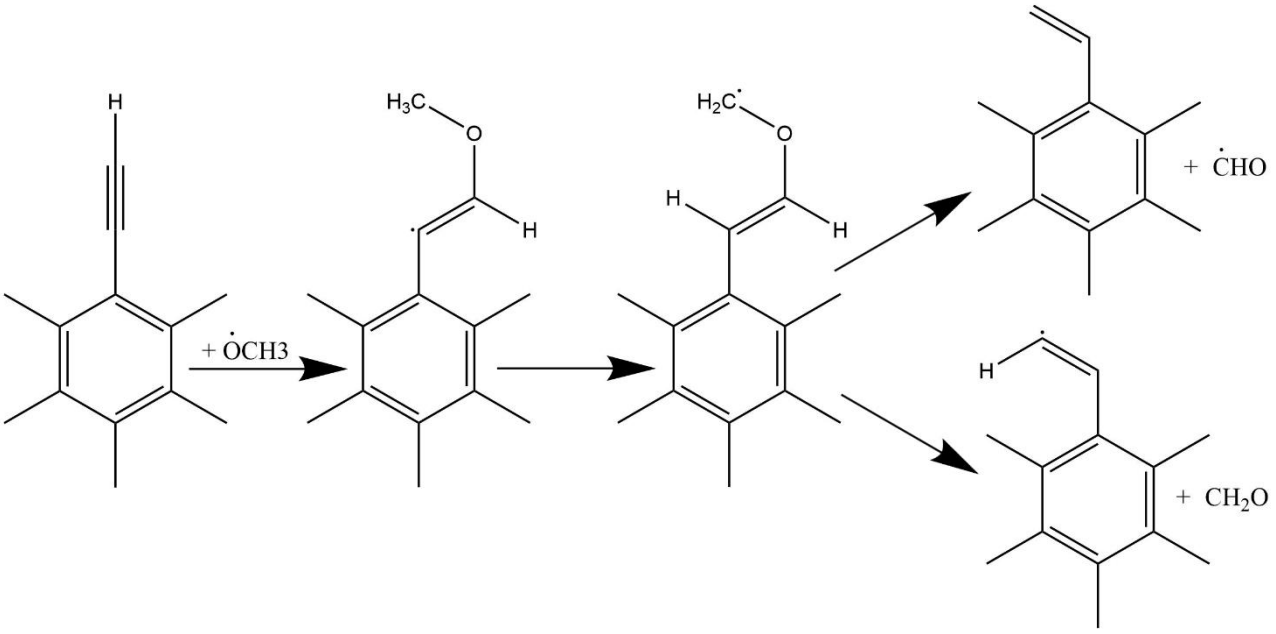

Figure 51. Detected reaction pathways of the addition of methoxyl radicals to a terminal sidechain carbon.

Both pathways lead to a reduction of the unsaturated sidechain. The production of the formyl radical, that subsequently forms carbon monoxide by dissociation of atomic hydrogen, is the reason for the increased amount of carbon monoxide formed for the calculations with species that possess sidechains.

As shown the methoxyl radicals mainly fragment, as was the case for the hydroperoxyl radicals. As a result, the oxidative capabilities of the methoxyl radicals for the investigated hydrocarbons could not be investigated. In fact, instead of the oxidation of the nascent soot structures, it was found that the methoxyl radicals often reduce the unsaturated sidechains.

7.3.5 Investigation of Kinetics of Oxidation by Atomic Oxygen and Hydroxyl Radicals on Representative Nascent Soot Structures

As shown in the previous chapter only two of the four investigated oxidizers lead to a fast oxidation of the tested nascent soot species. To investigate the reactions occurring with atomic oxygen and hydroxyl radicals, their kinetics have been studied further. Due to the limited oxidation capabilities and prominent self-dissociation or thermal-decomposition reactions of hydroperoxyl and methoxy radicals, these species have been deemed not to be sufficiently able to oxidize the hydrocarbons under the chosen conditions.

In order to investigate the kinetics of the oxidation reactions of oxygen and hydroxyl radicals more closely, the simulations presented in Figures 43 and 47 have been repeated with *one* representative structure for each of the 6 groups. This was done in order to normalize the amount of species of each group as presented in section 7.2 the number of different species generated in ReaxFF slightly varies and to aid investigation of reactions using the ChemTrayZer code by Döntgen et al.(330). Analyzation of the previous calculations with ChemTrayZer gave insufficient results for the simulations containing all structures of one group due to the fact that a single reaction

event was never observed twice since all reactants, although very similar in their chemistry, are different in nature. Upon using, *one unique*, but representative molecule for each family, we anticipate that a particular reaction may occur several times as the ChemTrayZer code needs the occurrence of one reaction multiple times, in order to estimate the kinetic constant of the reaction.

However, it has been found that the architecture of the aromatic structure can have an influence on the oxidation behavior.(40,79,80,224) That is in dependence of the neighboring atoms and the connection between atoms in the aromatic plane oxidative capability might change. That is a five-membered ring has other oxidation pathways than six-membered rings or a free edge site shows other pathways than an armchair or zigzag site. To address this the representative structures have been chosen in order to represent a wide range of structural features as can be seen in Table 13.

In order to show that the representative structures give similar kinetics like the simulations with all structures, the halftime of the two oxidizers have been determined and compared between the simulations containing all structures and the simulations containing the representative structures. The results are depicted in Figure 52 and 53 and the comparison shows that the differences are minor, meaning the representative structures are good substitutes for the structures of each group for the kinetic study.

Nonetheless, the investigation of the reactions using the ChemTrayZer code gave insufficient results, since the number of different reaction sites in each of the species is too high and the selectivity of the radicals too low, due to their high reactivity, in order to have a reaction occur multiple times. As a result, calculations of the rate constant using the ChemTrayZer code could not be performed with success.

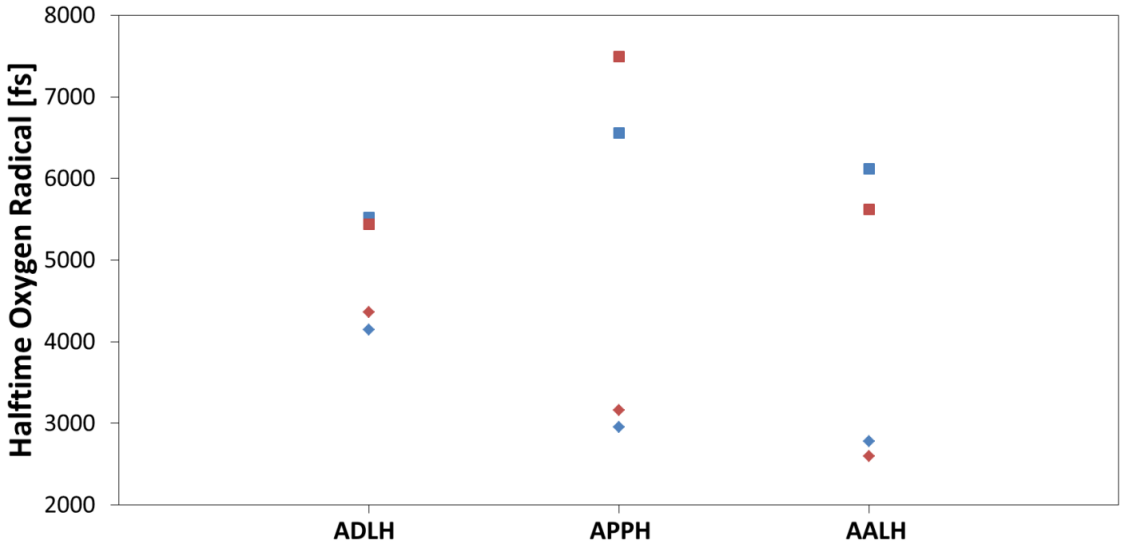

Figure 52. Average halftime of the atomic oxygen radicals for all calculations including all detected structures for one species (red) and the average halftime found for all calculations using representative species (blue), differentiated by species structural features and the species of one structural group with sidechains (diamonds) or without sidechains (square).

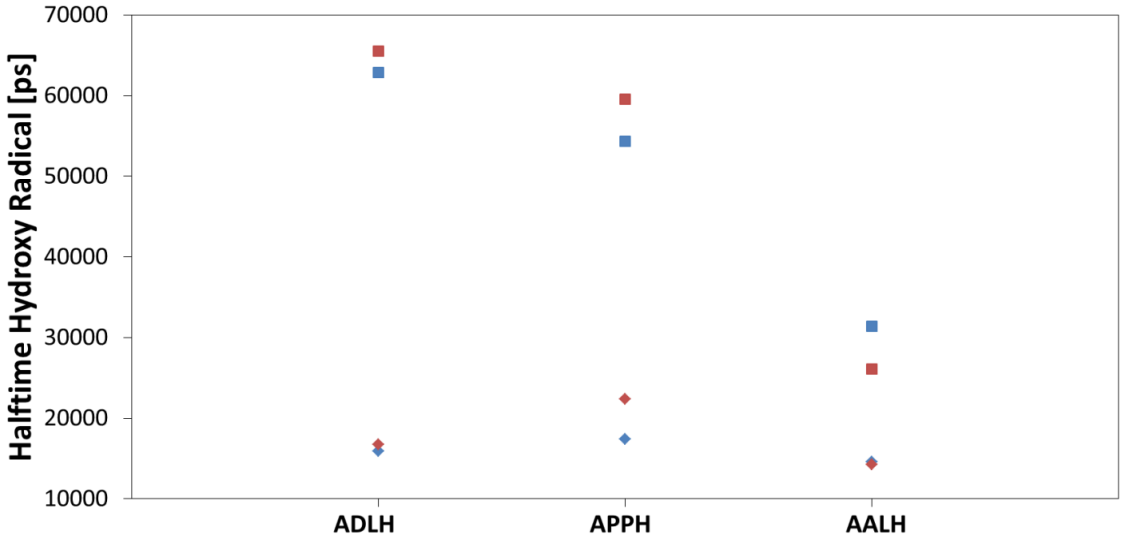

Figure 53. Average halftime of the hydroxyl radicals for all calculations including all detected structures for one species (red) and the average halftime found for all calculations using representative species (blue), differentiated by species structural features and the species of one structural group with sidechains (diamonds) or without sidechains (square).

The first assumption is that all consumption reactions of the oxidizer radicals follow a similar path. Meaning the assumption is that atomic oxygen is mainly consumed by addition reactions on the hydrocarbons and that a difference in kinetics due to different structural features of the hydrocarbons is negligible. The reaction equations are hence the following:

$$\text{O(rad)} \quad + \quad \text{C} \quad \rightarrow \quad \text{CO(rad)}$$

The rate of consumption r for the above reaction equation is as follows.

$$r = \frac{d[CO]}{dt} = -\frac{d[O]}{dt} = k'[O][C]$$

In the above equation $[CO]$ represents the concentration of formed oxygen-carbon sites, k' is the kinetic rate constant, and $[O]$ and $[C]$ give the concentrations of atomic oxygen and hydrocarbon reaction sites, respectively.

The second assumption is that the amount of carbon sites can be seen as quasi constant. That is that the depletion of carbon sites due to addition or abstraction of hydrogen is negligible as the sites are present to a large excess. As a result, the concentration of the carbon sites can be drawn into the reaction constant and the expression of the reaction rate becomes first order, as follows.

$$r = \frac{d[CO]}{dt} = -\frac{d[O]}{dt} = k[O]$$

The solution of the above equations can be achieved by integration over the time t. It is assumed that all oxidizer radicals are consumed after finite time, rendering the concentration of the oxidizer at infinite times $[O]_\infty$ to be zero. This gives the solution to the above equations, which is as follows.

$$[O](t) = [O]_0 e^{-kt}$$

Under these assumptions total rates of consumption for the calculations of the oxidation of the nascent soot structures by atomic oxygen can be expressed. $[O]_0$ represents the initial concentration

of oxygen. Using the equation for the rate of consumption the depletion of atomic oxygen during the calculations has been fitted.

The fits for the consumption of the atomic oxygen are shown in Figure 54 with their residuals for calculations at a temperature of 2500 K. Having obtained the kinetic rate constant k from the fits one can further estimate the energy barrier of the addition reaction, by fitting kinetic rate constant as a function of temperature. This follows the assumption that the kinetic rate constant is described by a simple Arrhenius-law, which is given in the following equation.

$$k(T) = Ae^{-\frac{E_A}{RT}}$$

A is a pre-exponential factor, which gives the frequency of collisions leading to a successful reaction, E_A gives the energetic barrier of the reaction and R is the universal gas constant. The pre-exponential factor can be expressed as temperature dependent as well but is assumed to be independent for the addition of oxygen on the hydrocarbon species. This assumption is taken since the pre-exponential factor has been described as temperature independent in other studies investigating oxidation by atomic oxygen. (89,331,333)

In order to linearly fit the kinetic rate constant, the logarithm of the exponential rate expression is taken, giving the following equation.

$$\ln\big(k(T)\big) = \ln(A) - \frac{E_A}{RT}$$

Therefore, by fitting $\ln\big(k(T)\big)$ over the reciprocal temperature one can determine the activation energy E_A. Similar simulations where hence calculated for temperatures of 1500 K, 1665 K, 1875 K and 2145 K.

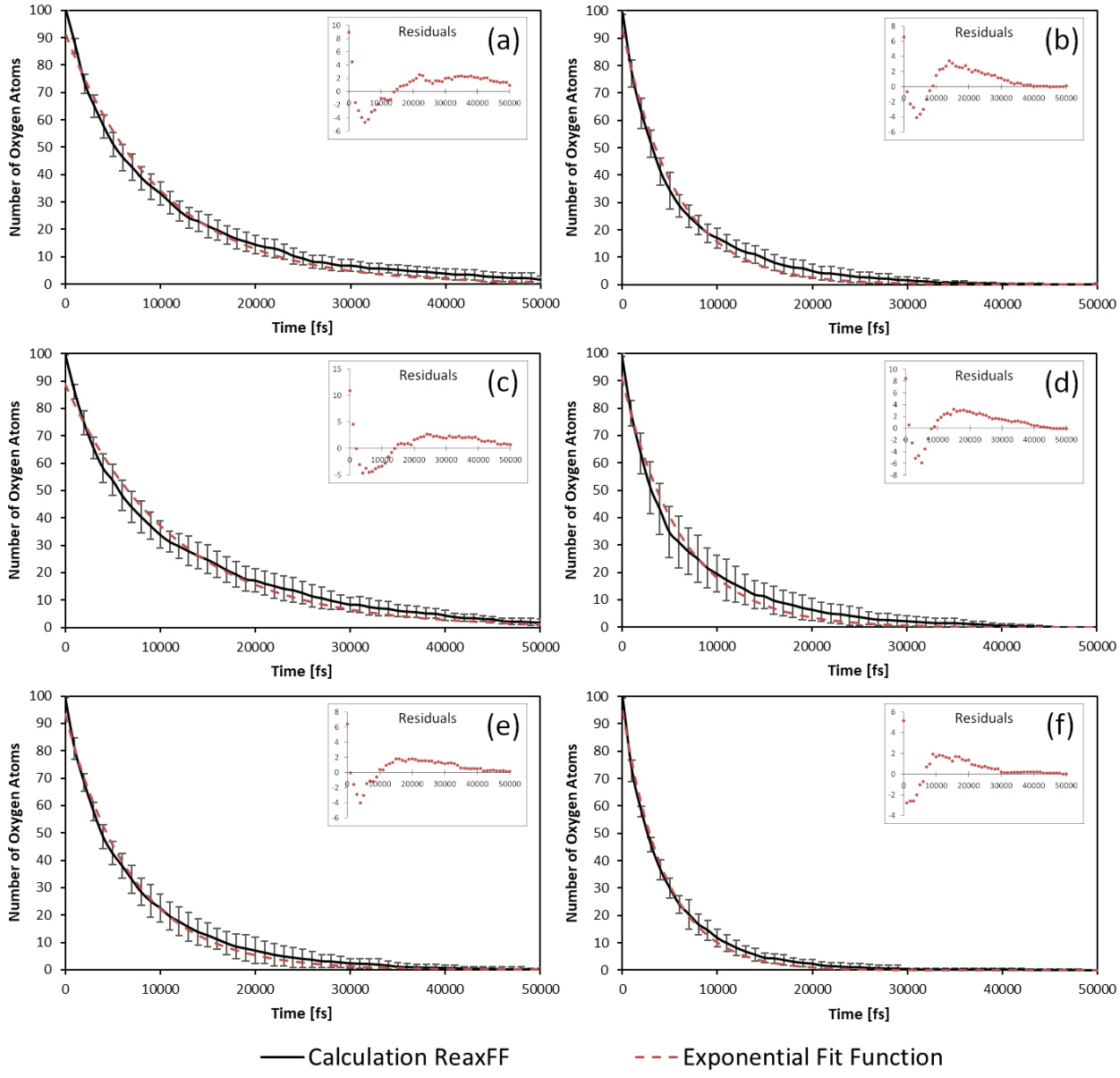

Figure 54. Number of atomic oxygen radicals over time (black) for (a) all ADLH species without sidechains, (b) all ADLH species with sidechains, (c) all APPH species without sidechains, (d) all APPH species with sidechains, (e) all AALH species without sidechains and (f) all AALH species with sidechains. The dashed red line gives the exponential fit of the consumption of atomic oxygen during the calculation. The residuals of the fit are given in the upper right corner of each graph.

Table 16. Fitted kinetic rate constants retrieved from the single exponential fits over the temperature range from 1500 K to 2500 K.

Temperature [K]	k(ADLH)	k(ADLHwSC)	k(APPH)	k(APPHwSC)	k(AALH)	k(AALHwSC)
2500	1.00E-04	1.82E-04	8.32E-05	1.72E-04	1.44E-04	2.25E-04
2145	5.80E-05	1.35E-04	5.34E-05	1.30E-04	9.33E-05	1.86E-04
1875	3.16E-05	1.08E-04	3.53E-05	1.02E-04	7.01E-05	1.46E-04
1665	2.40E-05	9.46E-05	2.27E-05	9.66E-05	5.18E-05	1.18E-04
1500	1.72E-05	8.27E-05	1.53E-05	8.15E-05	4.42E-05	1.06E-04

Table 17. Fitted activation energies retrieved from linear fits of the natural logarithm of the kinetic rate constant over the inverse temperature.

	ADLH	ADLHwSC	APPH	APPHwSC	AALH	AALHwSC
E_A (kcal/mol)	13.1	5.73	12.6	5.32	8.79	5.82

The plot of $\ln(k(T))$ over $\frac{1}{T}$ is shown in Figure 55, for the single exponential fits of the atomic oxygen decay for all tested species. The fitted reaction constants k and the fitted activation energies are given in Tables 16 and 17, respectively.

It was observed that, especially for short times, single exponential fits do not well reproduce the found data as indicated by the residuals shown in Figure 54. A double exponential fit reproduces the data much better, as shown in Figure 56. In terms of reactions assuming a double exponential decay means that there is a fast kinetic, dominating at short times, and a slower one that is relevant at longer times. No fast process could be detected that is sufficiently different from addition of oxygen on the hydrocarbons. For the hydrocarbon species possessing sidechains and AALH species one

could theorize that the fast process represents addition on the aliphatic carbon atoms, however, since also for species without sidechains double exponential fits improved the description of the consumption of atomic oxygen a definitive categorization of the two processes proves to be difficult.

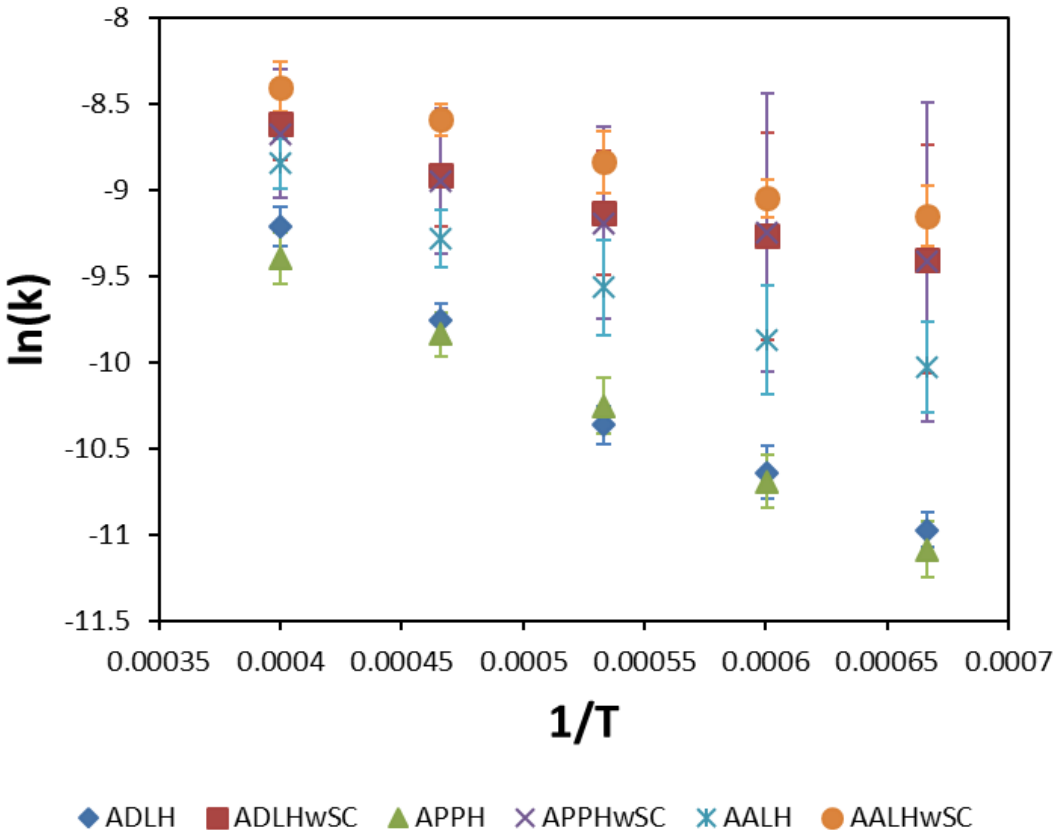

Figure 55. Natural logarithm of the fitted kinetic rate constant over the inverse temperature, for all differentiated species and a temperature range between 1500 K and 2500 K. The addition of "wSC" to the different structural groups denotes the presence of sidechains in the species of the structural group.

The double exponential fits are, furthermore, problematic, since the initial concentration of oxygen needs to be distributed into the atomic oxygen concentration following the fast reaction pathway and the concentration following the slower one, as given in the following equation.

$$[O](t) = [O]_{0_{slow}} e^{-k_{slow}t} + [O]_{0_{fast}} e^{-k_{fast}t}$$

Since the amount of $[O]_{0_{slow}}$ and $[O]_{0_{fast}}$ are initially unknown fitting these equations is troubling. A solution to this problem is attempted by assuming that for longer times the atomic oxygen following the fast process is mostly consumed and the exponential expression for the fast process is hence close to zero. Hence, the above equation can be expressed for long times as follows.

$$[O](t \gg 0) = [O]_{0_{slow}} e^{-k_{slow}t}$$

With this assumption fitting the above equation with a non-linear fit for times longer than 10 ps gives an estimate of $[O]_{0_{slow}}$. In Figure 56 both fits for the fast and the slow process are given, as well as the sum of the two exponentials and the residuals of the double exponential fits for calculations performed at 2500 K.

Again, the consumption of atomic oxygen was fitted over the range of temperatures from 1500K to 2500 K using double exponential fits, in order to investigate the temperature dependence of the rate constants. The logarithm of the slow and fast rate constant is plotted over the reciprocal temperature in Figure 57. Comparison with Figure 55 gives that the found constants for the slow process very much resemble the constants found for the single exponential fits, the error could be reduced significantly, however. The linear behavior of the logarithm of the rate constant over the inverse temperature again was plotted, and the fitted activation energies are shown in Table 18.

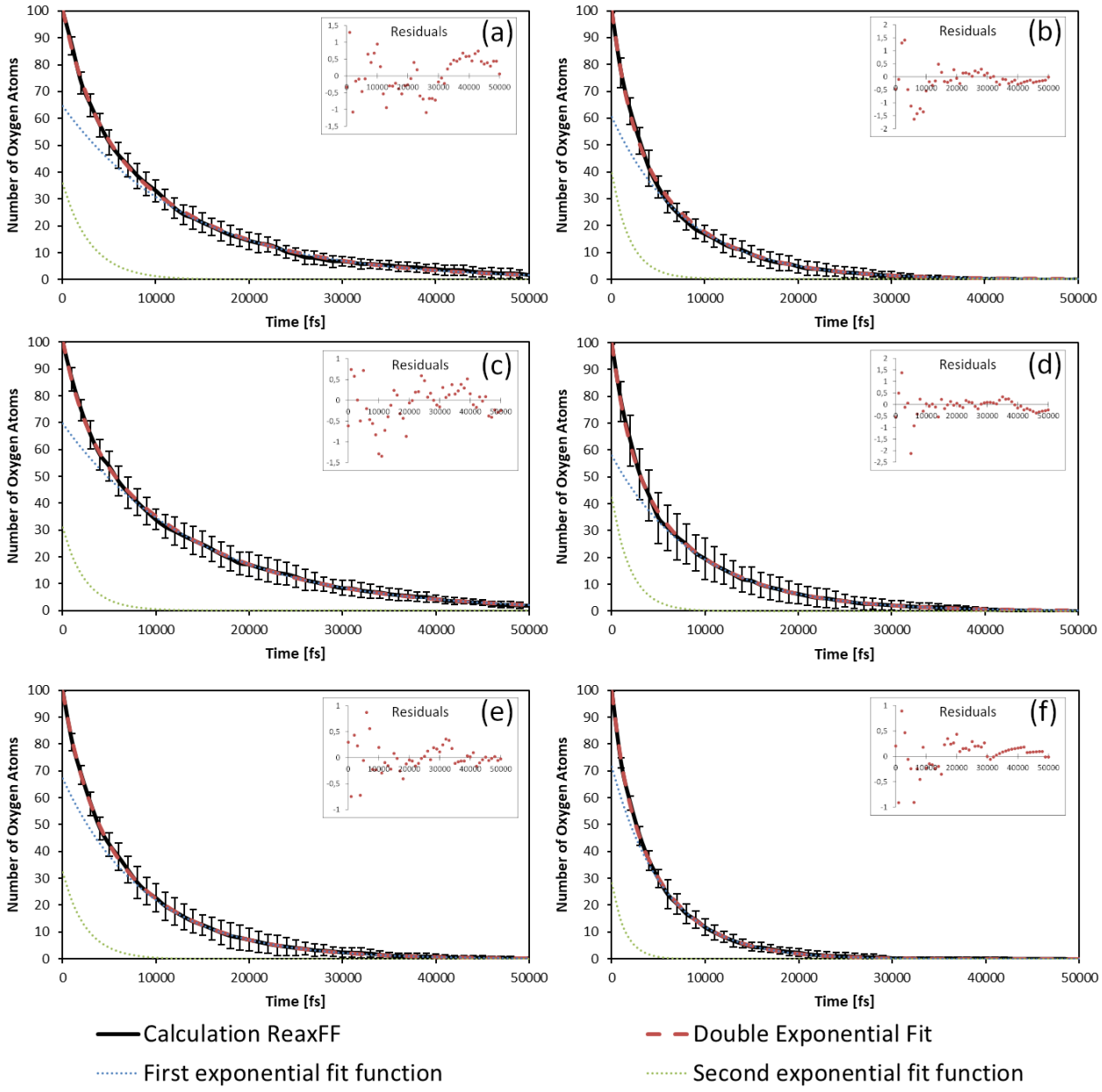

Figure 56. Number of atomic oxygen radicals over time (black) for (a) all ADLH species without sidechains, (b) all ADLH species with sidechains, (c) all APPH species without sidechains, (d) all APPH species with sidechains, (e) all AALH species without sidechains and (f) all AALH species with sidechains. The dashed red line gives the double exponential fit of the consumption of atomic oxygen during the calculation, with the two single exponential functions displayed as dotted blue and dotted green line. The residuals of the fit are given in the upper right corner of each graph.

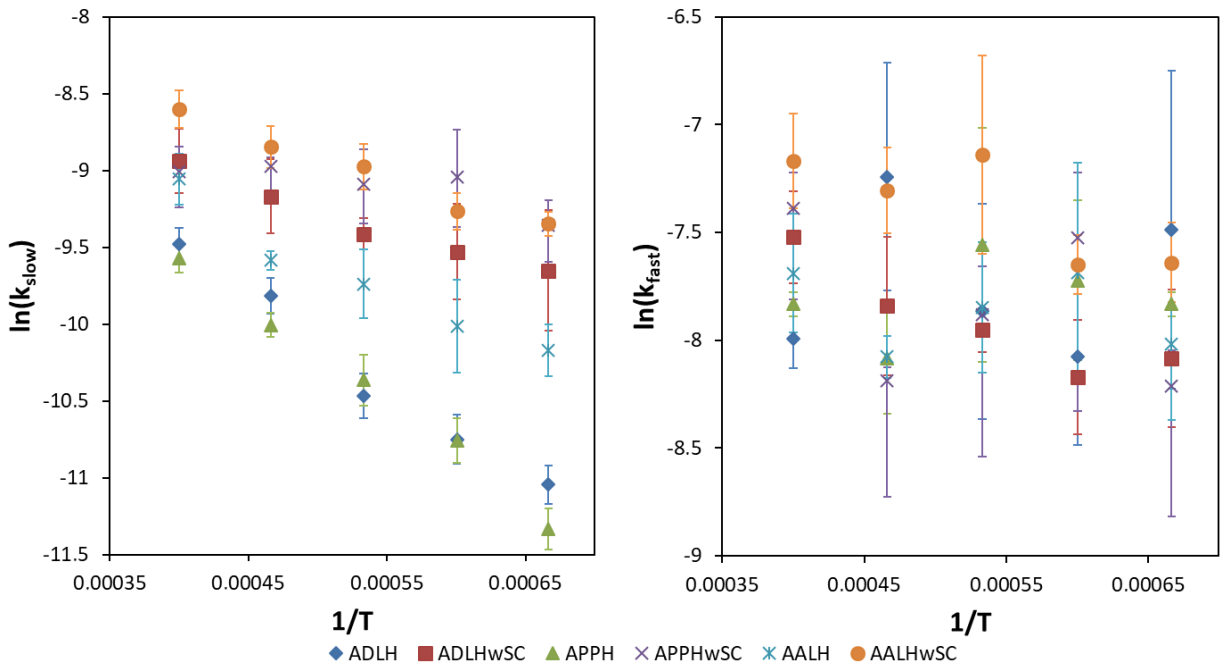

Figure 57. Natural logarithm of the fitted kinetic rate constant of the atomic oxygen consumption of the first exponential function of the double exponential fits (left) and the second exponential function of the double exponential fit (right) over the inverse temperature, for all differentiated species and a temperature range between 1500 K and 2500 K. The addition of "wSC" to the different structural groups denotes the presence of sidechains in the species of the structural group.

Table 18. Fitted activation energies retrieved from linear fits of the natural logarithm of the kinetic rate constant of the second exponential function of the double exponential fit (slow) over the inverse temperature.

	ADLH	ADLHwSC	APPH	APPHwSC	AALH	AALHwSC
E_A (kcal/mol)	12.1	4.18	12.7	2.27	7.91	5.68

The constants found for the fast kinetics on the other hand do not show any linear dependence over the inverse temperature whatsoever. This can be due to several reasons, like the constants

showing non-Arrhenius dependence. Also, the convolution with the slow process might not have been sufficiently deconvoluted using the double exponential plots leading to an error in the rate constants. As a result, further investigation of the kinetics is needed, which could not be undertaken due to the timely restrictions of the presented work.

The rate constants of the slow process fitted, and as a result the energy barriers of the process, are sufficiently similar to the constant and energies found for the single exponential fits. The range of activation energies fitted from these plots is wide, however, indicating some influence of the structure. A comparison to other studies again is difficult since, first of all, the process under investigation could not clearly be determined and secondly the addition of oxygen on aromatic molecules, if one assumes this is the process that is best described by the kinetics, on aromatic compounds is scarcely investigated for a range of different structures. For the adsorption of aromatic oxygen on graphene Sorescu et al. found adsorption activation energies of 44 kcal/mol.(352) Margulis et al. reported chemisorption energies of oxygen on the zigzag sites of carbon nanotubes between 25.37 kcal/mol and 62.26 kcal/mol.(353) Graphene and carbon nanotubes do not possess C–H sites, however, which has been the sites the oxygen exclusively reacted on in this study.

There have been several studies on the reaction of atomic oxygen with small aromatics. Their results are depicted in Table 19 stating the first author of the study, the aromatic molecule with which the reaction with atomic oxygen occurred, the energetic barrier proposed for the rate expression, the temperature and pressure range investigated in the study.

All the presented energetic barriers have been proposed for a general rate expression of the aromatic molecules with atomic oxygen, hence not differentiating between reaction pathways. A

recent theoretical study by Taatjes et al. gave an energetic barrier of the transition state for the addition of atomic oxygen to benzene of 5.7 kcal/mol. (354)

Table 19. Literature values found for the expression of the reaction rate of atomic oxygen with aromatic molecules. The first column gives the first author of the study and the reference. The second column gives the aromatic molecules used in the study. The third column gives the estimated energy barriers of the reaction of atomic oxygen with the aromatic molecules and columns four and five give the temperature and pressure ranges investigated in the studies, respectively.

First author	Aromat	Energy barrier reported	Temperature range	Pressure range
Nicovich et al. (331)	Benzene	4.91±0.15 kcal/mol	298 – 950 K	100 Torr
	Toluene	3.80±0.14 kcal/mol	298 – 932 K	100 Torr
Leidreiter et al.(333)	Benzene	4.67 kcal/mol	1200 – 1400 K	2 Torr
Tappe et al.(337)	Benzene	4.47±0.46 kcal/mol	305 – 865 K	3.62 –11.6 mbar
	Toluene	3.52±0.36 kcal/mol	305 – 873 K	3.95 –11.9 mbar
	Ethylbenzene	3.66±0.36 kcal/mol	300 – 868 K	2.16 – 4 mbar
Ko et al.(335)	Benzene	5.19 kcal/mol	600 K – 1310 K	180 – 450 Torr

The activation energies for reaction of aromatic hydrocarbons without sidechains in the present study are significantly higher, while the activation energies for species possessing sidechains lie in the same energy range. It is interesting to note, however, that an increase of activation energy was observed between toluene, ethylbenzene and benzene in the studies presented in Table 19, as the presence of sidechains also showed a significant impact on the activation energy in this study.

Frenklach und Wang gave an activation energy of 4.53 kcal/mol for the reaction of benzene with atomic oxygen forming phenolate.(89) This value is also used for oxidation of aromatic compounds

by atomic oxygen in Raj's mechanism.(96) Wang et al. gave an activation energy of 4.501 kcal/mol for the oxidation of naphthalene with atomic oxygen to ketene and phenyl.(97) The values of activation energy found for hydrocarbons possessing sidechains, for which a fast oxidation of the sidechain was observed after addittion of atomic oxygen, are in this region.

The question remains, how the values of oxygen addition and oxidation by atomic oxygen scale with the size of the aromatic molecule. The values reported in literature are mostly calculated for smaller aromatics, since a detailed *ab initio* calculation of larger aromatics is expensive due to the number of electrons involved. The fitted activation energies found for the ReaxFF calculations are higher, especially for the ADLH and APPH structures without sidechains, than what is found in literature. Hence, an increase in the activation energy between the aromatic molecule and the atomic oxygen would be assumed. Another indicator is the higher chemisorption energies for graphenes and carbon nanotubes. Barone et al. reported chemisorption energies of atomic oxygen on a single site of naphthalene and pyrene clusters to be 3.46 kcal/mol and 10.85 kcal/mol, respectively.(355) This supports the assumption that the energy barrier of the oxygen addition might increase with increasing size of aromatics. However, from the fitting of the ReaxFF calculations no further support of this assumption can be drawn apart from the comparisons to literature. Further investigations of these phenomena and further comparison to *ab initio* calculations are needed. These investigations were not possible to pursue due to the timely restrictions of this work, however.

Nonetheless, as presented, a wide range of activation and chemisorption energies can be found in literature. While the fits gave energies that are of the same magnitude as those found in literature, the comparison and an assignment to one process is difficult due to the not well resolved second process detected. The uncertainty of the approach must be assigned to the number of assumptions

taken in order to fit the consumption of atomic oxygen. One assumption taken that all oxygen atoms follow a similar reaction pathway, appeared only partly, since it was in the contrary observed that the atomic oxygen attacks on numerous different reaction sites, and no selectivity could be detected. Furthermore, the addition of atomic oxygen to hydrocarbons containing already an oxygen atom due to prior reactions or hydrocarbons that already underwent some oxidation and hence possess radical character has not been considered at all in the presented approach. Nevertheless, finding activation energies for the slow processes, presumably addition of atomic oxygen, by just graphical fitting gave reasonable results.

Furthermore, the investigation of rate constants for the simulation including hydroxyl radicals has been undertaken. The oxidation behavior of hydroxyl is more complicated than for the atomic oxygen radicals as can be seen by comparison of Figure 43 and 47.

While for the atomic oxygen radicals, addition on hydrocarbons appears to be the only process, even though this process may have two kinetics, oxidation of hydrocarbons by hydroxyl radicals clearly shows two processes. One being the hydrogen abstraction from hydrocarbon by hydroxyl radicals and the second being the addition of the radicals on the hydrocarbons. Hence following similar assumptions than for the atomic oxygen, that is hydrogen abstraction or addition all follow a similar path and that the concentration of the hydrocarbon reactive sites can be assumed to be constant, the concentration of hydroxyl radicals over time can be expressed by a double exponential decay.

$$[OH](t) = [OH]_{0_{H-abstraction}} e^{-k_{H-abstraction}t} + [OH]_{0_{Addition}} e^{-k_{Addition}t}$$

Following this assumption double exponential fits have been made for the calculations with hydroxyl radicals. These are shown for temperatures of 2500 K in Figure 58.

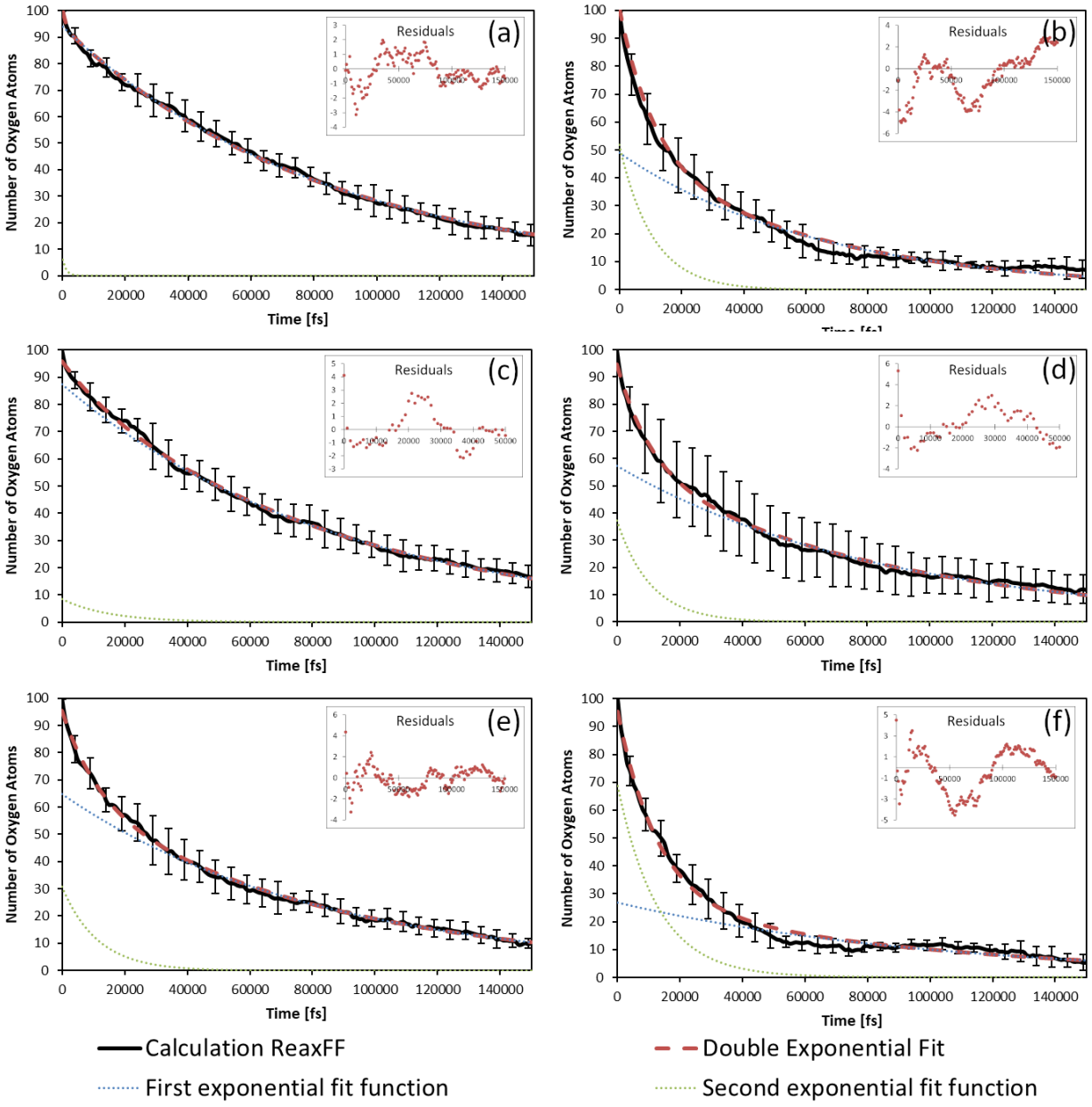

Figure 58. Number of hydroxyl radicals over time (black) for (a) all ADLH species without sidechains, (b) all ADLH species with sidechains, (c) all APPH species without sidechains, (d) all APPH species with sidechains, (e) all AALH species without sidechains and (f) all AALH species with sidechains. The dashed red line gives the double exponential fit of the consumption of atomic oxygen during the calculation, with the two single exponential functions displayed as dotted blue and dotted green line. The residuals of the fit are given in the upper right corner of each graph.

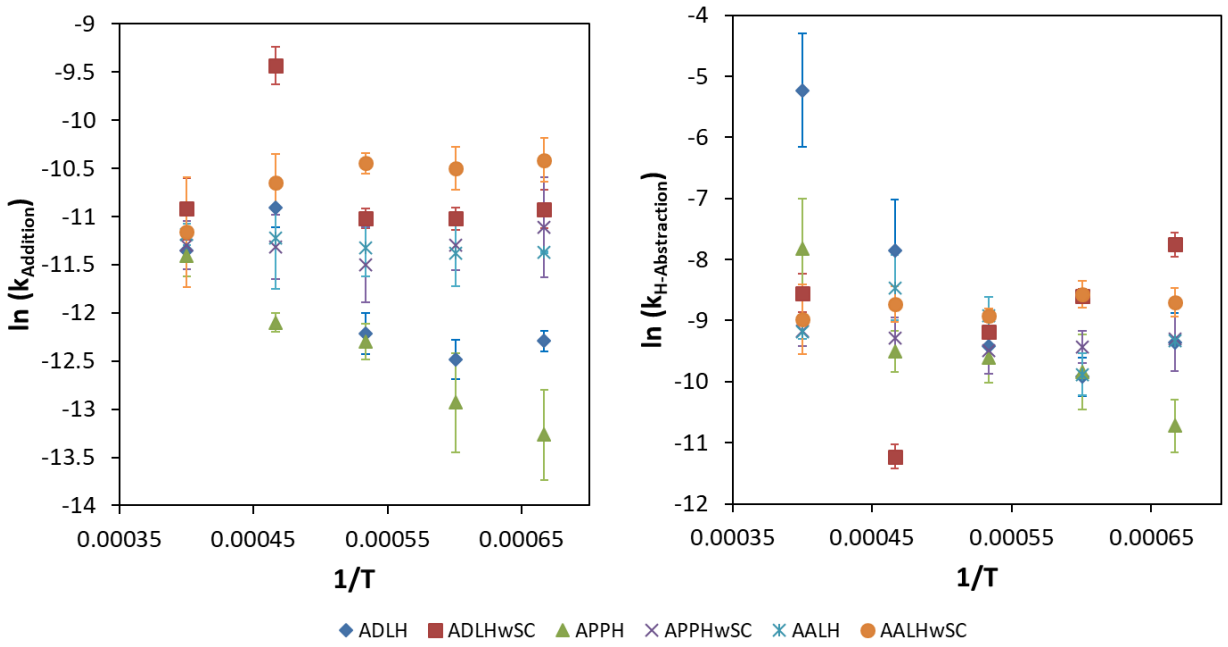

Figure 59. Natural logarithm of the fitted kinetic rate constant of hydroxyl consumption of the first exponential function of the double exponential fits (left) and the second exponential function of the double exponential fit (right) over the inverse temperature, for all differentiated species and a temperature range between 1500 K and 2500 K. The addition of "wSC" to the different structural groups denotes the presence of sidechains in the species of the structural group.

The residuals for the double exponential fits for the consumption of hydroxyl are significantly higher, as can be seen by comparison with Figure 56. Hence, the description of the concentration with the double exponential cannot be as clearly resolved as for the atomic oxygen calculations. This is partly due to the larger overlap of the two exponential functions.

As a result of this a resolution of each of the two exponentials proves to be difficult. Furthermore, the concentrations of hydroxyl radicals either abstracting hydrogen or adding to the hydrocarbons can largely differ as a result of the different structures of the hydrocarbons, as already discussed in subsection 6.2.2. This is also visible in the double exponential fits in Figure 58. While for the ADLH structures without sidechains the contribution of the second single exponential fit is

negligible, the contribution of the second single exponential fit for the ADLH species with sidechains is almost 50%.

Nevertheless, fits of the decay of hydroxyl radicals for different temperatures have been plotted in order to investigate the temperature dependency of the rate. The temperature range is the same as for the atomic oxygen, i.e., 1500K, 1665 K, 1875 K, 2145 K and 2500 K. The natural logarithm of the rate constants found over the inverse temperature is plotted in Figure 59 for the hydrogen abstraction (right) and the addition process (left). Both processes could be identified separately, since the found reaction rates also describe well the generation of the reaction product, that is oxygenated hydrocarbons for the addition of hydroxyl and water molecules for the hydrogen abstraction by hydroxyl.

As can be seen the rate constants have no linear dependency over the reciprocal temperature, hence not following simple Arrhenius like behavior. This is plausible, since one also finds in literature that the collision frequency term in the rate expression of the oxidation with hydroxyl is temperature dependent.(89,96,97) The logarithm of the rate constant and the inverse temperature do not show a linear relation, as shown in Figure 59, and hence the determination of the activation energies could not be achieved by linear fitting.

This shows the limitations of the presented approach of graphical fitting of kinetics for the reactions of different oxidizers. Nonetheless for the addition process of atomic oxygen reasonable activation energies could be found with this rather simple approach. Further investigation of the fast and slow processes would be needed, however. For the oxidation of hydrocarbons by hydroxyl the consumption of hydroxyl could be well fitted. However, the fitted rate constant could not give any insight into the energy surface of the oxidation reactions.

7.4. Conclusion

In this chapter initial investigation of the structure reactivity relationship for oxidative reactions have been investigated for the different structural classes found in chapter 5. In order to achieve this the different structural groups, that is ADLH, APPH and AALH structures, as presented in chapter 5, have been divided in the species of each respective group possessing sidechains and those which do not. ReaxFF calculations of all species of each of the groups have then been performed with four different oxidizers. The oxidizers chosen are atomic oxygen radicals, hydroxyl radicals, hydroperoxyl radicals, and methoxy radicals.

Investigation of the consumption and reaction products of atomic oxygen radicals gave that the initially identified groups, i.e., ADLH, APPH, and AALH structures, did not show a significant difference in reactivity towards the oxidizers. The presence of sidechains did show an increase in reactivity, however. This is due to additional reactive sites due to the presence of the sidechain.

The most prominent reaction pathways for the oxidation of the aromatic rings and the sidechains have been analyzed. It was found that addition of the atomic oxygen radicals to the aromatic hydrocarbons is in all cases the initial reaction step. Hydrogen abstraction from the hydrocarbons by the oxidizer radicals was only detected for species without sidechains. Through rearrangement reactions the added oxygen is either stabilized on the aromatic hydrocarbon or oxidizes the later by formation of carbon monoxide. The found reaction pathways give reasonable results by comparison to other studies (354) and highlight the impact of radical stabilization due to the aromatic plane.

The reactivity of hydroxyl radicals proved to be different from the atomic oxygen radicals. The hydrogen abstraction from aromatic hydrocarbons was much more pronounced. Furthermore, addition of hydroxyl radicals to the aromatic hydrocarbons without sidechains was observed to rarely occur. This is different for the hydrocarbon species that possess sidechains for which addition

of hydroxyl radicals to the sidechain is much more pronounced. As a result, reaction pathways and oxidation kinetics are significantly different. The observed reaction pathways have been analyzed and portrayed.

Furthermore, oxidation by hydroperoxyl radicals with the aromatic hydrocarbon has been investigated. It was found that oxidation of hydrocarbons by hydroperoxyl is hindered, since the hydroperoxyl radicals rapidly dissociate into molecular oxygen and hydrogen atoms. Consequently, the produced hydrogen atoms did interfere with the reactivity of the not dissociated hydroperoxyl radicals, leading to an addition to the radical and the dissociation into two hydroxyl radicals. As a result, the observed oxidation reactions with the aromatic hydrocarbons largely follow the oxidation pathways by hydroxyl radicals. The transfer of atomic oxygen from one of the hydroperoxyl radicals has been observed, but only as a rare event, and due to this reason, the reaction pathways and kinetics could not be investigated further.

Lastly the reactions of methoxy radicals with the hydrocarbons detected in chapter 5 has been investigated. It was observed that, like in the case of hydroperoxyl radicals, the methoxy radicals are mainly consumed by dissociation reaction forming formaldehyde. However, in the presence of aromatic hydrocarbons possessing sidechains the dissociation reactions are assisted by the sidechain carbon atoms, reducing the unsaturated sidechain and producing formaldehyde and formyl radicals.

To investigate the kinetics of the consumption of atomic oxygen radicals and hydroxyl radicals, the number of molecules of each group have been standardized in order to reduce structural differences between species in one group. Furthermore, the amount of carbon, hydrogen and oxygen atoms are kept constant for this approach. Attention was paid to still include sufficiently different reaction sites in order to retain different reactivities due to different reaction sites. Unfortunately, no differentiation of sites could be observed, apart from the different reactivities of aromatic and

aliphatic carbon atoms. Additionally, investigation using the ChemTrayZer code(330) showed, that due to this insufficient differentiation an analysis using this software was not possible.

Nevertheless, the consumption of the oxidizer radicals could be fitted graphically following some assumptions. It was found that for the consumption kinetics of atomic oxygen presumably two different reaction kinetics were observed. Plotting the logarithm of the detected kinetic constants over the inverse temperature gave a linear dependency for the slow addition reactions, indicating Arrhenius like reaction kinetics. Calculation of the energy barriers for the tested species showed differences due to different structural features. Comparison to other studies showed that the results of the fit gave reasonable results. The fast reaction kinetics could not be resolved due to a non-linear relation of the kinetic constants and the inverse temperature.

Furthermore, investigation of the kinetics of the reactions of hydroxyl radicals with the aromatic hydrocarbons have been attempted. For the hydroxyl radicals two processes, the abstraction of hydrogen from the aromatic hydrocarbons and addition of hydroxyl to the aromatic hydrocarbons, have been observed. Fitting the consumption due to the two reaction pathways with a double exponential decay gave reasonable results. Plotting the logarithm of the fitted kinetic constants over the inverse temperature gave that there is no linear relation, hence indicating no simple Arrhenius like temperature dependency of the kinetic constant. Presumably the collision factor of the Arrhenius equation needs to be expressed as a temperature dependent pre-factor, as was reported in literature.(36,96,97)

Nevertheless, investigation of the different reactivities of the aromatic hydrocarbon species detected in chapter 5 due to structural differences could be detected. The oxidation kinetics and reaction pathways have been largely influenced by the presence of aliphatic sidechain carbons. A number of reaction pathways could be observed for the investigated oxidizers. Moreover, the

kinetics of the addition of atomic oxygen to aromatic hydrocarbons has been fitted and gave reasonable results compared to literature.

The presented findings could help explain particle burn-out during soot oxidation.(76,204,205) That is the faster oxidation of the particle core compared to the shell. HRTEM studies have found that the particle core shows a more amorphous structure than the shell.(19,53,54,79) Violi et al. found that aromatics with sidechains form more stable dimers due to Van der Waals interactions, as the kinetic energy of the collision can be better converted.(159,162) The results presented in chapter 6, but also other ReaxFF studies modeling soot inception, have shown that sidechains play a significant role in the formation of larger molecular structures.(66,131,148) Also aliphatic links between the aromatic moieties have been argued to aid the soot inception.(45,142) Experimental studies on the molecular and structural composition of nascent soot confirmed the presence of sidechains and aliphatic links in the nascent soot structures.(56,301)

As graphitization by reaction with gas phase species does not occur in the particle core, which in turn is the reason for the structural difference of the particle core and shell,(55,356,357) the sidechains and aliphatic links of the nascent soot particles are preserved inside the particles. Soot burn out has been argued to occur due to diffusion of oxidizers into the inner particle and increased oxidation kinetics of the amorphous structures, due to more reaction sites.(18,72,203,322) Adding the argument of the different kinetics of the sidechain carbons compared to aromatic carbon, further supports this argumentation and could, moreover, explain, why the oxidizers are not already consumed during diffusion through the particle pores.

8. Conclusion

Soot production is governed by several different processes and the conditions under which the soot is formed greatly influence the properties of the generated particles. In order to understand this relationship, the processes involved in the soot formation need to be better understood. With modern diagnostic techniques and theoretical models, a large margin of the soot formation process has been revealed.(13,20,45,53,93,225) However, there is to date dissensus on the processes involved in soot inception and how to model these phenomena.(13) Lately, the process of bond formation between aromatic molecules has gained more interest and was argued to be relevant to soot inception.(66,135,152,358)

The impact of the combustion conditions, such as fuel composition or thermochemical surrounding, on the nanostructure of the soot particles has been shown multiple times experimentally, which is difficult to predict by theoretical models.(43,45,55,64,198,225,325,359) Consequently, a prognosis of the changes of soot nanostructure and subsequent changed in the oxidation behavior as a result of different combustion conditions by computational methods is problematic.

In this thesis, a multi-scale model approach has been developed to tackle unresolved question of the soot formation process. That is, how does the combustion conditions influence nascent soot structures, and in turn translate to the fully-grown particles, what aspects of soot inception are best described by bond formation between PAHs, and how does a change in the structural features impact reactivity and oxidative behavior of the soot.

The presented approach combines two techniques. The first is detailed chemical kinetic modeling of the gas phase during combustion. This is a technique capable of accurately describing the chemical processes in combustion, but in dependence of the chemical mechanism involved, is limited

towards the description of the transition of the gas-phase molecules to the solid-phase particles. The second method employed is reactive force field molecular dynamics, which is a powerful tool to model chemical processes and reactions but is limited towards the size and timescale it is capable to model.

In order to get a good understanding of the impact of single parameter changes on the gas-phase compositions, a broad parameters space has been investigated with the chemical kinetics calculations, scanning over different fuel compositions, equivalence ratios and temperatures. With the purpose of decoupling the thermal and chemical impact of fuel composition, the gas-phase generation was performed at fixed temperatures and pressures, allowing a careful comparison of the impact of fuel composition on the extracted precursor pools. In order to get a consistent representation of the gas-phase model for the ReaxFF calculations, the point of extraction was chosen in order to appear before soot inception independently of the parameters employed.

The translation of the gas phase was carefully thought, in order to give reasonable sized molecular representations relevant to the soot inception process. That is the molecules expected to be relevant to the soot inception process have been kept, while reducing the number of molecules in order to be able to insert it into the molecular modeling simulations. Investigation of the changes in the gas phase due to the changes in temperature, equivalence ratio and fuel composition have been investigated and showed to transfer well to the soot precursor pools extracted for ReaxFF modeling.

Furthermore, the capabilities of the ReaxFF approach were investigated in terms of force field parameters sets used and general input parameters for the molecular modeling simulations. Multiple force fields have been compared with regard towards their capabilities of capturing the processes involved in the soot inception process. It was found that an increase of temperature in the molecular modeling simulations invokes an acceleration of the reaction kinetics, without influencing the

reaction pathways significantly. An increased temperature requires a reduced time step, however, leading to an increased number of iteration steps to simulate the same time range. A compromise, giving the best results for the least computational costs, was identified and employed to model the bond formation between the soot precursors extracted from the modeled gas phase.

The combination of both – the macroscopic detailed kinetic gas phase modeling and the reactive force field molecular modeling – allows the examination of processes involved in chemical bond formation between soot precursors and the impact of combustion conditions on these processes and the resulting nanostructures. It was found that the modeling of bond formation between soot precursors gives structures whose physical properties compare well to the properties of nascent soot found in experiments. Additionally, the correlation of temperature with the rate under which the soot structures formed was translated to the ReaxFF through the soot precursor composition. This correlation is also found in experiments, where at increased temperatures, the rate of soot formation is also increased.(45)

A structural analysis of the extracted soot growth products gave that all structures could be grouped into one of three structural classes. These groups consist of aromatic directly linked hydrocarbons, aromatic pericondensed polycyclic hydrocarbons and aromatic aliphatically linked hydrocarbons. A correlation of the fuel composition used for the generation of the soot precursor pools and the number of aromatic aliphatically linked hydrocarbons generated could be shown. The same correlation could be found for aliphatic sidechains present in the generated soot structures to the aliphatic content of the parent fuel used to generate the initial precursor pool.

The presence of sidechains and aliphatic links in nascent soot precursors have also been detected in experimental studies.(45,56,301) The correlation found in this work compares well to the findings reported. Furthermore, it was argued that these structures might aid dimerization due to Van der

Waals forces, since dimers formed by collision are more prone to stick together as a result of additional vibrational modes and in turn better conversion of the kinetic energy of the collision.(159,162) Also other ReaxFF studies on soot inception stressed the importance of sidechain towards the formation of larger structures.(66,148,360)

A study of the interactions of the detected soot structures and radicals relevant to oxidation in the gas phase has been done. Relevant reaction pathways of the oxidation process of the different oxidizer radicals could be reported. Furthermore, the kinetics of some of the oxidizers were estimated, and the kinetics of the aromatic hydrocarbon oxidation by atomic oxygen values have been reported which are in reasonable agreement compared to experimental and other theoretical studies.

An impact of structural features for the aromatic hydrocarbons on their reactivity could also be reported, as species possessing sidechains showed different oxidation kinetics and reaction pathways, compared to species not possessing these sidechains. Hence the presence of sidechains was found to have an important role towards the oxidation reactivity of the nascent soot structures generated with the multi-scale approach. As the presence of sidechains was reported to also improve soot inception, this might be one additional argument to explain particle burn-out.(66,159,162,360)

High-resolution tunneling electron microscopy of soot particles gave that the inner core of particles is more amorphous than the outer graphitized shell.(19,20,79) Hence, arguing that the presence of sidechains in the particle core is increased compared to the particle shell, which has been subject to further reaction with the gas phase and as a result graphitization, is plausible.(55,356) The higher tendency of the sidechains to react with oxidizer radicals consequently gives that the inner particle would oxidize faster, than the shell.

The presented work is portraying a novel methodology to closely investigate certain phenomena of soot formation. The top-down multi-scale approach is combining two individual theoretical models as a means to model processes that are relevant to the understanding of the impact of combustion conditions on soot nanostructure and in turn the influence of nanostructure on reactivity towards gas-phase molecules.

The obtained results are in agreement with experimental findings. It was found that bond formation between soot precursor molecules as a mechanism for soot inception gives results also found by soot diagnostics. The detected correlation between the resulting structure of nascent soot particles and combustion conditions are plausible and agree well with other studies. Also, the change in oxidation kinetics due to structural changes helps to explain certain phenomena of soot oxidation. Furthermore, scanning the parameter range, as it is presented in this study, under laboratory conditions would be difficult. Consequently, the presented multi-scale approach – coupling detailed chemical kinetics to model gas-phase combustion and reactive force field molecular modeling to further magnify certain phenomena – is a valuable tool to investigate the underlying processes in soot formation for a wide range of parameters.

9. Appendix

A. Bond Order Correction in ReaxFF

Based on the uncorrected Bond orders BO'_{ij} an uncorrected overcoordination term Δ' is defined.

$$\Delta'_i = -Val_i + \sum_{j=1}^{neighbours(i)} BO'_{ij} \tag{A.1a}$$

The uncorrected overcoordination definition Δ'^{boc}_i for atoms bearing lone pairs after filling their valence, such as oxygen or nitrogen, needs to be treated differently, since these atoms can break up their lone pairs to involve them into bonding.

$$\Delta'^{boc}_i = -Val^{boc}_i + \sum_{j=1}^{neighbours(i)} BO'_{ij} \tag{A.1b}$$

The uncorrected overcoordination is then used to correct the bond orders BO'_{ij} using the scheme described in equations (B.2a-f)

$$BO^{\sigma}_{ij} = BO'^{\sigma}_{ij} \cdot f_1(\Delta'_i, \Delta'_j) \cdot f_4(\Delta'_i, BO'_{ij}) \cdot f_5(\Delta'_j, BO'_{ij})$$

$$BO^{\pi}_{ij} = BO'^{\pi}_{ij} \cdot f_1(\Delta'_i, \Delta'_j) \cdot f_1(\Delta'_i, \Delta'_j) \cdot f_4(\Delta'_i, BO'_{ij}) \cdot f_5(\Delta'_j, BO'_{ij})$$

$$BO^{\pi\pi}_{ij} = BO'^{\pi\pi}_{ij} \cdot f_1(\Delta'_i, \Delta'_j) \cdot f_1(\Delta'_i, \Delta'_j) \cdot f_4(\Delta'_i, BO'_{ij}) \cdot f_5(\Delta'_j, BO'_{ij})$$

$$BO_{ij} = BO^{\sigma}_{ij} + BO^{\pi}_{ij} + BO^{\pi\pi}_{ij} \tag{A.2a}$$

$$f_1(\Delta_i, \Delta_j) = \frac{1}{2} \cdot \left(\frac{Val_i + f_2(\Delta'_i, \Delta'_j)}{Val_i + f_2(\Delta'_i, \Delta'_j) + f_3(\Delta'_i, \Delta'_j)} + \frac{Val_j + f_2(\Delta'_i, \Delta'_j)}{Val_j + f_2(\Delta'_i, \Delta'_j) + f_3(\Delta'_i, \Delta'_j)} \right) \tag{A.2b}$$

$$f_2(\Delta'_i, \Delta'_j) = \exp(-p_{boc1} \cdot \Delta'_i) + \exp(-p_{boc1} \cdot \Delta'_j) \tag{A.2c}$$

$$f_2(\Delta'_i, \Delta'_j) = -\frac{1}{p_{boc2}} \cdot ln\left\{ \frac{1}{2} \left[\exp(-p_{boc2} \cdot \Delta'_i) + \exp(-p_{boc2} \cdot \Delta'_j) \right] \right\} \tag{A.2d}$$

$$f_4(\Delta'_i, BO'_{ij}) = \left\{ 1 + \exp\left(-p_{boc3} \cdot \left(p_{boc4} \cdot BO'_{ij} \cdot BO'_{ij} - \Delta'^{boc}_i \right) + p_{boc5} \right) \right\}^{-1} \tag{A.2e}$$

$$f_5(\Delta'_i, BO'_{ij}) = \left\{ 1 + \exp\left(-p_{boc3} \cdot \left(p_{boc4} \cdot BO'_{ij} \cdot BO'_{ij} - \Delta'^{boc}_j \right) + p_{boc5} \right) \right\}^{-1} \tag{A.2f}$$

The parameters $p_{boc1} - p_{boc5}$ are determined through optimization against a training set obtained from ab initio calculations and/or literature by using a single-parameter-based parabolic extrapolation model. This model determines the parameter which minimizes the sum of the squared error.

10.Bibliography

1. Jacobson MZ. Short-term effects of controlling fossil-fuel soot, biofuel soot and gases, and methane on climate, Arctic ice, and air pollution health. J Geophys Res Atmos. 2010;115(D14).
2. Bond TC, Doherty SJ, Fahey DW, Forster PM, Berntsen T, DeAngelo BJ, et al. Bounding the role of black carbon in the climate system: A scientific assessment. J Geophys Res Atmos. 2013;118(11):5380–552.
3. Oberdörster G, Oberdörster E, Oberdörster J. Nanotoxicology: An Emerging Discipline Evolving from Studies of Ultrafine Particles. Environ Health Perspect [Internet]. 2005;113(7):823–39. Available from: http://www.jstor.org/stable/3436201
4. Violi A. Effects of Combustion-Generated Nanoparticles on Cellular Membranes. Combust Sci Technol. 2016 Mar;188(4–5):769–75.
5. Lighty JS, Veranth JM, Sarofim AF. Combustion Aerosols: Factors Governing Their Size and Composition and Implications to Human Health. J Air Waste Manage Assoc. 2000 Jan;50(9):1565–618.
6. WHO Global Status Report on Road Safety 2013
7. WHO Global Status Report on Road Safety 2015.
8. Regulation (EC) No 715/2007 of the European Parliament and of the Council of 20 June 2007 on type approval of motor vehicles with respect to emissions from light passenger and commercial vehicles (Euro 5 and Euro 6). 2007.
9. Barone TL, Storey JME, Domingo N. An Analysis of Field-Aged Diesel Particulate Filter Performance: Particle Emissions before, during, and after Regeneration. J Air Waste Manage Assoc. 2010;60(8):968–76.
10. Matti Maricq M. Chemical characterization of particulate emissions from diesel engines: A review. J Aerosol Sci. 2007;38(11):1079–118.
11. Tien CL, Lee SC. Flame radiation. Prog Energy Combust Sci. 1982;8(1):41–59.
12. Haworth DC. Progress in probability density function methods for turbulent reacting flows. Prog Energy Combust Sci. 2010;36(2):168–259.
13. Wang H. Formation of nascent soot and other condensed-phase materials in flames. Proc Combust Inst. 2011;33(1):41–67.
14. Ospitali F, Smith DC, Lorblanchet M. Preliminary investigations by Raman microscopy of prehistoric pigments in the wall-painted cave at Roucadour, Quercy, France. J Raman Spectrosc. 2006;37(10):1063–71.
15. Pabst MA, Letofsky-Papst I, Bock E, Moser M, Dorfer L, Egarter-Vigl E, et al. The tattoos of the Tyrolean Iceman: a light microscopical, ultrastructural and element analytical study. J Archaeol Sci. 2009;36(10):2335–41.
16. Findik F, Yilmaz R, Köksal T. Investigation of mechanical and physical properties of several industrial rubbers. Mater Des. 2004;25(4):269–76.
17. Buschow KHJ. Encyclopedia of materials : science and technology. Elsevier; 2001
18. Song J, Song C, Lv G, Wang L, Bin F. Modification to Nagle/Strickland-Constable model with consideration of soot nanostructure effects. Combust Theory Model. 2012;16(4):639–49.
19. Vander Wal RL, Tomasek AJ. Soot nanostructure: dependence upon synthesis conditions. Combust Flame. 2004;136(1–2):129–40.

20. Vander Wal RL. Soot Nanostructure: Definition, Quantification and Implications. SAE International400 Commonwealth Drive, Warrendale, PA, United States; 2005.
21. Jung H, Kittelson DB, Zachariah MR. The influence of a cerium additive on ultrafine diesel particle emissions and kinetics of oxidation. Combust Flame. 2005;142(3):276–88.
22. Amirante R, Distaso E, Napolitano M, Tamburrano P, Di Iorio S, Sementa P, et al. Effects of lubricant oil on particulate emissions from port-fuel and direct-injection spark-ignition engines. Int J Engine Res. 2017;18(5–6):606–20.
23. Gidney JT, Twigg M V, Kittelson DB. Effect of Organometallic Fuel Additives on Nanoparticle Emissions from a Gasoline Passenger Car. Environ Sci Technol. 2010;44(7):2562–9.
24. Song J, Alam M, Boehman, AL. Impact of Alternative Fuels on Soot Properties and DPF Regeneration. Combust Sci Technol. 2007;179(9):1991–2037.
25. Boehman AL, Song J, Alam M. Impact of Biodiesel Blending on Diesel Soot and the Regeneration of Particulate Filters. Energy Fuels. 2005;19(5):1857–64.
26. van Gulijk C, Marijnissen JCM, Makkee M, Moulijn JA, Schmidt-Ott A. Measuring diesel soot with a scanning mobility particle sizer and an electrical low-pressure impactor: performance assessment with a model for fractal-like agglomerates. J Aerosol Sci. 2004;35(5):633–55.
27. Braun A, Huggins FE, Seifert S, Ilavsky J, Shah N, Kelly KE, et al. Size-range analysis of diesel soot with ultra-small angle X-ray scattering. Combust Flame. 2004;137(1–2):63–72.
28. Magnussen BF, Hjertager BH, Olsen JG, Bhaduri D. Effects of turbulent structure and local concentrations on soot formation and combustion in C2H2 diffusion flames. Seventeenth Symp Combust. 1979;17(1):1383–93.
29. D'Anna A, Kent JH. A model of particulate and species formation applied to laminar, nonpremixed flames for three aliphatic-hydrocarbon fuels. Combust Flame. 152(4):573–87.
30. D'Anna A, Violi A. Detailed Modeling of the Molecular Growth Process in Aromatic and Aliphatic Premixed Flames. Energy & Fuels. 2005;19(1):79–86.
31. Celnik MS, Sander M, Raj A, West RH, Kraft M. Modelling soot formation in a premixed flame using an aromatic-site soot model and an improved oxidation rate. Proc Combust Inst. 2009;32(1):639–46.
32. Omidvarborna H, Kumar A, Kim D-S. Recent studies on soot modeling for diesel combustion. Renew Sustain Energy Rev. 2015;48:635–47.
33. Mansurov ZA. Soot Formation in Combustion Processes (Review). Combust Explos Shock Waves. 2005;41(6):727–44.
34. Botero ML, Chen D, González-Calera S, Jefferson D, Kraft M. HRTEM evaluation of soot particles produced by the non-premixed combustion of liquid fuels. Carbon. 2016;96:459–73.
35. Miller JA, Melius CF. Kinetic and thermodynamic issues in the formation of aromatic compounds in flames of aliphatic fuels. Combust Flame. 91(1):21–39.
36. Frenklach M, Wang H. Detailed Mechanism and Modeling of Soot Particle Formation.
37. Violi A, D'Anna A, D'Alessio A. Modeling of particulate formation in combustion and pyrolysis. Chem Eng Sci. 54(15–16):3433–42.
38. Lapuerta M, Martos FJ, Herreros JM. Effect of engine operating conditions on the size of primary particles composing diesel soot agglomerates. J Aerosol Sci. 2007;38(4):455–66.
39. Cheng X, Chen L, Yan F, Dong S. Study on soot formation characteristics in the diesel combustion process based on an improved detailed soot model. Energy Convers Manag. 2013;75:1–10.

40. Ghiassi H, Perez P, Lighty JS, editors. The role of surface functional groups and nanostructure on the oxidation rate of soot derived from an oxygenated fuel. In: Western States Section of the Combustion Institute Spring Technical Meeting 2014. 2014.
41. Haynes BS, Wagner HG. Soot formation. Prog Energy Combust Sci. 1981;7(4):229–73.
42. Howard JB. Carbon addition and oxidation reactions in heterogeneous combustion and soot formation. Twenty-Third Symp Combust. 1991;23(1):1107–27.
43. Kennedy IM. Models of soot formation and oxidation. Prog Energy Combust Sci. 1997;23(2):95–132.
44. Tree DR, Svensson KI. Soot processes in compression ignition engines. Prog Energy Combust Sci. 33(3):272–309.
45. D'Anna A. Combustion-formed nanoparticles. Proc Combust Inst. 2009;32(1):593–613.
46. Karataş AE, Gülder ÖL. Soot formation in high pressure laminar diffusion flames. Prog Energy Combust Sci. 2012;38(6):818–45.
47. Tan JY, Bonatesta F, Ng HK, Gan S. Developments in computational fluid dynamics modelling of gasoline direct injection engine combustion and soot emission with chemical kinetic modelling. Appl Therm Eng. 2016;107:936–59.
48. Faraday M. (1861). W. Crookes (ed.). A Course of Six Lectures on the Chemical History of a Candle. Griffin, Bohn & Co. ISBN 1-4255-1974-1.
49. Kholghy MR, Kelesidis GA, Pratsinis SE. Reactive polycyclic aromatic hydrocarbon dimerization drives soot nucleation. Phys Chem Chem Phys. 2018;20(16):10926–38.
50. Sirignano M, Kent J, D'Anna A. Further experimental and modelling evidences of soot fragmentation in flames. Proc Combust Inst. 2015;35(2):1779–86.
51. Desgroux P, Faccinetto A, Mercier X, Mouton T, Aubagnac Karkar D, El Bakali A. Comparative study of the soot formation process in a "nucleation" and a "sooting" low pressure premixed methane flame. Combust Flame. 2017;184:153–66.
52. Miller JH. Aromatic excimers: evidence for polynuclear aromatic hydrocarbon condensation in flames. Proc Combust Inst. 2005;30(1):1381–8.
53. Vander Wal RL, Strzelec A, Toops TJ, Stuart Daw C, Genzale CL. Forensics of soot. Fuel. 2013;113:522–6.
54. Yehliu K, Vander Wal RL, Armas O, Boehman AL. Impact of fuel formulation on the nanostructure and reactivity of diesel soot. Combust Flame. 2012;159(12):3597–606.
55. Vander Wal RL, Yezerets A, Currier NW, Kim DH, Wang CM. HRTEM Study of diesel soot collected from diesel particulate filters. Carbon. 2007;45(1):70–7.
56. Schulz F, Commodo M, Kaiser K, Falco G, Minutolo P, Meyer G, et al. Insights into incipient soot formation by atomic force microscopy. Proc Combust Inst. 2019; 37(1):885–892.
57. Marinov NM, CASTALDI MJ, Melius CF, TSANG W. Aromatic and Polycyclic Aromatic Hydrocarbon Formation in a Premixed Propane Flame. Combust Sci Technol. 1997;128(1–6):295–342.
58. Norinaga K, Deutschmann O, Saegusa N, Hayashi J. Analysis of pyrolysis products from light hydrocarbons and kinetic modeling for growth of polycyclic aromatic hydrocarbons with detailed chemistry. J Anal Appl Pyrolysis. 2009;86(1):148–60.
59. Dobbins RA, Fletcher RA, Benner Jr. BA, Hoeft S. Polycyclic aromatic hydrocarbons in flames, in diesel fuels, and in diesel emissions. Combust Flame. 2006;144(4):773–81.

60. Shao C, Wang H, Atef N, Wang Z, Chen B, Almalki M, et al. Polycyclic aromatic hydrocarbons in pyrolysis of gasoline surrogates (n-heptane/iso-octane/toluene). Proc Combust Inst. 2019;37(1):993–1001.
61. Bohbot J, Gillet N, Benkenida A. IFP-C3D: an Unstructured Parallel Solver for Reactive Compressible Gas Flow with Spray. Oil Gas Sci Technol - Rev l'IFP. 2009;64(3):309–35.
62. Baburic M, Bogdan Z, Duic N. A new approach to CFD research: combining AVL's FIRE code with user combustion model. In: ITI 2002 Proceedings of the 24th International Conference on Information Technology Interfaces (IEEE Cat No02EX534). Univ. Zagreb;. p. 383–8.
63. CHEMKIN-PRO. San Diego: Reaction Design; 2018.
64. Violi A. Modeling of soot particle inception in aromatic and aliphatic premixed flames. Combust Flame. 2004;139(4):279–87.
65. Chenoweth K, C. T. van Duin A, Persson P, Cheng M-J, Oxgaard J, A. Goddard W. Development and Application of a ReaxFF Reactive Force Field for Oxidative Dehydrogenation on Vanadium Oxide Catalysts. J Phys Chem C. 2008;112(37):14645–54.
66. Han S, Li X, Nie F, Zheng M, Liu X, Guo L. Revealing the Initial Chemistry of Soot Nanoparticle Formation by ReaxFF Molecular Dynamics Simulations. Energy Fuels. 2017;31(8):8434–44.
67. Fitzer E, Kochling K-H, Boehm HP, Marsh H. Recommended terminology for the description of carbon as a solid (IUPAC Recommendations 1995). Pure Appl Chem. 67(3).
68. Ban S, Malek K, Huang C, Liu Z. A molecular model for carbon black primary particles with internal nanoporosity. Carbon. 2011;49(10):3362–70.
69. Watson AY, Valberg PA. Carbon Black and Soot: Two Different Substances. AIHAJ - Am Ind Hyg Assoc. 2001;62(2):218–28.
70. Maricq MM. An examination of soot composition in premixed hydrocarbon flames via laser ablation particle mass spectrometry. J Aerosol Sci. 2009;40(10):844–57.
71. Niessner R. The many faces of soot: characterization of soot nanoparticles produced by engines. Angew Chem Int Ed Engl. 2014;53(46):12366–79.
72. Stanmore BR, Brilhac J-F, Gilot P. The oxidation of soot: a review of experiments, mechanisms and models. Carbon. 39(15):2247–68.
73. Schenk M, Lieb S, Vieker H, Beyer A, Gölzhäuser A, Wang H, et al. Imaging Nanocarbon Materials: Soot Particles in Flames are Not Structurally Homogeneous. ChemPhysChem. 2013;14(14):3248–54.
74. Maricq MM, Xu N. The effective density and fractal dimension of soot particles from premixed flames and motor vehicle exhaust. J Aerosol Sci. 2004;35(10):1251–74.
75. Oberlin A, Thrower PA. Chemistry and Physics of Carbon, vol. 22. Marcel Dekker, Inc, New York. :1.
76. Ishiguro T, Suzuki N, Fujitani Y, Morimoto H. Microstructural changes of diesel soot during oxidation. Combust Flame. 1991;85(1):1–6.
77. Tighe CJ, Twigg M V, Hayhurst AN, Dennis JS. The kinetics of oxidation of Diesel soots and a carbon black (Printex U) by O2 with reference to changes in both size and internal structure of the spherules during burnout. Carbon. 2016;107:20–35.
78. Song J, Alam M, Boehman AL, Kim U. Examination of the oxidation behavior of biodiesel soot. Combust Flame. 2006;146(4):589–604.
79. Vander Wal RL, Tomasek AJ. Soot oxidation: Dependence upon initial nanostructure. Combust Flame. 2003;134(1–2):1–9.

80. Alfè M, Apicella B, Barbella R, Rouzaud J-N, Tregrossi A, Ciajolo A. Structure–property relationship in nanostructures of young and mature soot in premixed flames. Proc Combust Inst. 2009;32(1):697–704.
81. Vander Wal RL, Mueller CJ. Initial Investigation of Effects of Fuel Oxygenation on Nanostructure of Soot from a Direct-Injection Diesel Engine. Energy Fuels. 2006 Jan;20(6):2364–9.
82. Guerrero Peña GDJ, Alrefaai MM, Yang SY, Raj A, Brito JL, Stephen S, et al. Effects of methyl group on aromatic hydrocarbons on the nanostructures and oxidative reactivity of combustion-generated soot. Combust Flame. 2016;172:1–12.
83. Armas O, Yehliu K, Boehman AL. Effect of alternative fuels on exhaust emissions during diesel engine operation with matched combustion phasing. Fuel. 2010;89(2):438–56.
84. Li Z, Song C, Song J, Lv G, Dong S, Zhao Z. Evolution of the nanostructure, fractal dimension and size of in-cylinder soot during diesel combustion process. Combust Flame. 2011;158(8):1624–30.
85. Ye P, Sun C, Lapuerta M, Agudelo J, Vander Wal R, Boehman AL, et al. Impact of rail pressure and biodiesel fueling on the particulate morphology and soot nanostructures from a common-rail turbocharged direct injection diesel engine. Int J Engine Res. 2014;17(2):193–208.
86. Al-Qurashi K, Boehman AL. Impact of exhaust gas recirculation (EGR) on the oxidative reactivity of diesel engine soot. Combust Flame. 2008;155(4):675–95.
87. Stein SE, Fahr A. High-temperature stabilities of hydrocarbons. J Phys Chem. 1985;89(17):3714–25.
88. Dobbins RA, Fletcher RA, Lu W. Laser microprobe analysis of soot precursor particles and carbonaceous soot. Combust Flame. 1995;100(1):301–9.
89. Wang H, Frenklach M. A detailed kinetic modeling study of aromatics formation in laminar premixed acetylene and ethylene flames. Combust Flame. 110(1–2):173–221.
90. Richter H, Howard JB. Formation of polycyclic aromatic hydrocarbons and their growth to soot—a review of chemical reaction pathways. Prog Energy Combust Sci. 26(4–6):565–608.
91. Dobbins RA, Fletcher RA, Chang H-C. The evolution of soot precursor particles in a diffusion flame. Combust Flame. 1998;115(3):285–98.
92. D'Anna A, Violi A. A kinetic model for the formation of aromatic hydrocarbons in premixed laminar flames. Symp Combust. 27(1):425–33.
93. Appel J, Bockhorn H, Frenklach M. Kinetic modeling of soot formation with detailed chemistry and physics: laminar premixed flames of C2 hydrocarbons. Combust Flame. 2000;121(1–2):122–36.
94. Wang H, You X, Joshi A V, Davis SG, Laskin A, Egolfopoulos F, et al. USC mech version II. High-temperature combustion reaction model of H2/CO/C1-C4 compounds.
95. Slavinskaya NA, Frank P. A modelling study of aromatic soot precursors formation in laminar methane and ethene flames. Combust Flame. 2009;156(9):1705–22.
96. Raj A, Prada IDC, Amer AA, Chung SH. A reaction mechanism for gasoline surrogate fuels for large polycyclic aromatic hydrocarbons. Combust Flame. 2012;159(2):500–15.
97. Wang H, Deneys Reitz R, Yao M, Yang B, Jiao Q, Qiu L. Development of an n-heptane-n-butanol-PAH mechanism and its application for combustion and soot prediction. Combust Flame. 2013;160(3):504–19. 6
98. Keita M, Nicolle A, Bakali A El. A wide range kinetic modeling study of PAH formation from liquid transportation fuels combustion. Combust Flame. 2016;174:50–67.

99. Pope CJ, Miller JA. Exploring old and new benzene formation pathways in low-pressure premixed flames of aliphatic fuels. Proc Combust Inst. 28(2):1519–27.
100. Senosiain JP, Miller JA. The reaction of n- and i-C4H5 radicals with acetylene. J Phys Chem A. 2007;111(19):3740–7.
101. Tang W, Tranter RS, Brezinsky K. An optimized semidetailed submechanism of benzene formation from propargyl recombination. J Phys Chem A. 2006;110(6):2165–75.
102. Polino D, Parrinello M. Combustion chemistry via metadynamics: benzyl decomposition revisited. J Phys Chem A. 2015;119(6):978–89.
103. Melius CF, Colvin ME, Marinov NM, Pit WJ, Senkan SM. Reaction mechanisms in aromatic hydrocarbon formation involving the C5H5 cyclopentadienyl moiety. Symp Combust. 1996;26(1):685–92.
104. Mulholland JA, Lu M, Kim D-H. Pyrolytic growth of polycyclic aromatic hydrocarbons by cyclopentadienyl moieties. Proc Combust Inst. 2000;28(2):2593–9.
105. Lindstedt P, Maurice L, Meyer M. Thermodynamic and kinetic issues in the formation and oxidation of aromatic species. Faraday Discuss. 2002;119(0):409–32.
106. Frenklach M, Wang H. Detailed mechanism and modeling of soot particle formation. Springer Ser Chem Phys. 1994;(59).
107. Bittner JD, Howard JB. Composition profiles and reaction mechanisms in a near-sooting premixed benzene/oxygen/argon flame. Eighteenth Symp Combust. 1981;18(1):1105–16.
108. Yang T, Troy TP, Xu B, Kostko O, Ahmed M, Mebel AM, et al. Hydrogen-Abstraction/Acetylene-Addition Exposed. Angew Chemie Int Ed. 2016;55(48):14983–7.
109. Mebel AM, Georgievskii Y, Jasper AW, Klippenstein SJ. Pressure-dependent rate constants for PAH growth: formation of indene and its conversion to naphthalene. Faraday Discuss. 2016;195(0):637–70.
110. Lombaert K, Le Moyne L, Maleissye JT, Amouroux J. Experimental Study of PAH Engine Soot by Isotopic Tracing. Combust Sci Technol. 2006;178(4):707–28.
111. Kousoku A, Ashida R, Miyasato A, Miyake M, Miura K. Experimental study of gas-phase pyrolysis reaction of benzene to investigate the early stage of coke formation. J Chem Eng Japan. 2014;47(5):406–15.
112. Celnik M, Raj A, West R, Patterson R, Kraft M. Aromatic site description of soot particles. Combust Flame. 2008;155(1–2):161–80.
113. Lai JYW. Stochastic Simulation of Carbonaceous Nanoparticle Precursor Formation in Combustion. 2014;
114. Whitesides R, Frenklach M. Detailed kinetic Monte Carlo simulations of graphene-edge growth. J Phys Chem A. 2010;114(2):689–703.
115. Whitesides R, Domin D, Salomon-Ferrer R, Lester WA, Frenklach M. Graphene layer growth chemistry: five- and six-member ring flip reaction. J Phys Chem A. 2008;112(10):2125–30.
116. Shukla B, Koshi M. A novel route for PAH growth in HACA based mechanisms. Combust Flame. 2012;159(12):3589–96.
117. Johansson KO, Dillstrom T, Elvati P, Campbell MF, Schrader PE, Popolan-Vaida DM, et al. Radical–radical reactions, pyrene nucleation, and incipient soot formation in combustion. Proc Combust Inst. 2017;36(1):799–806.
118. Öktem B, Tolocka MP, Zhao B, Wang H, Johnston M V. Chemical species associated with the early stage of soot growth in a laminar premixed ethylene–oxygen–argon flame. Combust Flame. 2005;142(4):364–73.

119. Roy SP, Haworth DC. A Systematic Comparison of Detailed Soot Models and Gas-Phase Chemical Mechanisms in Laminar Premixed Flames. Combust Sci Technol. 2016;188(7):1021–53.
120. Dworkin SB, Zhang Q, Thomson MJ, Slavinskaya NA, Riedel U. Application of an enhanced PAH growth model to soot formation in a laminar coflow ethylene/air diffusion flame. Combust Flame. 2011;158(9):1682–95.
121. Zhao B, Yang Z, Li Z, Johnston M V, Wang H. Particle size distribution function of incipient soot in laminar premixed ethylene flames: effect of flame temperature. Proc Combust Inst. 2005;30(1):1441–8.
122. Zhang HR, Eddings EG, Sarofim AF, editors. Correlations between fuel structural features and benzene formation. In: AIChE Annual Meeting, Conference Proceedings. 2007.
123. Ashraf C, Jain A, Xuan Y, van Duin ACT. ReaxFF based molecular dynamics simulations of ignition front propagation in hydrocarbon/oxygen mixtures under high temperature and pressure conditions. Phys Chem Chem Phys. 2017;19(7):5004–17.
124. Ashraf C, van Duin ACT. Extension of the ReaxFF Combustion Force Field toward Syngas Combustion and Initial Oxidation Kinetics. J Phys Chem A. 2017;121(5):1051–68.
125. Mao Q, Ren Y, Luo KH, van Duin ACT. Dynamics and kinetics of reversible homo-molecular dimerization of polycyclic aromatic hydrocarbons. J Chem Phys. 2017;147(24):244305.
126. Mao Q, Hou D, Luo KH, You X. Dimerization of Polycyclic Aromatic Hydrocarbon Molecules and Radicals under Flame Conditions. J Phys Chem A. 2018;122(44):8701–8.
127. Mao Q, Luo KH. Trace metal assisted polycyclic aromatic hydrocarbons fragmentation, growth and soot nucleation. Proc Combust Inst. 2019;37(1): 1023-30
128. Chenoweth K, van Duin ACT, Goddard WA 3rd. ReaxFF reactive force field for molecular dynamics simulations of hydrocarbon oxidation. J Phys Chem A. 2008;112(5):1040–53.
129. van Duin ACT, Dasgupta S, Lorant F, Goddard WA. ReaxFF: A Reactive Force Field for Hydrocarbons. J Phys Chem A. 2001;105(41):9396–409.
130. Qian H-J, van Duin ACT, Morokuma K, Irle S. Reactive Molecular Dynamics Simulation of Fullerene Combustion Synthesis: ReaxFF vs DFTB Potentials. J Chem Theory Comput. 2011;7(7):2040–8.
131. Xue X, Meng L, Ma Y, Zhang C. Molecular Reactive Force-Field Simulations on the Carbon Nanocavities from Methane Pyrolisis. J Phys Chem C. 2017;121:7502–13.
132. Zhang C, Zhang C, Ma Y, Xue X. Imaging the C black formation by acetylene pyrolysis with molecular reactive force field simulations. Phys Chem Chem Phys. 2015;17(17):11469–80.
133. Frenklach M. Reaction mechanism of soot formation in flames. Phys Chem Chem Phys. 2002;4(11):2028–37.
134. Singh J, Patterson RIA, Kraft M, Wang H. Numerical simulation and sensitivity analysis of detailed soot particle size distribution in laminar premixed ethylene flames. Combust Flame. 2006;145(1–2):117–27.
135. Johansson KO, Head-Gordon MP, Schrader PE, Wilson KR, Michelsen HA. Resonance-stabilized hydrocarbon-radical chain reactions may explain soot inception and growth. Science. 2018;361(6406):997–1000.
136. Keller A, Kovacs R, Homann K-H. Large molecules, ions, radicals and small soot particles in fuel-rich hydrocarbon flames. Part IV. Large polycyclic aromatic hydrocarbons and their radicals in a fuel-rich benzene-oxygen flame. Phys Chem Chem Phys. 2000;2(8):1667–75.

137. Singh R, Frenklach M. A mechanistic study of the influence of graphene curvature on the rate of high-temperature oxidation by molecular oxygen. Carbon. 101:203–12.
138. Violi A, Sarofim AF, Truong TN. Mechanistic pathways to explain H/C ratio of soot precursors. Combust Sci Technol. 174(11–12):205–22.
139. Violi A, Venkatnathan A. Combustion-generated nanoparticles produced in a benzene flame: a multiscale approach. J Chem Phys. 2006;125(5):54302.
140. Izvekov S, Violi A. A Coarse-Grained Molecular Dynamics Study of Carbon Nanoparticle Aggregation. J Chem Theory Comput. 2006 Sep;2(3):504–12.
141. Violi A. Science-based model for particle formation from novel fuels. J Phys Conf Ser. 2008;125:12033.
142. Bockhorn H. Combustion generated fine carbonaceous particles. Karlsruhe: KIT Scientific Publishing; 2009.
143. Chung S-H. Computational Modeling of Soot Nucleation. PhD thesis. University of Michigan;
144. Elvati P, Dillstrom VT, Violi A. Oxygen driven soot formation. Proc Combust Inst. 2017;36(1):825–32.
145. Johansson KO, Dillstrom T, Monti M, El Gabaly F, Campbell MF, Schrader PE, et al. Formation and emission of large furans and oxygenated hydrocarbons from flames. Proc Natl Acad Sci U S A. 2016;113(30):8374–9.
146. Dillstrom T, Violi A. The effect of reaction mechanisms on the formation of soot precursors in flames. Combust Theory Model. 2017;21(1):23–34.
147. Mao Q, van Duin ACT, Luo KH. Formation of incipient soot particles from polycyclic aromatic hydrocarbons: A ReaxFF molecular dynamics study. Carbon. 2017;121(Supplement C):380–8.
148. Yuan H, Kong W, Liu F, Chen D. Study on soot nucleation and growth from PAHs and some reactive species at flame temperatures by ReaxFF molecular dynamics. Chem Eng Sci. 2019;195:748–57.
149. Frenklach M. Nucleation of Soot: Molecular Dynamics Simulation of Pyrene Dimerizaton. J Phys Chem A. 2014;118(8):1287-1292.
150. Balthasar M, Mauss F, Knobel A, Kraft M. Detailed modeling of soot formation in a partially stirred plug flow reactor. Combust Flame. 2002;128(4):395–409.
151. Mosbach S, Celnik MS, Raj A, Kraft M, Zhang HR, Kubo S, et al. Towards a detailed soot model for internal combustion engines. Combust Flame. 2009;156(6):1156–65.
152. Eaves NA, Dworkin SB, THOMSON MJ. The importance of reversibility in modeling soot nucleation and condensation processes. Proc Combust Inst. 2015;35(2):1787–94.
153. Eaves NA, Dworkin SB, Thomson MJ. Assessing relative contributions of PAHs to soot mass by reversible heterogeneous nucleation and condensation. Proc Combust Inst. 2017;36(1):935–45.
154. Kholghy MR, Eaves NA, Veshkini A, Thomson MJ. The role of reactive PAH dimerization in reducing soot nucleation reversibility. Proc Combust Inst. 2018
155. D'Alessio A, Barone AC, Cau R, D'Anna A, Minutolo P. Surface deposition and coagulation efficiency of combustion generated nanoparticles in the size range from 1 to 10 nm. Proc Combust Inst. 2005;30(2):2595–603.
156. Herdman JD, Miller JH. Intermolecular potential calculations for polynuclear aromatic hydrocarbon clusters. J Phys Chem A. 2008;112(28):6249–56.

157. Sabbah H, Biennier L, Klippenstein SJ, Sims IR, Rowe BR. Exploring the Role of PAHs in the Formation of Soot. J Phys Chem Lett. 2010;1(19):2962–7.
158. Totton TS, Misquitta AJ, Kraft M. A quantitative study of the clustering of polycyclic aromatic hydrocarbons at high temperatures. Phys Chem Chem Phys. 2012;14(12):4081–94.
159. Elvati P, Violi A. Thermodynamics of poly-aromatic hydrocarbon clustering and the effects of substituted aliphatic chains. Proc Combust Inst. 2013;34(1):1837–43.
160. Totton TS, Misquitta AJ, Kraft M. A First Principles Development of a General Anisotropic Potential for Polycyclic Aromatic Hydrocarbons. J Chem Theory Comput. 2010;6(3):683–95.
161. Totton TS, Misquitta AJ, Kraft M. A transferable electrostatic model for intermolecular interactions between polycyclic aromatic hydrocarbons. Chem Phys Lett. 510(1–3):154–60.
162. Chung S-H, Violi A. Peri-condensed aromatics with aliphatic chains as key intermediates for the nucleation of aromatic hydrocarbons. Proc Combust Inst. 2011;33(1):693–700.
163. Zhang H-B, Hou D, Law CK, You X. Role of Carbon-Addition and Hydrogen-Migration Reactions in Soot Surface Growth. J Phys Chem A. 2016;120(5):683–9.
164. Johansson KO, Zádor J, Elvati P, Campbell MF, Schrader PE, Richards-Henderson NK, et al. Critical Assessment of Photoionization Efficiency Measurements for Characterization of Soot-Precursor Species. J Phys Chem A. 2017;121(23):4475–85.
165. Martin JW, Slavchov RI, Yapp EKY, Akroyd J, Mosbach S, Kraft M. The Polarization of Polycyclic Aromatic Hydrocarbons Curved by Pentagon Incorporation: The Role of the Flexoelectric Dipole. J Phys Chem C. 2017;121(48):27154–63.
166. Menz WJ, Kraft M. The Suitability of Particle Models in Capturing Aggregate Structure and Polydispersity. Aerosol Sci Technol. 47(7):734–45.
167. Meyer CJ, Deglon DA. Particle collision modeling – A review. Miner Eng. 2011;24(8):719–30.
168. Richter H, Granata S, Green WH, Howard JB. Detailed modeling of PAH and soot formation in a laminar premixed benzene/oxygen/argon low-pressure flame. Proc Combust Inst. 2005;30(1):1397–405.
169. Raj A, Sander M, Janardhanan V, Kraft M. A study on the coagulation of polycyclic aromatic hydrocarbon clusters to determine their collision efficiency. Combust Flame. 2010;157(3):523–34.
170. Rogak SN. Modeling Small Cluster Deposition on the Primary Particles of Aerosol Agglomerates. Aerosol Sci Technol. 1997;26(2):127–40.
171. Patterson RIA, Kraft M. Models for the aggregate structure of soot particles. Combust Flame. 151(1–2):160–72.
172. Frenklach M, Harris SJ. Aerosol dynamics modeling using the method of moments. J Colloid Interface Sci. 1987;118(1):252–61.
173. Balthasar M, Frenklach M. Monte-Carlo simulation of soot particle coagulation and aggregation: The effect of a realistic size distribution. Proc Combust Inst. 2005;30(1):1467–74.
174. Xiong Y, Pratsinis SE. Formation of agglomerate particles by coagulation and sintering—Part I. A two-dimensional solution of the population balance equation. Aerosols Mater Process. 1993;24(3):283–300.
175. Park SH, Rogak SN. A novel fixed-sectional model for the formation and growth of aerosol agglomerates. J Aerosol Sci. 2004;35(11):1385–404.

176. Sander M, West RH, Celnik MS, Kraft M. A Detailed Model for the Sintering of Polydispersed Nanoparticle Agglomerates. Aerosol Sci Technol. 2009;43(10):978–89.
177. Sander M, Patterson RIA, Braumann A, Raj A, Kraft M. Developing the PAH-PP soot particle model using process informatics and uncertainty propagation. Proc Combust Inst. 2011;33(1):675–83.
178. Chen D, Totton TS, Akroyd JWJ, Mosbach S, Kraft M. Size-dependent melting of polycyclic aromatic hydrocarbon nano-clusters. Carbon. 67:79–91.
179. Chen D, Totton TS, Akroyd J, Mosbach S, Kraft M. Phase change of polycyclic aromatic hydrocarbon clusters by mass addition. Carbon. 77:25–35.
180. PARK SH, ROGAK SN, Bushe WK, WEN JZ, THOMSON MJ. An aerosol model to predict size and structure of soot particles. Combust Theory Model. 2005;9(3):499–513.
181. Mueller ME, Blanquart G, Pitsch H. A joint volume-surface model of soot aggregation with the method of moments. Proc Combust Inst. 2009;32 I:785–92.
182. Mueller ME, Blanquart G, Pitsch H. Hybrid Method of Moments for modeling soot formation and growth. Combust Flame. 2009;156(6):1143–55.
183. D'Anna A, Sirignano M, Kent J. A model of particle nucleation in premixed ethylene flames. Combust Flame. 2010;157(11):2106–15.
184. Veshkini A, Dworkin SB, Thomson MJ. Understanding soot particle size evolution in laminar ethylene/air diffusion flames using novel soot coalescence models. Combust Theory Model. 2016;20(4):707–34.
185. Hurt RH, Crawford GP, Shim H-S. Equilibrium nanostructure of primary soot particles. Proc Combust Inst. 2000;28(2):2539–46.
186. Bhowmick H, Biswas SK. Relationship between physical structure and tribology of single soot particles generated by burning ethylene. Tribol Lett. 2011;44(2):139–49.
187. Kholghy MR, Veshkini A, Thomson MJ. The core–shell internal nanostructure of soot – A criterion to model soot maturity. Carbon. 100:508–36.
188. Chen D, Zainuddin Z, Yapp E, Akroyd J, Mosbach S, Kraft M. A fully coupled simulation of PAH and soot growth with a population balance model. Proc Combust Inst. 2013;34(1):1827–35.
189. Veshkini A, Dworkin SB, THOMSON MJ. A soot particle surface reactivity model applied to a wide range of laminar ethylene/air flames. Combust Flame. 2015;161(12):3191–200.
190. Frenklach M, Wang H. Detailed modeling of soot particle nucleation and growth. Symp Combust. 1991;23(1):1559–66.
191. Kazakov A, Wang H, Frenklach M. Detailed modeling of soot formation in laminar premixed ethylene flames at a pressure of 10 bar. Combust Flame. 1995;100(1–2):111–20.
192. Singh J, Balthasar M, Kraft M, Wagner W. Stochastic modeling of soot particle size and age distributions in laminar premixed flames. Proc Combust Inst. 2005;30(1):1457–64.
193. Senneca O, Salatino P, Masi S. The influence of char surface oxidation on thermal annealing and loss of combustion reactivity. Proc Combust Inst. 2005;30(2):2223–30.
194. Senneca O, Salatino P. A semi-detailed kinetic model of char combustion with consideration of thermal annealing. Proc Combust Inst. 2011;33(2):1763–70.
195. Chen D, Akroyd J, Mosbach S, Kraft M. Surface reactivity of polycyclic aromatic hydrocarbon clusters. Proc Combust Inst. 2015;35(2):1811–8.
196. Leistner K, Nicolle A, Da Costa P. Detailed Kinetic Analysis of Soot Oxidation by NO 2 , NO, and NO + O 2. J Phys Chem C. 2012;116(7):4642–54.

197. Leistner K, Nicolle A, Berthout D, Costa P da. Kinetic modelling of the oxidation of a wide range of carbon materials. Combust Flame. 2012;159(1):64–76.
198. Guo H, Anderson PM, Sunderland PB. Optimized rate expressions for soot oxidation by OH and O2. Fuel. 2016;172:248–52.
199. Neoh KG, Howard JB, Sarofim AF. Soot Oxidation in Flames. In: Siegla DC, Smith GW, editors. Particulate Carbon: Formation During Combustion. Boston, MA: Springer US; 1981. p. 261-282
200. Sirignano M, Ghiassi H, D'Anna A, Lighty JS. Temperature and oxygen effects on oxidation-induced fragmentation of soot particles. Combust Flame. 2016;171:15–26.
201. Hurt RH, Calo JM. Semi-global intrinsic kinetics for char combustion modeling†. Combust Flame. 2001;125(3):1138–49.
202. Jaramillo IC, Gaddam CK, Vander Wal RL, Huang C-H, Levinthal JD, Lighty JS. Soot oxidation kinetics under pressurized conditions. Combust Flame. 2014;161(11):2951–65.
203. Bhatia SK, Perlmutter DD. A random pore model for fluid-solid reactions: I. Isothermal, kinetic control. AIChE J. 1980;26(3):379–86.
204. Smith IW. The combustion rates of coal chars: A review. Ninet Symp Combust. 1982 Jan;19(1):1045–65.
205. Neoh KG, Howard JB, Sarofim AF. Effect of oxidation on the physical structure of soot. Twent Symp Combust. 1985;20(1):951–7.
206. Nagle J, Strickland-Constable RF, editors. Oxidation of Carbon between 1000-2000 C. In: Proceedings of the fifth carbon conference. Pergamon Oxford; 1962.
207. Park C, Appleton JP. Shock-tube measurements of soot oxidation rates. Combust Flame. 1973;20(3):369–79.
208. Marsh H, Kuo K. Chapter 4 - Kinetics and Catalysis of Carbon Gasification. In: Introduction to Carbon Science. Butterworth-Heinemann; 1989. p. 107–51.
209. Miessen G, Behrendt F, Deutschmann O, Warnatz J. Numerical studies of the heterogeneous combustion of char using detailed chemistry. Proc 6th Intl Congr Toxic Combust. 2001;42(5–7):609–13.
210. Sánchez A, Mondragón F. Role of the Epoxy Group in the Heterogeneous CO2 Evolution in Carbon Oxidation Reactions. J Phys Chem C. 2007;111(2):612–7.
211. Li B, Su D. The Nucleophilicity of the Oxygen Functional Groups on Carbon Materials: A DFT Analysis. Chem – A Eur J. 2014;20(26):7890–4.
212. Dreyer DR, Park S, Bielawski CW, Ruoff RS. The chemistry of graphene oxide. Chem Soc Rev [Internet]. 2010;39(1):228–40. Available from: https://doi.org/10.1039/b917103g
213. Mehmood F, Pachter R, Lu W, Boeckl JJ. Adsorption and Diffusion of Oxygen on Single-Layer Graphene with Topological Defects. J Phys Chem C. 2013;117(20):10366–74.
214. Backreedy R, Jones JM, Pourkashanian M, Williams A. A study of the reaction of oxygen with graphite: Model chemistry. Faraday Discuss. 2002;119(0):385–94.
215. Sendt K, Haynes BS. Density functional study of the chemisorption of O2 on the armchair surface of graphite. Proc Combust Inst. 2005;30(2):2141–9.
216. SENDT K, HAYNES B. Density functional study of the chemisorption of O2 on the zig-zag surface of graphite. Combust Flame. 143(4):629–43.
217. Castro-Marcano F, Kamat AM, Russo Jr. MF, van Duin ACT, Mathews JP. Combustion of an Illinois No. 6 coal char simulated using an atomistic char representation and the ReaxFF reactive force field. Combust Flame. 2012;159(3):1272–85.

218. Li Z, Zhang W, Luo Y, Yang J, Hou JG. How graphene is cut upon oxidation? J Am Chem Soc. 2009;131(18):6320–1.
219. Hurt RH, Haynes BS. On the origin of power-law kinetics in carbon oxidation. Proc Combust Inst. 2005;30 II:2161–8.
220. Ghiassi H, Jaramillo IC, Lighty JS. Kinetics of Soot Oxidation by Molecular Oxygen in a Premixed Flame. Energy & Fuels. 2016;30(4):3463–72.
221. Ghiassi H, Toth P, Lighty JS. Sooting behaviors of n-butanol and n-dodecane blends. Combust Flame. 2014;161(3):671–9.
222. Seong HJ, Boehman AL. Studies of soot oxidative reactivity using a diffusion flame burner. Combust Flame. 2012;159(5):1864–75.
223. Raj A, Yang SY, Cha D, Tayouo R, Chung SH. Structural effects on the oxidation of soot particles by O2. Combust Flame. 2013;160(9):1812–26.
224. Frenklach M, Liu Z, Singh RI, Galimova GR, Azyazov VN, Mebel AM. Detailed, sterically-resolved modeling of soot oxidation: Role of O atoms, interplay with particle nanostructure, and emergence of inner particle burning. Combust Flame. 2018;188(Supplement C):284–306.
225. Frenklach M. New form for reduced modeling of soot oxidation: Accounting for multi-site kinetics and surface reactivity. Combust Flame. 2019;201:148–59.
226. Sirignano M, Kent J, D'Anna A. Modeling Formation and Oxidation of Soot in Nonpremixed Flames. Energy & Fuels. 2013;27(4):2303–15.
227. Strzelec A, Toops TJ, Daw CS. Oxygen reactivity of devolatilized diesel engine particulates from conventional and biodiesel fuels. Energy and Fuels. 2013;27(7):3944–51.
228. Cygan RT, Kubicki JD. Molecular Modeling Theory : Applications in the Geosciences
229. Razavi S, Koplik J, Kretzschmar I. Molecular Dynamics Simulations: Insight into Molecular Phenomena at Interfaces. Langmuir. 2014;30(38):11272–83.
230. Kollman P. Molecular Modeling. Annu Rev Phys Chem. 1987;38(1):303–16.
231. Sturluson A, Huynh MT, Kaija A, Laird C, Yoon S, Hou F, et al. The Role of Molecular Modeling & Simulation in the Discovery and Deployment of Metal-Organic Frameworks for Gas Storage and Separation. 2019
232. Mancera RL. Molecular modeling of hydration in drug design. Curr Opin Drug Discov Devel. 2007;10(3):275–80.
233. Allen MP, Tildesley DJ. Computer simulation of liquids.
234. Haile JM. Molecular dynamics simulation. Wiley professional paperback series. New York: Wiley; 1997. 489 p.
235. Frenkel D, Smit B. Understanding molecular simulation. 2nd ed. Vol. v. 1 H1-, Computational science series. San Diego, Calif.; London: Academic; 2002.
236. McQuarrie DA. Statistical mechanics. Sausalito, Calif. 2000.
237. Landau LD, Lifshitz EM. Statistical Physics. Vol. vol.5 TS. Elsevier Science; 2013.
238. Senftle TP, Hong S, Islam MM, Kylasa SB, Zheng Y, Shin YK, et al. The ReaxFF reactive force-field: development, applications and future directions. Npj Comput Mater. 2016;2:15011
239. Liang T, Shin YK, Cheng Y-T, Yilmaz DE, Vishnu KG, Verners O, et al. Reactive Potentials for Advanced Atomistic Simulations. Annu Rev Mater Res. 2013;43(1):109–29.
240. Iype E, Hütter M, Jansen APJ, Nedea S V, Rindt CCM. Parameterization of a reactive force field using a Monte Carlo algorithm. J Comput Chem. 2013;34(13):1143–54.

241. Barcaro G, Monti S, Sementa L, Carravetta V. Parametrization of a Reactive Force Field (ReaxFF) for Molecular Dynamics Simulations of Si Nanoparticles. J Chem Theory Comput. 2017;13(8):3854–61.
242. Hernández-Rivera E, Chowdhury S, Coleman SP, Ghassemi P, Tschopp MA. Integrating exploratory data analytics into ReaxFF parameterization. MRS Commun. 2018;8(03):1300–10.
243. Wang Y, Raj A, Chung SH. A PAH growth mechanism and synergistic effect on PAH formation in counterflow diffusion flames. Combust Flame. 2013;160(9):1667–76.
244. Daly DT, Nag P. Combustion Modeling of Soot Reduction in Diesel and Alternate Fuels using CHEMKIN®. Vol. 110, SAE Transactions. SAE International; 2001. p. 1448–58.
245. Glarborg P, Miller JA, Kee RJ. Kinetic modeling and sensitivity analysis of nitrogen oxide formation in well-stirred reactors. Combust Flame. 1986;65(2):177–202.
246. Brady BB, Robbin Martin L. Use of SURFACE CHEMKIN to model multiphase atmospheric chemistry: Application to nitrogen tetroxide spills. Atmos Environ. 1995;29(6):715–26.
247. Gordon S, Mcbride BJ. Computer Program for Calculation of Complex Chemical Equilibrium Compositions, Rocket Performance, Incident and Reflected Shocks, and Chapman-Jouguet Detonations. Interim Revision. 1976.
248. Park S, Wang Y, Chung SH, Sarathy SM. Compositional effects on PAH and soot formation in counterflow diffusion flames of gasoline surrogate fuels. Combust Flame. 2017;178(Supplement C):46–60.
249. An Y, Li X, Teng S, Wang K, Pei Y, Qin J, et al. Development of a soot particle model with PAHs as precursors through simulations and experiments. Fuel. 2016;179:246–57.
250. Raj A, Al Rashidi MJ, Chung SH, Sarathy SM. PAH Growth Initiated by Propargyl Addition: Mechanism Development and Computational Kinetics. J Phys Chem A. 2014;118(16):2865–85.
251. He Z, Zhou K, Xiao M, Wei F. Simulation of Soot Size Distribution in a Counterflow Flame. Int J Chem React Eng. 2015;13(1):95–101.
252. Pischinger F. Hansen J. SH. Grundlagen und Entwicklungslinien des dieselmotorischen Brennverfahren. VDI-Berichte. :61–93.
253. Inal F, Senkan SM. Effects of oxygenate additives on polycyclic aromatic hydrocarbons(pahs) and soot formation. Combust Sci Technol. 2002;174(9):1–19.
254. Desgroux P, Faccinetto A, Mercier X, Mouton T, Aubagnac Karkar D, El Bakali A. Comparative study of the soot formation process in a “nucleation” and a “sooting” low pressure premixed methane flame. Combust Flame. 2017;184:153–66.
255. Yehliu K, Armas O, Vander Wal RL, Boehman AL. Impact of engine operating modes and combustion phasing on the reactivity of diesel soot. Combust Flame. 2013;160(3):682–91.
256. Ergut A, Levendis YA, Richter H, Howard JB, Carlson J. The effect of equivalence ratio on the soot onset chemistry in one-dimensional, atmospheric-pressure, premixed ethylbenzene flames. Combust Flame. 2007;151(1–2):173–95.
257. Kellerer H, Müller A, Bauer H-J, Wittig S. Soot Formation in a Shock Tube under Elevated Pressure Conditions. Combust Sci Technol. 1996;113(1):67–80.
258. Müller A, Wittig S. Experimental Study on the Influence of Pressure on Soot Formation in a Shock Tube. In Springer, Berlin, Heidelberg; 1994. p. 350–70.
259. Olson DB, Pickens JC, Gill RJ. The effects of molecular structure on soot formation II. Diffusion flames. Combust Flame. 1985;62(1):43–60.

260. Akihama K, Takatori Y, Inagaki K, Sasaki S, Dean AM. Mechanism of the Smokeless Rich Diesel Combustion by Reducing Temperature. 2001.
261. Ono K, Matsukawa Y, Dewa K, Watanabe A, Takahashi K, Saito Y, et al. Formation mechanisms of soot from high-molecular-weight polycyclic aromatic hydrocarbons. Combust Flame. 2015;162(6):2670–8.
262. Jia Z, Huang H, Zhou W, Qi F, Zeng M. Experimental and Modeling Investigation of *n* -Decane Pyrolysis at Supercritical Pressures. Energy & Fuels. 2014;28(9):6019–28.
263. Bagley SP, Wornat MJ. Identification of Five- to Seven-Ring Polycyclic Aromatic Hydrocarbons from the Supercritical Pyrolysis of *n* -Decane. Energy & Fuels. 2011;25(10):4517–27.
264. Sinha S, Rahman RK, Raj A. On the role of resonantly stabilized radicals in polycyclic aromatic hydrocarbon (PAH) formation: pyrene and fluoranthene formation from benzyl–indenyl addition. Phys Chem Chem Phys. 2017;19(29):19262–78.
265. Goddard WA, van Duin A, Chenoweth K, Cheng M-J, Pudar S, Oxgaard J, et al. Development of the ReaxFF reactive force field for mechanistic studies of catalytic selective oxidation processes on BiMoO x. Top Catal. 2006;38(1–3):93–103.
266. Chenoweth K, van Duin ACT, Goddard III WA. The ReaxFF Monte Carlo Reactive Dynamics Method for Predicting Atomistic Structures of Disordered Ceramics: Application to the Mo3VOx Catalyst. Angew Chemie Int Ed. 2009;48(41):7630–4.
267. Shin YK, Kwak H, Vasenkov A V., Sengupta D, van Duin ACT. Development of a ReaxFF Reactive Force Field for Fe/Cr/O/S and Application to Oxidation of Butane over a Pyrite-Covered Cr_2O_3 Catalyst. ACS Catal. 2015;5(12):7226–36.
268. Zou C, van Duin ACT, Sorescu DC. Theoretical Investigation of Hydrogen Adsorption and Dissociation on Iron and Iron Carbide Surfaces Using the ReaxFF Reactive Force Field Method. Top Catal. 2012;55(5–6):391–401.
269. Wen J, Ma T, Zhang W, Psofogiannakis G, van Duin ACT, Chen L, et al. Atomic insight into tribochemical wear mechanism of silicon at the Si/SiO2 interface in aqueous environment: Molecular dynamics simulations using ReaxFF reactive force field. Appl Surf Sci. 2016;390:216–23.
270. Kulkarni AD, Truhlar DG, Goverapet Srinivasan S, van Duin ACT, Norman P, Schwartzentruber TE. Oxygen Interactions with Silica Surfaces: Coupled Cluster and Density Functional Investigation and the Development of a New ReaxFF Potential. J Phys Chem C. 2013;117(1):258–69.
271. Rahaman O, van Duin ACT, Bryantsev VS, Mueller JE, Solares SD, Goddard WA, et al. Development of a ReaxFF Reactive Force Field for Aqueous Chloride and Copper Chloride. J Phys Chem A. 2010;114(10):3556–68.
272. Achtyl JL, Unocic RR, Xu L, Cai Y, Raju M, Zhang W, et al. Aqueous proton transfer across single-layer graphene. Nat Commun. 2015;6(1):6539.
273. Liu L, Liu Y, Zybin S V, Sun H, Goddard WA. ReaxFF-lg: Correction of the ReaxFF Reactive Force Field for London Dispersion, with Applications to the Equations of State for Energetic Materials. J Phys Chem A. 2011;115(40):11016–22.
274. Verlackt CCW, Neyts EC, Jacob T, Fantauzzi D, Golkaram M, Shin Y-K, et al. Atomic-scale insight into the interactions between hydroxyl radicals and DNA in solution using the ReaxFF reactive force field. New J Phys. 2015;17(10):103005.

275. Han S, van Duin ACT, Goddard WA, Strachan A. Thermal Decomposition of Condensed-Phase Nitromethane from Molecular Dynamics from ReaxFF Reactive Dynamics. J Phys Chem B. 2011;115(20):6534–40.
276. Strachan A, van Duin ACT, Chakraborty D, Dasgupta S, Goddard WA. Shock Waves in High-Energy Materials: The Initial Chemical Events in Nitramine RDX. Phys Rev Lett. 2003;91(9):098301.
277. Chenoweth K, van Duin ACT, Goddard WA 3rd. ReaxFF reactive force field for molecular dynamics simulations of hydrocarbon oxidation. J Phys Chem A. 2008;112(5):1040–53.
278. Chenoweth K, van Duin ACT, Dasgupta S, Goddard WA 3rd. Initiation mechanisms and kinetics of pyrolysis and combustion of JP-10 hydrocarbon jet fuel. J Phys Chem A. 2009;113(9):1740–6.
279. Salmon E, van Duin ACT, Lorant F, Marquaire P-M, Goddard WA. Early maturation processes in coal. Part 2: Reactive dynamics simulations using the ReaxFF reactive force field on Morwell Brown coal structures. Org Geochem. 2009;40(12):1195–209.
280. Zhang J, Weng X, Han Y, Li W, Cheng J, Gan Z, et al. The effect of supercritical water on coal pyrolysis and hydrogen production: A combined ReaxFF and DFT study. Fuel. 2013;108:682–90.
281. Zheng M, Li X, Liu J, Wang Z, Gong X, Guo L, et al. Pyrolysis of Liulin Coal Simulated by GPU-Based ReaxFF MD with Cheminformatics Analysis. Energy & Fuels. 2014;28(1):522–34.
282. Zheng M, Li X, Liu J, Guo L. Initial Chemical Reaction Simulation of Coal Pyrolysis via ReaxFF Molecular Dynamics. Energy & Fuels. 2013;27(6):2942–51.
283. Srinivasan SG, van Duin ACT, Ganesh P. Development of a ReaxFF Potential for Carbon Condensed Phases and Its Application to the Thermal Fragmentation of a Large Fullerene. J Phys Chem A. 2015;119(4):571–80.
284. Mueller JE, van Duin ACT, Goddard WA. Development and Validation of ReaxFF Reactive Force Field for Hydrocarbon Chemistry Catalyzed by Nickel. J Phys Chem C. 2010;114(11):4939–49.
285. Kohn W, Sham LJ. Self-Consistent Equations Including Exchange and Correlation Effects. Phys Rev. 1965;140(4A):A1133–8.
286. Hohenberg P, Kohn W. Inhomogeneous Electron Gas. Phys Rev. 1964;136(3B):B864–71.
287. JÓNSSON H, MILLS G, JACOBSEN KW. Nudged elastic band method for finding minimum energy paths of transitions. In: Classical and Quantum Dynamics in Condensed Phase Simulations. WORLD SCIENTIFIC; 1998. p. 385–404.
288. Becke AD. Density-functional exchange-energy approximation with correct asymptotic behavior. Phys Rev A. 1988;38(6):3098–100.
289. Lee C, Yang W, Parr RG. Development of the Colle-Salvetti correlation-energy formula into a functional of the electron density. Phys Rev B. 1988;37(2):785–9.
290. E. Davico G, M. Bierbaum V, H. DePuy C, Barney Ellison G, R. Squires R. The C-H Bond Energy of Benzene. J Am Chem Soc. 2002;117(9):2590–9.
291. Totton TS, Misquitta AJ, Kraft M. Assessing the polycyclic aromatic hydrocarbon anisotropic potential with application to the exfoliation energy of graphite. J Phys Chem A. 2011;115(46):13684–93.
292. Grimme S. Accurate description of van der Waals complexes by density functional theory including empirical corrections. J Comput Chem. 2004;25(12):1463–73.

293. Iavarone S, Pascazio L, Sirignano M, Candia A, Fierro A, Arcangelis L, et al. Molecular dynamics simulations of incipient carbonaceous nanoparticle formation at flame conditions. Combust Theory Model. 2017;21(1):49–61.
294. Jin H, Xu B, Li H, Ku X, Fan J. Numerical investigation of coal gasification in supercritical water with the ReaxFF molecular dynamics method. Int J Hydrogen Energy. 2018;43(45):20513–24.
295. Jin H, Wu Y, Guo L, Su X. Molecular dynamic investigation on hydrogen production by polycyclic aromatic hydrocarbon gasification in supercritical water. Int J Hydrogen Energy. 2016;41(6):3837–43.
296. Chen Z, Sun W, Zhao L. Combustion Mechanisms and Kinetics of Fuel Additives: A ReaxFF Molecular Simulation. Energy & Fuels. 2018;32(11):11852–63.
297. Jensen BD, Wise KE, Odegard GM. The effect of time step, thermostat, and strain rate on ReaxFF simulations of mechanical failure in diamond, graphene, and carbon nanotube. J Comput Chem. 2015;36(21):1587–96.
298. Jensen BD, Bandyopadhyay A, Wise KE, Odegard GM. Parametric Study of ReaxFF Simulation Parameters for Molecular Dynamics Modeling of Reactive Carbon Gases. J Chem Theory Comput. 2012 Nov;8(9):3003–8.
299. Buch_Soot-Formation-in-Combustion_Bockhorn_1994
300. Mouton T, Mercier X, Desgroux P. Evidence of Nucleation Flames: A Valuable Tool for the Study of Soot Particles Inception. Proceedings of the European Combustion Meeting 2015
301. Adamson BD, Skeen SA, Ahmed M, Hansen N. Detection of Aliphatically Bridged Multi-Core Polycyclic Aromatic Hydrocarbons in Sooting Flames with Atmospheric-Sampling High-Resolution Tandem Mass Spectrometry. J Phys Chem A. 2018;122(48):9338–49.
302. Cain J, Laskin A, Kholghy MR, Thomson MJ, Wang H. Molecular characterization of organic content of soot along the centerline of a coflow diffusion flame. Phys Chem Chem Phys. 2014;16(47):25862–75.
303. D'Anna A, Kent JH. Modeling of particulate carbon and species formation in coflowing diffusion flames of ethylene. Combust Flame. 144(1–2):249–60.
304. Lowe JS, Lai JYW, Elvati P, Violi A. Towards a predictive model for polycyclic aromatic hydrocarbon dimerization propensity. Proc Combust Inst. 2015;35(2):1827–32.
305. Baerends EJ, Ziegler T, Atkins AJ, Autschbach J, Bashford D, Baseggio O, et al. ADF2017, SCM, Theoretical Chemistry, Vrije Universiteit, Amsterdam, The Netherlands, https://www.scm.com
306. Naber JD, Siebers DL. Effects of Gas Density and Vaporization on Penetration and Dispersion of Diesel Sprays. In SAE International; 1996.
307. Stein SE, Brown RL. Prediction of carbon-hydrogen bond dissociation energies for polycyclic aromatic hydrocarbons of arbitrary size. J Am Chem Soc. 1991;113(3):787–93.
308. Cynthia Barckholtz, Timothy A. Barckholtz and, Hadad CM. C−H and N−H Bond Dissociation Energies of Small Aromatic Hydrocarbons. 1999;
309. Luo Y-R. Handbook of bond dissociation energies in organic compounds. CRC Press; 2003. 380 p.
310. Irimiea C, Faccinetto A, Mercier X, Ortega I-K, Nuns N, Therssen E, et al. Unveiling trends in soot nucleation and growth: When secondary ion mass spectrometry meets statistical analysis. Carbon. 2019;144:815–30.

311. Apicella B, Carpentieri A, Alfè M, Barbella R, Tregrossi A, Pucci P, et al. Mass spectrometric analysis of large PAH in a fuel-rich ethylene flame. Proc Combust Inst. 2007;31(1):547–53.
312. Johansson KO, Lai JYW, Skeen SA, Popolan-Vaida DM, Wilson KR, Hansen N, et al. Soot precursor formation and limitations of the stabilomer grid. Proc Combust Inst. 2015;35(2):1819–26.
313. Faccinetto A, Desgroux P, Ziskind M, Therssen E, Focsa C. High-sensitivity detection of polycyclic aromatic hydrocarbons adsorbed onto soot particles using laser desorption/laser ionization/time-of-flight mass spectrometry: An approach to studying the soot inception process in low-pressure flames. Combust Flame. 2011;158(2):227–39.
314. Öktem B, Tolocka MP, Zhao B, Wang H, Johnston M V. Chemical species associated with the early stage of soot growth in a laminar premixed ethylene–oxygen–argon flame. Combust Flame. 2005;142(4):364–73.
315. Botero ML, Sheng Y, Akroyd J, Martin J, Dreyer JAH, Yang W, et al. Internal structure of soot particles in a diffusion flame. Carbon. 2019;141:635–42.
316. Liu Y, Song C, Lv G, Cao X, Wang L, Qiao Y, et al. Surface functional groups and sp 3 /sp 2 hybridization ratios of in-cylinder soot from a diesel engine fueled with n -heptane and n -heptane/toluene. Fuel. 2016;179:108–13.
317. Wang L, Song C, Song J, Lv G, Pang H, Zhang W. Aliphatic C–H and oxygenated surface functional groups of diesel in-cylinder soot: Characterizations and impact on soot oxidation behavior. Proc Combust Inst. 2013;34(2):3099–106.
318. Le KC, Lefumeux C, Bengtsson P-E, Pino T. Direct observation of aliphatic structures in soot particles produced in low-pressure premixed ethylene flames via online Raman spectroscopy. Proc Combust Inst. 2019;37(1):869–76.
319. Raj A, Man PLW, Totton TS, Sander M, Shirley RA, Kraft M. New polycyclic aromatic hydrocarbon (PAH) surface processes to improve the model prediction of the composition of combustion-generated PAHs and soot. Carbon. 48(2):319–32.
320. Frenklach M, Moriarty NW, Brown NJ. Hydrogen migration in polyaromatic growth. Symp Combust. 1998;27(2):1655–61.
321. Jaramillo IC, Gaddam CK, Vander Wal RL, Lighty JS. Effect of nanostructure, oxidative pressure and extent of oxidation on model carbon reactivity. Combust Flame. 2015;162(5):1848–56.
322. Jaramillo IC, Gaddam CK, Vander Wal RL, Huang C-H, Levinthal JD, Lighty JS. Soot oxidation kinetics under pressurized conditions. Combust Flame. 2014;161(11):2951–65.
323. Edwards DE, Zubarev DY, Lester WA, Frenklach M. Pathways to soot oxidation: reaction of OH with phenanthrene radicals. J Phys Chem A. 2014;118(37):8606–13.
324. Singh RI, Mebel AM, Frenklach M. Oxidation of Graphene-Edge Six- and Five-Member Rings by Molecular Oxygen. J Phys Chem A. 2015;119(28):7528–47.
325. Ono K, Matsukawa Y, Dewa K, Watanabe A, Takahashi K, Saito Y, et al. Formation mechanisms of soot from high-molecular-weight polycyclic aromatic hydrocarbons. Combust Flame. 2015;162(6):2670–8.
326. Du DX, Axelbaum RL, Law CK. The influence of carbon dioxide and oxygen as additives on soot formation in diffusion flames. Symp Combust. 1991;23(1):1501–7.
327. Liu H, Wang Z, Zhang J, Wang J, Shuai S. Study on combustion and emission characteristics of Polyoxymethylene Dimethyl Ethers/diesel blends in light-duty and heavy-duty diesel engines. Appl Energy. 2017;185:1393–402.

328. Pellegrini L, Marchionna M, Patrini R, Beatrice C, Del Giacomo N, Guido C. Combustion Behaviour and Emission Performance of Neat and Blended Polyoxymethylene Dimethyl Ethers in a Light-Duty Diesel Engine. 2012.
329. Brezinsky K. The high-temperature oxidation of aromatic hydrocarbons. Prog Energy Combust Sci. 1986;12(1):1–24.
330. Döntgen M, Przybylski-Freund M-D, Kröger LC, Kopp WA, Ismail AE, Leonhard K. Automated discovery of reaction pathways, rate constants, and transition states using reactive molecular dynamics simulations. J Chem Theory Comput. 2015;11(6):2517–24.
331. Nicovich JM, Gump CA, Ravishankara AR. Rates of reactions of atomic oxygen(3P) with benzene and toluene. J Phys Chem. 1982;86(9):1684–90.
332. Tabares FL, Gonzalez Urena A. Rate constant for the reaction of atomic oxygen(3P) with pyridine from 323 to 473 K. J Phys Chem. 1983;87(24):4933–6.
333. Leidreiter HI, Wagner HG. An Investigation of the Reaction between O(^{3} P) and Benzene at High Temperatures. Zeitschrift für Phys Chemie. 1989;165(1):1–7.
334. Crolla D, Foster DE, Kobayashi T, Vaughan NTS-CM-C, editors. Encyclopedia of Automotive Engineering. Chichester, UK: John Wiley & Sons, Ltd; 2014.
335. Ko T, Adusei GY, Fontijn A. Kinetics of the atomic oxygen(3P) + benzene reaction over a wide temperature range. J Phys Chem. 1991;95(22):8745–8.
336. Baulch DL, Bowman CT, Cobos CJ, Cox RA, Just T, Kerr JA, et al. Evaluated Kinetic Data for Combustion Modeling: Supplement II. J Phys Chem Ref Data. 2005;34(3):757–1397.
337. Tappe M, Schliephake V, Wagner HG. Reactions of Benzene, Toluene and Ethylbenzene with Atomic Oxygen (O ^{3} P) in the Gas Phase. Zeitschrift für Phys Chemie. 1989;162(2):129–45.
338. and JKP, Davis SR. Photochemical Reaction of Ozone and Benzene: An Infrared Matrix Isolation Study. 1999
339. Taatjes CA, Osborn DL, Selby TM, Meloni G, Trevitt AJ, Epifanovsky E, et al. Products of the Benzene + O(^{3} P) Reaction †. J Phys Chem A. 2010;114(9):3355–70.
340. Thanh Lam Nguyen, Jozef Peeters and, Vereecken L. Theoretical Reinvestigation of the O(3P) + C6H6 Reaction: Quantum Chemical and Statistical Rate Calculations†. 2007
341. and JMA, Domingo VM. Mechanism for the Gas-Phase Reaction between Formaldehyde and Hydroperoxyl Radical. A Theoretical Study. 2005
342. Skodje RT, Tomlin AS, Klippenstein SJ, Harding LB, Davis MJ. Theoretical Validation of Chemical Kinetic Mechanisms: Combustion of Methanol. J Phys Chem A. 2010;114(32):8286–301.
343. Jasper AW, Klippenstein SJ, Harding LB. Theoretical rate coefficients for the reaction of methyl radical with hydroperoxyl radical and for methylhydroperoxide decomposition. Proc Combust Inst. 2009;32(1):279–86.
344. Hoare DE, Milne GS. Role of hydroxyl and hydroperoxyl radicals in slow combustion of methane. Trans Faraday Soc. 1967;63(0):101.
345. Held TJ, Dryer FL. A comprehensive mechanism for methanol oxidation. Int J Chem Kinet. 1998;30(11):805–30.
346. Bittker, A. D. Detailed mechanism of toluene oxidation and comparison with benzene. 1988
347. Zhang X, Kumar A, Arnold U, Sauer J. Biomass-derived Oxymethylene Ethers as Diesel Additives: A Thermodynamic Analysis. Energy Procedia. 2014;61:1921–4.
348. Lumpp B, Rothe D, Pastötter C, Lämmermann R, Jacob E. OXYMETHYLENE ETHERS AS DIESEL FUEL ADDITIVES OF THE FUTURE. MTZ Worldw. 2011;72(3):34–8.

349. Qi DH, Chen H, Geng LM, Bian YZ, Ren XC. Performance and combustion characteristics of biodiesel–diesel–methanol blend fuelled engine. Appl Energy. 2010;87(5):1679–86.
350. Yao C, Cheung CS, Cheng C, Wang Y, Chan TL, Lee SC. Effect of Diesel/methanol compound combustion on Diesel engine combustion and emissions. Energy Convers Manag. 2008;49(6):1696–704.
351. Selby K, Waddington DJ. Reactions of oxygenated radicals in the gas phase. Part 4. Reactions of methylperoxyl and methoxyl radicals. J Chem Soc Perkin Trans 2. 1979;(9):1259.
352. Sorescu DC,, Jordan KD, Avouris P. Theoretical Study of Oxygen Adsorption on Graphite and the (8,0) Single-walled Carbon Nanotube. 2001
353. Margulis VA, Muryumin EE. Atomic oxygen chemisorption on the sidewall of zigzag single-walled carbon nanotubes. Phys Rev B. 2007;75(3):035429.
354. Taatjes CA, Osborn DL, Selby TM, Meloni G, Trevitt AJ, Epifanovsky E, et al. Products of the Benzene + O(^{3} P) Reaction †. J Phys Chem A. 2010;114(9):3355–70.
355. Barone V, Lelj F, Iaconis E, Illas F, Russo N, Jounou A. Quantum-mechanical study of the chemisorption of atomic and molecular oxygen on graphite clusters. J Mol Struct THEOCHEM. 1986;136(3–4):313–22.
356. Ossler F, Vallenhag L, Canton SE, Mitchell JBA, Le Garrec J-L, Sztucki M, et al. Dynamics of incipient carbon particle formation in a stabilized ethylene flame by in situ extended-small-angle- and wide-angle X-ray scattering. Carbon. 2013;51:1–19.
357. Gaddam CK, Vander Wal RL, Chen X, Yezerets A, Kamasamudram K. Reconciliation of carbon oxidation rates and activation energies based on changing nanostructure. Carbon. 2016;98:545–56.
358. Veshkini A, Eaves NA, Dworkin SB, Thomson MJ. Application of PAH-condensation reversibility in modeling soot growth in laminar premixed and nonpremixed flames. Combust Flame. 2016;167:335–52.
359. Totton TS, Chakrabarti D, Misquitta AJ, Sander M, Wales DJ, Kraft M. Modelling the internal structure of nascent soot particles. Combust Flame. 2010;157(5):909–14.
360. Wang Q-D, Hua X-X, Cheng X-M, Li J-Q, Li X-Y. Effects of fuel additives on the thermal cracking of n-decane from reactive molecular dynamics. J Phys Chem A. 2012;116(15):3794–801.

Titre : Développement d'une approche multi-échelle utilisant la cinétique chimique et la dynamique moléculaire des champs de forces réactives pour modéliser la formation et l'oxydation de la suie.

Mots clés : formation de suie, oxydation de suie, ReaxFF, l'approche multi-échelle

Résumé : Dans cette thèse doctorale, une approche multi-échelles a été appliquée aux processus de modélisation pendant la formation de la suie et l'oxydation précoce de la suie. En effet, des calculs cinétiques macroscopiques en phase gazeuse ont été réalisés, pour modéliser la combustion d'un combustible fossile modèle en phase gazeuse dans un réacteur fermé et hétérogène, à diverses conditions thermo-chimiques. À partir des résultats des calculs de cinétique macroscopiques, des molécules pertinentes pour la formation de suie, appelées précurseurs de suie, ont été extraites en fonction de certains critères. Ceci permet d'introduire de compositions de précurseurs de suie dans des boîtes de simulation pour modéliser la formation de liaisons entre les molécules de précurseurs de suie avec un champ de force réactive empirique en utilisant des simulations de dynamique moléculaire.

L'impact des trois paramètres utilisés dans les calculs cinétiques macroscopiques se traduit dans les compositions des précurseurs de suie obtenues avec les simulations dynamiques moléculaires. Il s'avère que la température joue un rôle clé dans la formation des liaisons chimiques entre les précurseurs de suie. On a pu constater que le nombre de molécules aromatiques liés par une chaine alkyle aliphatique, ainsi que la présence des chaînes alkyles latérales, augmente avec la quantité de décane dans le mélange initial.

La cinétique d'oxydation des structures de croissances des trois classes, et la présence éventuelle des chaines alkyle latérales, a été étudiée par dynamique moléculaire avec quatre oxydants différents. On a pu démontrer que la cinétique diffère selon le classement des produits de croissance, mais également la présence de chaines alkyles impacte la cinétique d'oxydation.

Title : Development of a multi-scale approach using chemical kinetics and reactive force field molecular dynamics to model soot formation and oxidation.

Keywords : soot inception, soot oxidation, ReaxFF, multi-scale approach

Abstract : In this PH.D. thesis a multiscale approach —combining macroscopic gas-phase kinetic calculations and atomistic reactive force field simulations – has been applied to model the soot inception and early soot oxidation. A combustion gas-phase has been modeled in a heterogeneous closed reactor under various conditions. From the results of the reaction kinetic calculations, molecules relevant to soot formation, so called soot precursors, have been extracted according to certain criteria. This is done in order to allow to introduce these soot precursor compositions in simulation boxes to model bond formation between soot precursor molecules with reactive force field molecular dynamics. The impact on the modeled gas-phase composition due to a change in temperature, fuel mixture and equivalence ratio translate to the soot precursor compositions.

The influence of the differing compositions has been investigated on the rate and structure of the molecules formed through bond formation between soot precursors. The resulting structures compare well to previously reported experimental results. The bond formation rate between soot precursors is found to be linearly correlated with the temperature at which the soot precursors are generated. Additionally, it is found that the amount of aliphatically linked molecules, as well as the presence of sidechains in the modeled structures increases with the amount of aliphatic content of fuel mixture.

The impact of structural differences in the structures generated by bond formation between soot precursor, on their oxidation kinetics is tested. It can be shown that the kinetics are different for species that possess an aliphatic sidechain compared to those that do not.

Institut Polytechnique de Paris
91120 Palaiseau, France